DEVELOPMENT OF LOW LEVEL ^{226}Ra ACTIVITY ANALYSIS FOR LIVE FISH USING GAMMA-RAY SPECTROMETRY

DEVELOPMENT OF LOW LEVEL ^{226}Ra ACTIVITY ANALYSIS FOR LIVE FISH USING GAMMA-RAY SPECTROMETRY

By:

Zahra Chandani, M.Sc.

A Thesis

Submitted to the School of Graduate Studies

In Partial Fulfillment of the Requirements

for the Degree

Master of Science

McMaster University

MASTER OF SCIENCE (2014) McMaster University

(Medical Physics) Hamilton, Ontario

TITLE: **Development of Low Level ^{226}Ra Activity Analysis for Live Fish Using Gamma-Ray Spectrometry**

AUTHOR: Zahra Chandani

SUPERVISOR: Professor Soo H. Byun

NUMBER OF PAGES: iv, 146

ABSTRACT:

Radium contamination in the lakes near uranium mines and its intake by fish and other aquatic species are of great concern in environmental radiation protection. As an alternative technique to Liquid Scintillation Counting, we present a gamma-ray spectrometric method for low level ^{226}Ra analysis, particularly in live fish. The HyperPure Ge and a 4π NaI(Tl) array were employed as gamma-ray spectrometers. The ^{226}Ra spectra for each spectrometer were collected in order to compare their analytical performance. From the HPGe ^{226}Ra spectra, a detection limit of 6.81 Bq with 99% confidence was determined for an hour counting with the three strongest peaks combined. For the 4π NaI(Tl) ^{226}Ra spectra, in order to optimize the spectral analysis, a method applied to nine different energy regions was attempted and it turned out that the detection limit is best when the total integral count subtracted by the corresponding background is used. The detection limit of the 4π NaI(Tl) was 0.99 Bq with 99% confidence for one hour counting. A benchmark simulation for point source position dependence on relative peak efficiency showed a good agreement with the experimental data. To extend ^{226}Ra analysis to volumetric aqueous samples, MCNP Monte Carlo simulations showed that for three cylindrical volume sources, as the simulated volume source size increased from 60 ml to 125 ml to 250 ml, the full-energy peak efficiency in the energy range of interest for ^{226}Ra decreased by approximately 3% for each size increase, due to attenuation in the source volume. A method has been proposed in order to demonstrate this technique for a live fish, whereby a fish injected with ^{226}Ra would be kept in its own special aquarium and its gamma-ray spectrum collected.

ACKNOWLEDGEMENTS:

I would like to extend my immense gratitude to my supervisor, Dr. Soo Hyun Byun, who's dedicated countless hours in providing me with knowledge and guidance, and for his tremendous kindness and patience. I would like to thank Dr. William Prestwich and Dr. David Chettle for always willing to help me out with any questions that I had regarding this project, and for sharing wonderful and insightful knowledge during the morning Tea Times.

During my two years at McMaster University, I've made many friendships with fellow students in the department, and would like to thank all of them for their incredible support and helpfulness.

The administrative staff for the Medical Physics department deserves Kudos for being the most awesomest, funniest, group of secretaries I've ever met. Thank you Nancy for taking time out your busy schedule to provide words of motivation and humour whenever I'd drop by the office. Thank you Fiona for all your hard work in making this particular Graduate Program the most vibrant at McMaster.

Most of all, I'd like to thank my family for being my inspiration. For all the sacrifices you've made for me, I'm forever grateful.

TABLE OF CONTENTS

LIST OF FIGURES:

LIST OF TABLES:

CHAPTER 1: INTRODUCTION

1.1 Properties of ^{226}Ra

Radium (Ra) isotopes are important from the perspective of radiation protection and environmental protection. Radium occurs in minute quantities in the environment, but its high toxicity has motivated the continuing interest in methodology research for determination of Ra isotope in various media. [Diab & Abdellah, 2013] Radium is a radioactive element for which no stable isotope is known. The mass numbers of the known isotopes range from 206 to 230. Among them, ^{226}Ra and ^{228}Ra are very significant from a radiological protection standpoint due to their relatively long half-lives, presence in nature, and high radiation dose per unit intake. ^{226}Ra and ^{228}Ra are usually the only radium isotopes of environmental interest because their half-lives (1620 and 6.7 years, respectively) are long enough to allow considerable environmental accumulation. [Weiner, 2008 *pp.* 322-324] Therefore much public health attention has focused on their assessment and control in water and soil. Radium concentrations in environmental media can be the result of natural processes (as in the case of some groundwater), or associated with either nuclear fuel cycle activities (such as uranium mining and milling) or in nonnuclear industry activities (such as phosphoric acid production and oil-field brine disposal) [Vandenhove *et al*, 2010]. Radium isotopes are important in radiation safety because they can be easily incorporated into bones due to having similar properties to other elements from Group II (*i.e.* calcium) and produce short lived progeny radionuclides of high specific activity.

^{226}Ra originates from the natural decay series of ^{238}U. ^{226}Ra decays by emitting alpha particles with an energy of 4.870 MeV to ^{222}Rn, accompanied with an emission of 186.2 keV (3.59 %) γ-ray. [Heath, 1997 pp. 528-531] This decay follows by a few short-lived decay daughters as shown below in the ^{226}Ra decay scheme:

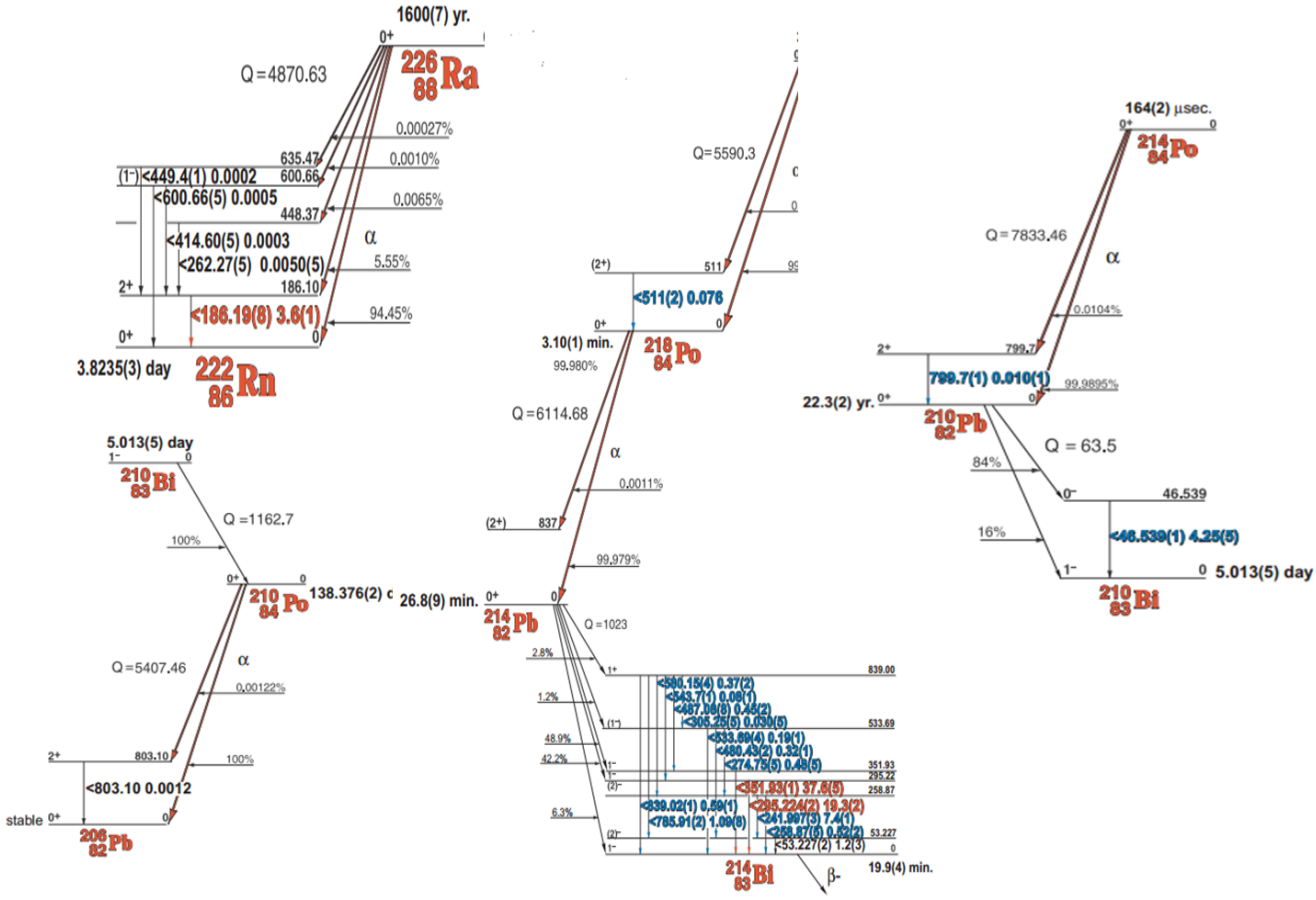

Figure 1.1: ^{226}Ra Decay Series [Heath, 1997 pp. 528-531]

^{226}Ra is of utmost concern because it not only is the most abundant of the radium isotopes, but, as can be seen from figure 1.1, it also decays into the most abundant radon isotope, ^{222}Rn. ^{222}Rn itself decays by the emission of an alpha particle. The daughter products are ^{218}Po, ^{214}Pb, and ^{214}Bi. These daughter products are highly radioactive and emit alpha particles as well as gamma-rays.

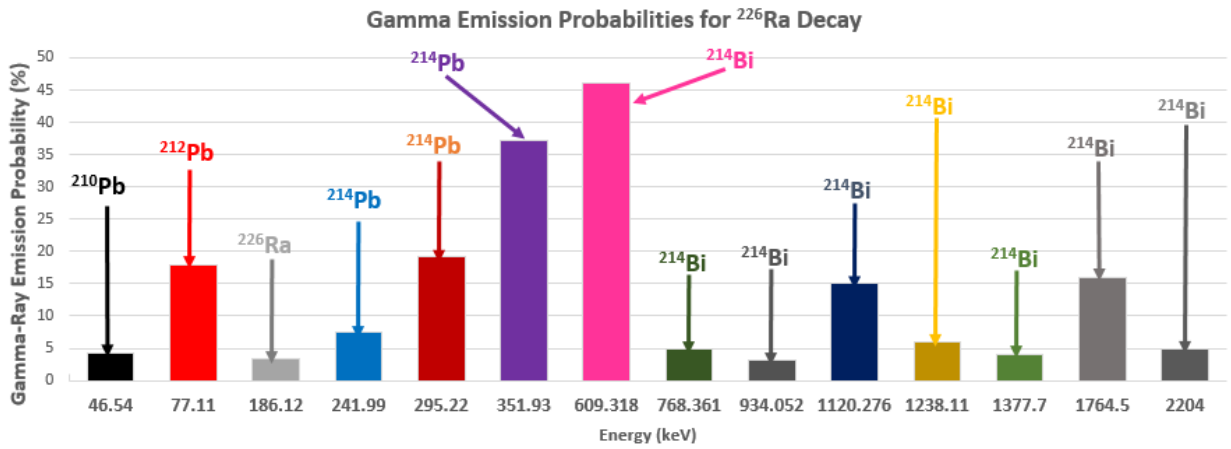

Figure 1.2: ^{226}Ra Gamma-Ray Emission Probability Chart [Heath, 1997 pp. 530]

Figure 1.2 shows the gamma-ray emission probability chart for ^{226}Ra and its progeny. It can be observed from figure 1.1 that the prevailing contribution to gamma-ray emissions in the ^{238}U decay chain occurs in the part of the decay chain below ^{226}Ra. Figure 1.2 shows that the majority of the total gamma-ray emissions in the chain occur in this sub series of the chain. A small contribution is made by ^{214}Pb but the vast majority is contributed by ^{214}Bi. The gamma-ray emissions range in energy from 0.2 to 2.5 MeV and are highly penetrating. Those nuclides prior to ^{226}Ra in the chain are very weak gamma-ray emitters when compared to ^{226}Ra and its decay products. Thus it is the short-lived progeny of radium that deliver majority of gamma-ray dose [Valkovic, 2000 *pp*. 11-14].

1.2 Biological effects of ^{226}Ra on aquatic organisms

Aquatic organisms display substantial ability to accumulate trace elements as well as radionuclides from water even when present in extraordinarily small concentrations. Compared to that on marine environment, information available on the distribution and the bioaccumulation of radionuclides in freshwater systems is scarce [Hameed *et al*, 1997]. Uptake of ^{226}Ra in biological systems undoubtedly depends upon the availability of the nuclide. ^{226}Ra, is the most

common radium isotope in natural waters because of the abundance and mobility of its parent ^{238}U in groundwater. [Vandenhove *et al*, 2010] Accurate information in relation to the biological effects of internally deposited alpha emitters including ^{226}Ra on non-human species in the environment is limited. This is because of the massive complexity of the ecosystem and its biodiversity. [Mothersill *et al*, 2014] The most important route of radium entry in organisms is through food or through ambient water [Hameed *et al*, 1997]. Among the aquatic fauna, relatively higher radioactivity concentrations are observed in shells and bones of animals than in soft tissues and muscle [Hameed *et al*, 1997]. Exposure in the environment is chronic and the doses are low, further complicating the task of attaining useful and relevant data [Mothersill *et al*, 2014].

1.3: McMaster University Radiation Biology Research Group's Investigation of Effects of Low Level ^{226}Ra in Fish

In 2012, the Radiation Biology Research Group at McMaster University established a study which sought to develop a rapid and reliable method for the determination of radionuclide contamination (especially ^{226}Ra) of aquatic biota (fish), measure the amount of radiation energy deposited by this radionuclide in the fish and to study some important effects on the fish caused by the ingestion of the radionuclide which could have adverse impacts on the individual fish and population. [Thompson, 2012] The approach in the study was to apply levels of radioactivity that actually occurred in the environment in uranium mining areas and to attempt to determine what if any impacts were caused by long-term exposure. [Mothersill *et al*, 2014]. The importance was on delicate biological endpoints such as induction of genomic instability, growth perturbation or intercellular signaling changes. [Mothersill *et al*, 2014] This was accomplished by implementing an environmentally pertinent 2-year dietary exposure investigation. This goal was achieved by

feeding fathead minnow fish species a steady ^{226}Ra diet consisting of between 1000 and 10,000 mBq/g of the isotope in their diet and monitoring the isotope levels in the fish. [Mothersill *et al*, 2014]. Essentially, assuming the size of the dissolved fish sample was 10 grams and equilibrium, the activity region which could be scaled to absorbed dose was 10 Bq to 100 Bq. The reason why such low levels of activity were investigated is because there was very limited biology data down at those levels. Their study observed what was happening in terms of such low level intake. In order to determine the ^{226}Ra in the fish, dose quantification was performed using the Liquid Scintillation Counting procedure, which will be described in detail below.

Figure 1.3: Species of Fathead Minnow used for ^{226}Ra analysis using Liquid Scintillation Technique [Mothersill et al, 2014]

1.4 Low Level ^{226}Ra Activity Quantification Techniques: Advantages & Disadvantages

A number of methods and techniques have been applied in the measurement of radium concentration in environmental media such as water, soil, and biological organisms. The following section addresses four of the typical methodologies used to detect and quantify radionuclides in various matrices. From a physics perspective, the four techniques to be discussed are gamma-ray spectrometry, alpha spectrometry, liquid scintillation counting & mass spectrometry.

1.4.1 Gamma-Ray Spectrometry

Gamma-ray spectrometry is a beneficial non-destructive method that allows the simultaneous determination of many radionuclides in a bulk sample, without the need for complicated and

time consuming radiochemical separations as embarked on for alpha spectrometry. [Diab & Abdellah, 2013] Particularly in samples where the radionuclide concentration is very low, each gamma-ray will be easily identified from other gamma-rays. [National Air and Radiation Environmental Laboratory, 2006]

Two of the main gamma-ray spectrometers used in low level ^{226}Ra analysis are High-Purity Germanium (HPGe) detectors and Sodium Iodide NaI(Tl) detectors. For high-resolution, radionuclide-specific gamma-ray spectrometry, HPGe detectors are most commonly used for identifying and quantifying the radionuclides and their activities. Samples of any matrix can be analyzed by these two detectors as long as the detectors are calibrated for the sample geometry and density (ρ) and radionuclide gamma-ray energy. Counting times can vary across a wide range, depending on the required detection limit [National Air and Radiation Environmental Laboratory, 2006]. NaI(Tl) scintillation detectors are known to have relatively poorer resolution than HPGe detectors, but are preferable in some particular types of analyses due to their relatively higher efficiency and their ability to operate under room temperature conditions, without the use of liquid nitrogen as in HPGe detectors. [Faanu *et al*, 2011] Instrumentation will be discussed in further detail in chapter 2.

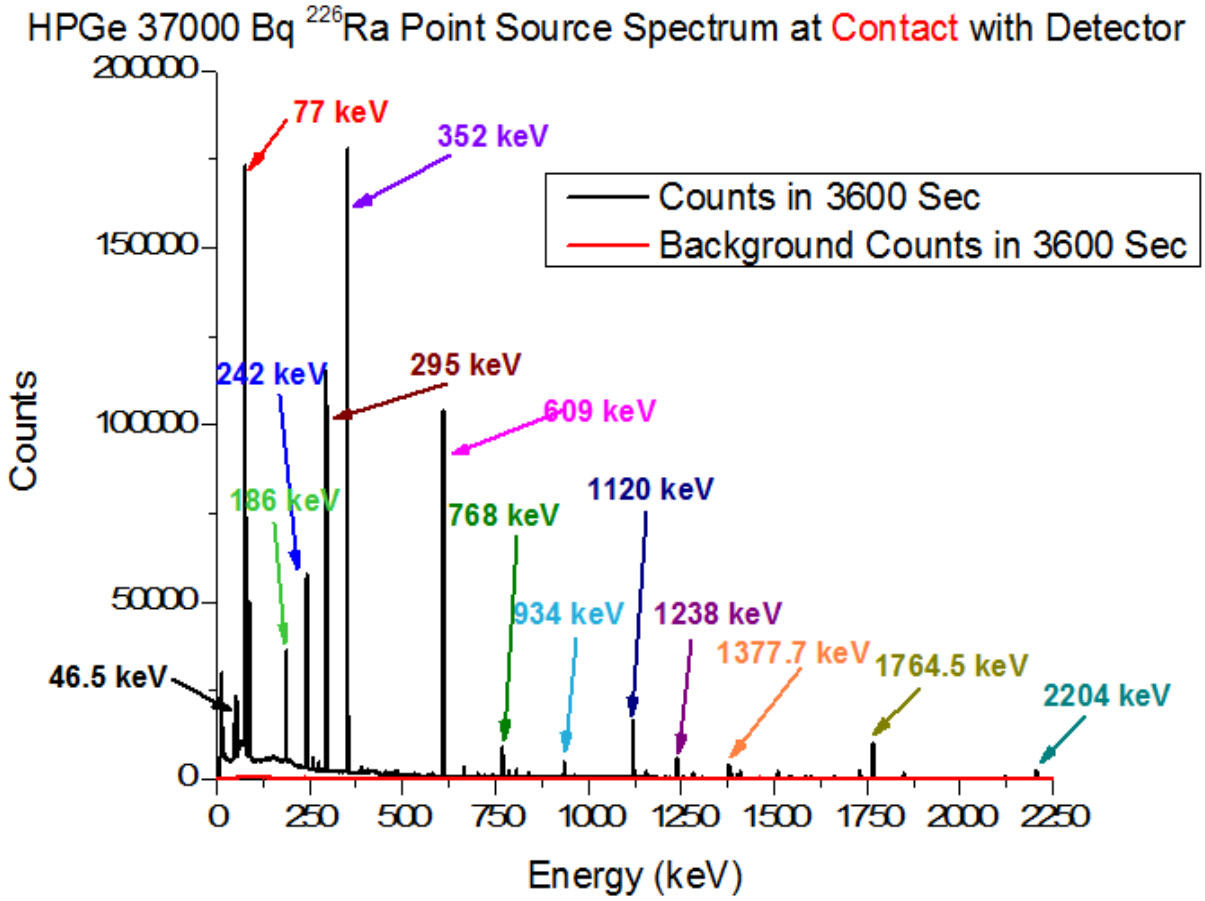

Figure 1.4: Gamma-Ray Spectrum Obtained for ^{226}Ra Point Source by a HPGe Gamma-Ray Spectrometer

Advantages:

The gamma-ray spectrometry technique is non-destructive, numerous radioisotopes can be measured simultaneously in one spectrum, and only physical preparation of the samples is needed. [Simsek & Cagatay, 2013] Gamma-ray spectrometry is the method of choice when a tedious sample treatment is not possible. Due to the low attenuation of gamma-rays, gamma-ray spectrometry offers the advantage that it can be used directly on unprocessed liquid or solid samples [Vandenhove *et al*, 2010].

Disadvantages:

Gamma-ray spectrometry is limited by the relatively poor efficiency of the HPGe detectors over a wide range of energy, the challenging task of precisely calibrating the efficiency of the detector, and the need to evaluate self-absorption effects. [Diab & Abdellah, 2013] Additionally, since environmental activity levels are quite low, if statistically better results are required, then lengthy counting times and relatively larger sample size are preferred. It is also challenging to minimize the background radioactivity levels around the detector. Any activity in the environmental sample itself essentially needs to be detected above the background activity. [Jabbar, 2010] Figure 1.4 below represents a gamma-ray spectrum obtained for a ^{226}Ra point source obtained for a 1 hour count by a HPGe Detector. It will be discussed in further in detail in chapter 3.

1.4.2 Alpha-Spectrometry:

Alpha-spectrometry is a radionuclide-specific method used in the laboratory to identify and quantify alpha-emitting radionuclides. Most laboratories employ an alpha-spectrometry system as a routine detection method to measure alpha-emitting radionuclides. [National Air and Radiation Environmental Laboratory, 2006] A high-resolution alpha spectrometry system utilized in a laboratory consists of a Si detector in a vacuum chamber electronically coupled to a multichannel analyzer operating over an energy range between 4 MeV and 8 MeV. [National Air and Radiation Environmental Laboratory, 2006] For routine low-level environmental radionuclide analyses, the typical sample processing time for most methods is one day for sample processing and one day for counting. [National Air and Radiation Environmental Laboratory, 2006]

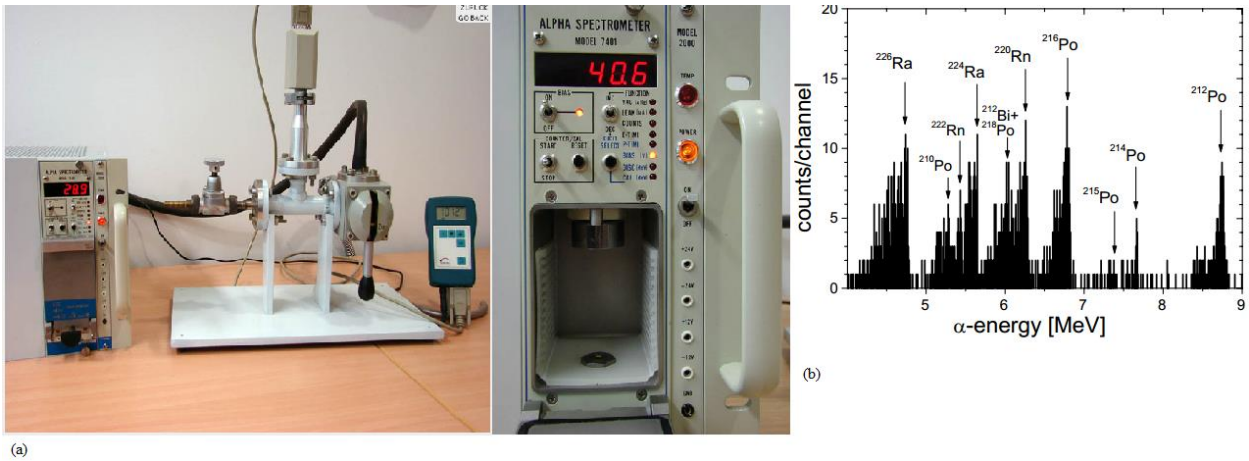

Figure 1.5: (a) Alpha Spectrometer [Vogt, 2009] & (b) Alpha spectrum obtained for a radium adsorbing manganese-oxide thin film exposed to a groundwater [Goldstein & Stirling, 2003]

Advantages:

In contrast to gamma-ray spectrometry, alpha-spectrometry presents the advantage of direct and simultaneous measurement of the activity of the isotopes of interest and not of its progeny, thus removing an important source of uncertainty. [Vandenhove *et al*, 2010] In this study however, the gamma-ray emissions are specifically of interest as the gamma-ray spectrometry technique is used. Additionally, alpha-spectrometry mostly features a considerably lower background contribution, permitting very low detection limits, even on smaller sample sizes, thus necessitating only a small sample size. [Vandenhove *et al*, 2010].

Disadvantages:

Because of the short range of alpha particles in matter, a sample must be chemically processed and the radionuclide deposited (electroplated or micro-precipitation) without interferences on a metal disk or filter paper mount. [National Air and Radiation Environmental Laboratory, 2006] Further disadvantages include self-absorption within the source and lengthy delays in between sampling and counting. [Simsek & Cagatay, 2013]

1.4.3 Liquid Scintillation Counting:

Liquid scintillation counting (LSC) involves the detection of light produced by the interaction of charged particles with an aqueous solution encompassing organic molecules (i.e., a scintillator as a solute) that transform the absorbed energy into light photons. A LSC is a low-resolution energy spectrometer that can make a distinction between pulses generated by alpha-interactions and those generated by beta-interactions and store the signals in two different spectral data files. [Vandenhove *et al*, 2010] As such, most LSC analyses involve the measurement of a single radionuclide when possible, thus eluding spectral interferences from other radionuclides. [National Air and Radiation Environmental Laboratory, 2006]

Advantages:

The main advantage of LSC is a remarkable reduction in background contribution in the alpha-channel (up to 30-fold) with respect to gamma-ray spectrometry. [Vandenhove *et al*, 2010] Combined with a practically 100% counting efficiency for alpha-particles in the liquid scintillation cocktail and no concerns about self-absorption in the source, this allows for low detection limits, comparable with alpha-spectrometry techniques, while at the same time offering a simplified source preparation. [Vandenhove *et al*, 2010]

Disadvantages:

Due to the fact that LSC is not a non-destructive sample processing method and is not a high-resolution spectrometer, sample analysis requires sample (non-aqueous) digestion into strong acid and chemical processing for the radionuclide of interest. In order to prepare a test source for counting, a sample must be processed so that contaminants are removed or the radionuclide (element) is isolated from the sample and chemically purified. [National Air and Radiation Environmental Laboratory, 2006] Solid samples must go through a digestion or an acid leaching process to make the radionuclide accessible for chemical purification. Precautionary measures

need to be taken in order to ensure that the chemical solution containing the purified radionuclide does not cause enhancement or degradation of the light output from the Liquid Scintillation cocktail used. [National Air and Radiation Environmental Laboratory, 2006] Measurement protocols may require correction for quenching, which is triggered by light degradation from chemical agents or color. [Simsek & Cagatay, 2013]

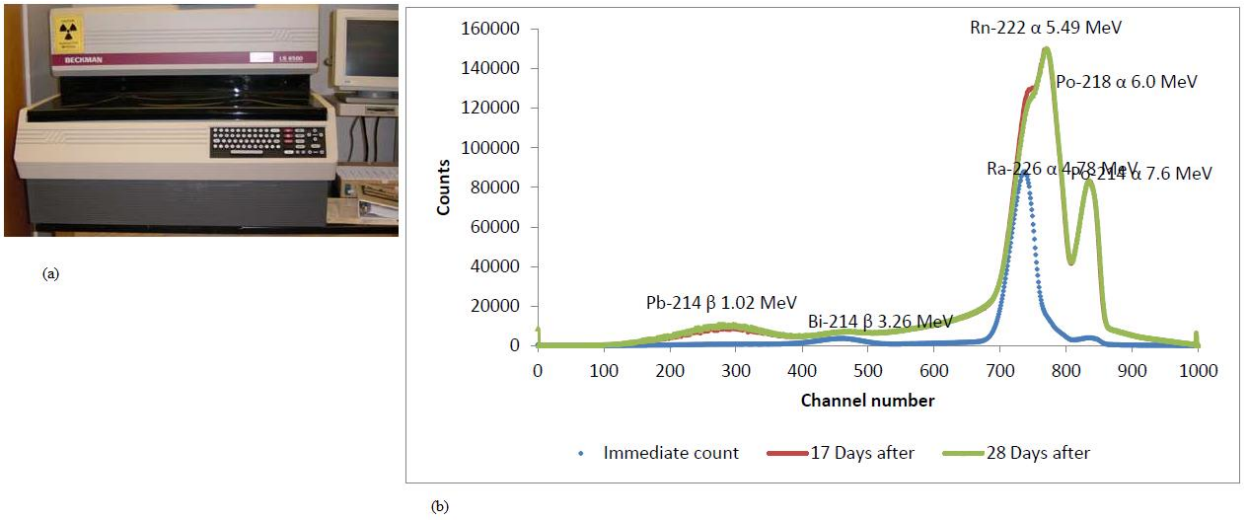

Figure 1.6: (a) Beckman LS 6500 Liquid Scintillation System [Ward, 2002] and (b) Beckman Liquid Scintillation Counter Spectrum Obtained for a sample of fish fed with ^{226}Ra diet for various counting times [Thompson, 2012]

Determination of ^{226}Ra in Fish using Liquid Scintillation Analysis

In a study performed by *Thompson*, 2012, a protocol was developed using the liquid scintillation method for ^{226}Ra contaminated fish species, particularly fathead minnows. The fish were fed a ^{226}Ra diet of 100 Bq/g. The objective was to study and monitor the uptake of ^{226}Ra in freshwater fish, and measure some important biological end points. The procedure was conducted by feeding fish with a steady supply of ^{226}Ra in their diet for 75 days. After 75 days, a group of five out of fifteen fish were selected at random and were sacrificed in order to be processed.

Calcination and acid digestion methods were chosen in order to obtain the sample in a liquid form for liquid scintillation counting. [Thompson, 2012] The calcination process in a furnace was necessary due to the fact that ^{226}Ra accumulates in the bone, and bone does not dissolve well in acid. After burning, a powdery ash was produced which then dissolves well in strong acid. [Thompson, 2012] A Beckman Liquid Scintillation Spectrometer was used to determine ^{226}Ra in the aqueous fish samples and the spectrum was observed. In order to evaluate the performance of the method for radionuclide analysis, the limit of detection was determined.

1.4.4 Mass Spectrometry

Detection of elements by mass spectrometry (MS) is not influenced by the atoms' radioactive or chemical properties. It is contingent only on the mass of the nucleus and the ion charge of the atom when applied to the mass spectrometer. Mass spectrometry measures the chemical concentration of solid particles with a specific mass. [Vandenhove *et al*, 2010] There is an assortment of methods by which samples may be introduced into the detection system. [National Air and Radiation Environmental Laboratory, 2006] The two variations of instrumentation most frequently used in the analysis of ^{226}Ra in water samples are thermal ionization mass spectrometry (TIMS) and inductively coupled plasma mass spectrometry (ICP-MS). [Vandenhove *et al*, 2010]

Advantages:

By and large, Mass Spectrometry techniques have superior quantification capabilities than radioactive decay-emission detection techniques for low-activity (< 0.1 Bq) samples of radionuclides with half-lives greater than about 100 years. [Vandenhove *et al*, 2010] Therefore mass spectrometry can theoretically offer a better detection limit for long-lived radioisotopes, such as ^{226}Ra. Decay-emission measurement techniques have difficulty distinguishing

background decay emissions per unit time from low-activity samples. [National Air and Radiation Environmental Laboratory, 2006]

Disadvantages:

As with most extremely sensitive analyses, mass spectrometry methods require sample preparation/digestion and chemical isolation and purification preceding introduction of the test source into the mass spectrometer. In addition, special highly purified reagents (e.g., nitric acid) and benchware (beakers, vials, etc.) must be used to avoid contamination of the sample with small trace quantities of the target element or radionuclide. [National Air and Radiation Environmental Laboratory, 2006]

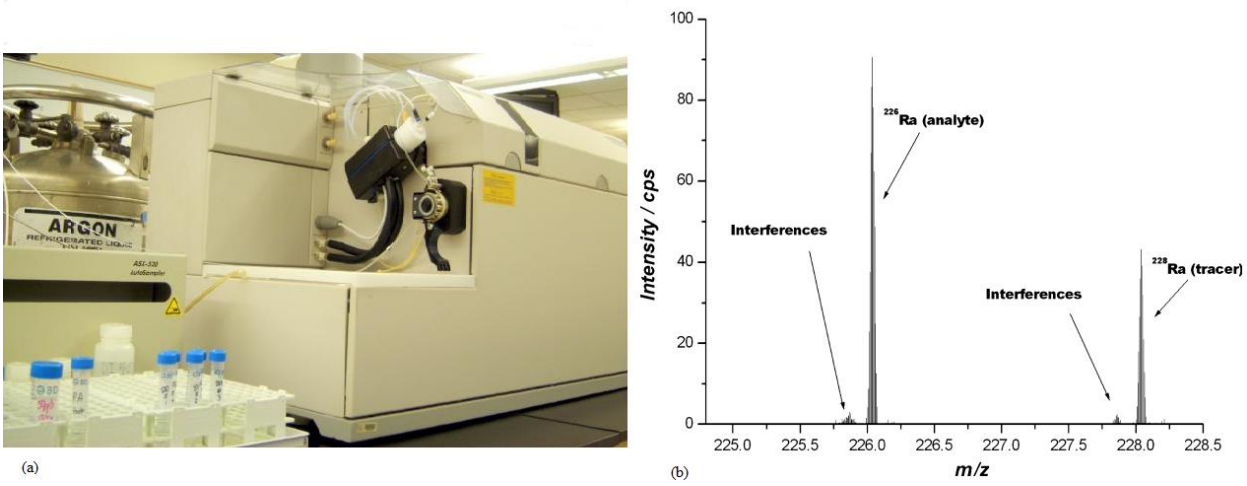

Figure 1.7: (a) Inductively Coupled Plasma Mass Spectrometer (ICP-MS) [New Mexico State University, 2013] and (b) Example mass spectrum obtained with an (ICP-MS) for a Caspian seawater sample containing ^{226}Ra [Varga, 2008]

1.5 Thesis Objectives:

The McMaster Radiation Biology group, in partnership with nuclear industry, has been investigating the effects of very low levels of ^{226}Ra in the environment, and in particular, its

uptake into fish and what happens in fish. When performing low level ^{226}Ra intake experiments, activity quantification is of greatest priority. The detection system must be able to measure activity at such low levels with statistical accuracy. This MSc project aims to measure and analyze ^{226}Ra radioactivity for live fish using gamma-ray spectrometry techniques using HPGe and 4π NaI(Tl) detectors, and determine the detection limit for both systems.

Radiation biologists measure and assess dose response curves. In a dose response curve, the horizontal axis represents absorbed dose, and the vertical axis represents the biological endpoint. This end point could represent for example, cell killing, or DNA damage as a function of absorbed dose. With cell survival curves, effectiveness per unit dose increases with increasing dose. If the absorbed dose range were to cover 10 data points of dose for example, then for each point, many fish data are required. Because biology data are usually unpredictable and unsteady, the more data available, the more beneficial. For example, if each point required data from 20 samples of fish, then for the next data point, another 20 fish would need to be grown, fed and sacrificed. Thus, it takes an incredible amount of time, space and resources to establish a dose response curve for fish contaminated with ^{226}Ra if using the liquid scintillation analysis technique. Furthermore, when fish are sacrificed, the sample cannot be taken to the liquid scintillation system right away. The sample must be burned and dissolved in strong acid, and it requires a lot of time commitment to perform these tasks. Sample preparation is tedious and lots of chemical preparation is involved. Whereas using live fish measurements are critically beneficial because with just one fish, many dose data points may be scanned. With gamma-ray spectrometry, sample preparation is comparatively easy, quick and non-destructive.

This project represents the first time where live fish measurements are to be used in order to analyze and quantify activity in ^{226}Ra contaminated fish. Previous approaches to analyzing ^{226}Ra

radioactivity in fish involved mass spectrometry and liquid scintillation analysis methods, which required fish sacrifice. The approach using live fish has not been performed before, and this projects aims to analyze the ^{226}Ra activity in live fish using gamma-ray spectrometry techniques assuming fair conditions for both the HPGe and 4π NaI(Tl) detector, and then seeks to determine which detector gives a lower detection limit, thus allowing activity levels in fish to be as low as possible.

If we are to be 95% confident of detecting a peak, the detection limit in counts of the peak would be:

$$L_D[Counts] = 2.71 + 3.29\sigma_0 \qquad (1.1)$$

Where 3.29 represents the risk coefficient, $2k_\propto$. If we are measuring the number of counts in a region-of-interest, then σ_0 represents the uncertainty in net counts close to zero, and can be shown to be $\sqrt{2C_B}$, where C_B represents the number of background counts. Background is partly due to external radiation and partly from within the sample itself [Gilmore, 2008 *pp* 251-253]. For a gamma-ray spectrometry measurement, the Detection Limit, in Bq, can be expressed as:

$$L_D[Bq] = \frac{L_D[Counts]}{\varepsilon_{abs} p_e t_c} = \frac{2.71+3.29\sqrt{2C_B}}{\varepsilon_{abs} p_e t_c} \qquad (1.2)$$

Where ε_{abs} represents the absolute efficiency of detector at the full-energy peak of interest, p_e represents the gamma-ray emission probability of the full-energy peak, and t_c represents the counting time used for spectrum acquisition. While equation 1.2 shows that detection limit improves with efficiency and the square root of the counting time, the background count rate will inevitably increase.

1.6 Literary Review

The amount of ^{226}Ra released during nuclear reprocessing activities is now present at such low concentrations in the environment that low-level techniques are becoming progressively imperative for environmental radioactivity measurement [Cinnaesakki, 2012] Many studies have been performed in order to acquire levels of ^{226}Ra radioactivity concentration in various environmental media. These studies were accomplished by using the various ^{226}Ra detection techniques mentioned above in section 1.4. Further, performance analysis results from these studies established detection limits for various counting times and shielding configurations for sources containing ^{226}Ra. A goal that was pursued by most studies was to lower the detection limit of their detection system, i.e. to obtain more statistical evidence in less time. [Verplancke, 1992]

Table 1.8.1: Review of significant studies on ^{226}Ra Detection Limit Results Using Various Detection Methods:

Publication	**^{226}Ra Source**	**Detection Method Used**	**Counting Time (sec)**	**Shielding Configuration**	**L_D**
1. Thompson (2012, Hamilton)	Fathead Minnow Fish Species fed with ^{226}Ra in diet	Liquid Scintillation Analysis	12000	N/A	7.46 mBq/g @ 95% Confidence
2. Mothersill *et al.* (2014, Hamilton)	Fathead Minnow Fish Species fed with ^{226}Ra in diet	Mass Spectrometry (ICP-MS)	N/A	N/A	0.3 Bq/L @ 95% Confidence
3. Faanu *et al.* (2011, Legon-Accra, Ghana)	Standard reference material containing mixed	ɣ-ray Spectrometry 3”x3” NaI(Tl)	86400	2 cm cylindrical lead shield	0.099 Bq @ 95% Confidence

	radionuclides including ^{226}Ra progeny				
4. Harb *et al.* (2014, Qena, Egypt)	Cultivated farms soil samples	ɣ -ray Spectrometry 3"x3" NaI(Tl)	194400	1 cm thick stainless steel & 3 cm thick lead	0.546 Bq/kg @ 95% Confidence
5. Keyser (2011, Oak Ridge, TN)	Standard reference material containing mixed radionuclides including ^{226}Ra progeny	ɣ -ray Spectrometry HPGe with well tube of carbon fiber material	154800	15 cm lead 0.1 cm tin 0.6 cm copper	2.04 mBq @ 95% Confidence
6. Chinnaesakki *et al.* (2012, Mumbai, India)	Soil sample containing ^{226}Ra	ɣ -ray Spectrometry HPGe with 50% Relative Efficiency	100000	7.5 cm lead	4.3 Bq/kg @ 95% Confidence
7. Jabbar (2010, Rechna Doab, Pakistan)	Soil sample containing ^{226}Ra	ɣ -ray Spectrometry HPGe with 30% Relative Efficiency	65000	15 cm lead 0.3 cm copper 0.4 cm tin	3.6 Bq/kg @ 95% Confidence
8. Kinsara *et al.* (2014, Jeddah, Saudi Arabia)	Soil equivalent standard containing ^{226}Ra	ɣ -ray Spectrometry HPGe with 40% Relative Efficiency	82800	Conventional ultra-low background shielding (Shielding Material &	1.3 Bq/kg @ 95% Confidence

				Dimensions Unspecified)	
9. Alrefae *et al.* (2013, Khaldia, Kuwait)	Standard reference material of mixed fish species containing ^{226}Ra (IAEA-414)	ɣ -ray Spectrometry HPGe with 80% Relative Efficiency	86400	Low background Ortec system (Shielding Material & Dimensions Unspecified)	3.67 Bq/kg @ 95% Confidence
10. Khandaker *et al.* (2012, Kuala-Lumpur, Malaysia)	Crushed samples of cement and bricks collected from construction sites	ɣ -ray Spectrometry HPGe with 30% Relative Efficiency	60000	Square Lead Shield 4 cm thick Length 14.5 cm Height 12.5 cm	0.8 Bq/kg @ 95% Confidence

The table above demonstrates that the Liquid Scintillation Analysis and Mass Spectrometry methods are far superior in detection limit compared with gamma-ray spectrometry methods, and that the well-type HPGe detector used in study #5 is far superior to the other HPGe detectors because of its exceptionally high efficiency and massive 15 cm lead shielding. In just 3.33 hours counting time, the Liquid Scintillation Analysis achieved detection limits comparable to those studies which used shielding and much longer counting times with their detectors. Due to the nature of the extremely low environmental levels of ^{226}Ra being analyzed in the above studies, very precise gamma-ray spectrometry analysis of weak sources was shown to be advantageous when the detector was shielded from the various activities present in most laboratories. The laboratory background was reduced drastically by putting the detector in a shield. [Verplancke, 1992]

In principle, full-energy peak efficiency will be proportional to the relative efficiency, which is provided in some of the above studies. In the table 1.8.1 above, Keyser, *2011* used a well-type HPGe detector in order to determine the system detection limit of various radionuclides as a function of counting time, including ^{226}Ra progeny. Due to the large solid angle of detection, a well-type detector provides a full-energy peak efficiency that is extremely large. If for instance we want to estimate the effect on system detection limit when the efficiency is increased by some constant *c*, in the case of a well type HPGe detector, we examine equation (1.2). Two detectors of the same type, in two completely different laboratories will be subjected to entirely different shielding conditions, thus the natural background radiation count will vary between the detectors. Thus, the detection limit will not be proportional to exactly the square root of the background count. Without knowledge of the background contribution from natural background and from within the source itself, it is difficult to estimate the exact improvement in detection limit. While the natural background contribution under the full-energy peak is reduced with adequate shielding, the full energy peak efficiencies are independent of shielding. Natural background radiation energies of interest when analyzing detection limit are those with similar energies from ^{226}Ra. Therefore, detector shielding is responsible for absorbing those gamma-rays. Thus, having shielding is extremely helpful when dealing with low level environmental ^{226}Ra radioactivity

analysis.

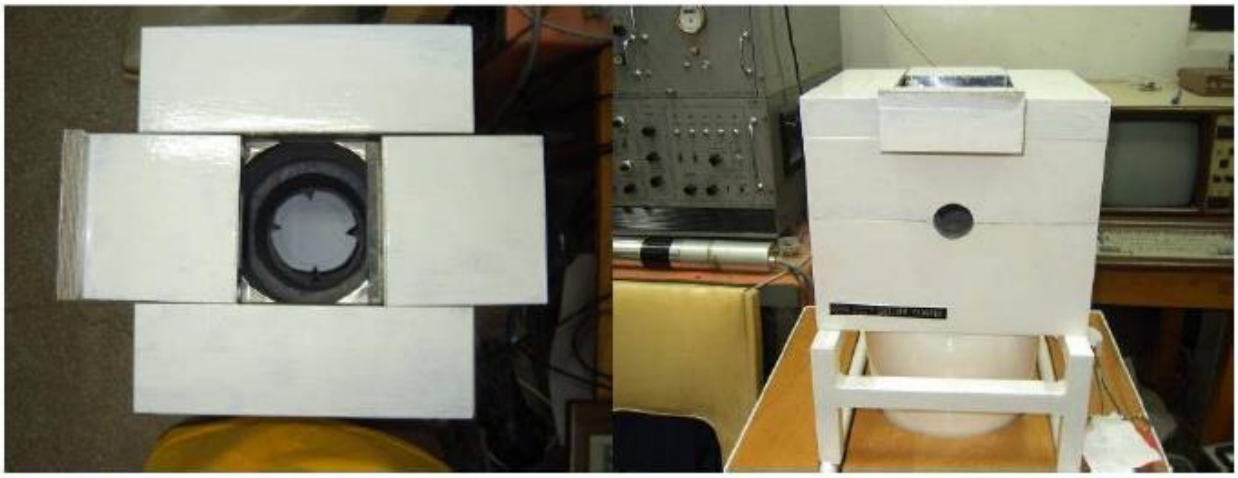

Figure 1.8: Example of a HPGe system heavily shielded with Lead [Daraban et al, 2012]

The above figure shows a HPGe system with typical heavily lead shielding. Referring to table 1.8.1, most of the studies reported their detection limit in terms of Bq/kg. Their results were normalized per sample mass. When analyzing a live fish sample, the fish itself is just a body, which increases in size, and the source is distributed within the fish body. The goal of this project was to develop an optimized method for measuring the activity of live fish and characterize the detection limit. This method intended to determine how much ^{226}Ra must a fish have in order for it to be detected with a given counting technique, namely using the HPGe & 4π NaI(Tl) detector. When considering a soil sample, there is background radiation inside the soil. Natural radionuclides in soil generate a significant component of the background radiation that the population is exposed to. Only natural radionuclides with $t_{\frac{1}{2}}$ comparable with the age of the earth or their corresponding decay products existing in terrestrial material such as ^{232}Th, ^{238}U, ^{235}U, ^{40}K and ^{14}C are of great interest. [Saleh, 2012] When considering a live fish fed with a ^{226}Ra diet, it contains natural ^{40}K background radiation within its body. As for external

background radiation in laboratory environments, the studies above have minimized that aspect with adequate detector shielding. Consequently, their results are mostly from the soil sample itself. If the soil sample volume is increased, then subsequently, background is changed. This is of significance due to fact that detection limit is proportional to the square root of the background counts. Accordingly, the above articles have detection limit results normalized per sample mass, assuming that the background count is proportional to sample mass. As an estimate, doubling the sample mass will approximately double the number of background counts, depending on detector size and sample volume.

With a heavily shielded system, the background on either side of and under the spectral lines of the source containing ^{226}Ra would be considerably less. The net peak area is not affected if the source isn't shielded, but the uncertainty in the net peak area does change. With a ^{226}Ra source, it's difficult to predict precisely how much effect heavy shielding will have on the spectrum obtained from the gamma-ray spectrometry results. This is due to the fact that it produces a Compton continuum, with many different gamma-rays emitted. Since lead reduces natural background by a significant factor, it is important to estimate the impact that a given thickness of lead shielding will have on the spectral analysis results for a ^{226}Ra sample.

Reduction in background radiation may be accomplished by installing a shield which will effectively absorb the unwanted radiations before they reach the detector. [Khandaker, 2012] Mathematically, the shielding effectiveness is expressed as

$$I = I_0 e^{-\mu x} \qquad (1.3)$$

Where I_0 is the intensity of the incident energy, μ is the linear attenuation co-efficient, x is the thickness of the shielding material. Lead is the conventional choice used as shielding material

due to its high density (11.342 g/cm^3), large atomic number (Z=82) and comparatively low buying cost. [Khandaker, 2012] In order to estimate by what factor the background radiation energies associated with radium would be attenuated by progressive centimetres of lead shielding, we may consider, as an absolute upper limit of attenuation, the linear attenuation coefficient, and the corresponding reduction factor $\frac{I}{I_o}$ at the energies of interest:

Table 1.8.2: Linear Attenuation Coefficients for Lead at the ^{226}Ra Spectral Energies and Reduction Factors at Lead Thickness of Interest: [Hubbell & Seltzer, 1996]

Energy (keV)	$\frac{\mu}{\rho}$ $(\frac{g}{cm^3})$	μ (cm^{-1})	$\frac{I}{I_0}$				
			$x = 2\ cm$	$x = 3\ cm$	$x = 4\ cm$	$x = 7.5\ cm$	$x = 15\ cm$
77	2.81	31.86	2.11×10^{-28}	3.06×10^{-42}	4.45×10^{-56}	1.64×10^{-104}	2.70×10^{-208}
186	1.28	14.55	2.30×10^{-13}	1.10×10^{-19}	5.30×10^{-26}	4.05×10^{-48}	1.64×10^{-95}
242	0.75	8.49	4.23×10^{-8}	8.71×10^{-12}	1.79×10^{-15}	2.4×10^{-28}	5.02×10^{-56}
295	0.43	4.91	5.44×10^{-5}	4.01×10^{-7}	2.96×10^{-9}	1.20×10^{-16}	1.04×10^{-32}
352	0.31	3.56	8.01×10^{-4}	2.27×10^{-5}	6.42×10^{-7}	2.45×10^{-12}	6.01×10^{-24}
609	0.12	1.40	6.12×10^{-2}	1.51×10^{-2}	3.74×10^{-3}	2.81×10^{-5}	7.92×10^{-10}
768	0.09	1.07	1.17×10^{-1}	4.02×10^{-2}	1.38×10^{-2}	3.23×10^{-4}	1.05×10^{-7}
934	0.08	0.87	1.75×10^{-1}	7.32×10^{-2}	3.06×10^{-2}	1.45×10^{-3}	2.10×10^{-6}
1120	0.07	0.74	2.28×10^{-1}	1.09×10^{-1}	5.21×10^{-2}	3.92×10^{-3}	1.54×10^{-5}
1238	0.06	0.67	2.60×10^{-1}	1.33×10^{-1}	6.77×10^{-2}	6.42×10^{-3}	4.12×10^{-5}
1377.7	0.06	0.63	2.84×10^{-1}	1.52×10^{-1}	8.09×10^{-2}	8.97×10^{-3}	8.04×10^{-5}
1764.5	0.05	0.56	3.29×10^{-1}	1.89×10^{-1}	1.08×10^{-1}	1.55×10^{-2}	2.41×10^{-4}
2204	0.05	0.5	3.58×10^{-1}	2.14×10^{-1}	1.28×10^{-1}	2.12×10^{-2}	4.50×10^{-4}

The above results show that there is an enormous amount of background radiation attenuation by various thicknesses of lead at the ^{226}Ra radiation energies of interest. However, as the amount of shielding decreases, then, as expected the reduction of background is less and less. At energies less than 609 keV, the attenuation factors for all lead thicknesses are so large that in theory, essentially all of the background is eliminated. In principle, the attenuation factors in table 1.8.2 can be used to approximate the reduction in natural background when lead shielding is used. The approximation doesn't account for the possibility that there also may be traces of radioactive materials in the lead, thus promoting secondary radiation. [Verplancke, 1992] Additionally, when analyzing the ^{226}Ra spectrum, some proportion of the apparent background is actually created indirectly by Compton scattering and so on from other gamma-rays in the radium, higher energy gamma-rays, which still contribute to the spectrum. Therefore the above estimates are only representative of an upper limit of the reduction we can expect.

According to *Verplancke*, 1992, when a source is measured by a standard 25% HPGe detector with a 10 cm thick lead shield installation, the environmental background is reduced by a factor of 1000. In principle this would enable the measurement of $\sqrt{1000} \approx 30$ times weaker sources with the same statistical accuracy. While shielding was not installed for the HPGe detector in this project, its effect on attenuating natural background radiation can be approximately estimated by scaling for the effect of shielding using the attenuation properties of lead and referring to table 1.8.2. Considering that the density of lead is $11.34 \frac{g}{cm^3}$, a 10 cm thick lead rectangular shield, with inner dimensions of $30\ cm\ x\ 30\ cm\ x\ 40\ cm$ and outer dimensions of $40\ cm\ x\ 40\ cm\ x\ 50\ cm$ would consist of a mass of approximately 500 kg.

CHAPTER 2: METHODOLOGY

Precise determination of radionuclides mainly depends on the detailed characterization of the selected detector. The most important characteristics of a gamma-ray detector are the energy resolution and the detection efficiency. This chapter outlines the properties, features and applicability of the two detectors used in this study, HPGe and 4π NaI(Tl). Also underlined will be the methodological approach used reduce the detection limit of ^{226}Ra as low as possible.

2.1 Instrumentation: General overview for gamma-ray detectors

The most commonly used gamma-ray spectrometers are made up of sodium iodide NaI(Tl) scintillation detectors or Hyper-Pure Germanium (HPGe) semiconductor detector, coupled to a multichannel analyzer. The energies of gamma-rays emitted from radionuclides in a sample of the material being investigated are generally presented in a spectrum as a function of the pulse height. [Faanu *et al*, 2011] Compared to germanium detectors, NaI(Tl) detectors have lower resolution. They are however, preferred in certain types of analyses owing to their relatively higher efficiency and the capability to operate at room temperature. The energy resolution of the NaI(Tl) detector is typically 80 keV at 1332 keV in contrast with HPGE detectors with resolution in a range 2 keV at 1332 keV. [Gilmore, 2008, pp 218] It is well known that the better the energy resolution, the more superior the detector is in terms of being able to resolve between two radionuclides whose energies lie close to each other. In addition to the high density of the crystal (about 3.67 g/cm^3), the higher effective atomic number accounts for the high efficiency of the NaI(Tl) compared to HPGe detectors [Faanu *et al*, 2011]

In general terms, if spectrometry and thus identification of radionuclides is of utmost importance, then the HPGe must be the detector of choice. In other situations, for example, if only one or two

nuclides are to be measured and therefore energy resolution is not of particular concern, scintillation detector systems are a reliable low cost option. While the number of counts in a germanium spectrum may be fewer in number than a NaI(Tl) detector, they are concentrated within a narrow energy interval, whereas the counts in the NaI(Tl) gamma-ray spectrum are spread over a wider interval. This allows potentially for easier peak identification with a germanium detector. Table 2.1 summarizes the major differences between NaI(Tl) and HPGe detectors.

Table 2.1: Comparison of the characteristics NaI(TI) and HPGe detectors [Gilmore, 2008, pp 218]

NaI(Tl)	**HPGe**
Cheaper (×10)	More Costly
More efficient (×10)	Less Efficient
Room-temperature operation	Low temperature operation (77 K)
Sensitive to temperature	Insensitive to temperature
Sensitive to anode voltage (V)	Insensitive to bias voltage
Poor energy resolution	Good energy resolution

2.2 Instrumentation used in this study

HPGe Detector:

Table 2.2 HPGe detector type and properties:

Detector Type:	Coaxial N-type

Detector Model:	GMX 30190
Detector Diameter:	57.5 mm
Detector Length:	56.0 mm
Operating Bias:	-3895 V
Relative Efficiency at 1.33 MeV, ^{60}Co:	27%
Resolution (FWHM) at 1.33 MeV, ^{60}Co:	2.09 keV
Signal Processing Electronics, Shaping Parameters & ADC:	
Preamplifier Type:	Resistor Feedback
Digital Signal Processing Model:	DSPEC-PLUS
Rise Time:	8 μs
Flattop Width:	2.4 μs
Amplification Gain:	0.8
ADC Conversion Gain:	16,384 Channels

The first gamma spectrometer used in this study was an HPGe detector. The specifications of the detector are given in table 2.2. The semiconductor detector used was made up of N-type high-purity germanium crystal. This detector belongs to the GAMMA-X series, a coaxial germanium detector with an ultra-thin entrance window. [Ortec, 2011] A thin entrance window is very beneficial for low level ^{226}Ra activity analysis, as it enables a wide gamma-ray energy range to be analyzed. The detector was connected to an RC feedback charge sensitive preamplifier. The detector high voltage bias was provided through the preamplifier. The output pulses from the preamplifier were collected by a digital signal processing electronics (DSPEC Plus, ORTEC).

Unlike the traditional analog signal processing where the pulses from the preamplifier are processed by a shaping amplifier and then digitized by a peak-sensing ADC, the DSPEC Plus digitally processes the pulses directly from the preamplifier using a quasi-trapezoid pulse shape. [Vo, 1999] Two important parameters controlling this pulse shape were the rise time, which was 8 μs, and flattop width, which was 2.4 μs. The rise time was roughly equivalent to twice the shaping time set on a analog shaping amplifier, and the flattop adjusted the width of the top of the quasi-trapezoid pulse. [Vo, 1999] The DSPEC Plus was connected to a PC. For spectrum collection, ORTEC GammaVision 32 Program was used. Throughout the experiment, the detector was biased at -3895V. The amplification gain was adjusted to 0.84 keV/channel, and ADC conversion gain was 16383 channels. The block diagram for the detector's signal processing is presented in figure 2.1.

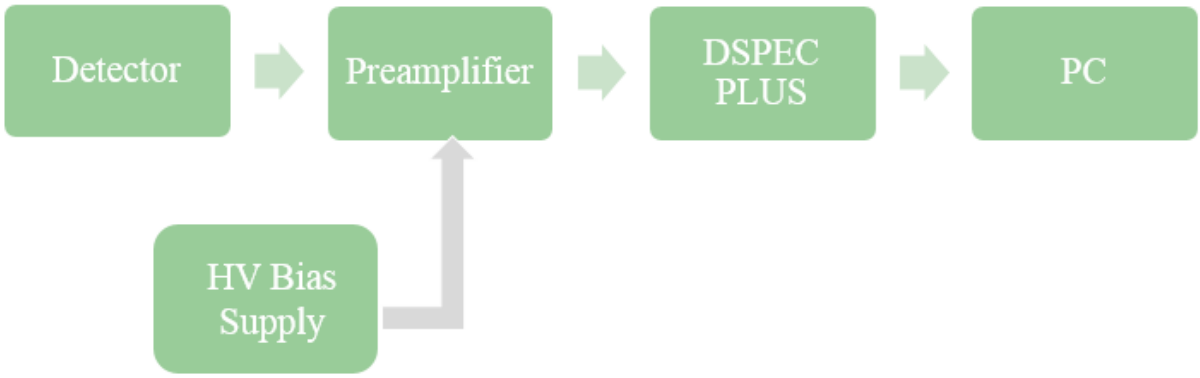

Figure 2.1: Block diagram for signal processing electronics used for the HPGe detector

The 4π NaI(Tl) Array:

As this study pertains to optimizing system detection limit with live fish measurements using gamma-ray spectrometry, activity quantification of a radioactive material dispersed in aquatic biota in the environment would greatly benefit from the employment of more than one detector to

enhance detection efficiency. In this study, the use of an array of nine different square-type NaI(Tl) detectors is proposed.

A 4π NaI(Tl) detector array has been developed at McMaster Accelerator Laboratory for *in vivo* neutron activation analysis, which requires low level gamma-ray spectrometry. [Byun et al, 2004] The spectrometer originally consisted of eight rectangular NaI(Tl) detectors with square cross-section. With this configuration, almost the whole direction of the gamma-ray emission was covered, except for the sample access hole. Recently, a ninth detector has been added to system in order to increase detection efficiency, this configuration produces a solid angle of 3.96π, almost 4π. The high efficiency is inevitably accompanied by much more severe coincidence summing than a single cylindrical or coaxial detector, and this makes experimental efficiency calibration difficult by limiting radionuclides available to coincidence-free sources, i.e. pure single-gamma emitters. [Byun et al, 2004]

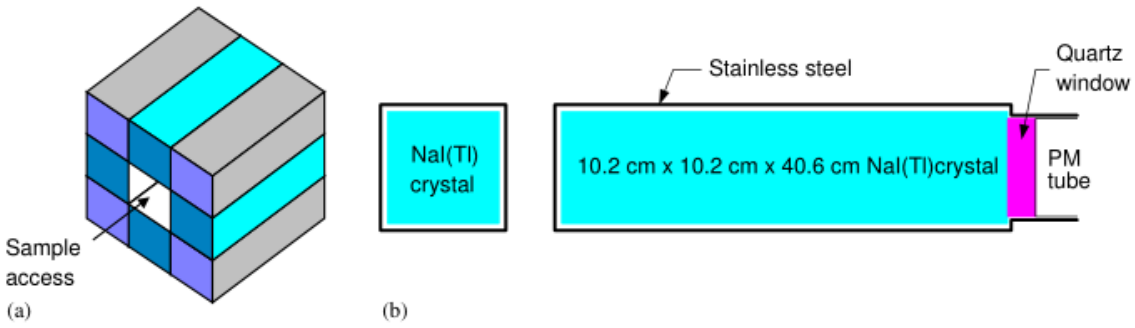

Figure 2.2: Layout of the 4π NaI(Tl) gamma-ray detector array (a) and the cross-sectional view of a detector unit (b). [Byun et al, 2004]

The cross-sectional size and the length of a NaI(Tl) crystal are $10.2\ cm\ x\ 10.2\ cm\ x\ 40.6\ cm$, respectively. The housing of the NaI(Tl) crystal is 1 mm thick Stainless steel. The ninth central

detector is a $10.2\ cm\ x\ 10.2\ cm\ x\ 10.2\ cm$ cube which has been placed at the back of the central aperture of the detector.

Figure 2.3: McMaster University 4π NaI(Tl) gamma-ray detector array

The photograph above illustrates the 4π NaI(Tl) gamma-ray detector array. The 4π NaI(Tl) detector has lead shielding incorporated in order to attenuate natural radiation. In addition, the detectors are surrounded with resin shielding. This is due to the fact that the McMaster Accelerator Facility performs a lot of experiments involving Neutron Activation. The resin is responsible for slowing down and absorbing the neutrons. Incoming neutrons undergo multiple scattering within the resin material. Eventually their energy is reduced to less than a few eV, and they then get absorbed by the boron in resin. Without the shielding, the fast neutrons would get absorbed by the Iodide in the NaI crystal, thus becoming radioactive. This would subsequently result in undesired β^- emission within the detector.

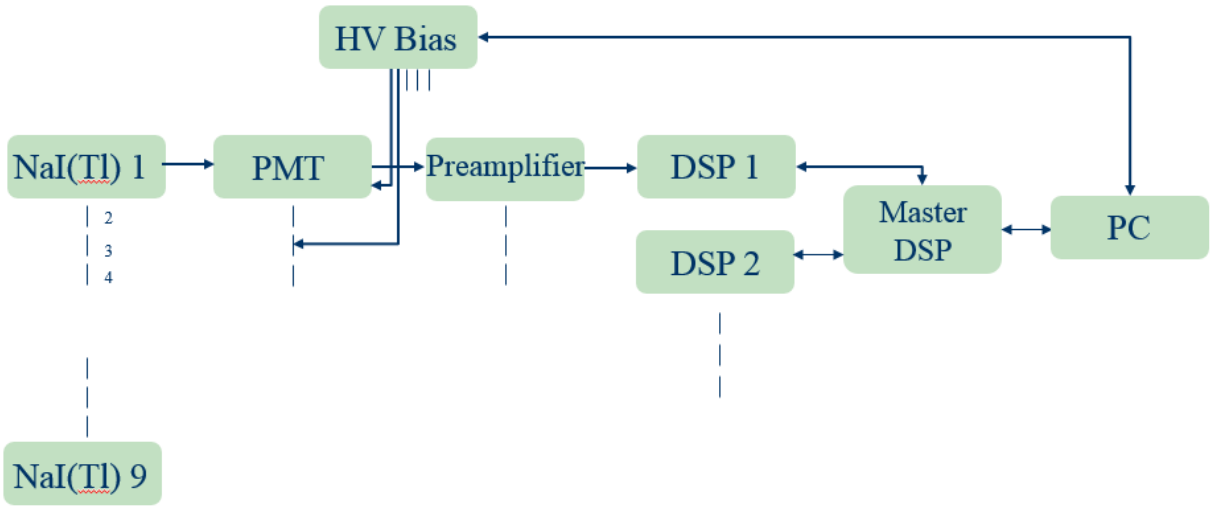

Figure 2.4: Signal Processing Electronics Block Diagram for the 4π NaI(Tl) Detector

The signal processing of each detector in the original eight NaI(Tl) gamma-ray detector array was configured to satisfy multi-mode spectroscopy including singles, coincidence and anticoincidence modes. The improved nine NaI(Tl) gamma-ray detector has been upgraded to Digital Processing Systems for each detector. Figure 2.4 shows the block diagram of the signal processing electronics. The figure below illustrates the nine DSP's connected to each of the detectors. A preamplifier for each detector can be seen behind each detector, which leads to the respective DSPs.

Figure 2.5: Digital Processing Systems Configuration for the 4π Nine NaI(Tl) Detector Array

Spectrum accumulation and on-line analysis are controlled by software. Since the PMT gain of each detector unit is slightly different and time-dependent gain drift is also different for each detector, the voltage of each unit was adjusted using the HV supply control software, written in Matlab, in order to keep all detector peak positions aligned with each other. The tuned condition is usually maintained up to a few days. [Byun et al, 2004] Spectra can be accumulated in singles, coincidence, and anti-coincident modes. Figure 2.6 below shows the PC which is used for spectrum accumulation, along with a snapshot of the software.

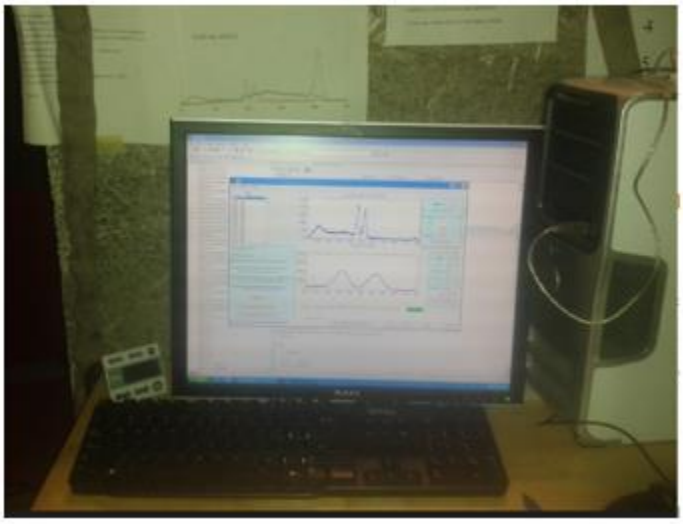

Figure 2.6: PC used for spectrum accumulation and on-line analysis

2.3 HPGe Detector Spectrum Collection Procedural Approach:

The first segment of this project involved efficiency characterization of the HPGe detector whose properties are mentioned above in the equipment section. A reference standard calibration point source located in a small vial and comprised of mixed $^{152/154}$Eu was used for the efficiency characterization. A source holder was connected to the detector. The source was inserted into the holder, 10 cm from the detector end cap, and was counted for 1 hour. The source-to-detector configuration is illustrated below.

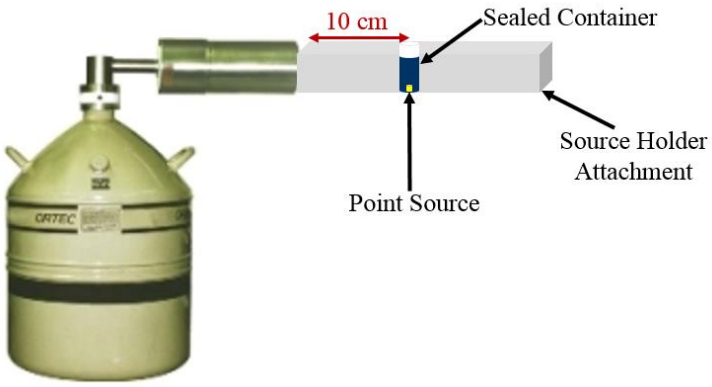

Figure 2.7: HPGe Detector Source-to-Detector Distance Configuration

The activity of the mixed source on Nov 25, 2009 was the following:

^{152}Eu: 1.20 MBq (5% uncertainty), ^{154}Eu: 145 kBq (5% uncertainty). [McMaster Med Phys 4R06/6R03 Lab Manual, 2007] An activity correction was subsequently applied for this mixed source. GammaVision 32 software was used for spectrum collection and setting the DSPEC Plus shaping properties. The following picture shows the spectrum collection process on the computer connected to the HPGe detector:

Figure 2.8: ORTEC GammaVision 32 software used for spectrum acquisition and on-line analysis

2.4 4π NaI(Tl) Detector Array Spectrum Collection Procedural Approach:

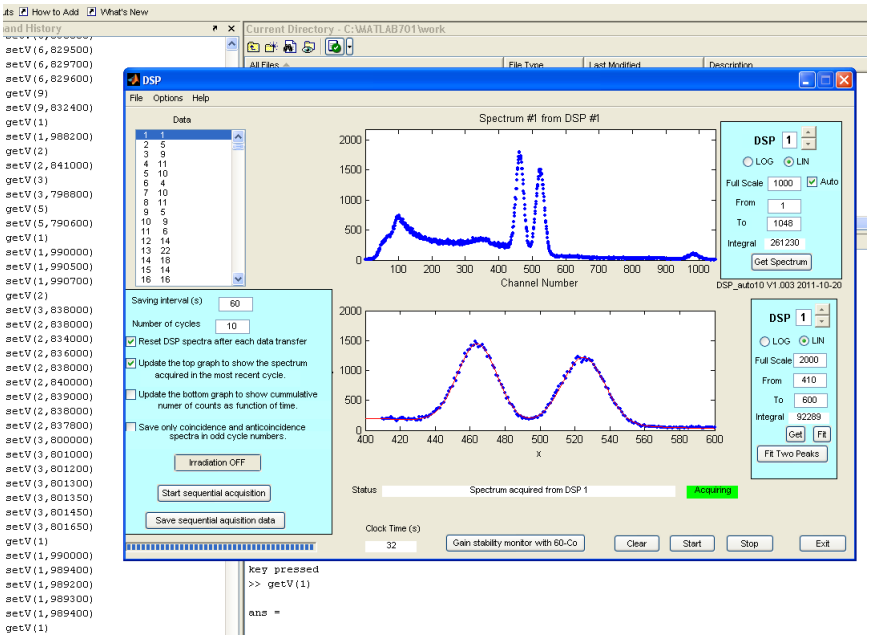

Figure 2.9: Spectrum acquisition software used for 4π NaI(Tl) Detector

In order to perform energy calibration of the 4π NaI(Tl) detector, a ^{60}Co point source was inserted into the detector. For each of the nine detectors, the pc software was used to acquire the spectrum. The software performed peak fitting for the ^{60}Co spectrum. The centroid channels corresponding to both the 1.17 MeV 1.332 MeV full-energy peaks were calculated and displayed by the software. The centroid of the 1.332 MeV peak was made to be aligned at channel 1000 by adjusting the high voltage gain of each detector individually using commands in Matlab. Figure 2.9 above shows the software used to perform this on-line analysis.

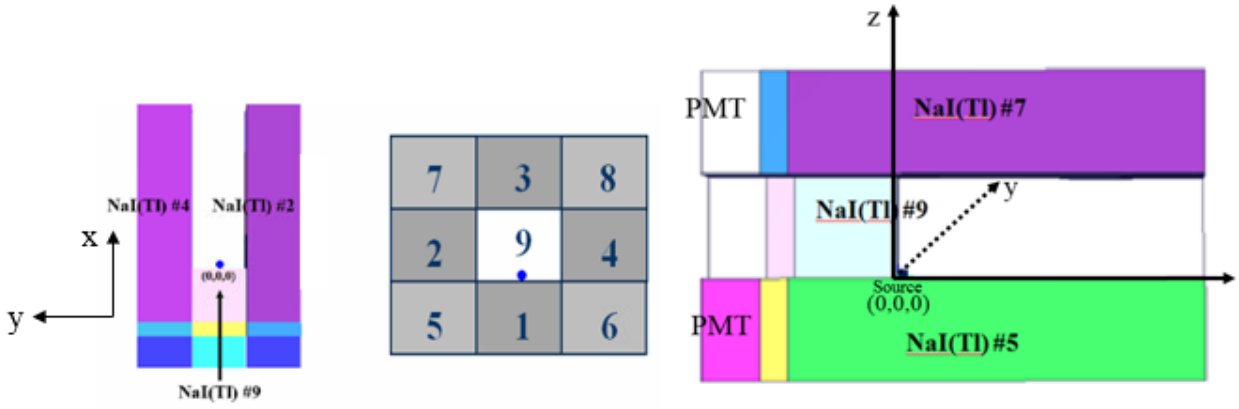

Figure 2.10: ^{226}Ra point source placement in 4π NaI(Tl) Detector

Once all the detectors were equally aligned, the 37 kBq ^{226}Ra point source, which was used for the HPGe detector efficiency calibration, was inserted into the central aperture of the 4π NaI(Tl) Detector and placed at the very back, touching the 9th central detector. See source placement in the figure above. The source was counted for 10 minutes and the spectrum was saved. The source was then moved 3 cm in the *+x* direction and was counted for 10 minutes. This process was repeated with the source position every 3 cm until it essentially reached the edge of the detector. The source was then removed and a 12 hour background count was performed. The

spectra for each of the source positions was plotted in Excel. In order to determine which peaks corresponded to what energies, the following energy calibration equation was obtained:

$$Energy\ (keV) = (1.3485 * \ Channel\ Number) - 20.339 \quad (2.1)$$

Using the acquired spectra for the ^{226}Ra point source, with the application of OriginPro peak fitting software, the four most well isolated spectral peaks were analyzed for each of the seven source positions. For each spectral line, the peak area per unit time was divided by the emission rate. A plot of relative peak efficiency dependence on source position was created for these four representative energies (609 keV, 1377.7 keV, 1764.5 keV & 2204 keV). These peaks were chosen because they were fairly well isolated, allowing for a greater degree of freedom with respect to defining the peak boundaries. This analytical method was performed in order to provide a benchmark against which the MCNP Monte Carlo method results could be assessed.

2.5 Optimization of 4π NaI(Tl) System Detection Limit:

For the 4π NaI(Tl) detector, in order to achieve the most ideal detection limit for ^{226}Ra, not only individual peaks, but entire energy interval regions needed to be considered. This was due to the fact that the entire spectrum consisted only of ^{226}Ra and daughter isotopes. Therefore, the surrounding and underlying Compton continuum contained valuable counts. The question needed to be addressed was, which energy interval would give the best detection limit? Resultantly, in order to optimize the 4π NaI(Tl) detection limit, a protocol was established and applied to nine different energy intervals. The following figure shows the nine spectral indices attempted for detection limit optimization for the ^{226}Ra point source spectrum obtained in the 4π NaI(Tl) Detector:

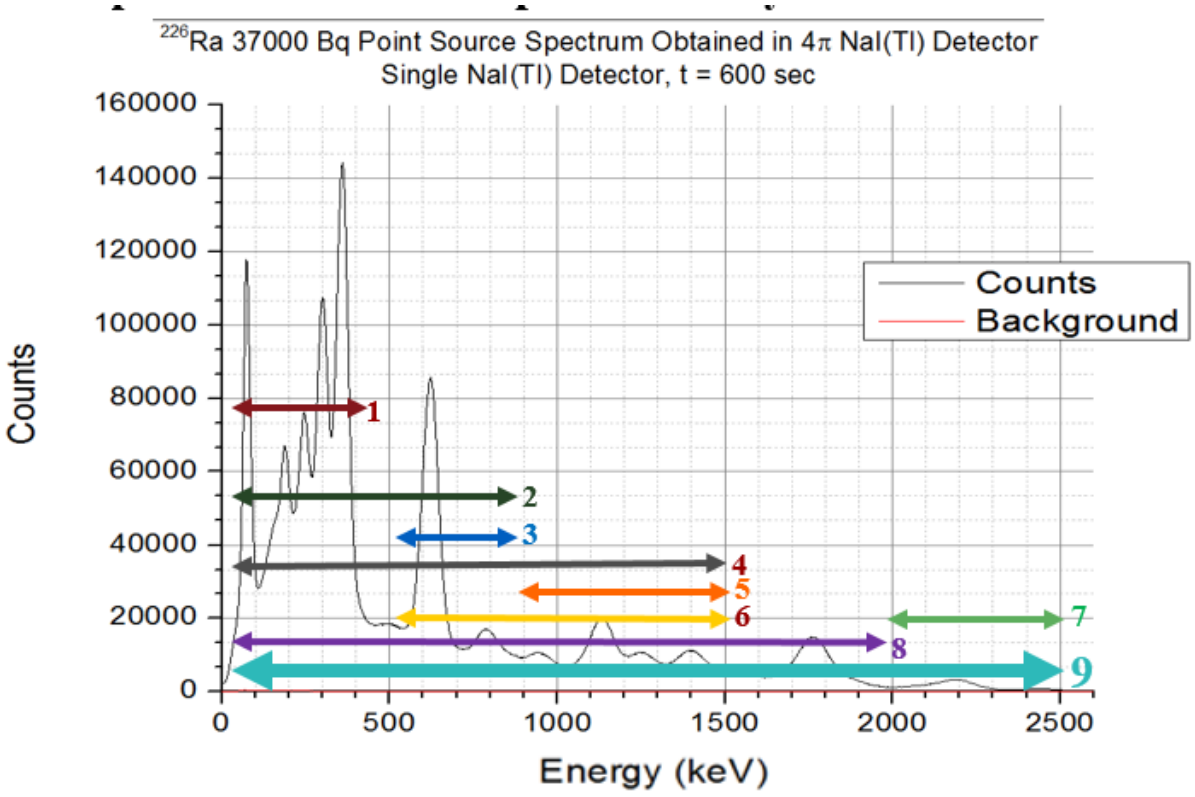

Figure 2.11: Nine spectral indices attempted for 4π NaI(Tl) Detection Limit Analysis

Due to the fact that detection limit is proportional to the square root of the background counts, index 7 was included in the analysis as it had a lower Compton contribution.

The algorithm was applied by using the following procedure:

1. For each spectral index of the 4π NaI(Tl) ^{226}Ra point source spectrum, ^{226}Ra integral and background integral were determined and background integral was subtracted from the ^{226}Ra integral (^{226}Ra integral – Background Integral)
2. Using the coefficients of confidence level, the detection limit in counts, L_D [counts], was calculated for each spectral index
3. The L_D in [counts] was divided by the sample counting time
4. The (^{226}Ra integral – Background Integral) was divided by the sample counting time
5. A calibration constant was created using the following formula:

$$Calibration\ Constant = \frac{\frac{(226_{Ra}\ Integral - Background\ Integral)}{t_c}\frac{counts}{sec}}{37000\ Bq} \quad (2.2)$$

6. The L_D for each spectral index was determined with the following final equation:

$$L_D\ [Bq] = \frac{\frac{L_D[counts]}{t_c\ [sec]}}{Calibration\ Constant\ [\frac{counts}{sec}/Bq]} \quad (2.3)$$

For an unknown ^{226}Ra source, its activity can be determined if the detector's absolute peak efficiency calibration curve has been determined for the same source-to-detector distance. Since the daughter radioisotopes are in secular equilibrium with their parent, they are decaying with the same disintegration rate as ^{226}Ra. The following equation can be used to determine the activity under the peak of any of the daughter radioisotopes:

$$Activity\ [Bq] = \frac{\frac{Area_{Peak} - Area_{Background}}{t_c}\frac{counts}{sec}}{\varepsilon_{abs} p_e} \quad (2.4)$$

Finally, system dead time was determined for the ^{226}Ra point source by calculating the difference between live time and DSP clock time.

CHAPTER 3: RESULTS & DISCUSSION

3.1 HPGe Detector Performance Analysis:

3.1.1 Energy Calibration:

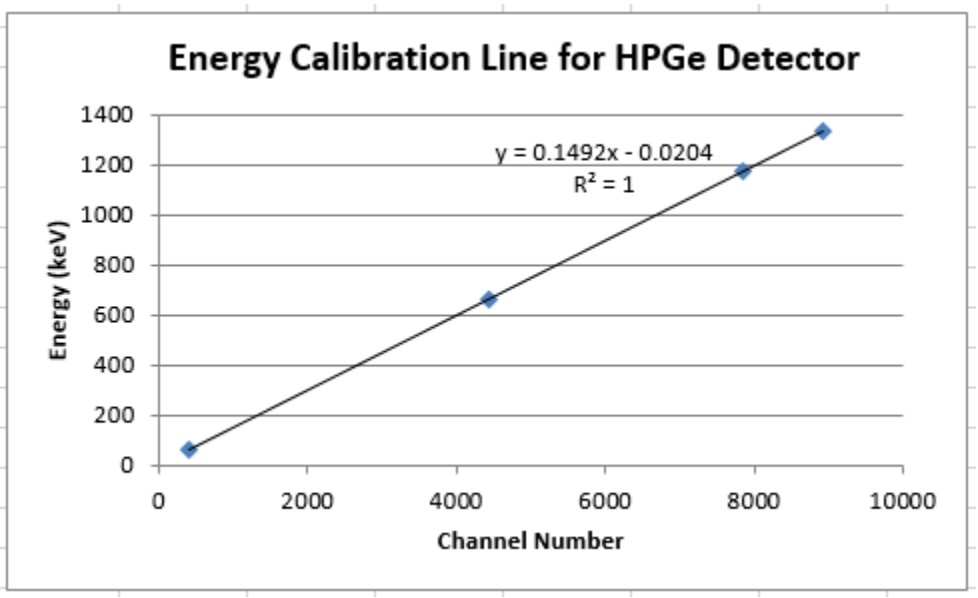

Figure 3.1: Energy calibration line used for HPGe detector to match channel numbers to their respective energies

Firstly, it was necessary to calibrate the germanium detector in energy and efficiency. A standard reference radionuclide point source located inside a small vial was used to calibrate the HPGe detector for energy as a function of channel number. This source contained multiple gamma emitters, notably ^{241}Am, ^{60}Co & ^{137}Cs. The following line of calibration was used to determine which peaks from the spectrum above corresponded to what energies.

The energy calibration curve was described by the following linear curve:

$$Energy\ (keV) = (0.1492 * Channel\ Number) - 0.0204 \quad (3.1)$$

The four gamma lines used to evaluate the energy calibration line from the standard reference point source were the 59.5 keV gamma-ray energy from ^{241}Am, the 662 keV gamma-ray energy from ^{137}Cs and the 1173 keV and 1332 keV gamma-ray energies from ^{60}Co. In GammaVision 32, a peak of interest was selected, and the software calibrated the peak in the channel to calibration energy. This calibration source containing a mixture of multi-gamma-ray nuclides was used because it was more convenient than using sources emitting only a single gamma-ray, and it covered a wide energy range, the most important energy region for purposes of ^{226}Ra source measurement.

3.1.2 HPGe Detector Efficiency Calibration:

Table 3.1: Characteristics of the mixed $^{152/154}$Eu point source

Isotope	**Activity on Reference Date [Bq]**	**Activity on Measurement Date (May 23, 2013) [Bq]**	**Uncertainty [%]**	**Ref. Date**	$t_{\frac{1}{2}}[yrs]$
^{152}Eu	1.20 x 10^6	9.97 x 10^5	5	Nov. 25, 2009	13.537
^{154}Eu	1.45 x 10^5	1.08 x 10^5	5	Nov. 25, 2009	8.593

A mixed $^{152/154}$Eu source was the initial point source used to characterize the efficiency of the HPGe detector. This source was calibrated by the manufacturer, and its characteristics are presented in the table above. An activity correction was required for the mixed source with respect to time elapsed since the reference date, in order to determine the emission rate. Since the gamma-ray peaks of interest pertaining to ^{226}Ra measurements are located between 50-2300 keV, the mixed $^{152/154}$Eu source was important in that it had peaks that could provide a fit around this interval needed for the calibration, essentially allowing for a comparison in efficiency calibration

between the mixed $^{152/154}$Eu point source with a ^{226}Ra point source. The mixed $^{152/154}$Eu source was placed 10 cm from the HPGe detector end cap. Such a large distance was chosen for efficiency calibration with this multi-gamma-ray emitter so as to avoid any uncertainty in the efficiency curve due to coincidence summing.

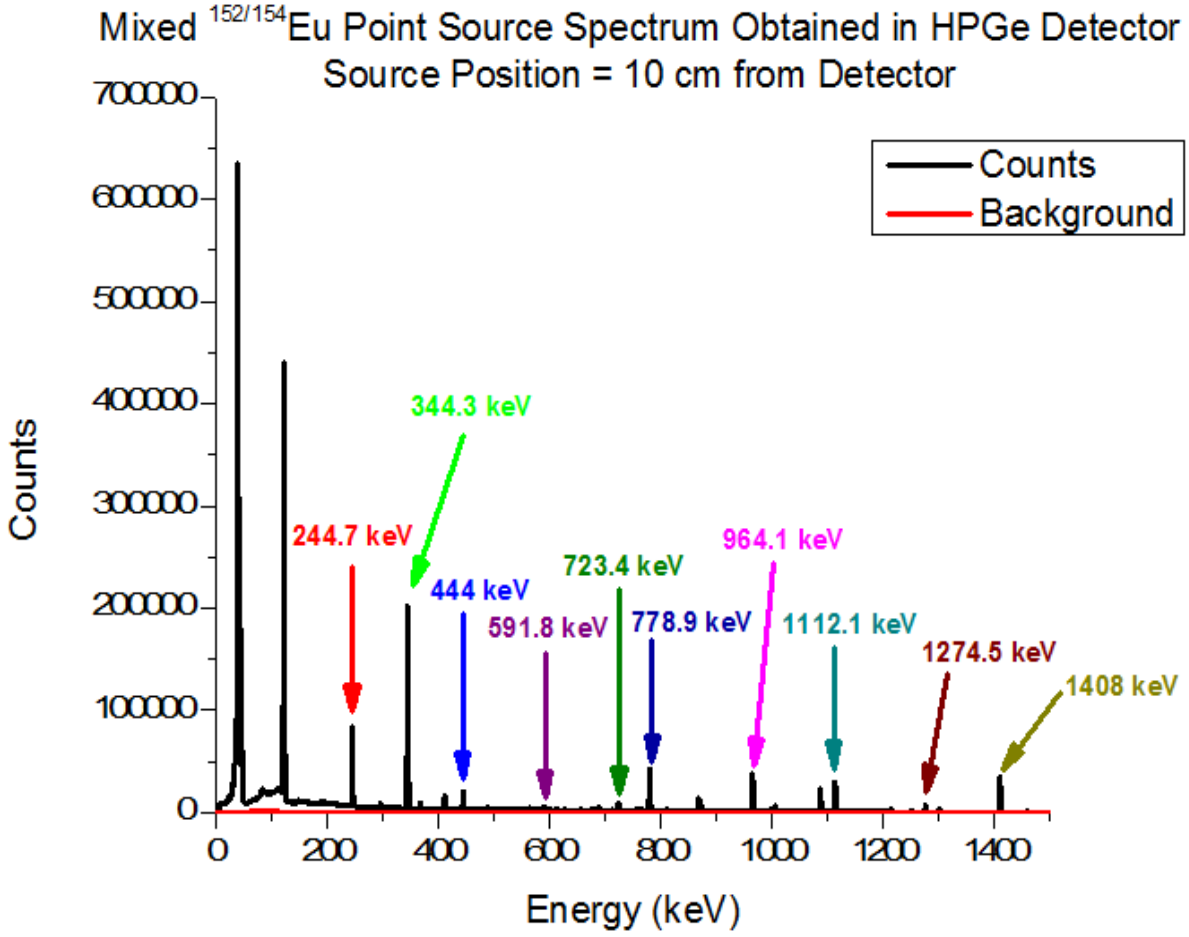

(a)

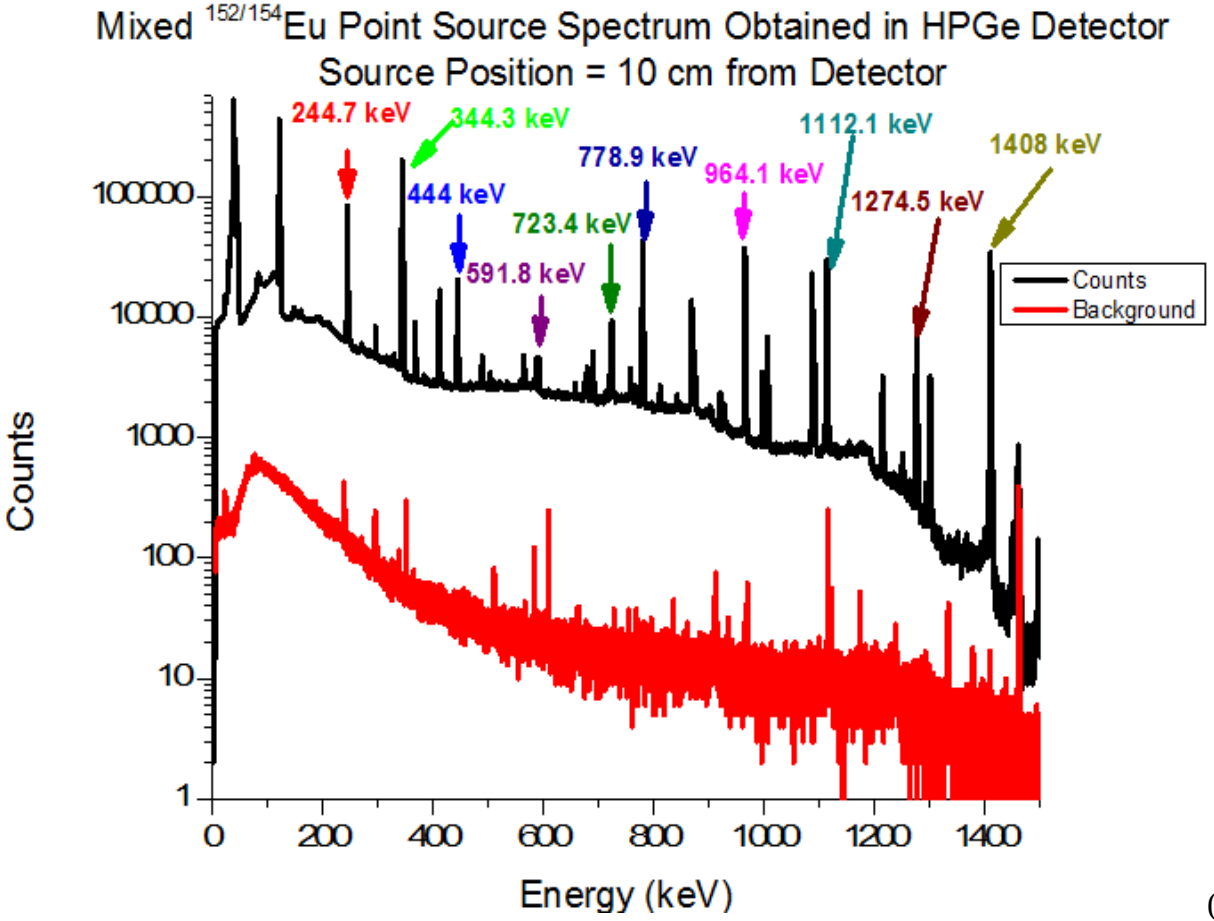

(b)

Figure 3.2: (a) Gamma-ray spectrum obtained for the mixed $^{152/154}$Eu source placed at 10 cm from the HPGe detector end cap for a 1 hour count. (b) Spectrum in logarithmic scale.

The above spectrum was obtained for the mixed $^{152/154}$Eu source placed at 10 cm from the HPGe detector end cap for a 1 hour count. This spectrum demonstrates that the mixed $^{152/154}$Eu source was a long-lived multi-gamma-ray emitter with gamma-rays being emitted over a wide range of energies. The spectrum was used in order to perform activity quantification for each of the labelled radionuclides in the sample by means of performing full-energy peak efficiency calibration. This spectrum emphasizes the capability of the HPGe detector to measure complex spectra and to distinguish between very close energy lines, in the limits of the values for the energy resolutions. The mixed $^{152/154}$Eu source was chosen as a suitable point source to use in the

HPGe detector efficiency calibration because its photon radiations cover the energy range of interest and also provide the highest possible accuracy. [Mann *et al*, 1991] As can be observed from the spectrum, the source emits intense gamma-rays with rather evenly-spaced energies between 100 keV and 1500 keV.

The efficiency calibration for the point source consisted of determining a function describing the full-energy peak (FEP) detection efficiency versus the gamma-ray energies. For convenience, the peak efficiency was calibrated in terms of absolute efficiency. The peak efficiency reflects the number of events detected in the full-energy peak over the total number of events emitted by the source. It depends on several variables like the gamma energy, the detector characteristics (dimensions, shape, material, etc.) and the source's relative placement. [Peralta, 2004]

Based on the energy spectrum, the peak efficiency can be considered as the number of events counted in the peak area N_{peak} per unit time over the total number of generated events from radioactive emission in the source per unit time, which can be expressed using the following equation:

$$\varepsilon_{peak} = \frac{Count\ Rate}{Emission\ Rate} = \frac{N_{peak}}{p_e t_c A(t)} \qquad (3.2)$$

Where p_e is the gamma-ray emission probability, and t_c is the counting time. In order to calculate the activity, knowledge of the half-life of the source, $t_{\frac{1}{2}}$, its activity at a reference time $A(t)$, and the time elapsed, *t*, since the reference time are required, where $A(t)$ can be determined by:

$$A(t) = A(0)e^{-\lambda t} \qquad (3.2)$$

Table 3.2: Efficiency characterization results for mixed $^{152/154}$Eu point source placed at 10 cm from detector end cap

Nuclide	Activity [Bq]	Energy (keV)	Emission Prob	Emission Rate (sec^{-1})	Area [counts]	Area Error [Counts]	Count Rate (sec^{-1})	ε_{abs}	ε_{abs} Error +/-
152	997000	244.7	0.075	74775	787477.9	22051.77	218.7438519	0.002925361	0.000167646
152	997000	344.3	0.266	265202	2096322	46516.28	582.3115278	0.002195728	0.000120112
152	997000	444	0.031	30907	204625.3	4436.53	56.84035667	0.001839077	0.000100227
154	108000	591.8	0.048	5184	27345.57	697.65	7.595991944	0.001465276	8.22499E-05
154	108000	723.4	0.197	21276	91091.12	2423.92	25.30308778	0.001189278	6.73607E-05
152	997000	778.9	0.13	129610	526115.3	9641.97	146.1431269	0.001127561	6.00458E-05
152	997000	964.1	0.145	144565	504724.1	8198.6	140.2011311	0.000969814	5.09855E-05
152	997000	1112.1	0.136	135592	423626.7	4345.72	117.6740769	0.000867854	4.42966E-05
154	108000	1274.5	0.355	38340	104448	1280.69	29.01333694	0.000756738	3.8958E-05
152	997000	1408	0.208	207376	536220.2	7454.69	148.9500569	0.000718261	3.72754E-05

The table above shows efficiency characterization results for the above spectrum. The efficiencies determined above are fairly low, with the highest full-energy peak efficiency (244.7 keV) being less than 1%. As shown in the figure above, not all gammas will interact with the full detector thickness. This effect will be less and less significant as the source is placed further away from the detector. [Peralta, 2004]

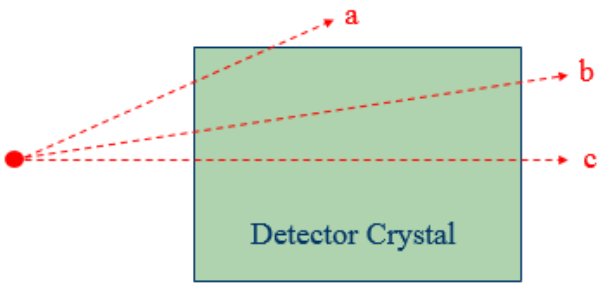

Figure 3.3: Several directions of gamma photons impinging upon the detector from a point isotropic radioactive source

Fundamentally, the detection efficiency depends mainly on the solid angle Ω under which the source is seen by the detector and on intrinsic factors characteristic of the detector. [L'Annunziata, 2012 *pp*. 265-266] A depiction of the solid angle is shown below for a point source located at distance *d* from a cylindrical detector with radius *a*:

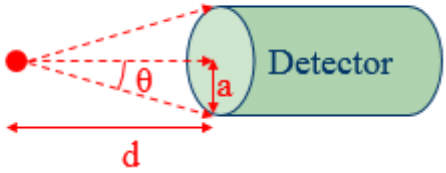

Figure 3.4: Solid angle representation for a point source with cylindrical detector with diameter "a" at distance "d"

The solid angle in this case becomes:

$$\Omega = \iint sin\theta \; d\theta d\varphi = 2\pi \left(1 - \frac{d}{\sqrt{d^2+a^2}}\right) [sr] \qquad (3.4)$$

When the distance *d* is close to 0, the solid angle becomes 2π, which is equivalent to that of a hemisphere. [Byun, 2007] If the distance is much longer than the radius *a*, the spherical surface area can be approximated to the cross-sectional area πa^2 and the solid angle becomes

$$\Omega = \frac{S}{r^2} \approx \frac{\pi a^2}{r^2} [sr] \qquad (3.5)$$

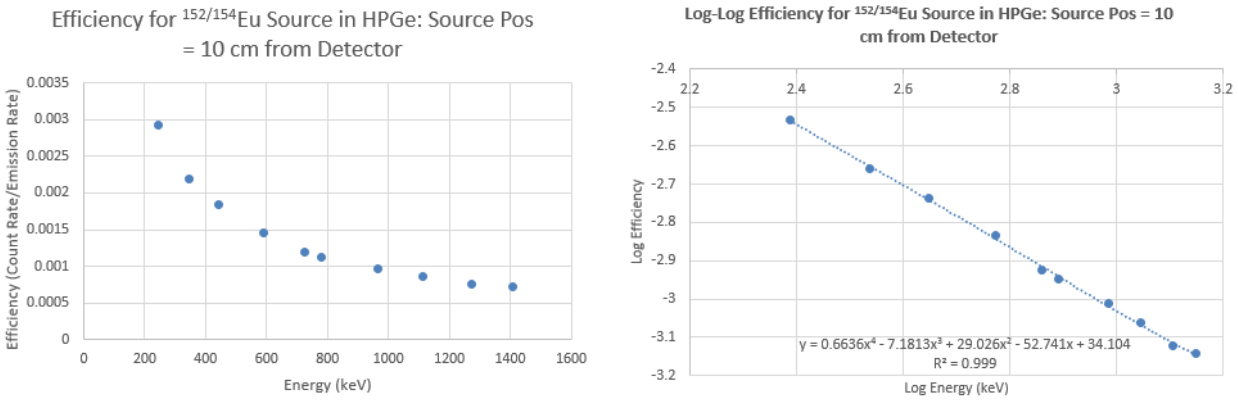

Figure 3.5: Peak efficiency dependence on energy for Mixed $^{152/154}$Eu Point Source Placed at 10 cm from detector along with log-log plot

The full-energy peak efficiency was plotted as a function of gamma-ray energy. The above figures show the peak efficiency dependence on energy for the mixed $^{152/154}$Eu point source placed at 10 cm from detector. The results were also plotted as a log-log function. The equation of the log-log efficiency curve was calculated by the Excel software as the following polynomial function:

$$Log(Efficiency) = 0.6636x^4 - 7.1813x^3 + 29.026x^2 - 52.741x + 34.104 \qquad (3.6)$$

In the above equation, $x = Energy\ (keV)$. The log-log plot was used in order to check for the accuracy of the constructed calibration curve and to facilitate interpolations. [Mann *et al*, 1991] This curve expressed a correlation coefficient of 0.99, which indicates a fairly good agreement between the function and the data points. The uncertainty of this calibration source is responsible for limiting the minimization of the uncertainty in the activity. [Folch, 2011] The calibration curve also emphasizes why the source position was chosen as 10 cm from the detector in this

case with the multi-gamma-ray emitter. Multi-gamma-ray sources emit gamma rays in cascade and for close sample-to-detector distances, there may be considerable coincidence summing resulting in inaccuracy in efficiency calibration. Thus, standard multi-gamma-ray sources are generally not used for efficiency calibration of a detector at close sample-to-detector distance. [Agarwal, 2012]

3.1.3 ^{226}Ra Point Source Measurements:

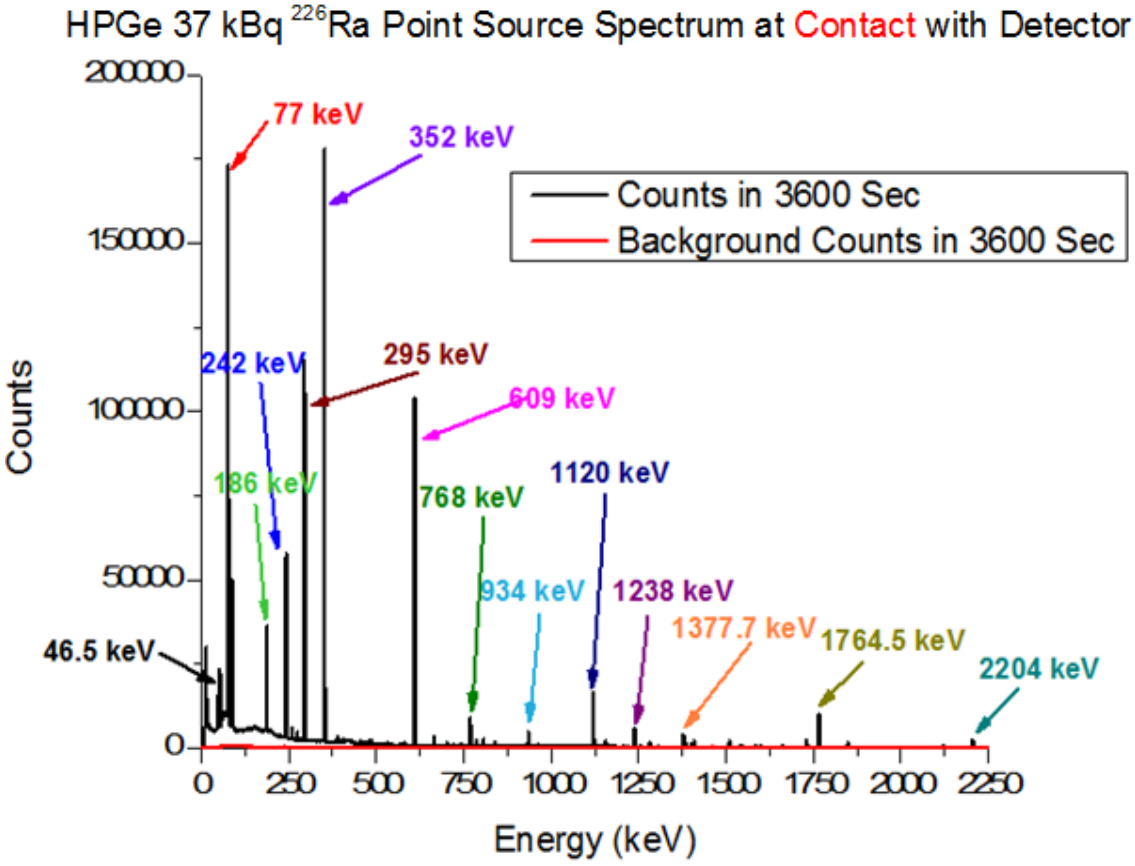

(a)

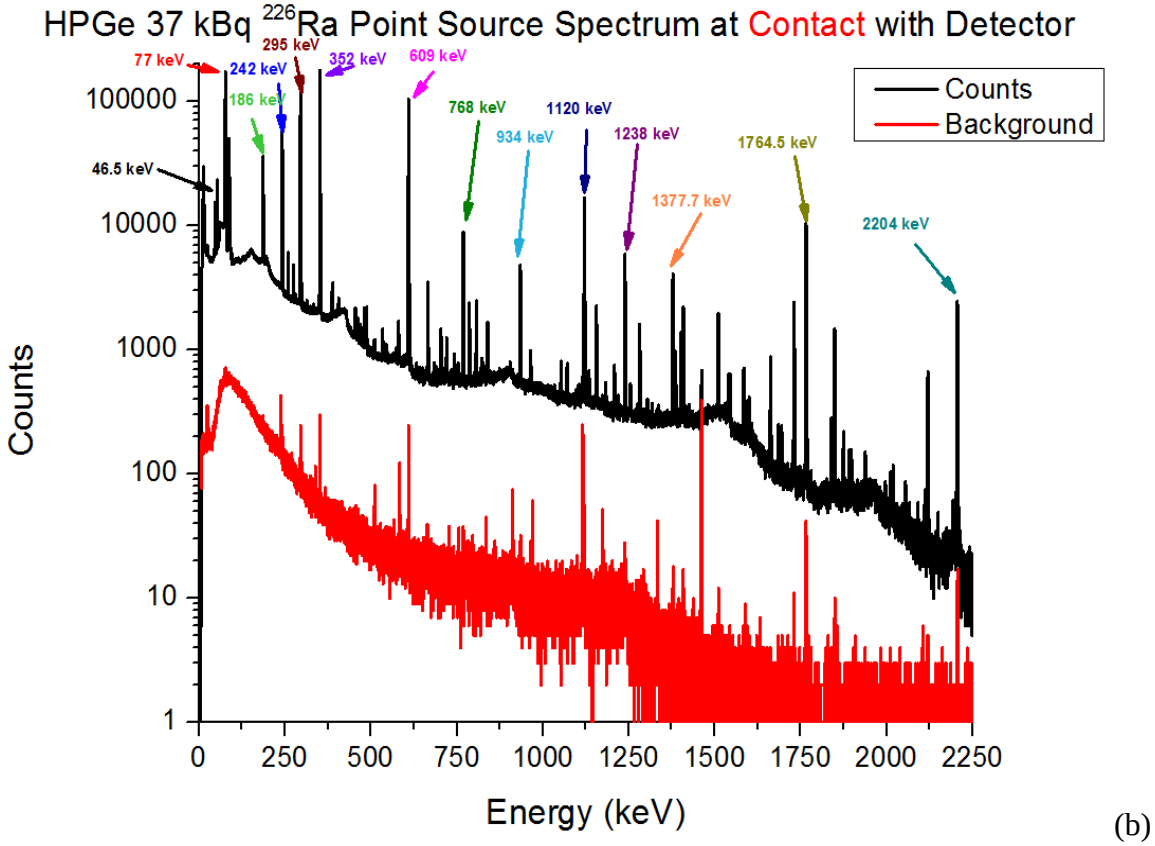

(b)

Figure 3.6: (a) HPGe ^{226}Ra 37 kBq point source spectrum at contact with detector for 1 hour count. (b) Spectrum in logarithmic scale.

A standard ^{226}Ra source was purchased by the McMaster radiation biology research group from Eckert and Ziegler on 1 st January 2010 with an activity of 10 µCi in 5 mL which is equal to 74 kBq per mL and purity greater than 99%. [Thompson, 2012] Using this standard source, a point calibration source was previously created by another research group in a small vial with an activity of 37 kBq and from here-on forwards will be mentioned in this study to describe the ^{226}Ra point source which was used for detector performance analysis. The ^{226}Ra point source was sealed to prevent Radon gas escaping, and thus allowing the Radon gas to reach secular equilibrium with its progeny. The source vial was placed at contact with the detector end cap of the HPGe detector and counted for one hour, followed by a one hour background count. The

above spectrum was obtained for the ^{226}Ra point source placed at contact with the HPGe detector end cap for a 1 hour count. It can be observed that many gamma lines were visible in the spectrum, particularly the energies mentioned in the gamma emission probably chart described in chapter 1, and these gamma-ray energies ranged between 77 keV and 2204 keV. It is worth mentioning that the background counts were extremely low, as can be seen from the background spectrum. The Compton continuum is evident in the lower energy range, where most of the daughter isotopes are dominated by ^{214}Pb emissions. The efficiency calibration of the HPGe detector was carried out using thirteen full-energy peaks gamma-ray obtained in the spectrum. The table below shows efficiency characterization results for the above spectrum:

Table 3.3: Efficiency Characterization Results for ^{226}Ra Point Source spectrum obtained for 1 hour count at contact with HPGe detector

Nuclide	Activity [Bq]	Energy (keV)	Emission Prob	Emission Rate (sec^{-1})	Area [Counts]	Area Error [Counts]	Count Rate (sec^{-1})	ε_{abs}	ε_{abs} Error +/-
^{226}Ra	37000	186	0.033	1221	223609.414	3360.3883	62.11	0.050871193	0.002655963
^{214}Pb	37000	242	0.075	2775	416373.59	6015.3658	115.66	0.041679038	0.0021692
^{214}Pb	37000	295	0.192	7104	891082.036	12253.258	247.52	0.034842735	0.00180682
^{214}Pb	37000	352	0.371	13727	1447664.77	18907.736	402.13	0.029294755	0.001513886
^{214}Bi	37000	609	0.461	17057	1013910.47	10122.166	281.64	0.016511801	0.000841886
^{214}Bi	37000	768	0.05	1850	88941.794	849.07958	24.71	0.013354624	0.000679793
^{214}Bi	37000	934	0.032	1184	47861.34	450.36561	13.29	0.01122873	0.000571292
^{214}Bi	37000	1120	0.15	5550	198667.627	1336.5616	55.19	0.009943325	0.000501646
^{214}Bi	37000	1238	0.059	2183	72417.934	439.29783	20.12	0.009214884	0.000464123
^{214}Bi	37000	1377.7	0.04	1480	48207.371	357.582	13.39	0.00904793	0.000457348

^{214}Bi	37000	1764.5	0.159	5883	152442.693	578.26167	42.35	0.007197891	0.000360929
^{214}Bi	37000	2204.1	0.05	1850	39235.451	218.56538	10.90	0.005891209	0.000296383

Two main items addressed during the peak fitting process were the background subtraction and designation of the peak limits through the definition of the region of interest for each fit, as these two factors have some interdependency. While the background counts were extremely low, the Compton continuum is an irreducible component and the standard way to subtract it was to fit the peak and background in a user-defined interval using some suitable combination of functions, like Gaussian functions for the peaks and a polynomial or exponential function for the background. [Peralta, 2014]. This procedure required the use of Origin peak fitting software.

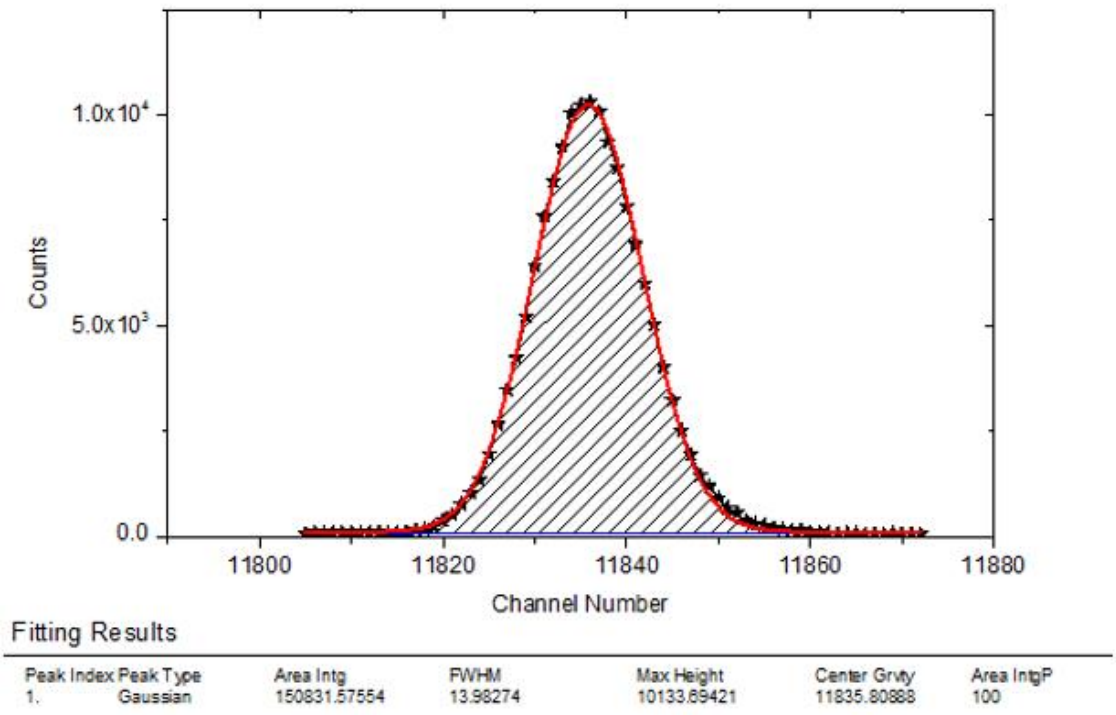

Figure 3.7: Example peak fitting by Origin software for ^{226}Ra peak at 1764.5 keV

The above diagram demonstrates how OriginPro performs the aforementioned peak fitting process. The figure demonstrates a Gaussian fit performed by Origin. Origin fits the peak onto the user defined background. Based on the data, the software selects the region-of-interests such that it encompass the full-energy peaks of the radionuclides of interest.

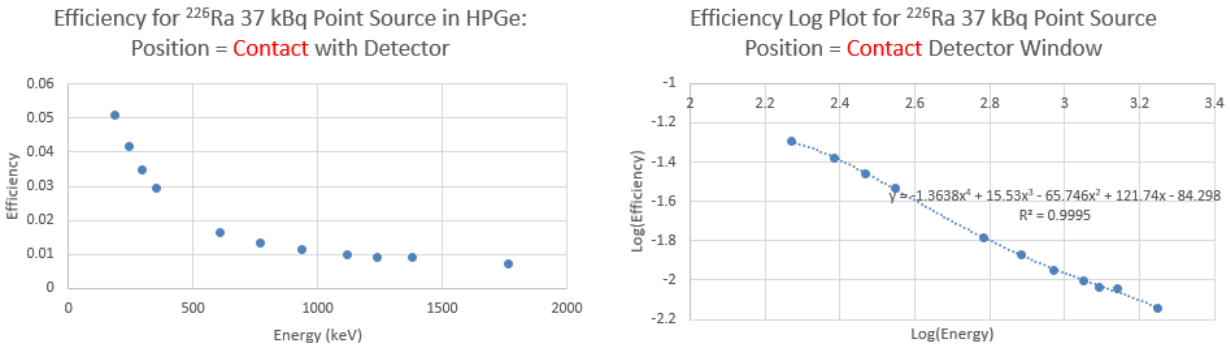

Figure 3.8: Peak Efficiency dependence on energy for 37 kBq ^{226}Ra Point Source placed at contact with detector

The full-energy peak efficiencies were then plotted as a function of the energy in a log-log plot using Excel and a polynomial function was obtained for the fit. The above figures show the Peak Efficiency dependence on energy for ^{226}Ra Point Source placed at contact with detector. The equation of the log-log efficiency curve was calculated by the Excel software as the following polynomial function:

$$Log(Efficiency) = -1.47x^4 + 16.685x^3 - 17.432x^2 + 130.14x - 89.918 \quad (3.7)$$

In the above equation, $x = Energy\ (keV)$. This curve expressed a correlation coefficient of 0.996, which indicates a fairly good agreement between the function and the data points. From the fitted efficiency calibration curve, one can determine the efficiencies at any energy from 186 keV to 2200 keV.

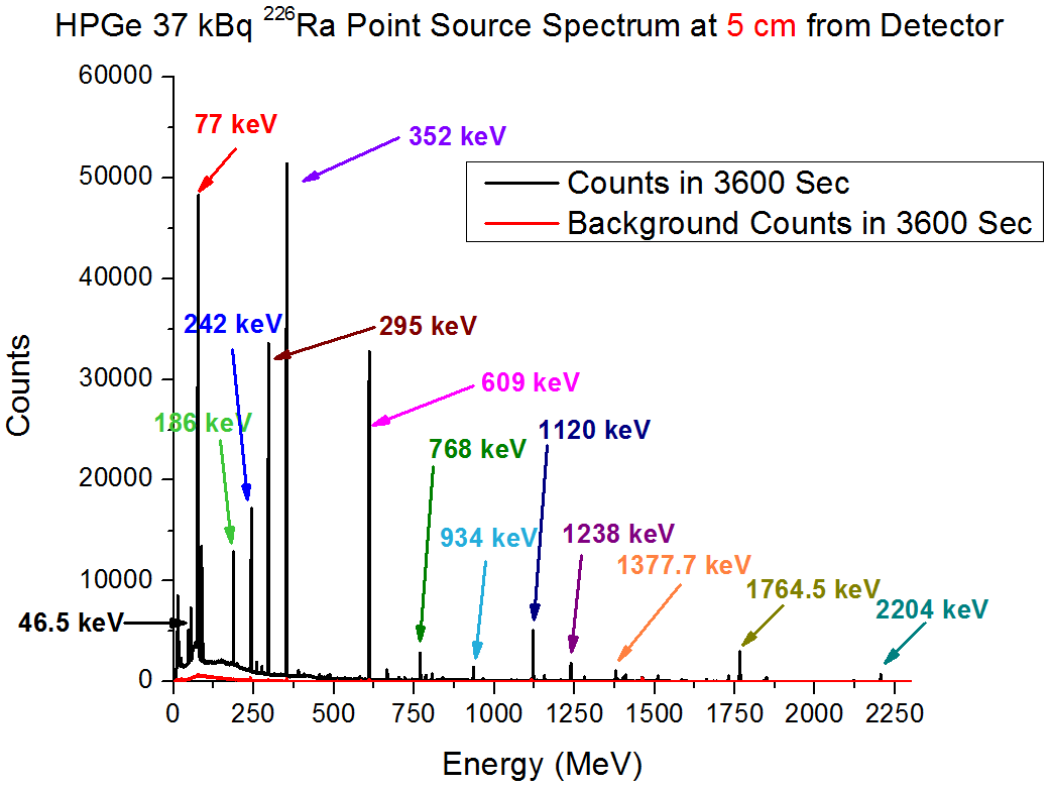
HPGe 37 kBq 226Ra Point Source Spectrum at 5 cm from Detector
Counts in 3600 Sec
Background Counts in 3600 Sec
77 keV
352 keV
242 keV
295 keV
609 keV
186 keV
768 keV
1120 keV
934 keV
1238 keV
1377.7 keV
1764.5 keV
2204 keV
46.5 keV
Counts
Energy (MeV)

(a)

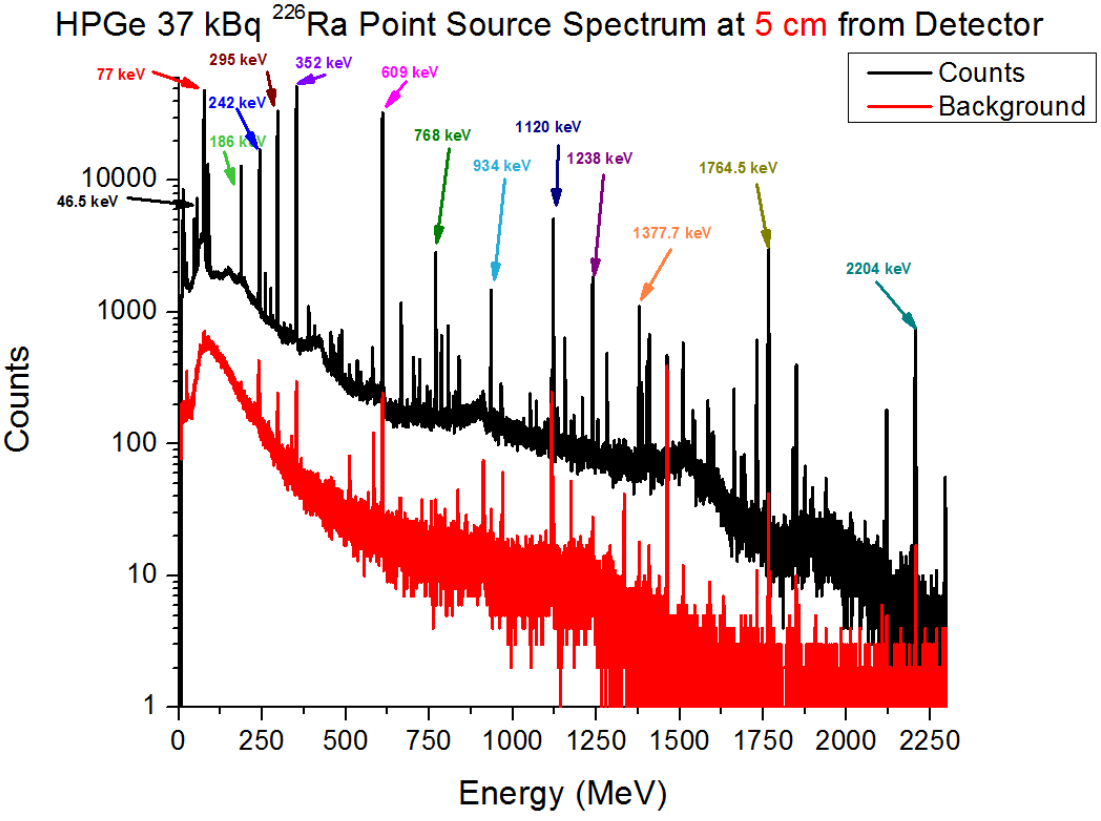
HPGe 37 kBq 226Ra Point Source Spectrum at 5 cm from Detector
Counts
Background
77 keV
295 keV
352 keV
609 keV
242 keV
186 keV
768 keV
1120 keV
934 keV
1238 keV
1764.5 keV
1377.7 keV
2204 keV
46.5 keV
Counts
Energy (MeV)

(b)

Figure 3.9: (a) HPGe ^{226}Ra 37 kBq point source spectrum at 5 cm from end cap of detector for 1 hour count. (b) Spectrum in logarithmic scale.

The ^{226}Ra point source was then moved to position of 5 cm away from the detector end cap, in order to assess the effect on detector performance when a different geometry is used. The sample was counted at this distance for 1 hour, followed by a 1 hour background count. The above spectrum was obtained for the mixed 37 kBq ^{226}Ra point source placed at 5 cm from detector.

The analysis which was performed for the point source at contact with the detector was repeated for this configuration using Origin Peak Fitting Software.

Table 3.4: Efficiency Characterization Results for ^{226}Ra Point Source spectrum obtained for 1 hour count at 5 cm from detector end cap in HPGe detector

Nuclide	**Activity [Bq]**	**Energy (keV)**	**Emission Prob**	**Emission Rate (sec^{-1})**	**Area [Counts]**	**Area Error [Counts]**	**Count Rate (sec^{-1})**	ε_{abs}	ε_{abs} **Error +/-**
^{226}Ra	37000	186	0.033	1221	70570.253	426.68	19.60	0.016054749	0.000805223
^{214}Pb	37000	242	0.075	2775	108359.669	626.51	30.10	0.010846814	0.000543151
^{214}Pb	37000	295	0.192	7104	229064.082	928.94	63.63	0.008956772	0.000449309
^{214}Pb	37000	352	0.371	13727	376870.113	1574.15	104.69	0.007626294	0.000382643
^{214}Bi	37000	609	0.461	17057	286612.38	974.84	79.61	0.004667559	0.000233917
^{214}Bi	37000	768	0.05	1850	25254.516	192.79	7.02	0.003791969	0.000191796
^{214}Bi	37000	934	0.032	1184	14176.273	133.82	3.94	0.00332589	0.000169232
^{214}Bi	37000	1120	0.15	5550	57451.452	223.39	15.96	0.002875448	0.000144206
^{214}Bi	37000	1238	0.059	2183	21151.696	120.33	5.88	0.002691466	0.000135442
^{214}Bi	37000	1377.7	0.04	1480	13632.351	109.20	3.79	0.002558624	0.000129563

^{214}Bi	37000	1764.5	0.159	5883	41124.229	165.48	11.42	0.001941764	9.74021E-05
^{214}Bi	37000	2204.1	0.05	1850	10527.671	91.33	2.92	0.001580731	0.000805223

The table above shows efficiency characterization results for the above spectrum.

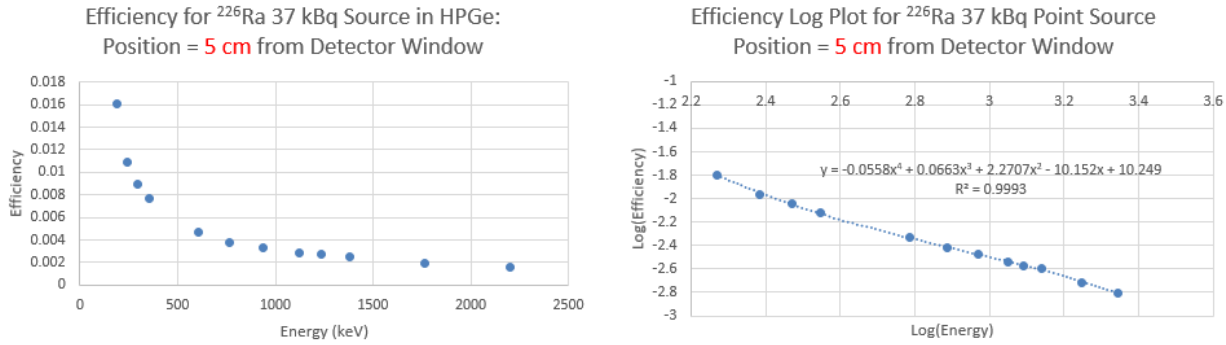

Figure 3.10: Peak Efficiency dependence on energy for ^{226}Ra Point Source placed at 5 cm from detector end cap

The above figure shows the Peak Efficiency dependence on energy for ^{226}Ra Point Source placed at 5 cm from detector. It can be clearly observed that the efficiency drops by greater than three when the source is moved 5 cm away from the detector end cap.

Table 3.5: Ratio of absolute efficiencies of ^{226}Ra point source at contact with respect to 5 cm from detector end cap

$Energy$ (keV)	$\frac{\varepsilon_{abs}(0\ cm)}{\varepsilon_{abs}(5\ cm)}$
186	3.168607183
242	3.842514309
295	3.890099581
352	3.841283197

609	3.537566638
768	3.521817821
934	3.376157961
1120	3.458008978
1238	3.423741559
1377.7	3.53624839
1764.5	3.706882505
2204.1	3.726889015

These results demonstrate that optimal efficiency results for ^{226}Ra are produced when the point source is placed in contact with the detector and that there is a strong distance dependence with respect to full-energy peak efficiency. As predicted by equation 3.4, as the distance *d* from the source to the detector increases, the solid angle increases.

3.1.4 Efficiency Scaling:

It was evident that moving the source with respect to the detector changes the number of gamma-rays incident on the detector. The next step was to establish a reference point source position and efficiency curve at that reference position, and then scale the results of all other geometries to the reference position using efficiency scaling. The efficiency scaling principle can be used to approximately calculate the efficiency of the detector under measurement conditions different from those of the reference position, based on the solid angle. Its application avoids time-consuming measurement sequences [Radu *et al*, 2010].

Efficiency scaling is achieved by means of solid angle ratio scaling. Thus if one wishes to approximate the efficiency of any source position at a particular energy as a function of the reference efficiency at the same energy, the following relationship may be used:

$$\varepsilon(E,P) = \varepsilon(E,P_o) * \frac{\Omega_P}{\Omega_{P_0}} \qquad (3.8)$$

Where $\varepsilon(E,P_o)$ and $\varepsilon(E,P)$ are the efficiencies, at energy, E, of a point source located at positions P_o and P, respectively. [Samah, 2013]. When using the above equation, it is important to consider that as the distance between the source and detector is altered, the angular range of the path length varies, and thus the average cord length is different for each source position. Equation 3.8 does not take this path length difference into account, thus only providing a reasonable approximation.

The calculations below attempt to scale the detector efficiency curves at 10 cm and 5 cm up to contact to determine to how accurately do the scaled efficiency curves superimpose on top of the curve representing ^{226}Ra point source position at contact. The radius of the container housing the ^{226}Ra Point Source vial was approximately 1.58 cm. Therefore, the following solid angle was calculated in order to compare the source efficiency calibration curves between the $^{152/154}$Eu Source at 10 cm and ^{226}Ra at 1.58 cm from the detector:

$$\frac{\Omega(1.58\ cm)}{\Omega(10\ cm)}$$

Table 3.6: Effective Solid Angle Scaling Results for position = 10 cm scaled to contact with detector

Europium Position = 10 cm

$d\ (cm)$	$a\ (cm)$	$\sqrt{d^2+a^2}$	$\frac{d}{\sqrt{d^2+a^2}}$	$1-\frac{d}{\sqrt{d^2+a^2}}$	$2\pi*(1-\frac{d}{\sqrt{d^2+a^2}})$
10.3	2.875	10.69371895	0.963182224	0.036817776	0.231333 [sr]
Radium Position = 1.58 cm					
$d\ (cm)$	$a\ (cm)$	$\sqrt{d^2+a^2}$	$\frac{d}{\sqrt{d^2+a^2}}$	$1-\frac{d}{\sqrt{d^2+a^2}}$	$2\pi*(1-\frac{d}{\sqrt{d^2+a^2}})$
1.88	2.875	3.435116446	0.547288579	0.452711421	2.844469746 [sr]
$\frac{\boldsymbol{\Omega\ (1.58\ cm)}}{\boldsymbol{\Omega\ (10\ cm)}} = \mathbf{12.2960}$					

Here, '*d*' represents the distance from the source to the crystal, and '*a*' represents the radius of the germanium crystal. The distance from the source to the crystal was measured and an additional 0.3 cm was added to the value, because the distance from the end cap to the crystal was 0.3 cm.

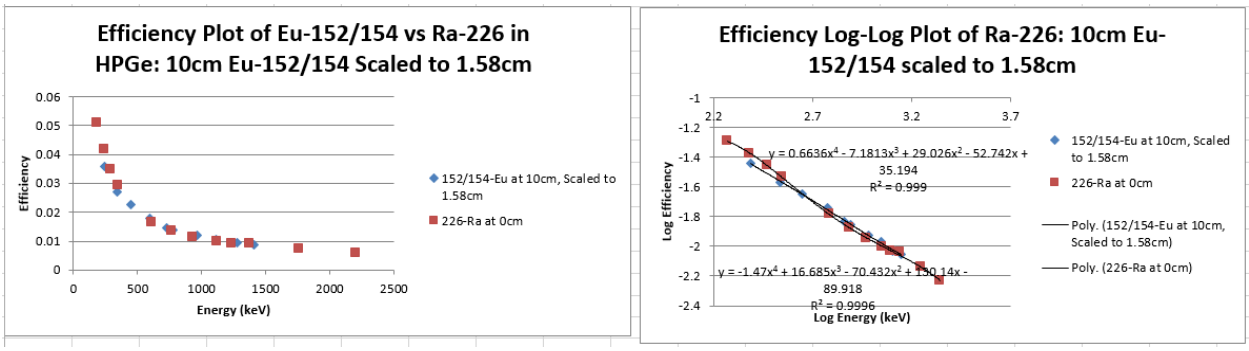

Figure 3.11: Comparison between ^{226}Ra point source at contact and $^{152/154}$Eu point source 10 cm scaled to contact of full-energy peak efficiency as a function of energy along with corresponding log-log plot

All of the full-energy peak efficiencies calculated for the mixed $^{152/154}$Eu source were multiplied by this solid angle in order to scale the efficiency curve up to the case of contact with detector. A

log-log plot of full-energy peak efficiency as a function of the energy was created and the two curves superimposed on each other. Figure 3.11 shows these scaling results. This figure shows very good agreement between the polynomial function from the efficiency calibration of the ^{226}Ra point source at contact with the detector, and the polynomial function resulting from the scaling of the mixed $^{152/154}$Eu source at 10 cm up to the contact case, and shows that moving the source 10 cm from detector end cap results in an absolute efficiency reduction of greater than twelve.

Next, the following solid angle was calculated in order to compare the source efficiency calibration curves between the ^{226}Ra point source at 5cm from the detector with that at 1.58 cm from the detector:

$$\frac{\boldsymbol{\Omega(1.58\ cm)}}{\boldsymbol{\Omega(5\ cm)}}$$

Table 3.7: Effective Solid Angle Scaling Results for position = 5 cm scaled to contact with detector

Radium Position = 5 cm					
$d\ (cm)$	$a\ (cm)$	$\sqrt{d^2+a^2}$	$\frac{d}{\sqrt{d^2+a^2}}$	$1-\frac{d}{\sqrt{d^2+a^2}}$	$2\pi*(1-\frac{d}{\sqrt{d^2+a^2}})$
5.3	2.875	6.029562588	0.879002402	0.120997598	0.76025 [sr]
Radium Position = 1.58 cm					
$d\ (cm)$	$a\ (cm)$	$\sqrt{d^2+a^2}$	$\frac{d}{\sqrt{d^2+a^2}}$	$1-\frac{d}{\sqrt{d^2+a^2}}$	$2\pi*(1-\frac{d}{\sqrt{d^2+a^2}})$
1.88	2.875	3.435116446	0.547288579	0.452711421	2.844469746 [sr]
$\frac{\boldsymbol{\Omega\ (1.58\ cm)}}{\boldsymbol{\Omega\ (5\ cm)}} = \mathbf{3.7415}$					

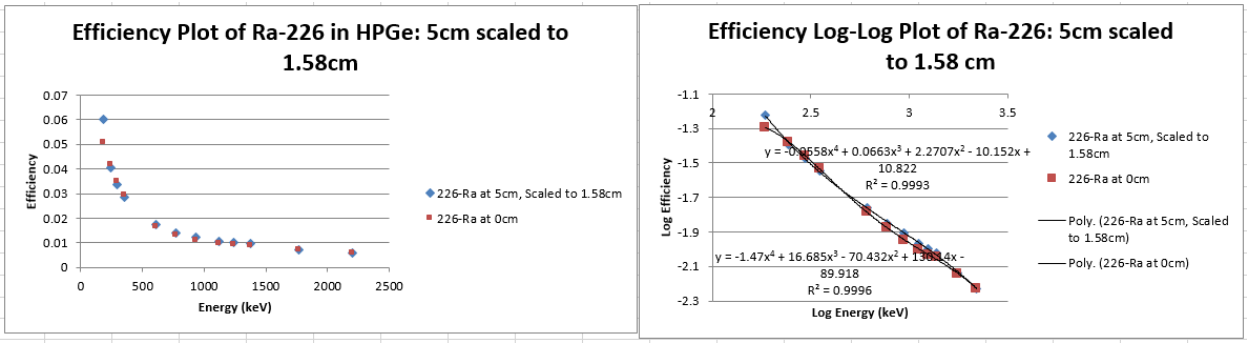

Figure 3.12: Comparison between ^{226}Ra point source at contact and ^{226}Ra point source 5 cm scaled to contact of full-energy peak efficiency as a function of energy along with corresponding log-log plot

All of the full-energy peak efficiencies calculated for the ^{226}Ra point source at 5 cm from the detector were multiplied by this solid angle in order to scale the efficiency curve up to the case of contact with detector. A log-log plot of full-energy peak efficiency as a function of the energy was created and the two curves superimposed on each other. The above figure shows these scaling results. The figure above shows very good agreement between the scaling of the polynomial function from the efficiency calibration of the ^{226}Ra point source at contact with the detector, and the polynomial function resulting from the scaling of the ^{226}Ra source at 5 cm up to the contact case. In order to validate this claim, a simple comparison was made between the values of ratio of the solid angle of the ^{226}Ra point source at contact with respect to the solid angle of the ^{226}Ra point source at 5 cm from the detector end cap, $\frac{\boldsymbol{\Omega\ (1.58\ cm)}}{\boldsymbol{\Omega\ (5\ cm)}}$, and the ratio of the absolute efficiency of the ^{226}Ra point source at contact with respect to the absolute efficiency of the ^{226}Ra point source at 5 cm from the detector end cap, $\frac{\varepsilon_{abs}\ \boldsymbol{(1.58\ cm)}}{\varepsilon_{abs}\ \boldsymbol{(5\ cm)}}$. For example, at 242 keV, the ratio of the absolute efficiency, ε_{abs}, for the ^{226}Ra point source at contact with respect to 5 cm

from the detector end cap, $\frac{\varepsilon_{abs}\ (\mathbf{1.58\ cm})}{\varepsilon_{abs}\ (\mathbf{5\ cm})}$ was 3.84. It was shown above that $\frac{\mathbf{\Omega}\ (\mathbf{1.58\ cm})}{\mathbf{\Omega}\ (\mathbf{5\ cm})}$ =3.74. Both values are within 3% of each other. For the contact case, although this multi-gamma-ray emitter was placed at a close source-to-detector distance, the source-detector distance '*d*' in this study was calculated from the detector itself rather than from the end cap of the detector which was at 0.3 cm distance from the crystal. This would, in principle make the solid angle larger. As mentioned earlier, any experimental error in the calibration sources come from activity accuracy, resulting in differences between the mixed $^{152/154}$Eu and ^{226}Ra efficiency calibration curves when they are overlaid on top of each other.

3.1.5 HPGe Detection Limit Analysis:

The following table shows the Detection Limit for the $^{152/154}$Eu Source at a position of 10 cm from the detector with 95% and 99% Confidence Intervals:

Table 3.8: HPGe detection limit calculation for mixed $^{152/154}$Eu point source at 10 cm from end cap of detector at (a) 95% Confidence Interval and (b) 99% Confidence Interval

$Energy\ (keV)$	x_1 Channel Number	x_2 Channel Number	$Background\ Counts\ (C_B)$	$\sqrt{2C_B}$	$2k_\alpha$	L_D [Counts] 95% $C.I.$	Emission Prob.	ε_{abs}	t_c [sec]	$L_D\ [Bq]$ 95% $C.I.$
244.7	1623	1702	10832	147.1869559	3.29	484.2450851	0.075	0.002925361	3600	613.08683
344.3	2286	2352	4018	89.6437393	3.29	294.9279023	0.266	0.002195728	3600	140.26625
444	2950	3017	2359	68.687699	3.29	225.9825297	0.031	0.001839077	3600	1101.0594
591.8	3955	4021	1491	54.6076918	3.29	179.659306	0.048	0.001465276	3600	709.55578
723.4	4759	4926	2998	77.4338427	3.29	254.7573425	0.197	0.001189278	3600	302.04705
778.9	5202	5261	913	42.7317212	3.29	140.5873627	0.13	0.001127561	3600	266.41605
964.1	6448	6508	1134	47.6235236	3.29	156.6813926	0.145	0.000969814	3600	309.49844
1112.1	7407	7533	4248	92.173749	3.29	303.2516342	0.136	0.000867854	3600	713.69897
1274.5	8513	8612	695	37.2827038	3.29	122.6600955	0.355	0.000756738	3600	126.83143
1408	9431	9484	246	22.181073	3.29	72.97573017	0.208	0.000718261	3600	135.68453

(a)

$Energy$ (keV)	x_1 Channel Number	x_2 Channel Number	$Background$ $Counts$ (C_B)	$\sqrt{2C_B}$	$2k_\propto$	L_D [Counts] 99% $C.I.$	Emission Prob.	ε_{abs}	t_c [sec]	L_D $[Bq]$ 99% $C.I.$
244.7	1623	1702	10832	147.1869559	4.652	684.713719	0.075	0.002925361	3600	866.8936
344.3	2286	2352	4018	89.6437393	4.652	417.022675	0.266	0.002195728	3600	198.3339
444	2950	3017	2359	68.687699	4.652	319.535176	0.031	0.001839077	3600	1556.878
591.8	3955	4021	1491	54.6076918	4.652	254.034982	0.048	0.001465276	3600	1003.299
723.4	4759	4926	2998	77.4338427	4.652	360.222236	0.197	0.001189278	3600	427.089
778.9	5202	5261	913	42.7317212	4.652	198.787967	0.13	0.001127561	3600	376.7074
964.1	6448	6508	1134	47.6235236	4.652	221.544632	0.145	0.000969814	3600	437.6252
1112.1	7407	7533	4248	92.173749	4.652	428.79228	0.136	0.000867854	3600	1009.157
1274.5	8513	8612	695	37.2827038	4.652	173.439138	0.355	0.000756738	3600	179.3373
1408	9431	9484	246	22.181073	4.652	103.186352	0.208	0.000718261	3600	191.8554

(b)

The following table shows the Detection Limit for the ^{226}Ra Source at a position of 5 cm from the detector with 95% and 99% Confidence Intervals:

Table 3.9: HPGe detection limit calculation for ^{226}Ra point source at 5 cm from end cap of detector at (a) 95% Confidence Interval and (b) 99% Confidence Interval

$Energy$ (keV)	x_1 Channel Number	x_2 Channel Number	$Background$ $Counts$ (C_B)	$\sqrt{2C_B}$	$2k_\propto$	L_D [Counts] 95% $C.I.$	Emission Prob.	ε_{abs}	t_c [sec]	L_D $[Bq]$ 95% $C.I.$
186	1241	1266	6436	113.454837	3.29	373.2664137	0.033	0.016054749	3600	195.70366
242	1609	1635	4428	94.1063228	3.29	309.609802	0.075	0.010846814	3600	105.71795
295	1964	1990	3327	81.572054	3.29	268.3720577	0.192	0.008956772	3600	43.349296
352	2346	2372	3309	81.351091	3.29	267.6450894	0.371	0.007626294	3600	26.276609
609	4069	4102	2530	71.133677	3.29	234.0297973	0.461	0.004667559	3600	30.211891
768	5128	5173	868	41.6653333	3.29	137.0789466	0.05	0.003791969	3600	200.83226
934	6247	6293	658	36.2767143	3.29	119.35039	0.032	0.00332589	3600	311.5039
1120	7494	7533	877	41.8807832	3.29	137.7877767	0.15	0.002875448	3600	88.738363
1238	8292	8324	477	30.8868904	3.29	101.6178694	0.059	0.002691466	3600	177.75698
1377.7	9216	9269	305	24.6981781	3.29	81.25700595	0.04	0.002558624	3600	220.54228
1764.5	11817	11856	501	31.6543836	3.29	104.142922	0.159	0.001941764	3600	93.698727
2204.1	14759	14812	54	10.3923048	3.29	34.19068279	0.05	0.001580731	3600	120.16481

(a)

$Energy$ (keV)	x_1 Channel Number	x_2 Channel Number	$Background$ $Counts$ (C_B)	$\sqrt{2C_B}$	$2k_\propto$	L_D [Counts] 99% $C.I.$	Emission Prob.	ε_{abs}	t_c [sec]	L_D $[Bq]$ 99% $C.I.$
186	1241	1266	6436	113.454837	4.652	527.791901	0.033	0.016054749	3600	276.72141
242	1609	1635	4428	94.1063228	4.652	437.782614	0.075	0.010846814	3600	149.48326
295	1964	1990	3327	81.572054	4.652	379.473195	0.192	0.008956772	3600	61.295114
352	2346	2372	3309	81.351091	4.652	378.445275	0.371	0.007626294	3600	37.154646
609	4069	4102	2530	71.133677	4.652	330.913865	0.461	0.004667559	3600	42.719063
768	5128	5173	868	41.6653333	4.652	193.827131	0.05	0.003791969	3600	283.97315
934	6247	6293	658	36.2767143	4.652	168.759275	0.032	0.00332589	3600	440.46083
1120	7494	7533	877	41.8807832	4.652	194.829403	0.15	0.002875448	3600	125.47443
1238	8292	8324	477	30.8868904	4.652	143.685814	0.059	0.002691466	3600	251.34513
1377.7	9216	9269	305	24.6981781	4.652	114.895924	0.04	0.002558624	3600	311.84276
1764.5	11817	11856	501	31.6543836	4.652	147.256192	0.159	0.001941764	3600	132.48829
2204.1	14759	14812	54	10.3923048	4.652	48.3450021	0.05	0.001580731	3600	169.91085

(b)

The following table shows the Detection Limit for the ^{226}Ra Source at a position of contact the detector with 95% and 99% Confidence Intervals:

Table 3.10: HPGe detection limit calculation for ^{226}Ra point source at contact with detector at (a) 95% Confidence Interval and (b) 99% Confidence Interval

$Energy$ (keV)	x_1 Channel Number	x_2 Channel Number	$Background$ $Counts$ (C_B)	$\sqrt{2C_B}$	$2k_\propto$	L_D [Counts] 95% $C.I.$	Emission Prob.	ε_{abs}	t_c [sec]	L_D $[Bq]$ 95% $C.I.$
186	1241	1266	6436	113.454837	3.29	373.2664137	0.033	0.050871193	3600	61.763308
242	1609	1635	4428	94.1063228	3.29	309.609802	0.075	0.041679038	3600	27.512702
295	1964	1990	3327	81.572054	3.29	268.3720577	0.192	0.034842735	3600	11.143493
352	2346	2372	3309	81.351091	3.29	267.6450894	0.371	0.029294755	3600	6.8405811
609	4069	4102	2530	71.133677	3.29	234.0297973	0.461	0.016511801	3600	8.5403031
768	5128	5173	868	41.6653333	3.29	137.0789466	0.05	0.013354624	3600	57.02517
934	6247	6293	658	36.2767143	3.29	119.35039	0.032	0.01122873	3600	92.265794
1120	7494	7533	877	41.8807832	3.29	137.7877767	0.15	0.009943325	3600	25.661693
1238	8292	8324	477	30.8868904	3.29	101.6178694	0.059	0.009214884	3600	51.918926
1377.7	9216	9269	305	24.6981781	3.29	81.25700595	0.04	0.00904793	3600	62.366173
1764.5	11817	11856	501	31.6543836	3.29	104.142922	0.159	0.007197891	3600	25.276962
2204.1	14759	14812	54	10.3923048	3.29	34.19068279	0.05	0.005891209	3600	32.242658

(a)

$Energy$ (keV)	x_1 Channel Number	x_2 Channel Number	$Background$ $Counts$ (C_B)	$\sqrt{2C_B}$	$2k_\propto$	L_D [Counts] 99% $C.I.$	Emission Prob.	ε_{abs}	t_c [sec]	L_D $[Bq]$ 99% $C.I.$
186	1241	1266	6436	113.454837	4.652	527.7919017	0.033	0.050871193	3600	87.332192
242	1609	1635	4428	94.1063228	4.652	437.7826137	0.075	0.041679038	3600	38.902459
295	1964	1990	3327	81.572054	4.652	379.4731952	0.192	0.034842735	3600	15.756695
352	2346	2372	3309	81.351091	4.652	378.4452753	0.371	0.029294755	3600	9.672457
609	4069	4102	2530	71.133677	4.652	330.9138654	0.461	0.016511801	3600	12.075833
768	5128	5173	868	41.6653333	4.652	193.8271305	0.05	0.013354624	3600	80.63255
934	6247	6293	658	36.2767143	4.652	168.7592749	0.032	0.01122873	3600	130.46215
1120	7494	7533	877	41.8807832	4.652	194.8294034	0.15	0.009943325	3600	36.285165
1238	8292	8324	477	30.8868904	4.652	143.6858141	0.059	0.009214884	3600	73.412415
1377.7	9216	9269	305	24.6981781	4.652	114.8959245	0.04	0.00904793	3600	88.184631
1764.5	11817	11856	501	31.6543836	4.652	147.2561925	0.159	0.007197891	3600	35.741163
2204.1	14759	14812	54	10.3923048	4.652	48.34500193	0.05	0.005891209	3600	45.590531

(b)

The objective of the HPGe performance analysis was to assess the detection limit of the detector for ^{226}Ra, at two different source-to-detector distances, particularly 5 cm and contact. Equation 1.2 was used in order to calculate the detection limit in Bq. Since $L_D \propto \frac{1}{\varepsilon_{abs}}$, the detection limit analysis was validated by comparing the values for $\frac{\varepsilon_{abs}(1.58\ cm)}{\varepsilon_{abs}(5\ cm)}$ with $\frac{L_D(5cm)}{L_D(1.58\ cm)}$ @ 99% CI. As can be observed in the table below, the two ratios show very good agreement with each other at all energies.

Table 3:10: Comparison of ratios of $\frac{\varepsilon_{abs}(1.58\ cm)}{\varepsilon_{abs}(5\ cm)}$ *with* $\frac{L_D(5cm)}{L_D(1.58\ cm)}$ @ 99% CI.

$Energy\ (keV)$	$\frac{L_D(5\ cm)}{L_D(1.58\ cm)}$	$\frac{\varepsilon_{abs}\ (1.58\ cm)}{\varepsilon_{abs}\ (5\ cm)}$
186	3.16860713	3.168607183
242	3.84251536	3.842514309
295	3.89009818	3.890099581
352	3.84128355	3.841283197
609	3.53756719	3.537566638
768	3.52181842	3.521817821
934	3.37615647	3.376157961
1120	3.45800778	3.458008978
1238	3.4237413	3.423741559
1377.7	3.53624889	3.53624839
1764.5	3.70688304	3.706882505
2204.1	3.72688802	3.726889015

The next step was to combine the strongest peaks in order to obtain the lowest possible detection limit for the system. This was accomplished by using the Inverse Mean Variance Theorem for the three strongest peaks of the ^{226}Ra in the case of contact with the detector, 295 keV, 352 keV and 609 keV.

The system detection limit at the 95% confidence interval was determined to be:

$$L_D\ [Bq] of\ 3\ Strongest\ Peaks\ @\ 95\%\ CI. \coloneqq \sqrt{\frac{1}{(L_{D_{295\ keV}})^{-2}+(L_{D_{352\ keV}})^{-2}+(L_{D_{609\ keV}})^{-2}}} = 4.815\ Bq \qquad (3.9)$$

The system detection limit at the 99% confidence interval was determined to be:

$$L_D\ [Bq] of\ 3\ Strongest\ Peaks\ @\ 99\%\ CI. = 6.808\ Bq \quad (3.10)$$

This method in essence uses error propagation in order to combine detection limits. This method was used in order to exclude unnecessary background counts which occur in the energy regions between peaks of interest, which cause an increase in the detection limit. According to the study conducted by Mothersill et al, 2014, the dietary exposure to fish at environmentally relevant levels were *10, 100, 1000 and 10,00 mBq/g*. In the context of live fish, because these environmentally relevant levels are so low, a lower system detection limit than what the HPGe offers is highly desired. The next section describes the performance analysis results obtained with the 4π NaI(Tl) Detector.

3.2 4π NaI(Tl) Detector Performance Analysis:

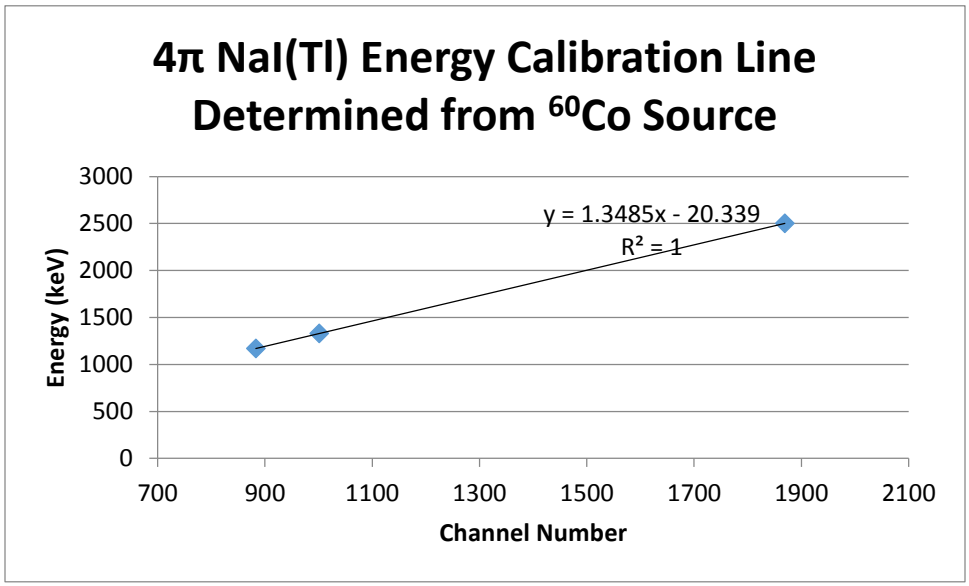

Figure 3.13: Energy calibration line for 4π NaI(Tl) detector

A ^{60}Co reference point source was inserted into the aperture of the 4π NaI(Tl) detector, and an energy calibration was performed by matching the 1173 keV, 1332 keV and 2500 keV sum peak gamma-ray energies with their respective channels and creating a linear energy calibration graph

in Excel. The following energy calibration line was used to determine which peaks corresponded to which energies:

The following equation was calculated for the energy calibration line:

$$Energy\ (keV) = 1.3485 * (Channel\ Number) - 20.339 \quad (3.11)$$

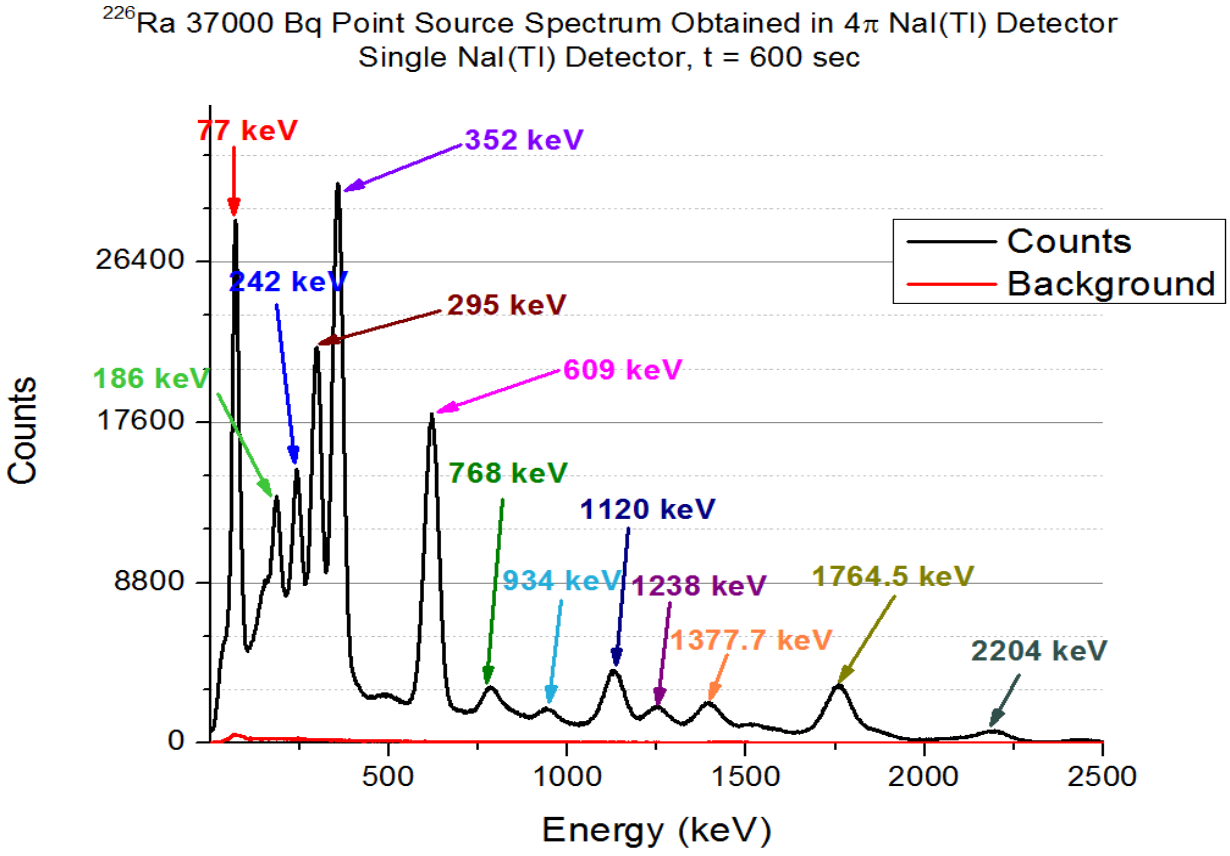

Figure 3.14 ^{226}Ra 37 kBq point source spectrum obtained by 4π NaI(Tl) detector for 10 minute count at source position in centre of detector

The 37 kBq ^{226}Ra point source was inserted into the aperture of the 4π NaI(Tl) detector. The spectrum in figure 3.14 was obtained for the ^{226}Ra point source placed at pos = 15 cm in the

aperture of the detector for a 10 minute count, acquired in singles mode. Recall from chapter 2, that the reference position at 0 cm was the position at the very end of the aperture of the detector, touching the ninth central detector. Position = 15 cm represents positioning the source 15 cm away from this reference position. Following the ^{226}Ra point source count, a 12 hour background count was conducted. The process of conducting 10 minute counts for point source was repeated by moving the source in 3 cm intervals between 0 and 30 cm, where 0 cm represented the reference position, and 30 cm the front edge of the detector.

An inherent property observable from the above spectrum is the limited energy resolution of the system. Thirteen of the fourteen peaks which were visible in the HPGe detector could be observed (minus the 46.5 keV ^{210}Pb peak, see figure 1.2). The 609 keV gamma ray from ^{214}Bi has a higher yield than any of the ^{214}Pb photons and any of the other higher-energy photons from ^{214}Bi and, with the 4π NaI(Tl) being a large-volume detector, this peak was evidently the largest peak in the entire pulse height distribution. Further, it can be observed that in the lower energy portion of the spectrum, where most of the daughter isotopes consist of ^{214}Pb, there is a lot of cluttering of the peaks and interference from adjacent peaks. The higher energy portion of the spectrum consists of more well isolated peaks, but with lower counts. It is also observable that the background was extremely small throughout the entire energy range of the spectrum.

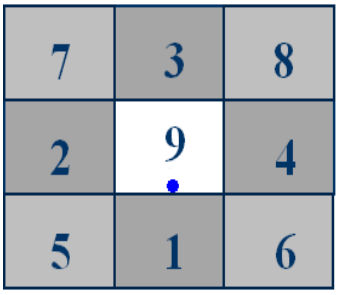

Figure 3.15 Configuration of the 4π NaI(Tl) detector assembly and placement of point source

It should also be noted from the above detector configuration, that detectors 5, 6, 7 & 8 are corner detectors and they are relatively shielded by their adjacent counterparts, detectors 1, 2 3 & 4. Also, detector 9 is much smaller compared to the eight outer detectors.

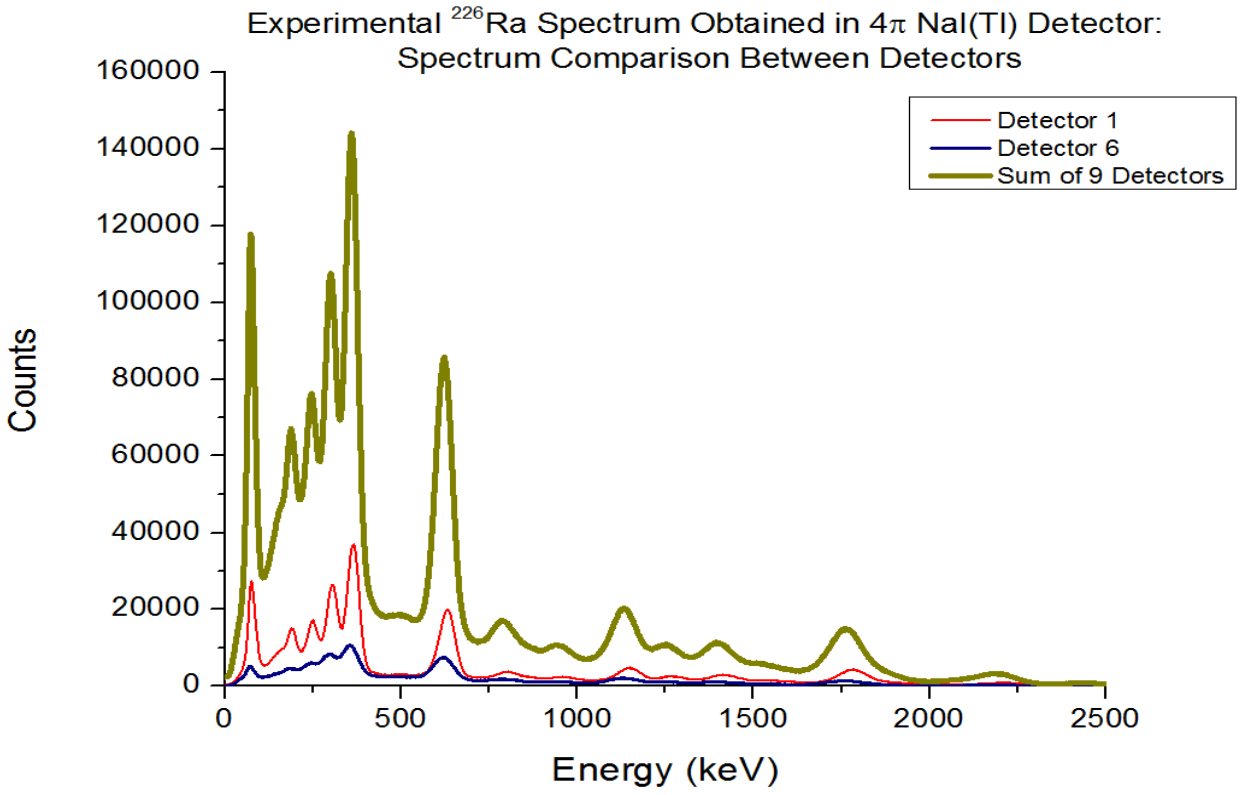

Figure 3.16 Individual 4π NaI(Tl) detector spectra for detectors 1 and 6 compared with summed spectrum

The above figure shows the individual detector spectra of detector 1 compared with detector 6 to show the weakness of detector 6. Due to the limited energy resolution of the 4π NaI(Tl) detector, the spectrum of the ^{226}Ra point source contained peaks which overlapped, especially in the lower energy region, thus, making it difficult to determine the region-of-interests for the full-energy peak efficiencies of the daughter radionuclides in the region between 50 keV and 500 keV in the spectrum. In order to achieve as low a detection limit as possible, and considering that the entire

spectrum consisted of ^{226}Ra and its daughter isotopes, including valuable information in the Compton continuum, as underlined in chapter 2, a spectral analysis algorithm in order to optimize system detection limit was established and applied to different energy region intervals.

Table 3.11: Nine spectral indices attempted for detection limit optimization algorithm for 1 hour counting with (a) 95% Confidence and (b) 99% Confidence

Index	x_1 (keV)	x_2 (keV)	(^{226}Ra Integral – Background Integral)	$2k_{\propto}$	$\sqrt{2C_B}$	L_D [Counts]	L_D [Bq] @ 95% CI
1	0	465	114866335	3.29	1001.03	3293.40	1.06
2	0	900	161122363	3.29	1138.43	3745.43	0.86
3	560	900	38599161	3.29	447.53	1472.39	1.41
4	0	1630	191560610	3.29	1176.06	3869.25	0.75
5	900	1475	26860715	3.29	282.32	928.84	1.28
6	560	1475	65459876	3.29	529.14	1740.88	0.98
7	1990	2510	3483978	3.29	113.48	373.34	3.96
8	50	1990	202242909	3.29	1181.39	3886.77	0.71
9	50	2520	205731308	3.29	1186.83	3904.66	0.70

(a)

Index	x_1 (keV)	x_2 (keV)	(^{226}Ra Integral – Background Integral)	$2k_{\propto}$	$\sqrt{2C_B}$	L_D [Counts]	L_D [Bq] @ 99% CI
1	0	465	114866335	4.652	1001.03	4656.81	1.50
2	0	900	161122363	4.652	1138.43	5295.97	1.22
3	560	900	38599161	4.652	447.53	2081.93	2.00
4	0	1630	191560610	4.652	1176.06	5471.05	1.06
5	900	1475	26860715	4.652	282.32	1313.36	1.81
6	560	1475	65459876	4.652	529.14	2461.57	1.39
7	1990	2510	3483978	4.652	113.48	527.89	5.61
8	50	1990	202242909	4.652	1181.39	5495.82	1.01
9	50	2520	205731308	4.652	1186.83	5521.11	0.99

(b)

In order to compare results with the HPGe performance analysis, the counting time was scaled for 1 hour counting. The above table shows the detection limits for nine different energy intervals for 1 hour counting, using the procedure described in the methodology for the point source located at 15 cm. It is observed that index nine had the lowest detection limit for a 1 hour count. This region incorporated the entire spectrum's energy range. The next lowest detection limit for spectral index 8 incorporated the first twelve of fourteen visible full energy peaks. This result is significant because it shows that with the ^{226}Ra source, every count in the entire spectrum contains important information. If we examine the ^{226}Ra decay scheme, the decay consists of ^{226}Ra and its daughters, namely ^{214}Pb and ^{214}Bi, and this is exactly what was observed in the spectrum. Spectral analysis should consist of the entire region. In essence, there are no boundaries, the entire region is the region-of-interest, as there is no spectral interference from any other nuclide other than ^{226}Ra and its daughters. Further, since the NaI(Tl) crystal has a higher Z- number compared to the Ge crystal, the photoelectric effect is higher for the NaI(Tl) detector. This results in a large Peak-to-Compton ratio for the NaI(Tl) compared to the HPGe, which has a larger Compton contribution. This explains why the peak areas were considerably larger for the 4π NaI(Tl) detector compared to the HPGe detector.

Table 3.12: Spectral index #9 attempted for detection limit optimization algorithm for 24 hour counting with (a) 95% Confidence and (b) 99% Confidence

Index	x_1 (keV)	x_2 (keV)	L_D [Counts]	L_D [Bq] @ 95% CI
9	50	2520	19934.08801	0.15

(a)

Index	x_1 (keV)	x_2 (keV)	L_D [Counts]	L_D [Bq] @ 99% CI
9	50	2520	28186.4369	0.21

(b)

The above table shows the detection limit algorithm results for 24 hour counting for spectral index nine, using the procedure described in the methodology for the point source located at 15 cm. This detection limit is significantly lower than that obtained for the HPGe, and thus presents more relevance for live fish analysis, especially at environmentally relevant levels, which are often in order of mBq's. These results also confirm that $L_D \propto \frac{1}{\sqrt{t_c}}$ as expected. From a health physics perspective, it is very important to be able to measure ^{226}Ra dose at very low levels. For example, low level ^{226}Ra releases in aquatic environments involved with uranium mining are normally at trace levels, far below emission standards. The detection limit results for the 4π NaI(Tl) detector demonstrate that there is a real incentive to go beyond the detection limits that the HPGe detector offers for ^{226}Ra.

3.3 HPGe Detector Performance Analysis Comparison with Literature:

The following section attempts to perform a comparison between the above determined detection limits for the HPGe and 4π NaI(Tl) systems with those presented in literature, cited in section 1.8.

Firstly, it is important to realize that laboratory background levels were different between all the results cited in literature and the results analyzed in this project, due to different room and detector shielding configurations used in each study. In order to assume a fair condition for the

above results with literature, the same conditions for background shielding must exist. Therefore, theoretically, for a fair comparison, in order to attain realistic comparative results, either shielding should be added to the detectors involved in this study, or shielding should be removed from those which were involved in the literary review. Further, referring to table 1.8.1, the previous studies involved in assessing system detection limit for ^{226}Ra all used a variety of counting times. Any comparative analysis will require scaling of counting times such that they are equal.

The detection limits for the three strongest ^{226}Ra point source peaks in the HPGe detector, 295 keV, 352 keV & 609 keV, and the overall combined detection limit, $L_{D,Combined}$ achieved in this study for the HPGe detector, 6.808 Bq at 95% confidence, was scaled for counting time, reflective of the counting times presented in the studies from the literary review. The background spectrum from this study was also scaled for counting time, and the results are summarized in the table below.

Table 3.13 HPGe system detection limits in this study for ^{226}Ra point source at contact with detector for different counting times, reflective of those counting times used in literary review studies

295 keV							
t_c **[sec]**	*86400*	*154800*	*100000*	*65000*	*82800*	*60000*	*12000*
C_B **[counts]**	87240	156305	100972.2	65631.94	83605	60583.33	12116.67
$L_D[Bq]$ @ **95% Confidence**	2.3776	1.77629	2.21003	2.74121	2.4288	2.85314	6.37981
$L_D[Bq]$ @ **99% Confidence**	3.362	2.512	3.125	3.876	3.434	4.034	9.021
352keV							
t_c **[sec]**	*86400*	*154800*	*100000*	*65000*	*82800*	*60000*	*12000*
C_B **[counts]**	86064	154198	99611.11	64747.22	82478	59766.67	11953.33

$L_D[Bq]$ @ 95% Confidence	1.4536	1.08596	1.35114	1.67589	1.4849	1.74432	3.90041
$L_D[Bq]$ @ 99% Confidence	2.055	1.536	1.91	2.37	2.1	2.466	5.515
609 keV							
t_c [sec]	*86400*	*154800*	*100000*	*65000*	*82800*	*60000*	*12000*
C_B [counts]	60936	109177	70527.78	45843.06	58397	42316.67	8463.333
$L_D[Bq]$ @ 95% Confidence	1.7464	1.3047	1.62329	2.01344	1.78394	2.09566	4.68603
$L_D[Bq]$ @ 99% Confidence	2.469	1.845	2.295	2.847	2.522	2.963	6.626
$L_{D,Combined}[Bq]$ 95% Confidence (Inverse Mean Variance Theorem)	1.011	0.7554	0.9399	1.1658	1.033	1.2134	2.7132
$L_{D,Combined}[Bq]$ @ 99% Confidence (Inverse Mean Variance Theorem)	1.43	1.068	1.329	1.649	1.461	1.715	3.836

Table 3.14: 4π NaI(Tl) Spectral index #9 attempted for detection limit optimization algorithm for 54 hour counting with (a) 95% Confidence and (b) 99% Confidence

Index	x_1 (keV)	x_2 (keV)	L_D [Counts]	L_D [Bq] @ 95% CI
9	50	2520	29901.13	**0.10**

(a)

Index	x_1 (keV)	x_2 (keV)	L_D [Counts]	L_D [Bq] @ 99% CI
9	50	2520	42279.63	0.15

(b)

In literary studies #3 and #4, a NaI(Tl) detector was used in order to assess the system detection limit for a ^{226}Ra source. In the first study by Faanu *et al, 2012*, the standard reference source was counted for 86400 seconds while using a 2 cm thick lead shield, and in the second study by Harb *et al*, 2014, the soil sample source was counted for 54 hours, while using a 3 cm thick lead shield. When scaling the 4π NaI(Tl) counting time to 54 hours, the above table shows the results that were calculated for system detection limit for index 9 after applying the spectral analysis optimization algorithm for 54 hour (194,400 sec) counting. Index nine is of most relevance as the entire energy range offers the lowest detection limit in the 4π NaI(Tl) detector.

Table 3.15: Spectral index #9 attempted for detection limit optimization algorithm for 200 minute counting with (a) 95% Confidence and (b) 99% Confidence

Index	x_1 (keV)	x_2 (keV)	L_D [Counts]	L_D [Bq] @ 95% CI
9	50	2520	7428.99	0.40

(a)

Index	x_1 (keV)	x_2 (keV)	L_D [Counts]	L_D [Bq] @ 99% CI
9	50	2520	10504.46	0.57

(b)

Further, in order to compare the liquid scintillation analysis study detection limit results to those from this study, the above results were obtained for system detection limit for index 9 after applying the spectral analysis optimization algorithm for 200 minute (12,000 sec) counting.

Examining the above results for combined HPGe system detection limit at the various counting times, it is observed that at 95% confidence, the lowest detection limit achieved was 0.76 Bq for a count time of 43 hours. A 24 hour count resulted in a detection limit of 1.01 Bq. This meant that approximately doubling the counting time resulted in a 25% reduction in the detection limit. Furthermore, the reduction in detection limit between 60,000 sec and 154,800 sec is approximately 38%.

Table 1.8.2 represents the absolute upper limit of natural background attenuation for the reasoning mentioned in section 1.8. When examining table 1.8.2, the three energies used for assessing HPGe system detection limit in this study, 295 keV, 352 keV & 609 keV represent energies at which theoretically, natural background is essentially eliminated when lead shielding greater than 2 cm is used. However due to secondary radiation introduced in the shield and from the source via Compton scattering, attenuation cannot be evaluated as straightforwardly. The background contribution in a detector when performing gamma-ray spectrometry is from two components: from natural background radiation and from inside the source itself. The majority of the detection limit results presented in section 1.8 are normalized in terms of sample mass. While

these detection limits are expressed in specific activity, it is not known if the background from those studies were exactly proportional to sample mass or not depending the natural background contribution. Further, the exact background counts in the literary review studies are unknown, so there is no certain method of determining the actual reduction of background counts from the shielding.

When the detection limit is reported per sample mass, it is assumed that the source is uniformly distributed inside the sample, thus enabling switching back and forth between detection limit in Bq and detection limit in Bq per sample mass. Therefore, in order to perform a direct comparison between the detection limits found in the literary studies and those obtained in this study, the normalized detection limit results from the literary review will be multiplied by their indicated sample masses.

Table 3.16: Comparison between detection limits from this study and literary review studies

Publication	**Counting Time t_c (sec)**	**Sample Mass (kg)**	$\frac{L_D}{sample\ mass}$	**Publication: $L_D[Bq]$ @ 95% Confidence** $\left(\frac{L_D}{sample\ mass}\right)\ x\ sample\ mass$	**This Study: $L_D[Bq]$ @ 95% Confidence (Scaled for t_c)**
1. Thompson (2012, Hamilton)	12000	0.02	7.46 mBq/g	**0.1492**	**HPGe: 2.7132** **4π NaI(Tl): 0.40**
2. Mothersill *et al.* (2014, Hamilton)	N/A	0.018	0.3 Bq/L	**0.0054**	**--**
3. Faanu *et al.* (2011, Legon-Accra, Ghana)	86400	--	0.099 Bq	**0.099**	**0.21**

4. Harb *et al.* (2014, Qena, Egypt)	194400	0.5	0.546 Bq/kg	**0.273**	**0.10**
5. Keyser (2011, Oak Ridge, TN)	154800	--	2.04 mBq	**0.00204**	**0.7554**
6. Chinnaesakki *et al.* (2012, Mumbai, India)	100000	0.3	4.3 Bq/kg	**1.29**	**0.9399**
7. Jabbar (2010, Rechna Doab, Pakistan)	65000	0.2	3.6 Bq/kg	**0.72**	**1.1658**
8. Kinsara *et al.* (2014, Jeddah, Saudi Arabia)	82800	0.5	1.3 Bq/kg	**0.65**	**1.033**
9. Alrefae *et al.* (2013, Khaldia, Kuwait)	86400	0.17	3.67 Bq/kg	**0.62**	**1.011**
10. Khandaker *et al.* (2012, Kuala-Lumpur, Malaysia)	60000	0.308	0.8 Bq/kg	**0.24**	**1.2134**

The detection limit obtained by Keyser, 2.04 mBq over a counting time of 154800 seconds implies that due to the 4π geometry of the well-type detector, his detector had far superior detector efficiency than the detector used in this study. In this study, the absolute peak efficiencies for 295 keV, 352 keV and 609 keV for the ^{226}Ra source at contact with the detector were 3.4%, 2.9% and 1.7%, respectively. The well-type detector used by Keyser was customized to achieve absolute peak efficiencies many times higher, and this may help explain the

discrepancy between the L_D value achieved by Keyser 2.04 mBq, and that from this study for the HPGe detector scaled for 43 hours, 755 mBq.

From table 3.16, the detection limit value in this study obtained for the 4π NaI(Tl) of 0.1 Bq for a 54 hour counting time is better than the value of 0.273 Bq from the corresponding publication #4 by 173%. This can be attributed to the fact that a nine detector array was used in this study, whereas only one NaI(Tl) detector was used in the publication. For a 24 hour count time, the value of 0.099 Bq obtained in study #3 by *Faanu et al*. is 112% better than the value of 0.21 Bq obtained in this study. This may be attributed to the fact that within the lead shield from the literary study were also copper, cadmium and Plexiglas (3 mm each) to absorb x-rays and other photons that might be produced in the lead. For the HPGe detector, the detection limit value in this study obtained when scaled to a counting time of 100000 seconds, 0.94 Bq is better than the detection limit comparatively with the value determined in the literary study #6, by Chinnaesakki *et al*, of 1.329 Bq by 41.3%. Publications #7, #8 & 9 obtained detection limits of 0.72, 0.65 and 0.62 Bq, whereas the comparative results obtained from this study when scaled for t_c are 1.17, 1.03 and 1.01, respectively, for percentage variations of 62.5%, 58.5% and 62.9%, respectively. The detection limit value in this study obtained when scaled to t_c = 60000 sec, 1.21 Bq had a percentage variation of 400%. The large discrepancy for study #10 may be owing to the fact that a square shield was used with dimensions of 14.5 cm length and 12.5 cm height in addition to the 4 cm thickness. All of the above comparative results are reasonable considering the fact that for those results in which the detection limit from the literary studies was better than the corresponding values from this study, the studies from the literature used heavy shielding in order to eliminate natural background radiation. If this study had used similar shielding, perhaps the results would have agreed better with the literature. For the liquid scintillation analysis study,

the comparative results, 1718% variation for the HPGe result for 12000 sec from this study, and 168% variation for the 4π NaI(Tl) result for 12000 sec from this study demonstrate that the liquid scintillation method provides far superior detection limits compared to gamma-ray spectrometry. However, as emphasized in chapter 1, this method cannot be used for live fish radioactivity analysis, therefore the 4π NaI(Tl) is the best detector to use with live fish. Likewise with Mass Spectrometry, superior detection limit but fish would need to be sacrificed and sample preparation is tedious. This comparative analysis demonstrates that shielding and efficiency are fundamental components which significantly influence the detection limit of a system.

3.4 4π NaI(Tl) System Dead Time Determination:

For the 10 minute count, the system dead time was determined in the following manner:

Table 3.17 a) 4π NaI(Tl) ^{226}Ra 37 kBq Point Source Spectrum Collection Properties

Irradiation start: N/A
Irradiation stop: 13-Jun-2014 16:00:09
Acquisition start: 13-Jun-2014 16:01:27
Saving interval 600 s.
Saving cycles completed 6.

b) 4π NaI(Tl) ^{226}Ra 37 kBq Point Source Dead Time Calculation

DSP Live Time (s)	DSP Clock Time (s)	(DSP Clock Time) - (DSP Live Time) (s)	Dead Time (%)	Average Dead Time (%)
576.974	599.961	22.987	3.831	**3.833**
577.378	600.330	22.952	3.823	
577.347	600.314	22.967	3.826	

577.365	600.346	22.980	3.828	
577.254	600.324	23.069	3.843	
577.268	600.357	23.089	3.846	

Average dead time was determined to be 3.833% which demonstrates that the 4π NaI(Tl) detector is excellent for low level environmental radioactivity analysis, as a low dead time can be maintained, allowing for reasonable counting time. With low environmental levels, counting times are already very large, thus having a small dead time is integral, especially with short-lived radionuclides. The dead time of the background spectrum was calculated in a similar manner, and it was determined that the average dead time for background was 0.02%.

DSP Live Time (s)	**DSP Clock Time (s)**	**(DSP Clock Time) - (DSP Live Time) (s)**	**Dead Time (%)**	**Average Dead Time (%)**
1799.859	1800.224	0.365	0.02	**0.02**
1800.258	1800.624	0.366	0.02	
1800.246	1800.612	0.366	0.02	
1800.244	1800.609	0.365	0.02	
1800.238	1800.603	0.365	0.02	
1800.212	1800.578	0.366	0.02	

Chapter 4: MCNP Monte Carlo Simulations:

4.1 Efficiency Calibration Challenge for Live Fish

The experimental methodology involved experimentally analyzing the detection limit of the HPGe detector and 4π NaI(Tl) detector. The spectral analysis optimization algorithm applied to the 4π NaI(Tl) detector showed that a detection limit 6.8 times lower could be achieved relative to the HPGe detector.

The concept of efficiency was the foundation of the detection limit analysis. It is common practice, when determining the activity of gamma-ray emitters with gamma-ray spectrometers, to compare measurements of an unknown source with those of a calibrated source of equivalent geometry and density [Daraban *et al*, 2012]. If the full-energy peak efficiency of a source is known, then with the knowledge that the efficiency is equal to the count rate over the emission rate, an unknown source's activity can be quantified, provided the same geometry and material composition was used. This is particularly important with environmental samples.

A major challenge that arises with ^{226}Ra radioactivity analysis in live fish is that tiny fish keep growing in terms of their size. Each time the fish's size changes, a new experimental efficiency calibration would have to be performed in the detector of interest. In addition, one must take into consideration the size of the water tank, as a larger fish requires a larger tank. However, with the introduction of a larger tank, self-attenuation effects become more prominent. Under these conditions, experimental efficiency calibration of volume sources with arbitrary shape becomes very tedious and costly to be fulfilled. Many different-sized ^{226}Ra phantoms would have to be prepared and analyzed.

A beneficial way to overcome these difficulties is through the use of Monte Carlo simulations, which takes into account the comprehensive characteristics of the detector and sample, in calculating the full-energy peak efficiencies. A common program used for the calculation of efficiencies in volume sources is MCNP-Monte Carlo N-Particle transport code. [MCNP User Manual, Version 5, 2003 *pp* 1-3, Gilmore, 2008 *pp* 157-158]. MCNP is a general-purpose Monte Carlo N-Particle code that can be used to compute neutron, photon, electron, or coupled neutron/photon/electron transport within an arbitrary three-dimensional configuration of materials in geometric cells. [Redd, 2003, *pp* 9-10] In the context of the complicated fish plus water container geometry, MCNP can be used to duplicate theoretically the probabilistic process as gamma rays travel from the fish body medium, through the water tank, and into the detector.

From the perspective of live fish simulations, the program works by defining a single gamma-ray originating within the fish body and being emitted in a random direction within the body. It then follows its transport as it scatters through the body, through the water tank, and if it is not attenuated in the source, then determines what interactions it undergoes within the detector to create the detector signal. By specifying a very large number of incident gamma-rays, the code performs this radiation transport a very large number of times in order to generate an efficiency curve that takes into account the size and shape of the body and water tank and any self-absorption within it.

By performing accurate simulations, accurate efficiency calibrations curves may be obtained for any arbitrary volume. In order to validate the simulations, the computational efficiency calibrations can be compared to benchmark experiments. Additionally, performing simulations using point source geometry is a beneficial precursor to performing arbitrary volume source

measurements. It allows verification to ensure that all computations have been performed correctly.

4.2 Methodology for MCNP Input Card Used to Build the 4π NaI(Tl) Detector Array

In order to ensure an accurate detector response, the 4π NaI(Tl) detector was modeled in detail. A pulse-height tally (MCNP F8) was performed over the active region of the detector crystal to determine the pulse-height spectrum.

The 4π Nine-NaI(Tl) Assembly was built by using manufacturer's specifications. Each of the eight outer NaI(Tl) detectors consisted of a $10.2\ cm\ x\ 10.2\ cm\ x\ 40.6\ cm$ NaI crystal (Thallium doping ignored), a 2.77 cm optical quartz window, and a 5.71 cm PMT void, with a 1mm thick stainless steel housing, according to the figure shown below:

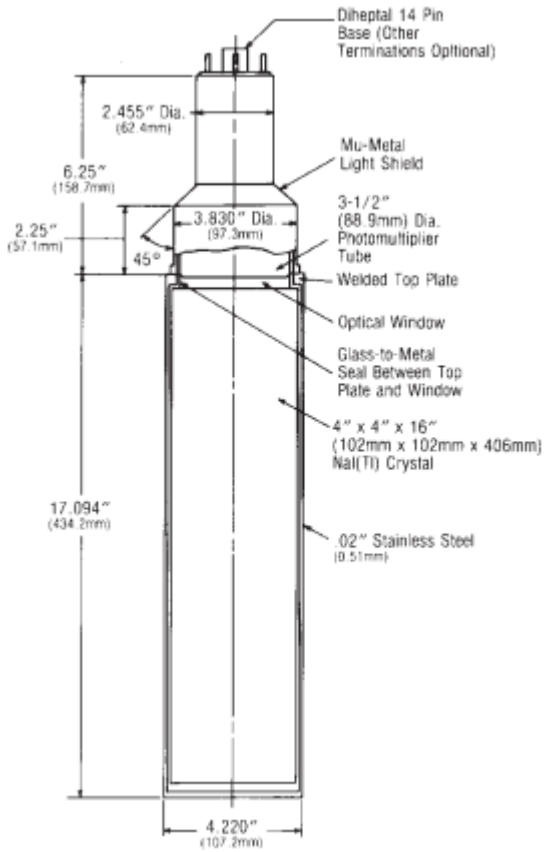

Figure 4.1: Squareline 10.2 *cm x* 10.2 *cm x* 40.6 *cm long NaI(Tl) assembly [Saint-Gobain, 1997]*

The dimensions and physical characteristics of the detector as built in MCNP are outlined below:

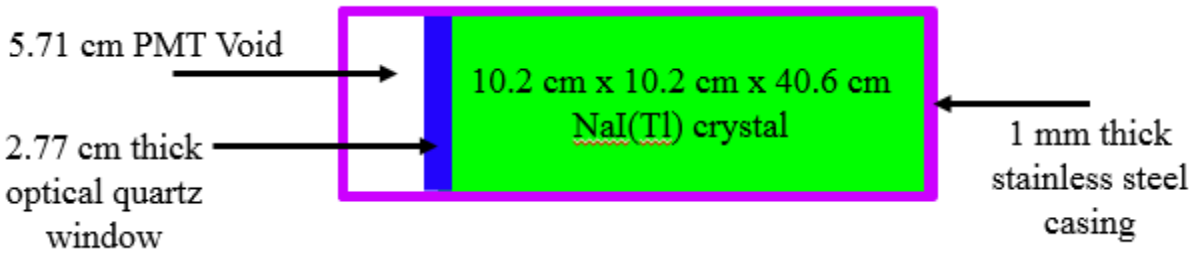

Figure 4.2: Geometrical representation of one of NaI(Tl) detector's used to build the 4π array

The ninth central NaI(Tl) Detector was modelled with the same specifications as above but with a 10.2 *cm x* 10.2 *cm x* 10.2 *cm* NaI crystal. In order to proceed building the entire nine detector array, three detectors, #5, #1 and #6 were built adjacent to each other and formed the base of the detector. Detectors #2, #9 and #4 were positioned on top of the bottom three detectors, respectively. Detector #9 was positioned at the back of the array. Finally, detectors #7, #3 & #8 were positioned on top of the middle row of detectors, respectively. The figure below shows the modelled 4π Nine-NaI(Tl) Assembly with the central aperture visible:

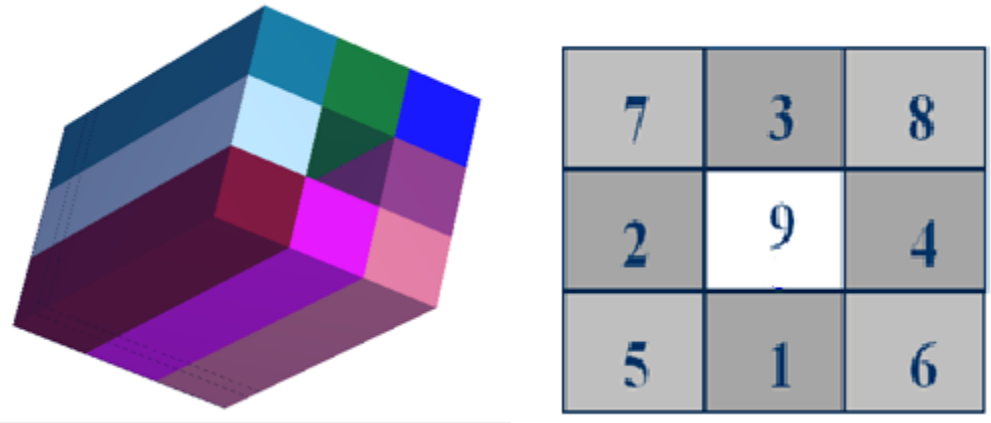

Figure 4.3: MCNP 4π Nine-NaI(Tl) Assembly and Detector Configuration

4.2.1 Source Definition

When building the input card, a point source was represented as a $5\ mm\ x\ 5\ mm$ cylindrical source. This source was assigned a vacuum matrix. The source particle was specified as a photon. In the input file, there were 1 million source particles emitted, also known as particle histories. In order to define the cylindrical point source, a reference point for the sampling position was assigned using the POS function. The AXS function was used to assign a reference vector for the direction cosines of the axis, so in essence the AXS function represents the source's directional vector. The RAD function was used to assign the radial distance from the sampling position. The radius was sampled using the SP card. The SP card is used to define the power law $p(x) = c|x|^a$ with $f = -21$, a built-in probability function which is used to generate a continuous probability density function for the source. [Hussein, 1997, *pp* 51] The syntax used for the built-in function was $-21\ a$. For radial sampling, the value of *a* was set to 1. The SI card was used to set the radial limits between the sampling position and r, which for the case of our point source was 0.25 cm. This implies that the radial sampling density is proportional to r. [Hussein, 1997, *pp* 51] The EXT function was used to specify the distance from the sampling position along the AXS vector. This value represents the distance of the ends of the cylinder from the sampling position. The EXT function was sampled using the SP card. The value of *a* for the power law was set to 0. The two built-in functions used for the cylindrical source, $-21\ 1\ and\ -\ 21\ 0$ together sampled a uniform distribution over the source volume. The SI card was used to set the distance of the ends the cylinder between the sampling position and distance *h*, which in the case of our point source was 0.5 cm.

Each simulation consisted of assigning the originating photon a single energy. Simulations were run for energies spanning 40 keV to 5000 keV in approximately 100 keV increments.

4.2.2 Tally Card:

The desired result in the simulation component of this study is a pulse height spectrum since it produces the distribution of the energy deposited in a cell, as in the γ-ray energy spectrum in a physical model of a detector. Pulse height spectra simulations are implemented in MCNP in the F8 tally. This tally is based on the following fundamental approaches [Damon, 2005, *pp* 53-54]:

• The energy bins in γ-spectra simulations correspond to the energy deposited in the detector cell summed over all the tracks of a history.

• No integral is evaluated, but the deposited energy in a cell is calculated based on the detailed microscopic radiation tracking.

• If the photon does not undergo interactions in a specified cell, no energy is deposited and the photon does not contribute to the pulse height spectrum.

Each energy bin was specified to be of width 0.01 MeV.

4.2.3 Particle Tracks Representation within Detector

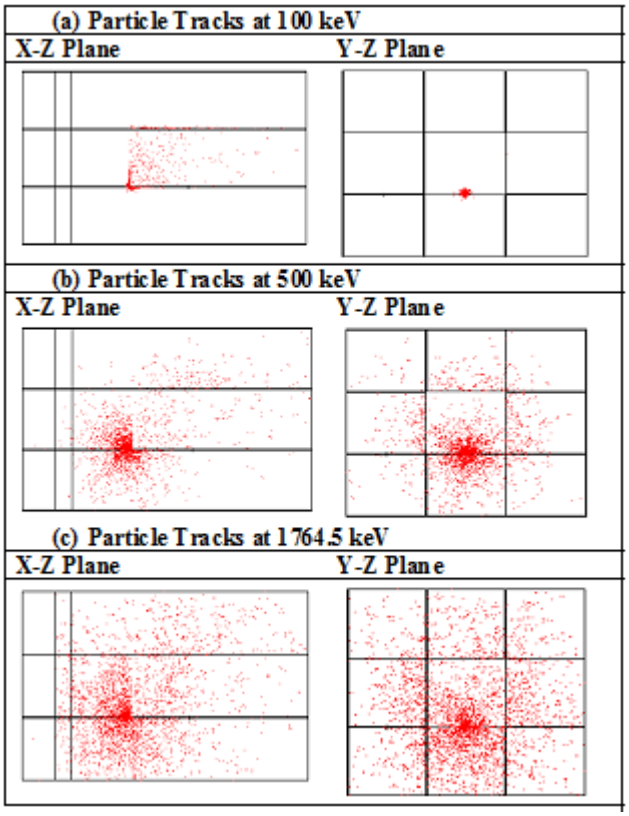

Figure 4.4: Particle tracks within 4π NaI(Tl) detector at three representative energies (a)100 kev, (b)500 keV & (c)1764.5 keV

The above figure shows particle tracks for a point in the 4π NaI(Tl) array at three representative mono-energies. The point source is located on top of detector 1 touching the front edge of the central ninth detector at position = 0 cm. Particle tracks represent collision points in the detectors. The MCNP Visual Editor computes and displays the paths of particles histories. Visualization of these paths improves understanding of both the physics of the problem and the efficiency of the calculation. The view is a 2-Dimensional cross sectional view in the X-Z and Y-Z planes.

From figure 4.4, it is observed that at 100 keV, most collisions are concentrated in the vicinity of the point source. This is the energy region where photoelectric absorption is dominant, and since

the energy is fairly low, photons do not travel very far. At 500 keV, the gamma-ray interactions within the detector occur all throughout the detector. This is the region where Compton scattering is dominant. At 1764.5 keV, the particle collisions are less concentrated around the point source compared to 100 keV and 500 keV, and the collisions can be seen in the NaI(Tl) crystal regions far beyond the source location. At such a high energy, pair production and Compton scattering both are competing processes, and a photon can travel farther. Also at this energy, a large proportion of the photons travel through the detector without interacting. Multiple Compton and pair production events result in many collisions at many different points within the detector. The point source was positioned in the reference position for the particle tracks simulation as shown in figure 4.5

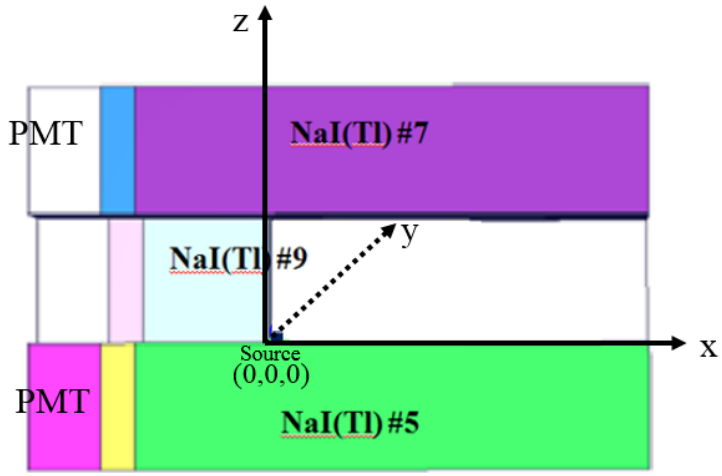

Figure 4.5 Reference point source position used for particle track measurements

4.2.4 Simulation for Point Source

The mono-energetic point source was modeled as a 5 mm x 5 mm cylindrical source. It was positioned in the reference position shown in figure 4.5. The program was run with an initial mono-energy of 40 keV and an output file was produced with the F8 pulse height tally results for each of the nine detectors. Using a spreadsheet, the tallies for all nine detectors were summed up

and plotted. The peak efficiency for each detector, in the energy bin of the input photon energy, was summed up. This same process was repeated for 53 different representative mono-energies. For each mono-energy, the summed peak efficiency was plotted as a function of incident energy. Further, the full-energy peak efficiency dependence on source position was plotted for several representative energies. The source was then positioned three centimetres away from its current position, in the +x direction, and the same process above was repeated for all 53 energies. Efficiency measurements were simulated at 0 cm, 3 cm, 6 cm, 9 cm, 12 cm, 15 cm, 18 cm, 21 cm, 24 cm, 27 cm, and 30 cm along the length of the detector. The point source placement and detector configuration is shown in the figure below.

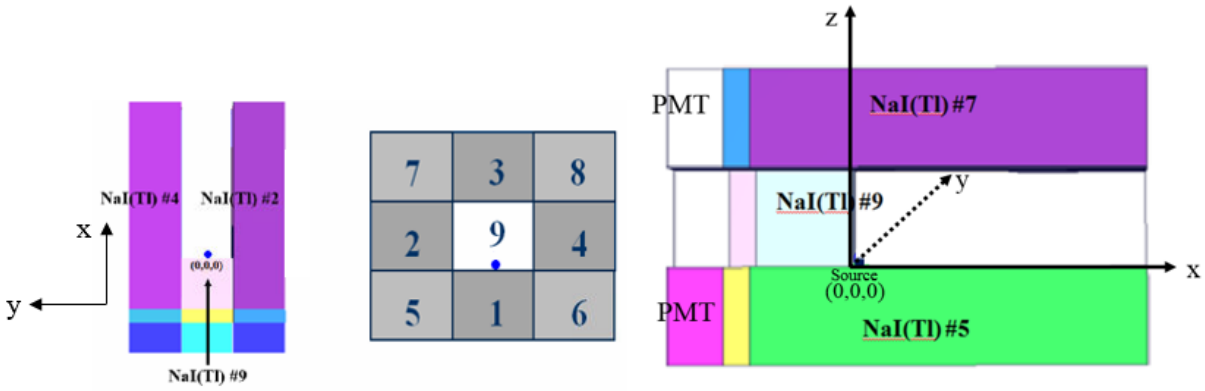

Figure 4.6: MCNP Point source placement and detector configuration

4.2.5 Extension to Volume Sources:

Figure 4.7: Sizes of bottles used for simulation of aqueous volume source

Following point source simulations, the cylindrical source was expanded and assigned a water matrix. This was accomplished by defining the source as a cylindrical cell placed in the central aperture of the detector and assigning the cell material as water. The central aperture of the detector was assigned an air matrix. The cylindrical source was expanded to represent three different sized bottles, representative of Nalgene bottles. Three different sizes were 60 ml, 125 ml, and 250 ml as shown above.

For each simulation, the volume source was placed in the central aperture of the detector, on top of detector one, touching the front edge of the central 9th detector. The simulation was run at that position for 31 different mono-energies, (increments of approximately 100 keV). The same process was repeated for the other two volume sources. Source placement and detector configuration is shown in figure 4.8 below. Further, the F8 pulse height tally was then simulated for both a ^{226}Ra point source and ^{226}Ra volume source. The source definition cards were built from the gamma emission probability table given in chapter 1.

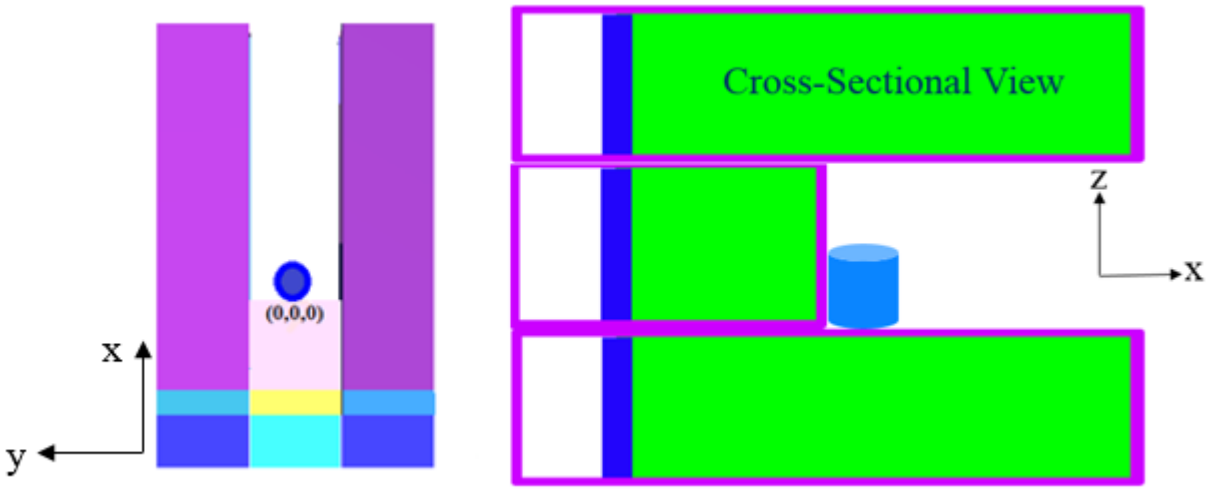

Figure 4.8: Volume Source placement in 4π NaI(Tl) Detector

4.2.6 Fish-Like Cylindrical Source Simulations:

In order to simulate live fish in a container, it is extremely beneficial if the fish's localization and movement patterns are known. Due to the random movements of the fish, this localization can be anywhere within the container. The fish movement pattern and its subsequent radioactivity analysis was performed by selecting locations in the container, modelling a cylindrical fish-like source in those locations, and running simulations to determine peak efficiencies as a function of position within the container. Eighteen different source positions were scanned in a $10\ cm\ x\ 10\ cm\ x\ 13\ cm$ container filled with water; nine positions in the centre of the container, and nine additional positions moved laterally to the side of the container. Each volume source was modelled as a horizontal cylinder of dimensions $2\ cm\ x\ 4\ cm$, and assigned a water medium. The simulation results were used to plot peak efficiencies as a function of source position, and to plot total detected events as a function of source position at several representative energies. The source positions 1-9 are shown in figure 4.9. The coordinates of source positions 1-18 are shown in table 4.1.

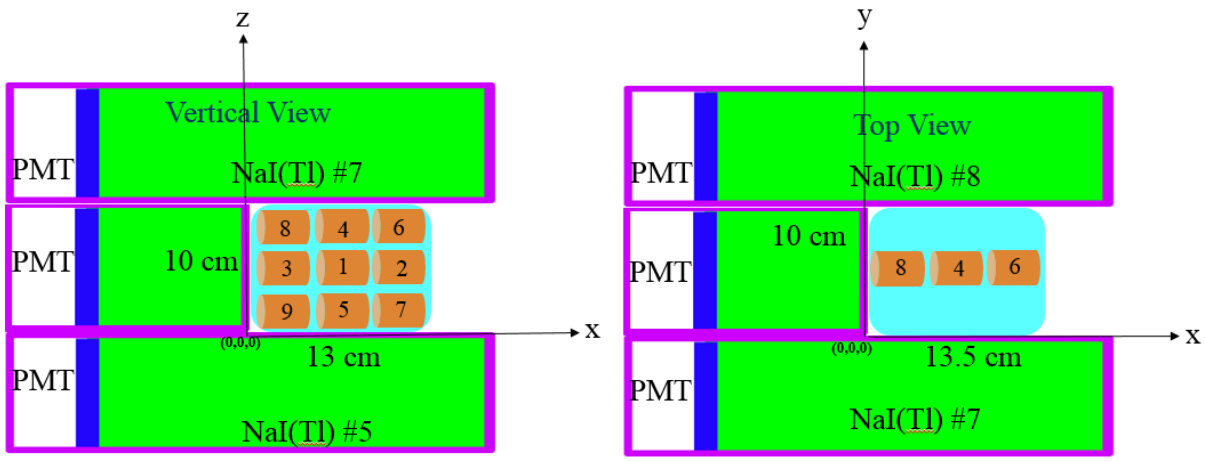

Figure 4.9: Fish-Like Cylindrical Source Positions used for Peak Efficiency Calibration

Table 4.1: Fish-Like Cylindrical Source Position Coordinates for Positions 1 – 18

Source Position	Coordinates (cm)
1	(4.3,0,5)
2	(8.6,0,5)
3	(0,0,5)
4	(4.3,0,9)
5	(4.3,0,1)
6	(8.6,0,9)
7	(8.6,0,1)
8	(0,0,9)
9	(0,0,1)
10	(4.3,-4,5)
11	(8.6,-4,5)
12	(0,-4,5)
13	(4.3,-4,9)
14	(4.3,-4,1)
15	(8.6,-4,9)
16	(8.6,-4,1)
17	(0,-4,9)
18	(0,-4,1)

4.3 Simulation Results and Discussion:

4.3.1 Point Source Position Dependence

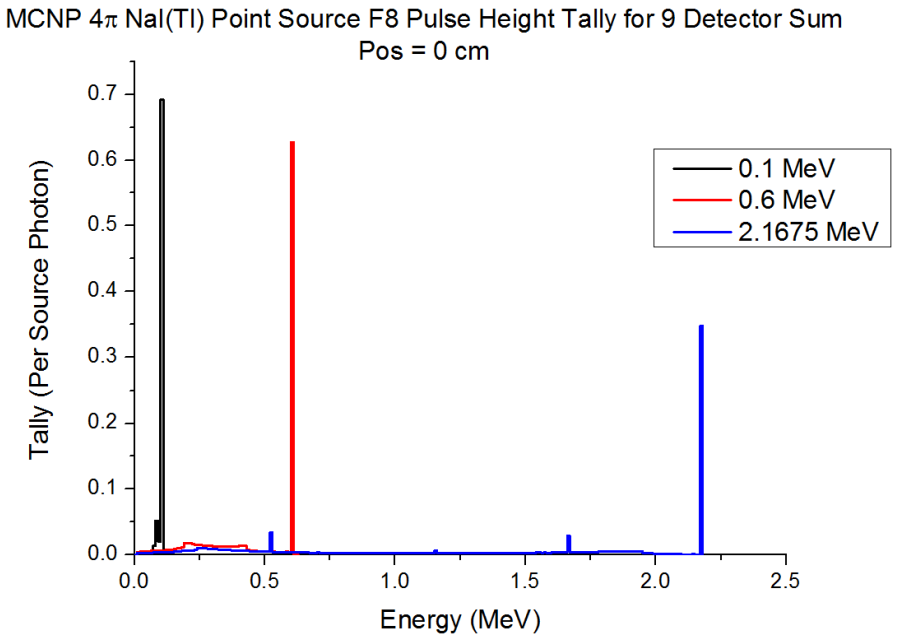

(a)

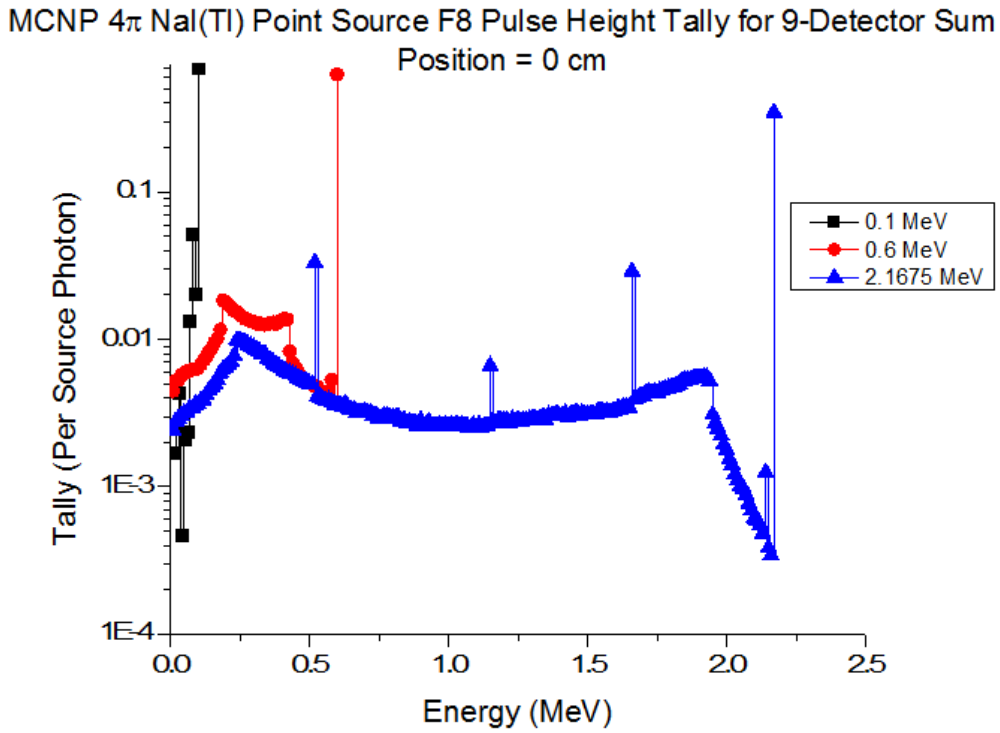

(b)

Figure 4.10: (a) Point source F8 pulse height tally for 9-detector sum at position = 0 cm at three representative energies. (b) Spectrum in logarithmic scale

The above figure shows the F8 pulse height tally (normalized per source photon) for the point source at position = 0 cm for three representative energies. At 0.1 MeV, photoelectric absorption is dominant at this energy, thus a single full-energy peak is observed. At 0.6 MeV, Compton scattering is the dominant mode of interaction, and a Compton continuum can be observed in addition to the full-energy peak. At 2.1675 MeV, pair production is the dominant mode of interaction, with Compton scattering also present. The annihilation peak, single escape peak and full-energy peak can be observed.

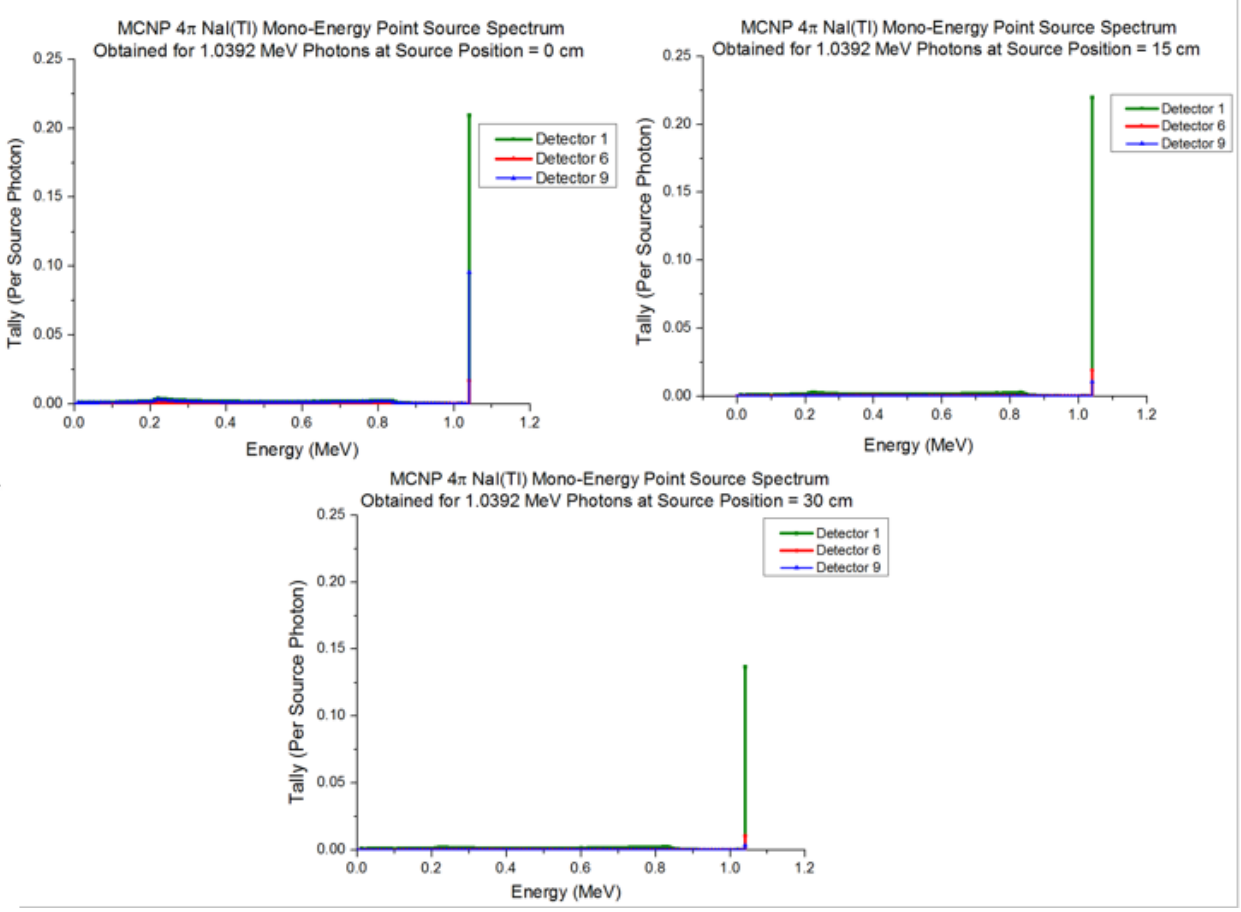

Figure 4.11: Point source F8 pulse height tally spectrum for 1.0392 MeV photon in detectors 1, 6 & 9 at positions = 0, 15 and 30 cm

The above figure shows the F8 pulse height tally (normalized per source photon) for 1.0392 photons at three different point source positions: 0 cm, 15 cm, & 30 cm. As the point source is moved further outwards in the detector, the detector 9 tally gets smaller, however, the detector 1 tally remains the largest, whereas the detector 9 tally is very small, as expected. Detector 9 being the smallest detector, is relatively weak compared to detectors 1, 2, 3 and 4, and as the source gets moved further away, less photons reach it.

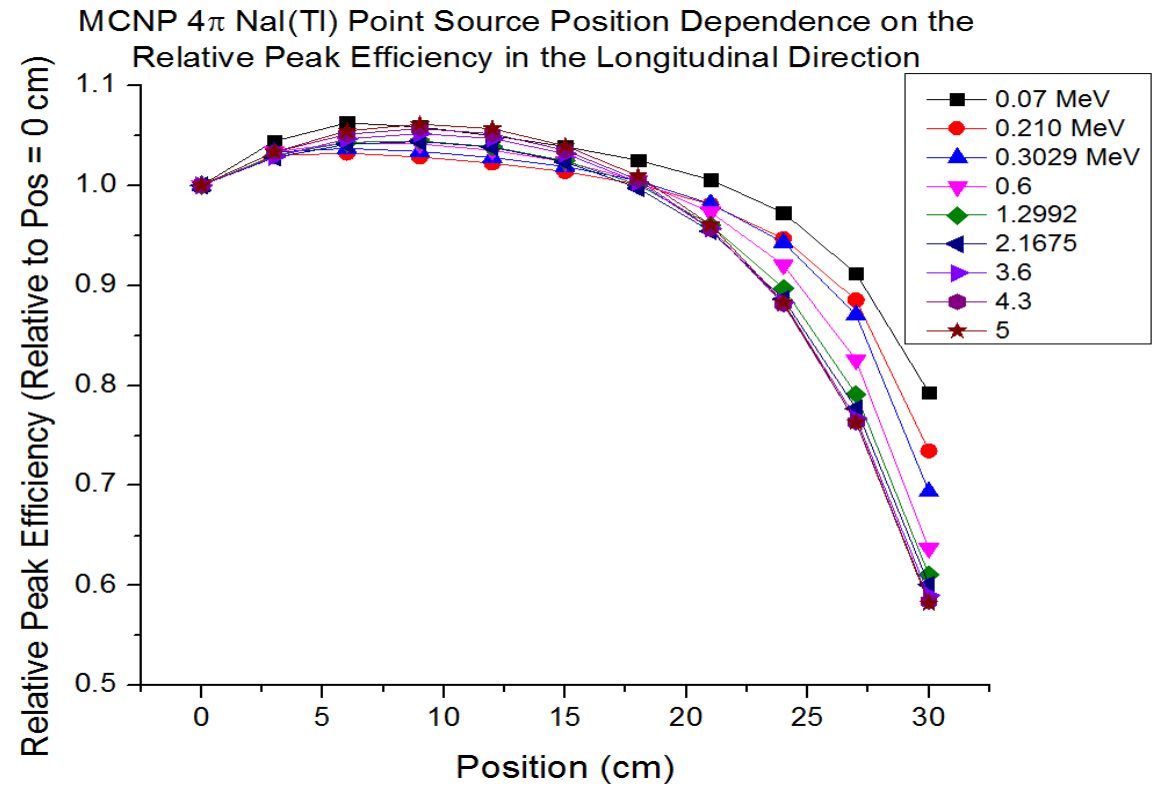

(a)

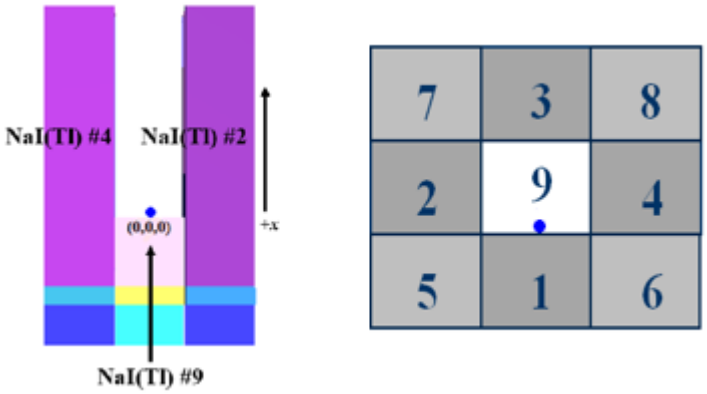

(b)

Figure 4.12: (a) Point source position dependence on relative peak efficiency of 4π NaI(Tl) detector at several representative energies. (b) 4π NaI(Tl) Detector Configuration

The above figure shows the mono-energy peak efficiency dependence on point source position in the detector along x-axis at several representative energies. It can be well observed that approximately between positions 0 cm and 20 cm along the x-axis, there is a volume where there

is very little variation in efficiency. This is significant for the live fish measurements, and it allows us a large finite volume in which the fish can move, with a minimal change in efficiency. As expected, efficiency drops off significantly at the outer edge of the detector closer to position 30 cm. It is to be expected since the solid angle at this point is approximately 2π. When the source was moved up and down along the z-axis (transverse), it was observed the efficiency changed very slightly. The figure below demonstrates that the relative peak efficiency with respect to transverse position varies extremely slightly with position, with a less than 1.2% variation between positions and the relative total detected events vary by less than 6%.

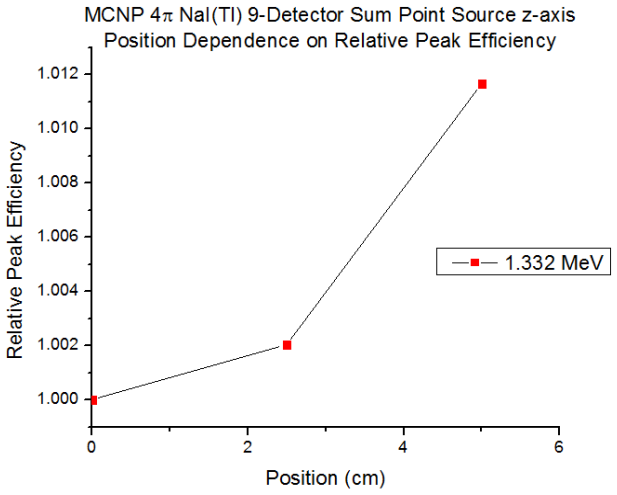

(a)

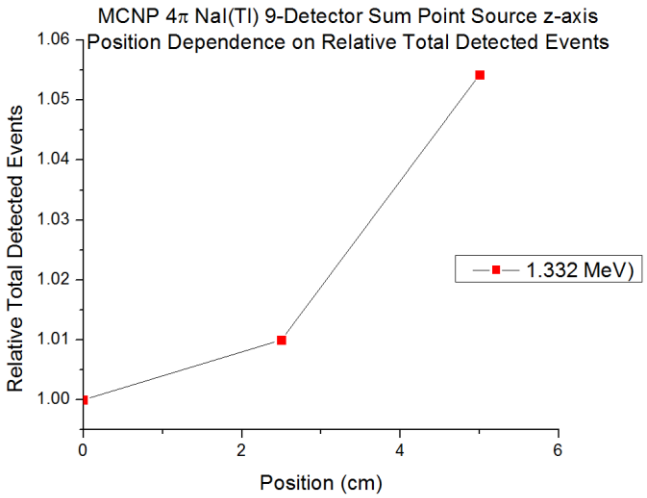

(b)

Figure 4.13 Point source position dependence on (a) relative peak efficiency and (b) relative total detected events of 4π NaI(Tl) detector along z-axis at 1.332 MeV

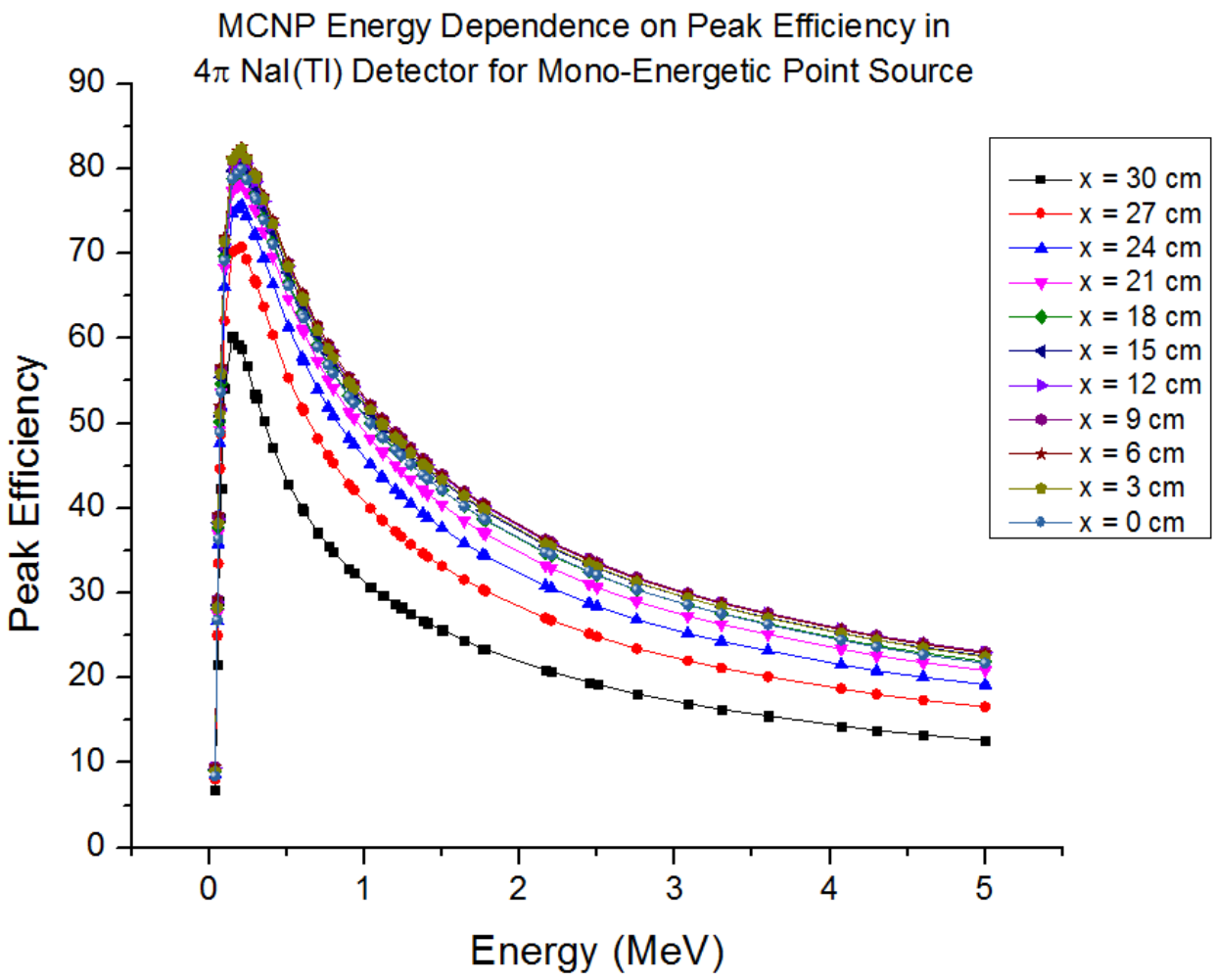

Figure 4.14 Point source full-energy peak efficiency dependence on photon energy at all representative source positions

The above figure shows a plot of point source energy dependence on peak efficiency at all positions measured. All of the curves follow the same pattern. The maximum efficiency occurs around 0.250 MeV, where photoelectric absorption dominates, and then drops off at higher energies, where Compton and pair production events dominate.

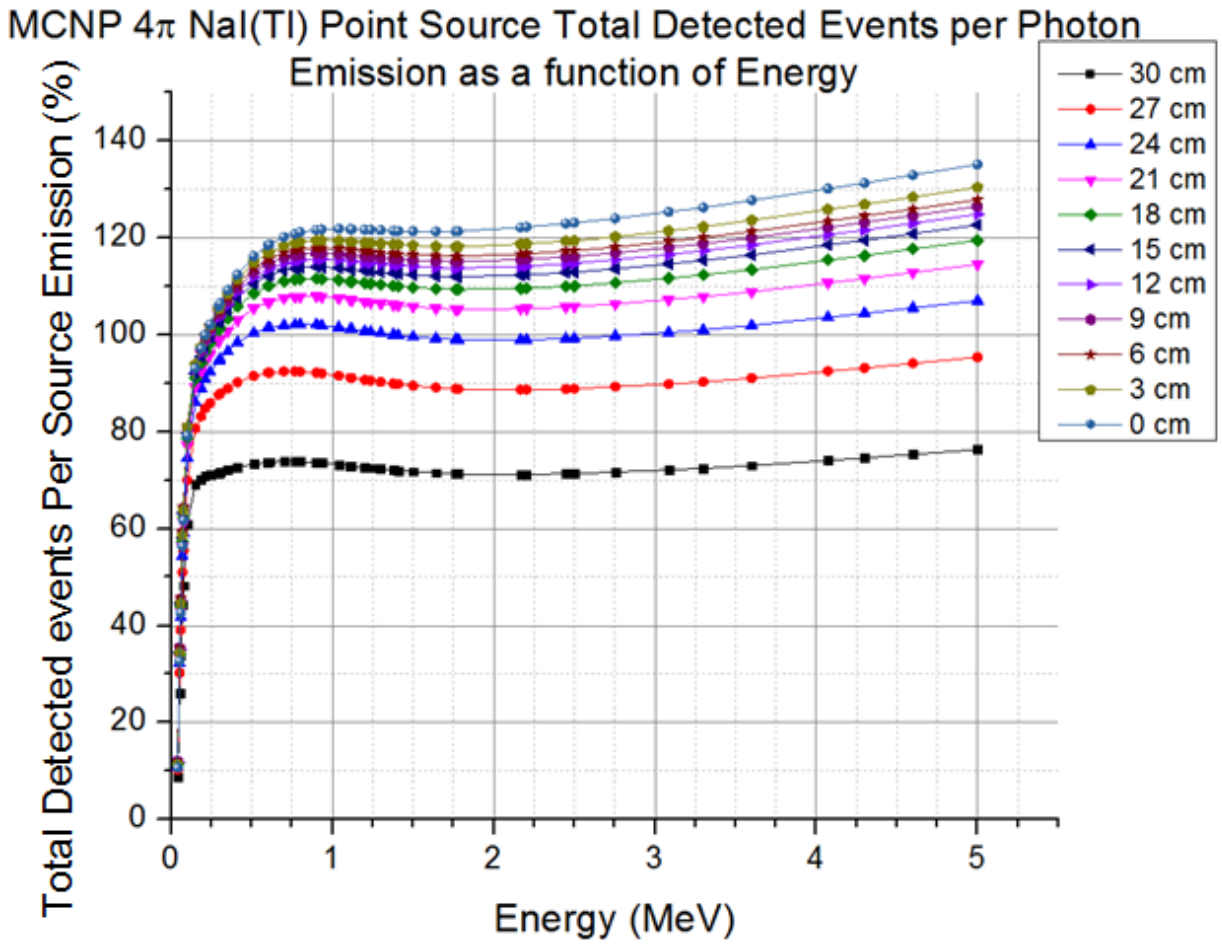

Figure 4.15 Point source total detected events dependence on photon energy at all representative source positions

The above figure shows a plot of total detected events as function of energy at all positions measured. It is observed that total detected events exceeds 100%. This is due to simultaneous pair production events in two detectors during the emission of two gamma-rays, 180^{o} apart, and due to Compton collisions in one detector and photoelectric absorption in another detector.

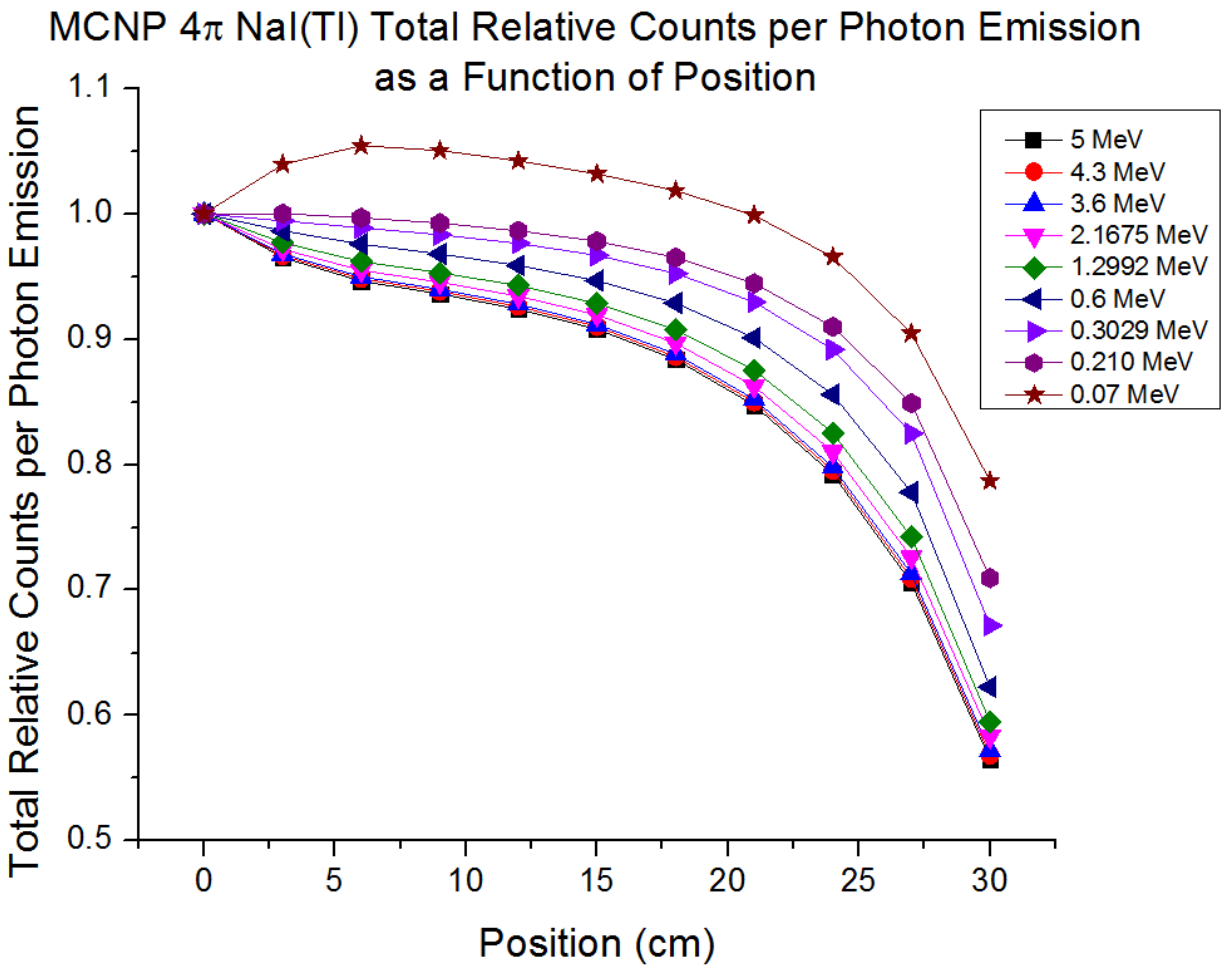

Figure 4.16: Point source position dependence on total relative counts per photon emission in the 4π NaI(Tl) detector at several representative energies

The above graph shows the total relative detected events as a function of position. This graph demonstrates that the greatest number of total detected occur between 0 – 15 cm. As the source is moved further away from detector 9, the solid angle decreases. The reduction in solid angle becomes more pronounced after 20 cm, as gamma-rays have a greater tendency to escape from the aperture of the detector. At 30 cm, the solid angle essentially becomes 2π. The large efficiency between 0-20 cm allows a greater degree of freedom when deciding how large the source container should be modelled. Thus this graph shows why ultimately the 4π NaI(Tl)

detector is the ideal detector to use when performing low level ^{226}Ra radioactivity analysis in live fish.

4.3.2 Comparison of MCNP and Experimental Relative Peak Efficiencies

The four most well isolated peaks in the experimental spectrum obtained for the ^{226}Ra point source were 609 keV, 1377 keV, 1764.5 keV and 2204 keV. The relative full-energy peak efficiencies were experimentally analyzed using OriginPro peak fitting software four these four full-energy peaks as a function of position. The corresponding mono-energetic relative peak efficiencies were simulated in MCNP and a comparison was performed. The following figures show the results:

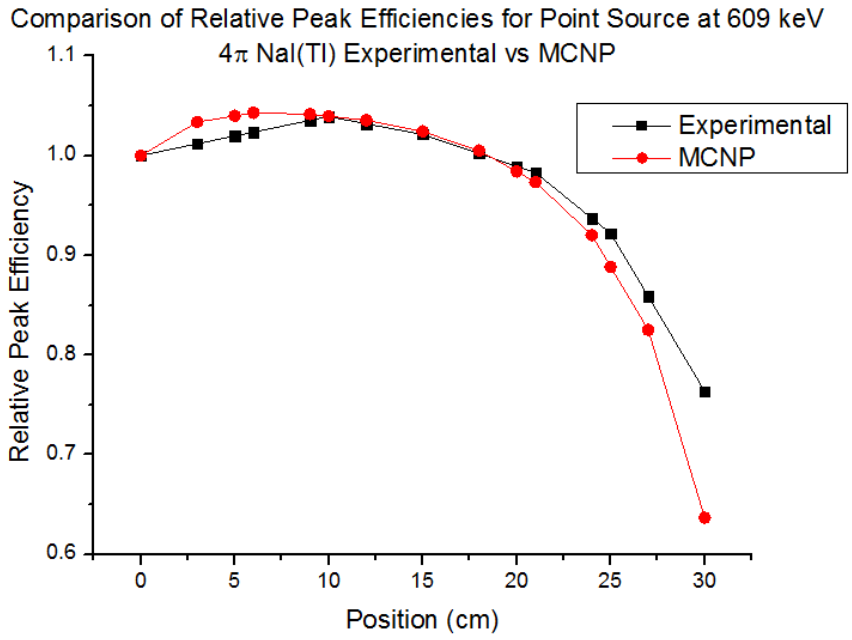

Figure 4.17: Comparison of experimental vs. MCNP relative peak efficiencies for a point source as a function of position at 609 keV in the 4π NaI(Tl) detector

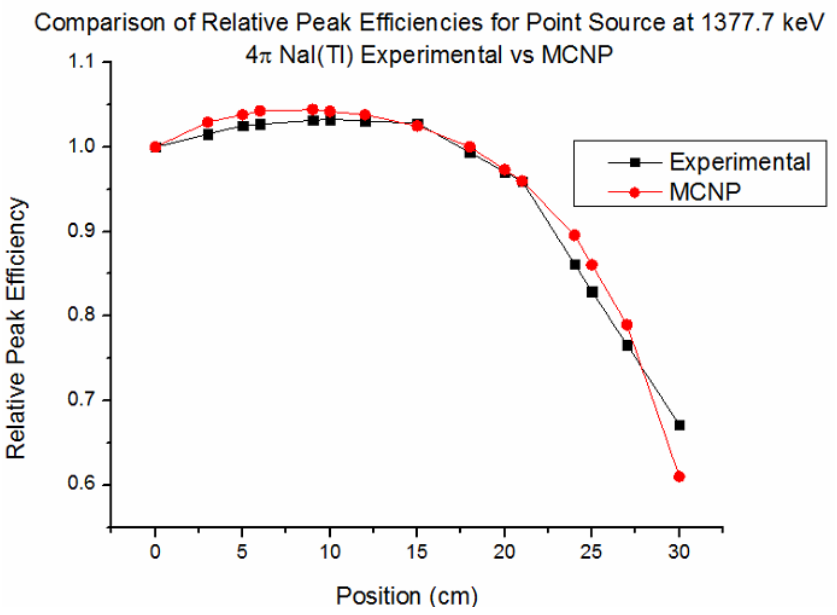

Figure 4.18: Comparison of experimental vs. MCNP relative peak efficiencies for a point source as a function of position at 1377.7 keV in the 4π NaI(Tl) detector

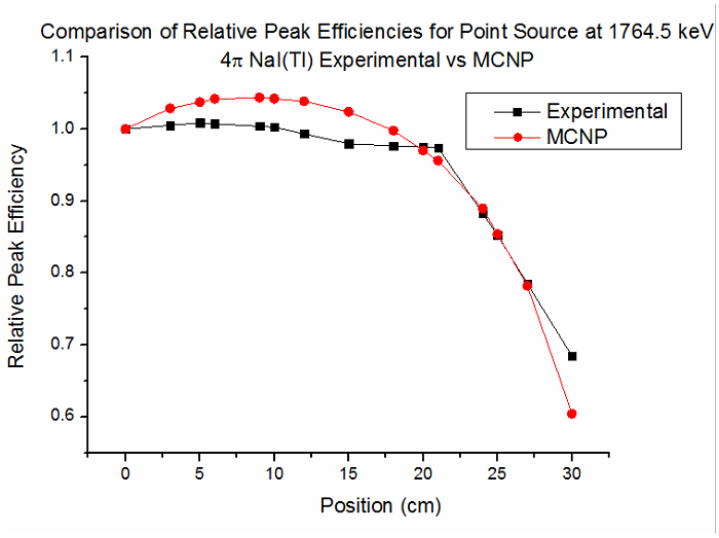

Figure 4.19: Comparison of experimental vs. MCNP relative peak efficiencies for a point source as a function of position at 1764.5 keV in the 4π NaI(Tl) detector

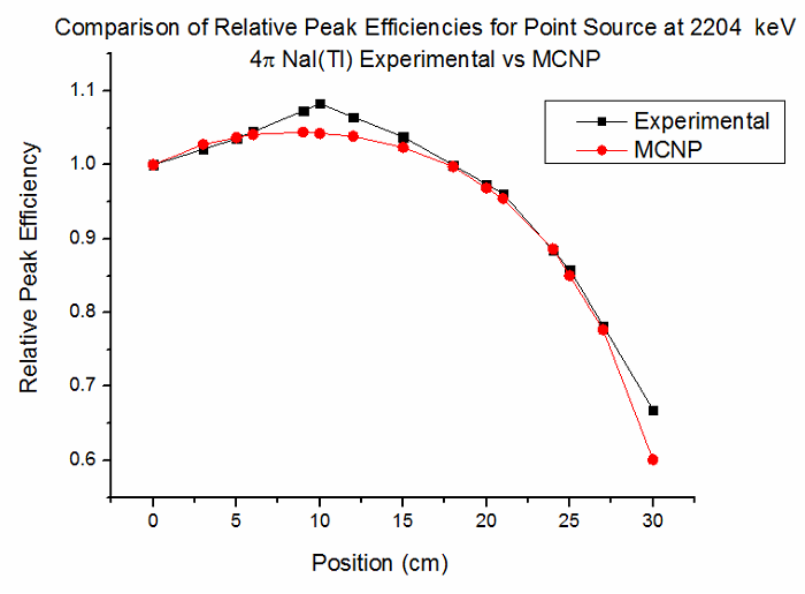

Figure 4.20: Comparison of experimental vs. MCNP relative peak efficiencies for a point source as a function of position at 2204 keV in the 4π NaI(Tl) detector

As the above four figures demonstrate, for these four peaks, the experimental MCNP results agree very well with the Experimental benchmark. This result experimentally validates the MCNP simulations, as it shows that detector parameters were well optimized in MCNP. The MCNP code can be used to correct for efficiency for any arbitrarily shaped source. There are a few positions in each figure where the experimental relative efficiency differs from the MCNP relative efficiency by approximately 5% - 10%. This can be attributed to many reasons. The most prominent reason would be that an initial guess for the peak baseline has to be entered into the OriginPro peak fitting software. Between different positions, this peak baseline may have shifted a little bit, thus affecting the counts in the peak, and subsequently, the full-energy peak efficiency.

4.3.3 ^{226}Ra Point Source Simulation

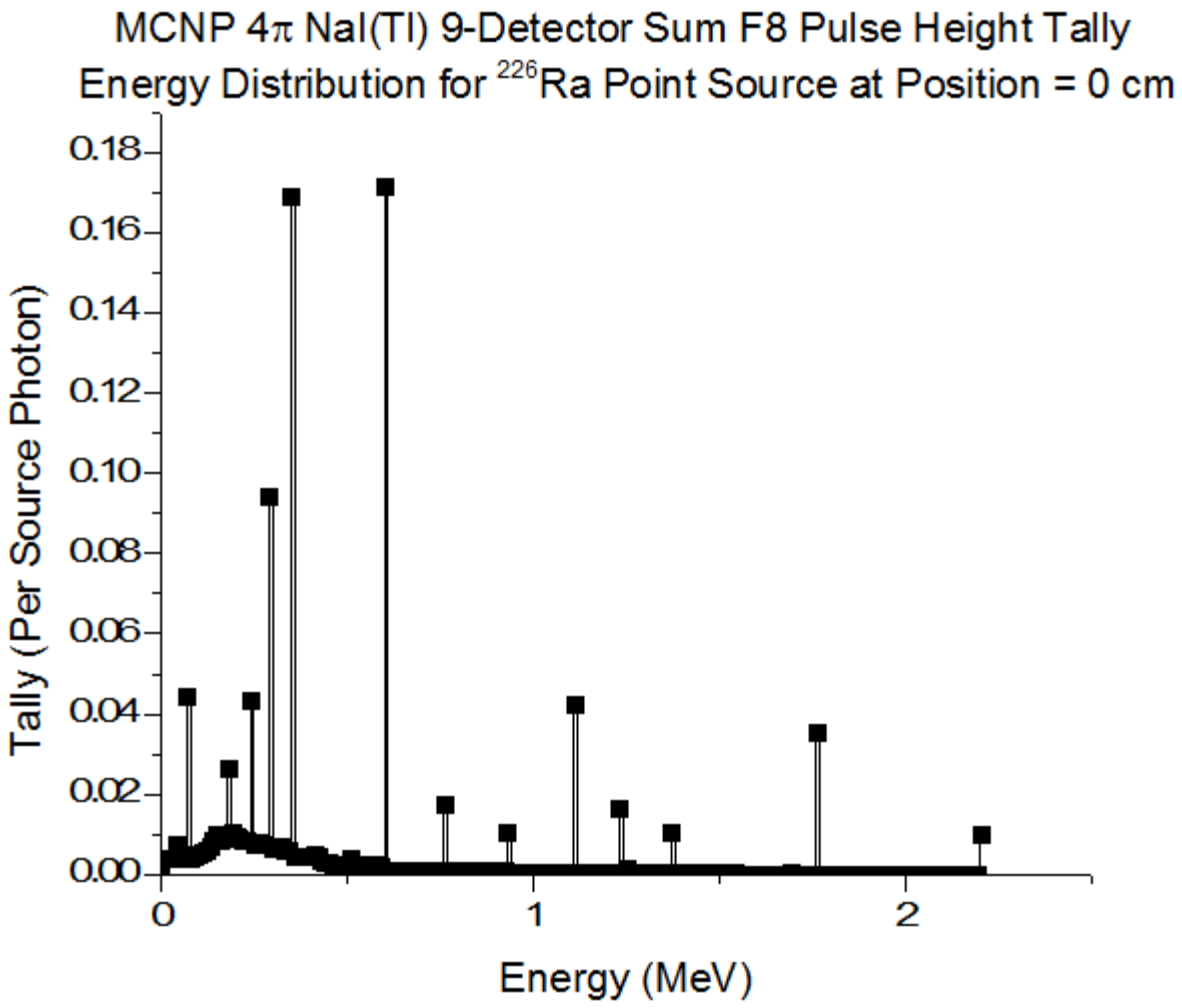

Figure 4.21: ^{226}Ra point source simulation results: F8 pulse height tally spectrum for 4π NaI(Tl) detector

A 0.5 *cm x* 0.5 *cm* ^{226}Ra cylindrical point source was simulated and assigned a vacuum matrix. It was then simulated at reference position = 0 cm. The source definition card was built using emission probabilities from the table for ^{226}Ra. The F8 pulse height tally for the 4π NaI(Tl) detector is shown above. On the basis of the gamma-ray emission probability table, this is the expected plot. As expected, the lower energy region, which is dominated by ^{214}Pb emissions, has a large Compton continuum, whereas the higher energy region, dominated by ^{214}Bi emissions, has a low Compton contribution and several well-isolated peaks. Also, just as was observed in

the experimental ^{226}Ra point source spectrum for the 4π NaI(Tl) detector, the 352 keV and 609 keV peaks are the strongest and most intense.

4.3.4 Simulation Results for Volumetric Sources:

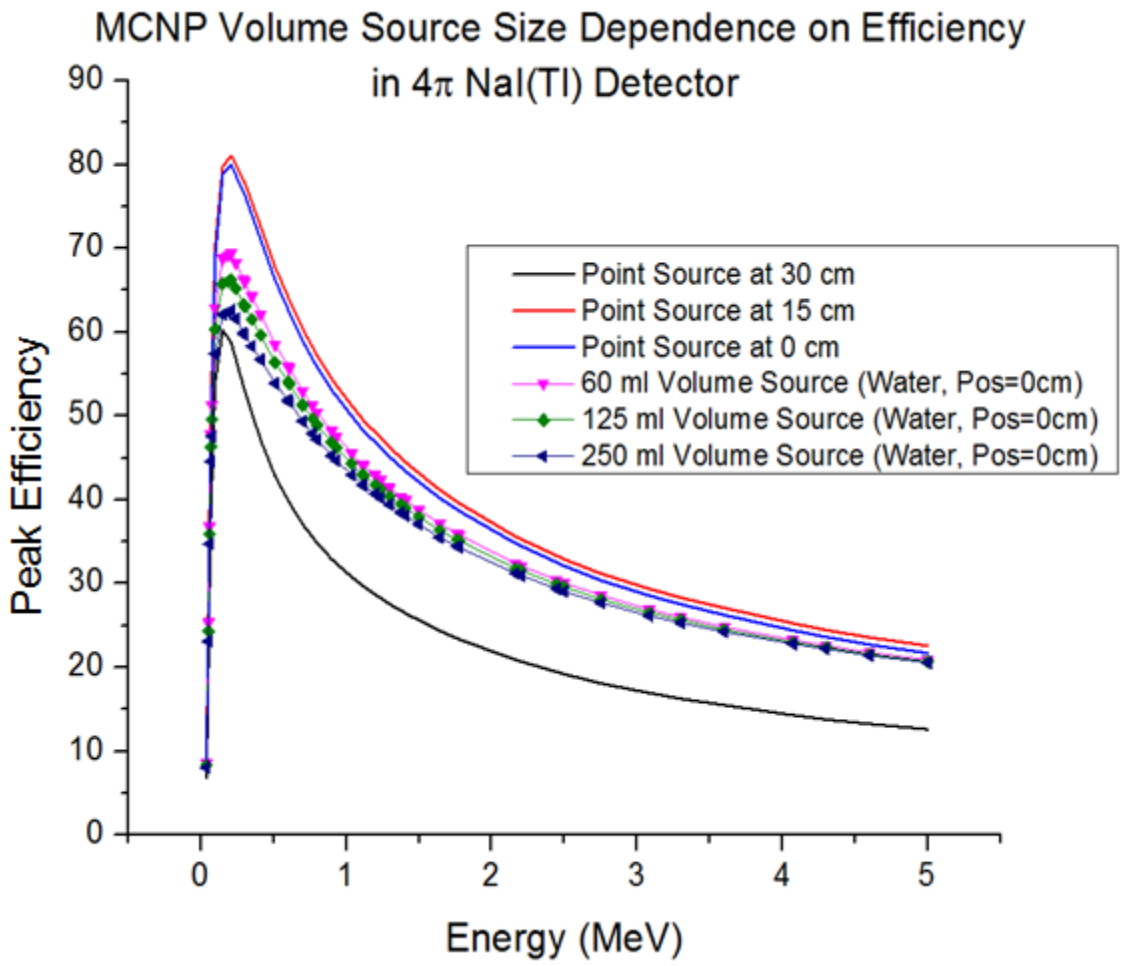

Figure 4.22: Volume source size dependence on full-energy peak efficiency at three different volume phantom sizes, comparative to point source results at various positions

The above plot shows the peak efficiency dependence on energy for the three different sized volume phantoms, 60 ml, 125 ml & 250 ml, and its comparison with peak efficiency dependence on energy for point sources at three representative positions. As the bottle size increases, the efficiency decreases slightly. For example, at 210 keV, the full-energy peak efficiency decreases by approximately 5% when the bottle size increases from 60 ml to 125 ml, and approximately by

10% when the bottle size increases from 60 ml to 250 ml. At 2 MeV, the full-energy peak efficiency decreases by approximately 1% when the bottle size increases from 60 ml to 125 ml, and approximately by 1.5% when the bottle size increases from 60 ml to 250 ml. The self-absorption effect is quite evident. Increasing volume results in increasing photon attenuation. When comparing the full-energy peak efficiency curves for the volume sources at position = 0 cm with the point sources at positions 0 cm and 15 cm, it is quite evident that the full-energy peak efficiencies are smaller for the volume sources. This can be attributed to the effective solid angle principle.

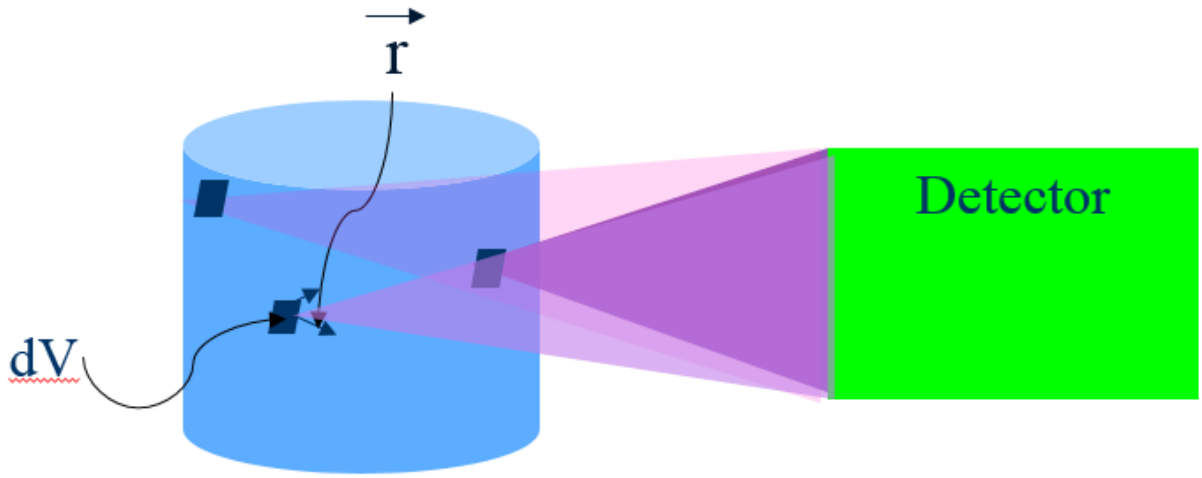

Figure 4.23: Effective Solid Angle within a Volume source

This decrease in efficiency with increasing volume source can be explained by the effective solid angle principle. Suppose an arbitrary volume source contains an infinite amount of differential volume elements dV. Each differential volume element within the source contributes to the detector a different solid angle $\Omega(\vec{r})$ as a function of the directional vector $\vec{r}$. A point source is just a single point in space, and thus contributes only one solid angle. However, with a volume source, the solid angles corresponding to each differential volume element $\Omega(\vec{r})dV$ are integrated

over the sum of all the differential elements within the source. Resultantly, an average solid angle is computed using the following equation:

$$\overrightarrow{\Omega} = \frac{\int \Omega(\vec{r}) dV}{\int dV} \qquad (4.1)$$

Where $\int dV$ represents the sum of all the volume elements within the source. This average solid angle is referred to as the effective solid angle and is responsible for the decreasing efficiency.

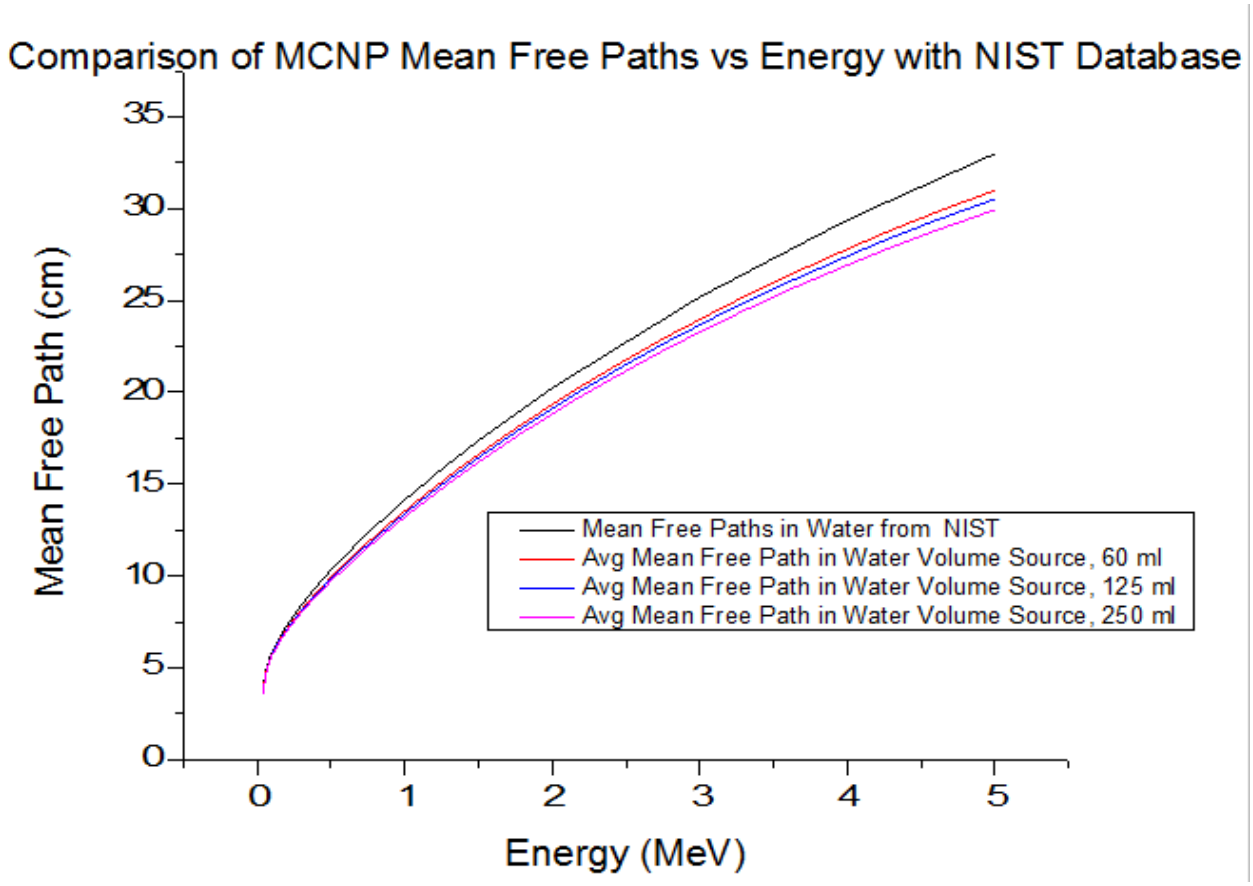

Figure 4.24: Comparison of MCNP-computed mean free paths of photons in volume sources with values for mean free path in water from NIST database [Hubbell & Seltzer, 1996]

From the MCNP output files for all three volume sources, the mean free paths were computed by the program for each cell, including the source cell. The average mean free paths in each of the three volume sources as a function of energy were plotted and compared with the results from the NIST database for mean free paths in water as a function of energy. The results are shown in

the figure above. It can be observed that mean free path decreases slightly as the source size increases, and the results agree very well with the results from the NIST database. At 5 MeV, for example, the difference between the mean free path from the NIST database and that computed for the 60 ml source differ by greater than 5 cm. At 1 MeV, the mean free paths of all three volume sources are within 0.5 cm of each other and within 1 cm of the value from the NIST database.

An aqueous ^{226}Ra volume source was simulated for each bottle size. The source definition card was built using emission probabilities from the table for ^{26}Ra. The F8 pulse height tallies were compared for each source. As expected, the as the source size increased, the tally (per source photon) decreased slightly. This can be attributed to a greater amount of self-attenuation within the source with increasing volume size.

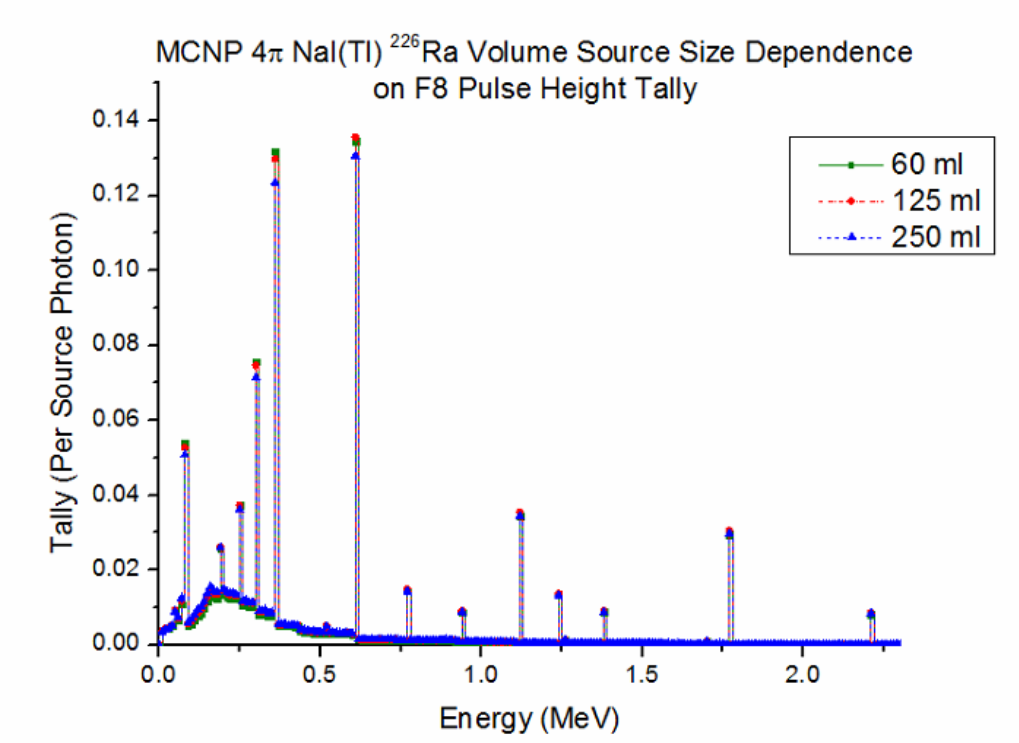

Figure 4.26: ^{226}Ra aqueous volume source simulation results: F8 pulse height tally spectrum for 9-detector sum for three different volume phantom sizes

4.3.5 Point Source in a Water Container

(a) Movement of point source along x-axis

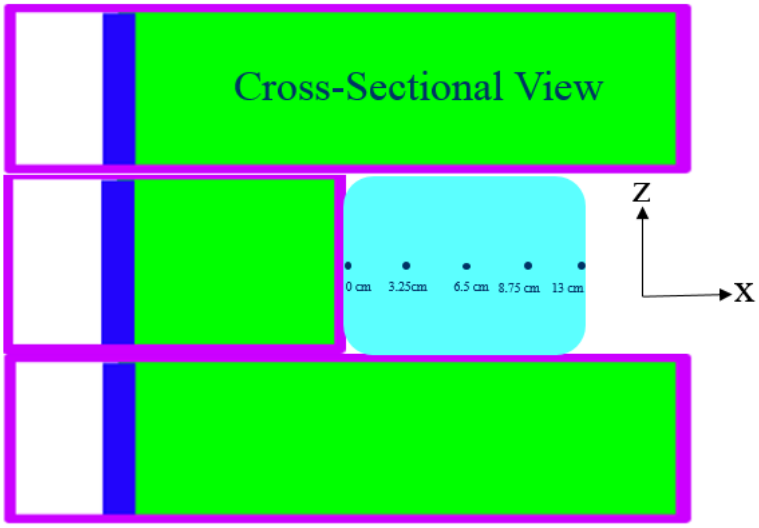

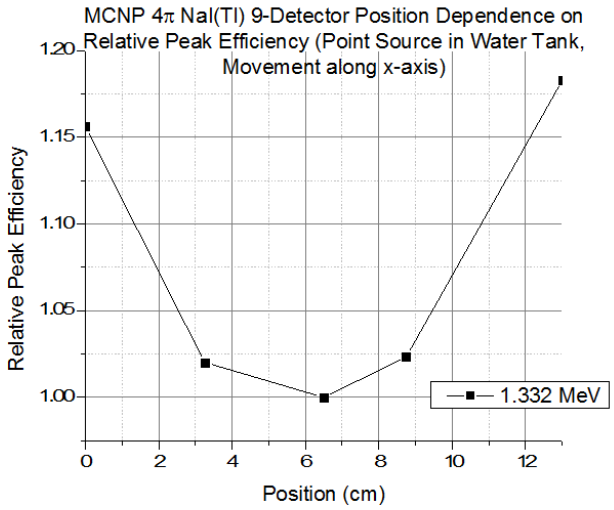

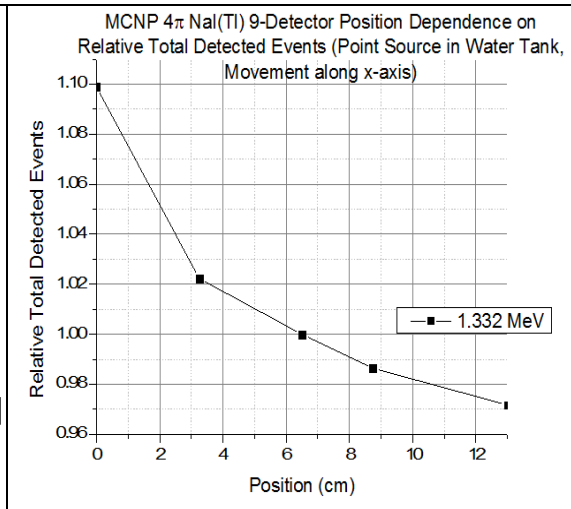

(b) Movement of point source along y-axis

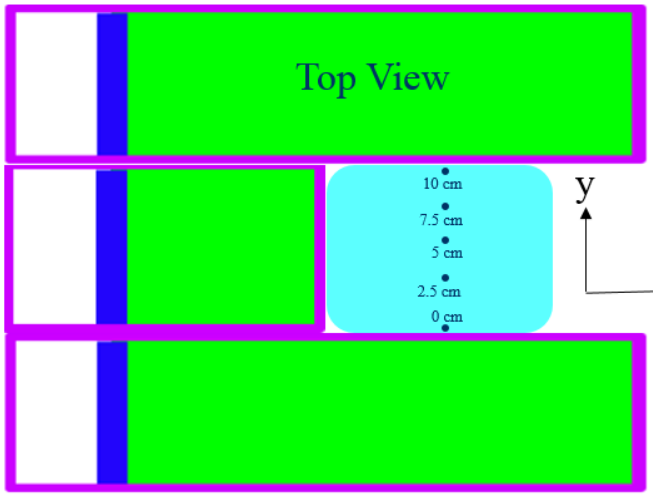

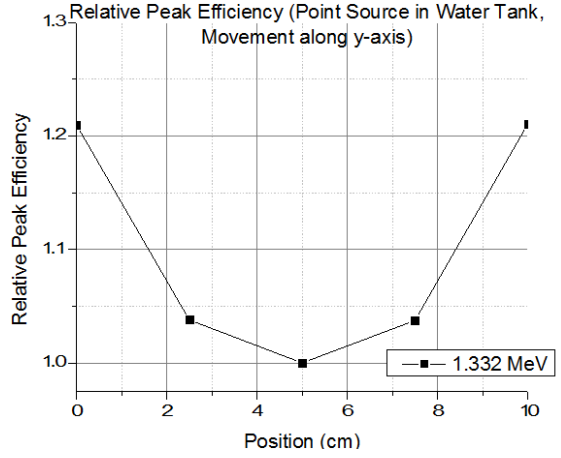

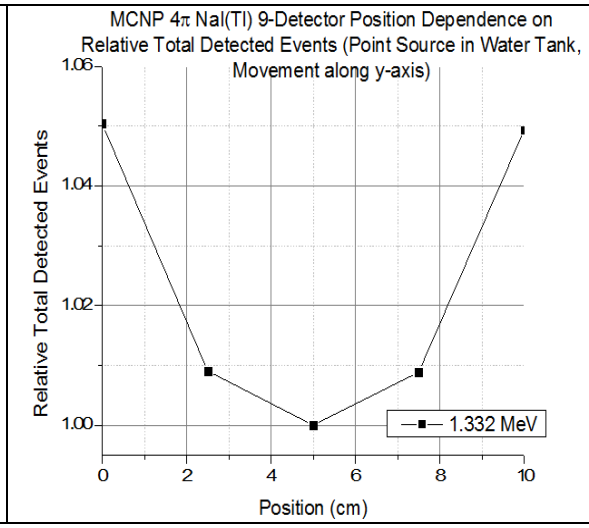

(c) Movement of point source along z-axis

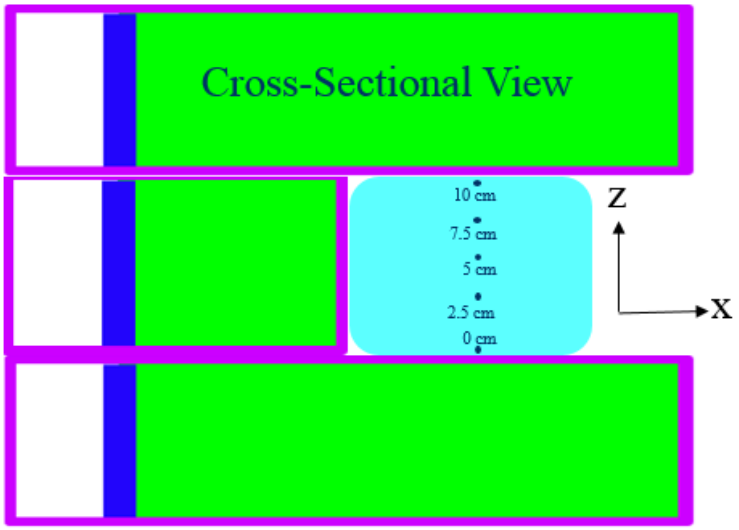

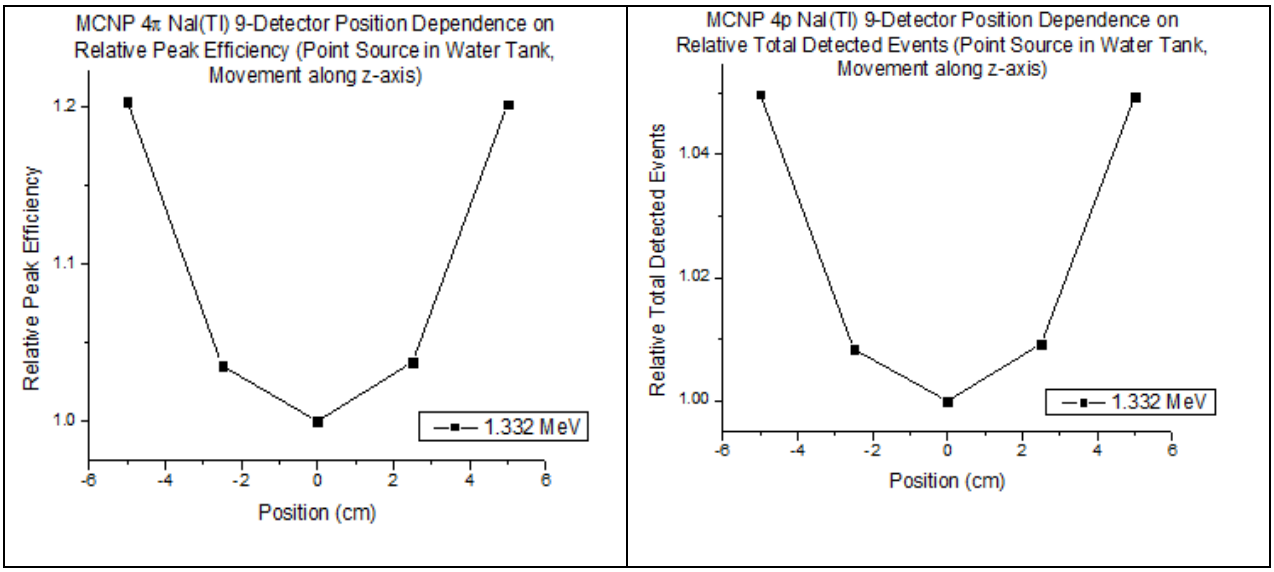

Figure 4.27 Point Source Position Dependence in 13 *cm x* 10 *cm x* 10 *cm Water Tank on Relative Peak Efficiency and Relative Total Detective Events per Source Photon along (a) x-axis, (b) y-axis, (c) z-axis at 1.332 MeV*

The figure above demonstrates the attenuation properties for a point source in a water tank, and the subsequent effect on efficiency. When the source was positioned along each axis, a symmetric pattern was observed in relative peak efficiency dependence about the centre of each axis. Along the x-axis, the difference in relative peak efficiency between 0 cm and 6.5 cm was 15% and between 6.5 cm and 13 cm it was 18%. This can be explained by examining figure 4.12. Relative to position = 0 cm, the relative peak efficiency is slightly higher at 13 cm than it is at 0 cm. The relative total detected events per photon emission drops as the source moves further along the x-axis. This can be attributed to the decreasing solid angle as the source is moved further away from the back of the central aperture of the detector. Along the y-axis and z-axis, we obtain a symmetric pattern in both relative peak efficiency and relative total counts. Along the y-axis, the difference in relative peak efficiency between position 5 cm and either end of the tank is 20%. The difference in relative total counts between position 5 cm and either end of the

tank is 5%. Along the z-axis, the difference in relative peak efficiency between position 5 cm and either end of the tank is 10%. The difference in relative total counts between position 5 cm and either end of the tank is 2.5%. These results demonstrate that at the centre of the water tank, attenuation is greatest, as there is a greater distance of water that a gamma-ray originating from the source would have to travel through in order to reach the detector, increasing the chance of absorption in the tank. Subsequently, efficiency is lowest at the centre of the tank. The symmetric nature of the source position dependence on relative peak efficiency is reflective of the symmetric geometry of the 4π NaI(Tl) detector.

4.4 Fish-Like Cylindrical Source Simulations:

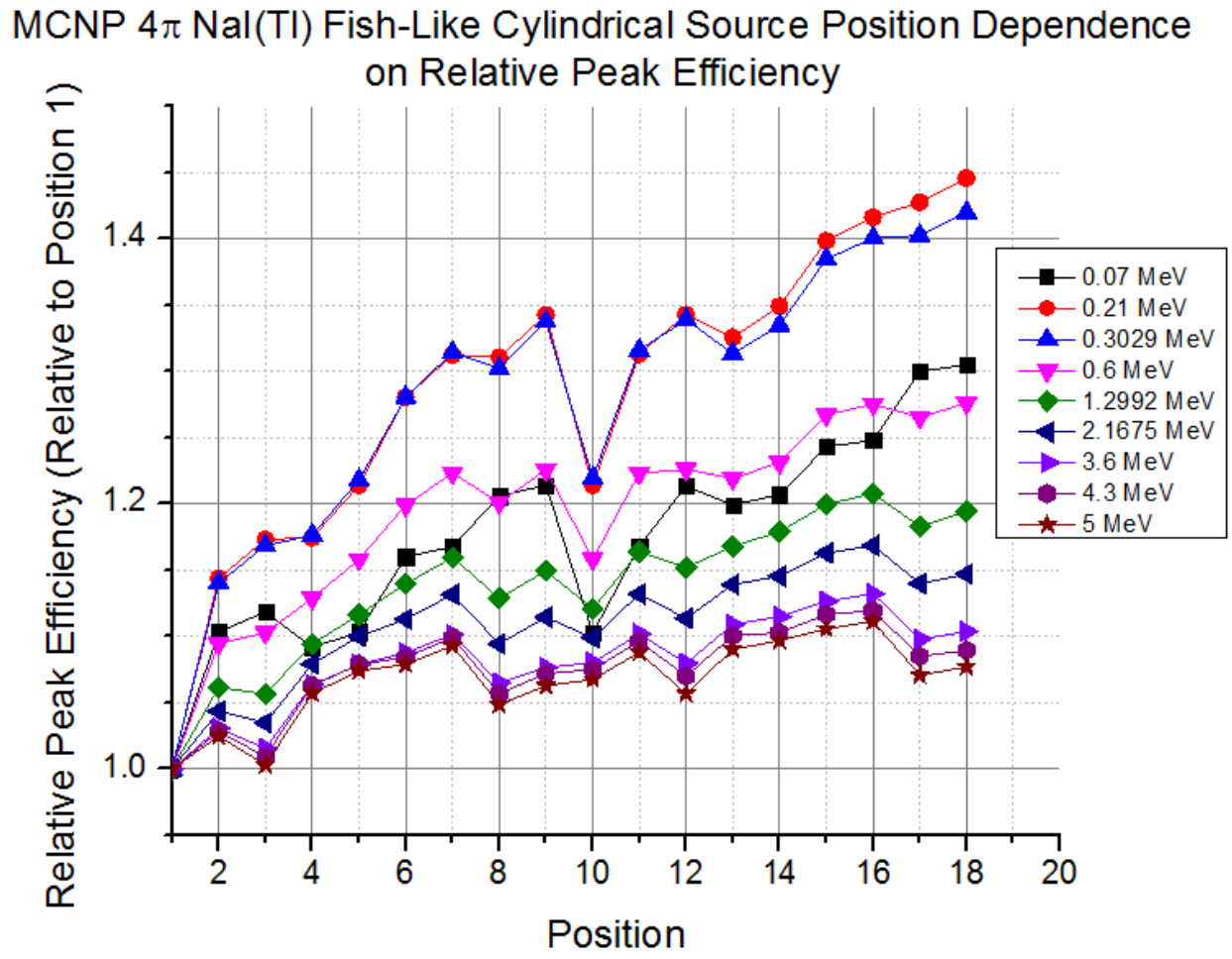

Figure 4.28 Fish-like cylindrical source position dependence on relative peak efficiency at several representative energies (Refer to table 4.1 for source position coordinates)

As described in the methodology section, a $2\ cm\ x\ 4\ cm$ fish like cylindrical volume source was scanned at eighteen different positions in a $13\ cm\ x\ 10\ cm\ x\ 10\ cm$ water filled container. The source was assigned a water matrix, as the tissue composition of a fish body is very similar to that of water. The source positions 1-9 have been illustrated in figure 4.9 and the coordinates for positions 10-18 have been shown in table 4.1. The results for relative peak efficiency dependence on source position at several representative energies are shown above in figure 4.28. This graph presents some important information. When performing a qualitative analysis of figure 4.28, positions 1-9 are centred on the y-axis, however are shifted relative to the x and z axes. Positions 10-18 are on the same x and z axes as positions 1-9 however have been shifted 4 cm in the –y direction. At 0.210 MeV and 0.302 MeV, the peak efficiency variability is quite high between positions 1 and 18 (>40%). For position 10-18, the source is shifted close to NaI(Tl) #7, and for lower energy regions where the Photoelectric effect dominates, it is expected that peak efficiency would be very high compared to the centre of the tank, where attenuation plays a key role. It is expected that source position dependence on relative peak efficiency between positions #1 & #10, #2 & #11, #3 & #12, #8 & #17, #4 & #13, #6 & #15, #9 & #18, #5 & #14, and #7 & #16 will present similar quantitative results as figure 4.27(b), which shows a point source in a water tank was shifted along the y-axis. Comparing positions 1 and 10 in figure 4.28, efficiency decreases and self-absorption in the tank increases relative to the other positions, and, as predicted from figure 4.27(b), the efficiency variation between positions 1 and 10 should be approximately 20% at 1.332 MeV when a point source is shifted between 0 cm and 5 cm along the y-axis. According to figure 4.28, the efficiency variation between positions 1 and 10 is 10%.

Between positions #2 & #11, #3 & #12, #8 & #17, #4 & #13, #6 & #15, #9 & #18, #5 & #14, and #7 & #16, the variation in relative full-energy peak efficiency varies between 5% and 10% at 1.2992 MeV. Moving the source along the z-axis, for example between positions #3 & #8, the variation in efficiency is approximately 5%. From figure 4.27(c), the predicted variation in efficiency when moving a point source in a water tank from 0 cm to 5 cm along the z-axis is 10%. Moving the source along the x-axis, for example between positions #3 & #1, the variation in efficiency is approximately 5%. From figure 4.27(a), the predicted variation in efficiency when moving a point source in a water tank from 0 cm to 6.5 cm along the x-axis is 15%. These ±10% discrepancies in efficiency variation between point source in water tank and volume source in water tank are reasonable, because the point source has been expanded into a volume source, resulting in a lesser distance between the two positions than if they were point sources. The largest relative peak efficiencies occur at positions 9 and 18, where the fish would be right on top detector 1 and in very close vicinity to detector 9.

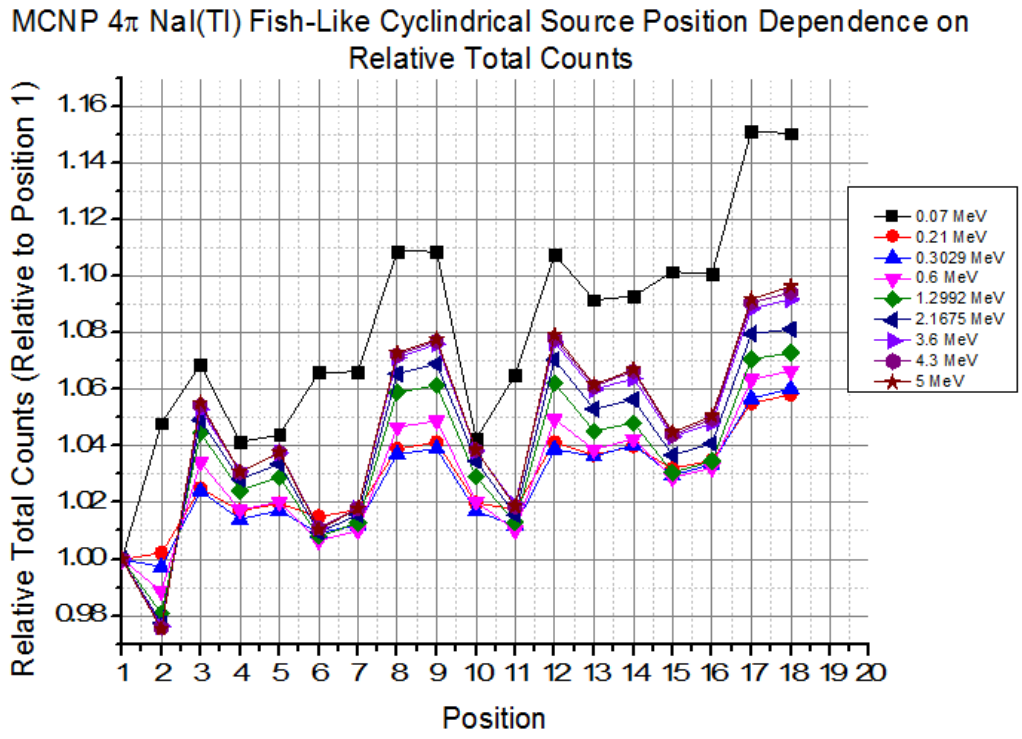

Figure 4.29 Fish-like cylindrical source position dependence on relative total counts at several representative energies (Refer to table 4.1 for source position coordinates)

The above figure shows the dependence of total relative counts on source position for positions 1-18. At positions #2 and #11, the solid angle is the worst, therefore the total detected events are the lowest. Comparing positions #1 and #10, the variation in total detected events is approximately 3%. Figure 4.27(b) shows a predicted 5% variation when the point source is shifted along the y-axis between 0 cm and 5 cm. Along the x-axis, the variation in total detected events is 3% between positions 9 and 5, whereas figure 4.27(a) shows a predicted 2% variation when the point source shifted 6.5 cm along the x-axis. Along the z-axis, the variation in total detected events is 1% between positions 3 and 9, whereas figure 4.27(c) shows a predicted 2.5% variation when the point source shifted 5 cm along the z-axis. These results show that while self-absorption does occur, the detector exhibits minimal variation (<10%) in relative total detected events. This result demonstrates that fish localization does not significantly affect relative total counting results. A mini aquarium could be built in the dimensions of 10 cm^3 and the fish could comfortably swim around without resulting in significant loss in the detected events.

CHAPTER 5: CONCLUSIONS AND FUTURE DIRECTIONS

5.1 Significant Findings

In order to quantify ^{226}Ra radioactivity in live fish exposed to very low, trace environmental levels of the radionuclide, the objective of this study was to analyze the detection limit of low level ^{226}Ra in live fish using the gamma spectroscopy technique, particularly using an HPGe detector and the 4π NaI(Tl) detector. Individual peak spectral analysis was performed for a ^{226}Ra point source in the HPGe detector. Combining the detection limits of the three strongest peaks, an overall detection limit was obtained of 6.801 Bq for a one hour count with 99% confidence. In order to optimize the detection limit for ^{226}Ra in the 4π NaI(Tl) detector, a spectral analysis algorithm was implemented and applied to nine different energy intervals in the spectrum for the ^{226}Ra point source, and it was found that the energy interval between 50 keV – 2520 keV, essentially the entire energy range, presented the lowest detection limit of 0.99 Bq for a one hour count with 99% confidence. It has been experimentally demonstrated that the 4π NaI(Tl) system offers a detection limit improvement of over six times lower when compared to the HPGe detector.

The results for the 4π NaI(Tl) system demonstrate that the total area in the spectrum contains valuable information in order to optimize the detection limit, and the entire energy range acts as the boundary of interest. At the onset of this study, it was well understood that due to the larger relative size and high Z atomic number of the NaI(Tl) crystal, the NaI(Tl) detector presents a far superior efficiency than the HPGe detector, and thus it was assumed that this detector must be ideal for low level analysis. This assumption needed to be proved, and thus a meticulous performance analysis by means of evaluation of detection limit was attempted for the two different systems. Both detectors have the ability to detect gamma-rays from live fish

contaminated with ^{226}Ra radioactivity. In terms of the feasibility of low level fish activity quantification, both detectors were treated with fair condition.

In order to proceed with the performance comparison, a physical live fish was not required, the ^{226}Ra point source was a precursor to determining system detection limits. Once the performance was successfully determined using the point source, then with a bigger source, such as a live fish, or an arbitrary volume source, the results would not be expected to change significantly. It was successfully demonstrated that when using the 4π NaI(Tl) detector to perform low level ^{226}Ra radioactivity analysis, and with a sufficiently long counting time, the activity in live fish be detected at levels representative of those that may be present in the aquatic environment.

In addition, MCNP Monte Carlo simulations of full-energy peak efficiency of a small point source were validated by the benchmark experimental performance analysis. A comparison between the experimental and MCNP results of full-energy peak efficiency dependence on point source position for four different well-isolated peaks of the ^{226}Ra spectrum showed that the two methods agreed very well with each other.

With the assistance of MCNP Monte Carlo simulations, volume source size dependence on relative full-energy peak efficiency and relative total detected events per photon emission demonstrated that as the source volume was increased, the efficiency decreased due to attenuation in the source. These simulations are of great importance, when considering that a fish keeps increasing in size. A larger fish body volume results in a loss in efficiency, and thus an increase in detection limit. Monte Carlo simulations demonstrated the relative total detected events for a fish-like cylindrical source varies by less than 10% for any energy between 0.2 MeV and 5 MeV as a fish travels from one location of the tank to another.

5.2 Benchmark Volume Sources Planned

In order to experimentally determine volume source size dependence on the 4π NaI(Tl) detector on relative efficiency, benchmark volume source measurements have been planned. Three aqueous ^{226}Ra volume sources will be made in Nalgene bottles. The bottle sizes are 60 ml, 125 ml, and 250 ml. The bottles to be used are shown below:

Figure 5.1: ^{226}Ra Phantoms to be made in the following Nalgene bottles: 60 ml, 125 ml & 250 ml

The procedure will be performed by making a diluted solution from an existing ^{226}Ra stock solution with activity concentration of 74000 Bq/ml. First, an amount of 16 µl of the stock solution will be pipetted into a test tube containing a 3.184 ml of distilled water. This new diluted solution will have an activity concentration of 370 Bq/ml. Table 5.1 describes the procedure of creating the diluted solution.

Table 5.1: Summary of procedure to make diluted ^{226}Ra solution

Solution:	Solution amount to be used (ml):	Activity Concentration (Bq/ml):
(A) – Original (Stock Solution)	$16\ x10^{-3}$	74,000
(B) – To be Made by Dilution of (A)	3.2 ($16\ x10^{-3}\ ml$ of solution (A) into 3.184 ml buffer of distilled water)	370

From the test tube containing the diluted solution (B) with activity concentration of 370 Bq/ml, 1 ml will be pipetted into each Nalgene bottle. For the 60 ml bottle, 59 ml of distilled water will be added. For the 125 ml bottle, 124 ml of distilled water will be added. For the 250 ml bottle, 249 ml of distilled water will be added. Thus each phantom will have a total activity of 370 Bq, each bottle containing different activity concentrations. The following table summarizes these activity concentrations:

Table 5.2: Activity Concentrations for each ^{226}Ra Phantom

Phantom Volume (ml):	Sampled Volume from Diluted Solution (B) (ml):	Amount of Distilled Water to be Added (ml):	Total Activity of Phantom (Bq)	Activity Conc. (Bq/ml):
60	1	59	370	6.17
125	1	124	370	2.96
250	1	249	370	1.48

First, the 60 ml phantom will be inserted into the 4π NaI(Tl) detector, touching the front edge of the 9th central detector as shown in the figure below.

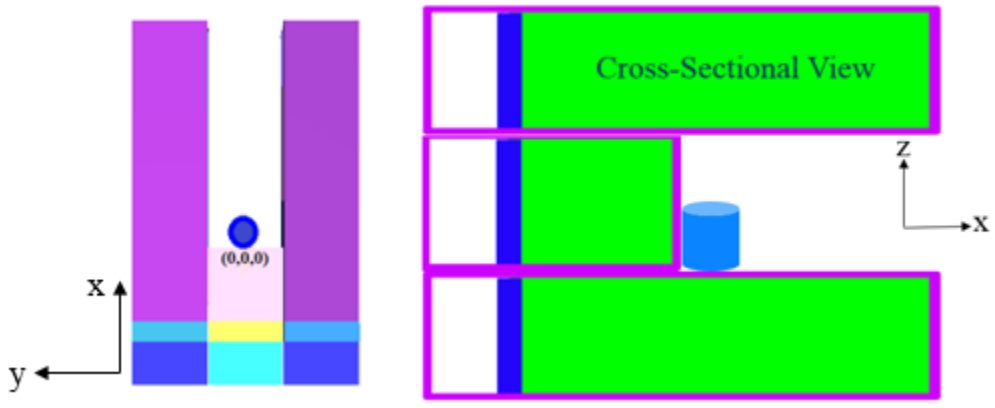

Figure 5.3: Placement of volume source in 4π NaI(Tl) detector

The spectrum for each will be collected for twelve hours. The same procedure will repeated with the 125 ml and 250 ml sources. A twelve hour background count will performed following the phantom measurements. For each source, the volume size dependence on relative full-energy peak efficiency and on relative total detected events per photon emission will be calculated. Finally, as was done with the ^{226}Ra point source measurement, using five of the volume source spectrum's most well-isolated peaks, the volume size dependence on relative full-energy peak efficiency will be used as a benchmark with which to compare the results determined using the Monte Carlo MCNP simulations, from figure 4.22.

5.3 Extension to Live Fish Measurements

In order to solidify this study, it would be highly desirable to inject a live fish, in particular a Fathead Minnow or Zebrafish, with a small amount of ^{226}Ra solution. The activity expected within the fish would be between 1 Bq and 10 Bq based on the detection limit of 0.70 obtained for a one hour count in the 4π NaI(Tl). In order to differentiate background radiation from the injected ^{226}Ra, control fish can be used. The background integral from the control fish can be measured and then subtracted from the spectrum obtained for the injected fish. Since it has been

demonstrated that the spatial variation of efficiency within an approximately one litre-sized tank changes very little within the tank, a special mini aquarium of approximately $10\ cm\ x\ 10\ cm\ x\ 10\ cm$ can be customized (i.e. drilling holes in lid to allow in some oxygen) and inserted and pushed into the back of the aperture of the 4π NaI(Tl) detector. Standard fish holders can also be used to keep the fish located in any position of interest within the container. Performance analysis can be performed in the same manner as was performed with the point source. ^{226}Ra radioactivity analysis will also be performed with the tank of water in which the fish was swimming, and its spectrum will be collected and analyzed. The fish will be regularly inserted into a fresh tank of water. As a further expansion in this study, in addition to analyzing live fish samples which have been injected with ^{226}Ra, a small population of fish can be obtained from freshwater lake environments and these samples can be measured in the 4π NaI(Tl) detector.

Utilizing Monte Carlo simulations, the full-energy peak efficiency calibration curve can be determined for any fish plus water container geometry of interest. From equation (3.2). At radioactive equilibrium, the disintegration rate of the parent ^{226}Ra and daughter isotopes are equal, and any well-isolated daughter peaks in the spectrum, including those of ^{214}Pb and ^{214}Bi can be used to determine the activity of their parent. By determining N_{peak}, the net area under the peak of interest, then the full-energy peak efficiency curve can be used to determine the

activity of any daughter ^{226}Ra radioisotope of interest.

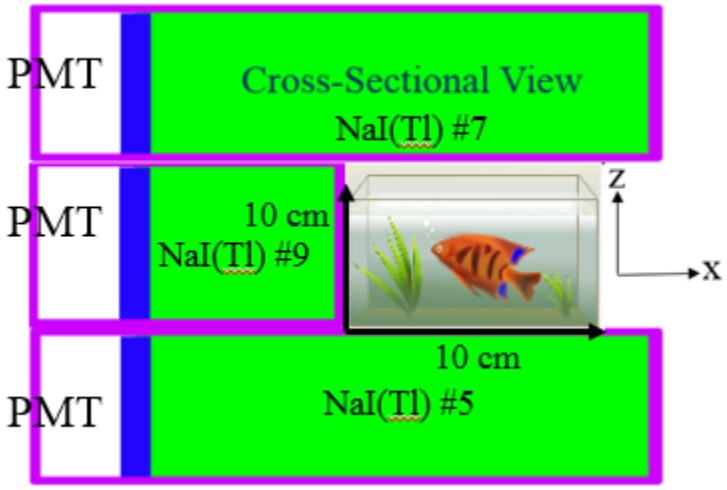

Figure 5.4: Placement of fish inside mini-aquarium

APPENDIX A:

A1 MCNP Input file for 5 *mm x* 5 *mm* cylindrical point source with energy of 1332 keV

[MCNP User Manual, Version 5, 2003]

```
4pi: Detector Response Function of 4-Pi NaI(Tl) for Mono-Energetic Pt Source
c     Eight 10.2 x 10.2 x 40.6 cm Long crystals w/1mm thick steel can
c     Ninth 10.2 x 10.2 x 10.2 cm crystal w/1mm thick steel can
c     Nine Thin Quartz Optical Windows 2.69 x 10 x 10 cm
1     1 -3.67 -1 $imp:p=1 $ NaI crystal
2     2 -8.0 -2 1 3 4 $imp:p=1 $ Steel can
3     3 -2.65 -3 $imp:p=1 $ Quartz Window
4     0 -4 $ $imp:p=1 PMT Vaccuum
5     0 2 7 11 15 19 23 27 31 35 -5 $imp:p=1 $ Sphere of Exclusion
6     0 5 $ $imp:p=0 $ Universe
7     1 -3.67 -6 $ NaI Crystal
8     2 -8.0 -7 6 8 9 $ Steel can
9     3 -2.65 -8 $ Quartz Window
10    0 -9 $ PMT Vaccuum
11    1 -3.67 -10 $ NaI Crystal
12    2 -8.0 -11 10 12 13 $ Steel can
13    3 -2.65 -12 $ Quartz Window
14    0 -13 $ PMT Vaccuum
15    1 -3.67 -14 $ NaI Crystal
16    2 -8.0 -15 14 16 17 $ Steel can
17    3 -2.65 -16 $ Quartz Window
18    0 -17 $ PMT Vaccuum
19    1 -3.67 -18 $ NaI Crystal
20    2 -8.0 -19 18 20 21 $ Steel can
21    3 -2.65 -20 $ Quartz Window
22    0 -21 $ PMT Vaccuum
23    1 -3.67 -22 $ NaI Crystal
24    2 -8.0 -23 22 24 25 $ Steel can
25    3 -2.65 -24 $ Quartz Window
26    0 -25 $ PMT Vaccuum
27    1 -3.67 -26 $ NaI Crystal
28    2 -8.0 -27 26 28 29 $ Steel can
29    3 -2.65 -28 $ Quartz Window
30    0 -29 $ PMT Vaccuum
31    1 -3.67 -30 $ NaI Crystal
32    2 -8.0 -31 30 32 33 $ Steel can
33    3 -2.65 -32 $ Quartz Window
34    0 -33 $ PMT Vaccuum
35    1 -3.67 -34 $ NaI Crystal Detector 9
36    2 -8.0 -35 34 36 37 $ Steel can Detector 9
37    3 -2.65 -36 $ Quartz Window Detector 9
38    0 -37 $ PMT Vaccuum Detector 9
```

```
1      RPP -20.3 20.3 -5.1 5.1 -10.251 -0.051 $ NaI Crystal
2      RPP -28.779 20.351 -5.151 5.151 -10.302 0 $ Steel can
3      RPP -23.069 -20.3 -5.1 5.1 -10.251 -0.051 $ Quartz Window
4      RPP -28.779 -23.069 -5.1 5.1 -10.251 -0.051 $ PMT Vaccuum
5      SO 100
6      RPP -20.3 20.3 5.202 15.402 -10.251 -0.051 $ NaI Crystal
7      RPP -28.779 20.351 5.151 15.453 -10.302 0 $ Steel can
8      RPP -23.069 -20.3 5.202 15.402 -10.251 -0.051 $ Quartz Window
9      RPP -28.779 -23.069 5.202 15.402 -10.251 -0.051 $ PMT Vaccuum
10      RPP -20.3 20.3 15.504 25.704 -10.251 -0.051 $ NaI Crystal
11      RPP -28.779 20.351 15.453 25.755 -10.302 0 $ Steel can
12      RPP -23.069 -20.3 15.504 25.704 -10.251 -0.051 $ Quartz Window
13      RPP -28.779 -23.069 15.504 25.704 -10.251 -0.051 $ PMT Vaccuum
14      RPP -20.3 20.3 -5.1 5.1 0.051 10.251 $ NaI Crystal
15      RPP -28.779 20.351 -5.151 5.151 0 10.302 $ Steel can
16      RPP -23.069 -20.3 -5.1 5.1 0.051 10.251 $ Quartz Window
17      RPP -28.779 -23.069 -5.1 5.1 0.051 10.251 $ PMT Vaccuum
18      RPP -20.3 20.3 -5.1 5.1 10.353 20.553 $ NaI Crystal
19      RPP -28.779 20.351 -5.151 5.151 10.302 20.604 $ Steel can
20      RPP -23.069 -20.3 -5.1 5.1 10.353 20.553 $ Quartz Window
21      RPP -28.779 -23.069 -5.1 5.1 10.353 20.553 $ PMT Vaccuum
22      RPP -20.3 20.3 5.202 15.402 10.353 20.553 $ NaI Crystal
23      RPP -28.779 20.351 5.151 15.453 10.302 20.604 $ Steel can
24      RPP -23.069 -20.3 5.202 15.402 10.353 20.553 $ Quartz Window
25      RPP -28.779 -23.069 5.202 15.402 10.353 20.553 $ PMT Vaccuum
26      RPP -20.3 20.3 15.504 25.704 10.353 20.553 $ NaI Crystal
27      RPP -28.779 20.351 15.453 25.755 10.302 20.604 $ Steel can
28      RPP -23.069 -20.3 15.504 25.704 10.353 20.553 $ Quartz Window
29      RPP -28.779 -23.069 15.504 25.704 10.353 20.553 $ PMT Vaccuum
30      RPP -20.3 20.3 15.504 25.704 0.051 10.251 $ NaI Crystal
31      RPP -28.779 20.351 15.453 25.755 0 10.302 $ Steel can
32      RPP -23.069 -20.3 15.504 25.704 0.051 10.251 $ Quartz Window
33      RPP -28.779 -23.069 15.504 25.704 0.051 10.251 $ PMT Vaccuum
34      RPP -20.3 -10.14 5.202 15.402 0.051 10.251 $ NaI Crystal
35      RPP -28.779 -10.089 5.151 15.453 0 10.302 $ Steel can
36      RPP -23.069 -20.3 5.202 15.402 0.051 10.251 $ Quartz Window
37      RPP -28.779 -23.069 5.202 15.402 0.051 10.251 $ PMT Vaccuum

mode    p
imp:p 1 1 1 1 0 1 1 1 1 1 1 1 1 1 1 1 1 1 1 1 1 1 1 1 1 1 1 1 1 1 1 1 1 1 1 1
    1
F8:p 1
E8 0 0.01 0.02 0.03 0.04 0.05 0.06 0.07 0.08 0.09 0.10 0.11 0.12 0.13
    0.14 0.15 0.16 0.17 0.18 0.19 0.20 0.21 0.22 0.23 0.24 0.25 0.26 0.27 0.28
    0.29 0.30 0.31 0.32 0.33 0.34 0.35 0.36 0.37 0.38 0.39 0.4 0.41 0.42 0.43
    0.44 0.45 0.46 0.47 0.48 0.49 0.50 0.51 0.52 0.53 0.54 0.55 0.56 0.57
    0.58 0.59 0.60 0.61 0.62 0.63 0.64 0.65 0.66 0.67 0.68 0.69 0.70 0.71
    0.72 0.73 0.74 0.75 0.76 0.77 0.78 0.79 0.80 0.81 0.82 0.83 0.84 0.85
```

0.86 0.87 0.88 0.89 0.90 0.91 0.92 0.93 0.94 0.95 0.96 0.97 0.98 0.99 1.00
1.01 1.02 1.03 1.04 1.05 1.06 1.07 1.08 1.09 1.10 1.11 1.12 1.13 1.14 1.15
1.16 1.17 1.18 1.19 1.20 1.21 1.22 1.23 1.24 1.25 1.26 1.27 1.28 1.29 1.30
1.31 1.32 1.33 1.34 1.35 1.36 1.37 1.38 1.39 1.40 1.41 1.42 1.43 1.44 1.45
1.46 1.47 1.48 1.49 1.50 1.51 1.52 1.53 1.54 1.55 1.56 1.57 1.58 1.59 1.60
1.61 1.62 1.63 1.64 1.65 1.66 1.67 1.68 1.69 1.70 1.71 1.72 1.73 1.74 1.75
1.76 1.77 1.78 1.79 1.80 1.81 1.82 1.83 1.84 1.85 1.86 1.87 1.88 1.89 1.90
1.91 1.92 1.93 1.94 1.95 1.96 1.97 1.98 1.99 2.00 2.01 2.02 2.03 2.04 2.05
2.06 2.07 2.08 2.09 2.10 2.11 2.12 2.13 2.14 2.15 2.16 2.17 2.18 2.19 2.20
2.21 2.22 2.23 2.24 2.25 2.26 2.27 2.28 2.29 2.30 2.31 2.32 2.33 2.34 2.35
2.36 2.37 2.38 2.39 2.40 2.41 2.42 2.43 2.44 2.45 2.46 2.47 2.48 2.49 2.50
2.51 2.52 2.53 2.54 2.55 2.56 2.57 2.58 2.59 2.60 2.61 2.62 2.63 2.64 2.65
2.66 2.67 2.68 2.69 2.70 2.71 2.72 2.73 2.74 2.75 2.76 2.77 2.78 2.79 2.80
2.81 2.82 2.83 2.84 2.85 2.86 2.87 2.88 2.89 2.90 2.91 2.92 2.93 2.94 2.95
2.96 2.97 2.98 2.99 3.00 3.01 3.02 3.03 3.04 3.05 3.06 3.07 3.08 3.09 3.10
3.11 3.12 3.13 3.14 3.15 3.16 3.17 3.18 3.19 3.20 3.21 3.22 3.23 3.24 3.25
3.26 3.27 3.28 3.29 3.30 3.31 3.32 3.33 3.34 3.35 3.36 3.37 3.38 3.39 3.40
3.41 3.42 3.43 3.44 3.45 3.46 3.47 3.48 3.49 3.50 3.51 3.52 3.53 3.54 3.55
3.56 3.57 3.58 3.59 3.60 3.61 3.62 3.63 3.64 3.65 3.66 3.67 3.68 3.69 3.70
3.71 3.72 3.73 3.74 3.75 3.76 3.77 3.78 3.79 3.80 3.81 3.82 3.83 3.84 3.85
3.86 3.87 3.88 3.89 3.90 3.91 3.92 3.93 3.94 3.95 3.96 3.97 3.98 3.99 4.00
4.01 4.02 4.03 4.04 4.05 4.06 4.07 4.08 4.09 4.10 4.11 4.12 4.13 4.14 4.15
4.16 4.17 4.18 4.19 4.20 4.21 4.22 4.23 4.24 4.25 4.26 4.27 4.28 4.29 4.30
4.31 4.32 4.33 4.34 4.35 4.36 4.37 4.38 4.39 4.40 4.41 4.42 4.43 4.44 4.45
4.46 4.47 4.48 4.49 4.50 4.51 4.52 4.53 4.54 4.55 4.56 4.57 4.58 4.59 4.60
4.61 4.62 4.63 4.64 4.65 4.66 4.67 4.68 4.69 4.70 4.71 4.72 4.73 4.74 4.75
4.76 4.77 4.78 4.79 4.80 4.81 4.82 4.83 4.84 4.85 4.86 4.87 4.88 4.89 4.90
4.91 4.92 4.93 4.94 4.95 4.96 4.97 4.98 4.99 5.00 5.01 5.02 5.03 5.04 5.05
5.06 5.07 5.08 5.09 5.10 5.11 5.12 5.13 5.14 5.15 5.16 5.17 5.18 5.19 5.20
5.21 5.22 5.23 5.24 5.25 5.26 5.27 5.28 5.29 5.30 5.31 5.32 5.33 5.34 5.35
5.36 5.37 5.38 5.39 5.40 5.41 5.42 5.43 5.44 5.45 5.46 5.47 5.48 5.49 5.50
5.51 5.52 5.53 5.54 5.55 5.56 5.57 5.58 5.59 5.60 5.61 5.62 5.63 5.64 5.65
5.66 5.67 5.68 5.69 5.70 5.71 5.72 5.73 5.74 5.75 5.76 5.77 5.78 5.79 5.80
5.81 5.82 5.83 5.84 5.85 5.86 5.87 5.88 5.89 5.90 5.91 5.92 5.93 5.94 5.95
5.96 5.97 5.98 5.99 6.00 6.01 6.02 6.03 6.04 6.05 6.06 6.07 6.08 6.09 6.10
6.11 6.12 6.13 6.14 6.15 6.16 6.17 6.18 6.19 6.20 6.21 6.22 6.23 6.24 6.25
6.26 6.27 6.28 6.29 6.30 6.31 6.32 6.33 6.34 6.35 6.36 6.37 6.38 6.39 6.40
6.41 6.42 6.43 6.44 6.45
F18:p 7
E18 0 0.01 0.02 0.03 0.04 0.05 0.06 0.07 0.08 0.09 0.10 0.11 0.12 0.13
0.14 0.15 0.16 0.17 0.18 0.19 0.20 0.21 0.22 0.23 0.24 0.25 0.26 0.27 0.28
0.29 0.30 0.31 0.32 0.33 0.34 0.35 0.36 0.37 0.38 0.39 0.4 0.41 0.42 0.43
0.44 0.45 0.46 0.47 0.48 0.49 0.50 0.51 0.52 0.53 0.54 0.55 0.56 0.57
0.58 0.59 0.60 0.61 0.62 0.63 0.64 0.65 0.66 0.67 0.68 0.69 0.70 0.71
0.72 0.73 0.74 0.75 0.76 0.77 0.78 0.79 0.80 0.81 0.82 0.83 0.84 0.85
0.86 0.87 0.88 0.89 0.90 0.91 0.92 0.93 0.94 0.95 0.96 0.97 0.98 0.99 1.00
1.01 1.02 1.03 1.04 1.05 1.06 1.07 1.08 1.09 1.10 1.11 1.12 1.13 1.14 1.15
1.16 1.17 1.18 1.19 1.20 1.21 1.22 1.23 1.24 1.25 1.26 1.27 1.28 1.29 1.30

1.31 1.32 1.33 1.34 1.35 1.36 1.37 1.38 1.39 1.40 1.41 1.42 1.43 1.44 1.45
1.46 1.47 1.48 1.49 1.50 1.51 1.52 1.53 1.54 1.55 1.56 1.57 1.58 1.59 1.60
1.61 1.62 1.63 1.64 1.65 1.66 1.67 1.68 1.69 1.70 1.71 1.72 1.73 1.74 1.75
1.76 1.77 1.78 1.79 1.80 1.81 1.82 1.83 1.84 1.85 1.86 1.87 1.88 1.89 1.90
1.91 1.92 1.93 1.94 1.95 1.96 1.97 1.98 1.99 2.00 2.01 2.02 2.03 2.04 2.05
2.06 2.07 2.08 2.09 2.10 2.11 2.12 2.13 2.14 2.15 2.16 2.17 2.18 2.19 2.20
2.21 2.22 2.23 2.24 2.25 2.26 2.27 2.28 2.29 2.30 2.31 2.32 2.33 2.34 2.35
2.36 2.37 2.38 2.39 2.40 2.41 2.42 2.43 2.44 2.45 2.46 2.47 2.48 2.49 2.50
2.51 2.52 2.53 2.54 2.55 2.56 2.57 2.58 2.59 2.60 2.61 2.62 2.63 2.64 2.65
2.66 2.67 2.68 2.69 2.70 2.71 2.72 2.73 2.74 2.75 2.76 2.77 2.78 2.79 2.80
2.81 2.82 2.83 2.84 2.85 2.86 2.87 2.88 2.89 2.90 2.91 2.92 2.93 2.94 2.95
2.96 2.97 2.98 2.99 3.00 3.01 3.02 3.03 3.04 3.05 3.06 3.07 3.08 3.09 3.10
3.11 3.12 3.13 3.14 3.15 3.16 3.17 3.18 3.19 3.20 3.21 3.22 3.23 3.24 3.25
3.26 3.27 3.28 3.29 3.30 3.31 3.32 3.33 3.34 3.35 3.36 3.37 3.38 3.39 3.40
3.41 3.42 3.43 3.44 3.45 3.46 3.47 3.48 3.49 3.50 3.51 3.52 3.53 3.54 3.55
3.56 3.57 3.58 3.59 3.60 3.61 3.62 3.63 3.64 3.65 3.66 3.67 3.68 3.69 3.70
3.71 3.72 3.73 3.74 3.75 3.76 3.77 3.78 3.79 3.80 3.81 3.82 3.83 3.84 3.85
3.86 3.87 3.88 3.89 3.90 3.91 3.92 3.93 3.94 3.95 3.96 3.97 3.98 3.99 4.00
4.01 4.02 4.03 4.04 4.05 4.06 4.07 4.08 4.09 4.10 4.11 4.12 4.13 4.14 4.15
4.16 4.17 4.18 4.19 4.20 4.21 4.22 4.23 4.24 4.25 4.26 4.27 4.28 4.29 4.30
4.31 4.32 4.33 4.34 4.35 4.36 4.37 4.38 4.39 4.40 4.41 4.42 4.43 4.44 4.45
4.46 4.47 4.48 4.49 4.50 4.51 4.52 4.53 4.54 4.55 4.56 4.57 4.58 4.59 4.60
4.61 4.62 4.63 4.64 4.65 4.66 4.67 4.68 4.69 4.70 4.71 4.72 4.73 4.74 4.75
4.76 4.77 4.78 4.79 4.80 4.81 4.82 4.83 4.84 4.85 4.86 4.87 4.88 4.89 4.90
4.91 4.92 4.93 4.94 4.95 4.96 4.97 4.98 4.99 5.00 5.01 5.02 5.03 5.04 5.05
5.06 5.07 5.08 5.09 5.10 5.11 5.12 5.13 5.14 5.15 5.16 5.17 5.18 5.19 5.20
5.21 5.22 5.23 5.24 5.25 5.26 5.27 5.28 5.29 5.30 5.31 5.32 5.33 5.34 5.35
5.36 5.37 5.38 5.39 5.40 5.41 5.42 5.43 5.44 5.45 5.46 5.47 5.48 5.49 5.50
5.51 5.52 5.53 5.54 5.55 5.56 5.57 5.58 5.59 5.60 5.61 5.62 5.63 5.64 5.65
5.66 5.67 5.68 5.69 5.70 5.71 5.72 5.73 5.74 5.75 5.76 5.77 5.78 5.79 5.80
5.81 5.82 5.83 5.84 5.85 5.86 5.87 5.88 5.89 5.90 5.91 5.92 5.93 5.94 5.95
5.96 5.97 5.98 5.99 6.00 6.01 6.02 6.03 6.04 6.05 6.06 6.07 6.08 6.09 6.10
6.11 6.12 6.13 6.14 6.15 6.16 6.17 6.18 6.19 6.20 6.21 6.22 6.23 6.24 6.25
6.26 6.27 6.28 6.29 6.30 6.31 6.32 6.33 6.34 6.35 6.36 6.37 6.38 6.39 6.40
6.41 6.42 6.43 6.44 6.45

F28:p 11

E28 0 0.01 0.02 0.03 0.04 0.05 0.06 0.07 0.08 0.09 0.10 0.11 0.12 0.13
0.14 0.15 0.16 0.17 0.18 0.19 0.20 0.21 0.22 0.23 0.24 0.25 0.26 0.27 0.28
0.29 0.30 0.31 0.32 0.33 0.34 0.35 0.36 0.37 0.38 0.39 0.4 0.41 0.42 0.43
0.44 0.45 0.46 0.47 0.48 0.49 0.50 0.51 0.52 0.53 0.54 0.55 0.56 0.57
0.58 0.59 0.60 0.61 0.62 0.63 0.64 0.65 0.66 0.67 0.68 0.69 0.70 0.71
0.72 0.73 0.74 0.75 0.76 0.77 0.78 0.79 0.80 0.81 0.82 0.83 0.84 0.85
0.86 0.87 0.88 0.89 0.90 0.91 0.92 0.93 0.94 0.95 0.96 0.97 0.98 0.99 1.00
1.01 1.02 1.03 1.04 1.05 1.06 1.07 1.08 1.09 1.10 1.11 1.12 1.13 1.14 1.15
1.16 1.17 1.18 1.19 1.20 1.21 1.22 1.23 1.24 1.25 1.26 1.27 1.28 1.29 1.30
1.31 1.32 1.33 1.34 1.35 1.36 1.37 1.38 1.39 1.40 1.41 1.42 1.43 1.44 1.45
1.46 1.47 1.48 1.49 1.50 1.51 1.52 1.53 1.54 1.55 1.56 1.57 1.58 1.59 1.60
1.61 1.62 1.63 1.64 1.65 1.66 1.67 1.68 1.69 1.70 1.71 1.72 1.73 1.74 1.75

1.76 1.77 1.78 1.79 1.80 1.81 1.82 1.83 1.84 1.85 1.86 1.87 1.88 1.89 1.90
1.91 1.92 1.93 1.94 1.95 1.96 1.97 1.98 1.99 2.00 2.01 2.02 2.03 2.04 2.05
2.06 2.07 2.08 2.09 2.10 2.11 2.12 2.13 2.14 2.15 2.16 2.17 2.18 2.19 2.20
2.21 2.22 2.23 2.24 2.25 2.26 2.27 2.28 2.29 2.30 2.31 2.32 2.33 2.34 2.35
2.36 2.37 2.38 2.39 2.40 2.41 2.42 2.43 2.44 2.45 2.46 2.47 2.48 2.49 2.50
2.51 2.52 2.53 2.54 2.55 2.56 2.57 2.58 2.59 2.60 2.61 2.62 2.63 2.64 2.65
2.66 2.67 2.68 2.69 2.70 2.71 2.72 2.73 2.74 2.75 2.76 2.77 2.78 2.79 2.80
2.81 2.82 2.83 2.84 2.85 2.86 2.87 2.88 2.89 2.90 2.91 2.92 2.93 2.94 2.95
2.96 2.97 2.98 2.99 3.00 3.01 3.02 3.03 3.04 3.05 3.06 3.07 3.08 3.09 3.10
3.11 3.12 3.13 3.14 3.15 3.16 3.17 3.18 3.19 3.20 3.21 3.22 3.23 3.24 3.25
3.26 3.27 3.28 3.29 3.30 3.31 3.32 3.33 3.34 3.35 3.36 3.37 3.38 3.39 3.40
3.41 3.42 3.43 3.44 3.45 3.46 3.47 3.48 3.49 3.50 3.51 3.52 3.53 3.54 3.55
3.56 3.57 3.58 3.59 3.60 3.61 3.62 3.63 3.64 3.65 3.66 3.67 3.68 3.69 3.70
3.71 3.72 3.73 3.74 3.75 3.76 3.77 3.78 3.79 3.80 3.81 3.82 3.83 3.84 3.85
3.86 3.87 3.88 3.89 3.90 3.91 3.92 3.93 3.94 3.95 3.96 3.97 3.98 3.99 4.00
4.01 4.02 4.03 4.04 4.05 4.06 4.07 4.08 4.09 4.10 4.11 4.12 4.13 4.14 4.15
4.16 4.17 4.18 4.19 4.20 4.21 4.22 4.23 4.24 4.25 4.26 4.27 4.28 4.29 4.30
4.31 4.32 4.33 4.34 4.35 4.36 4.37 4.38 4.39 4.40 4.41 4.42 4.43 4.44 4.45
4.46 4.47 4.48 4.49 4.50 4.51 4.52 4.53 4.54 4.55 4.56 4.57 4.58 4.59 4.60
4.61 4.62 4.63 4.64 4.65 4.66 4.67 4.68 4.69 4.70 4.71 4.72 4.73 4.74 4.75
4.76 4.77 4.78 4.79 4.80 4.81 4.82 4.83 4.84 4.85 4.86 4.87 4.88 4.89 4.90
4.91 4.92 4.93 4.94 4.95 4.96 4.97 4.98 4.99 5.00 5.01 5.02 5.03 5.04 5.05
5.06 5.07 5.08 5.09 5.10 5.11 5.12 5.13 5.14 5.15 5.16 5.17 5.18 5.19 5.20
5.21 5.22 5.23 5.24 5.25 5.26 5.27 5.28 5.29 5.30 5.31 5.32 5.33 5.34 5.35
5.36 5.37 5.38 5.39 5.40 5.41 5.42 5.43 5.44 5.45 5.46 5.47 5.48 5.49 5.50
5.51 5.52 5.53 5.54 5.55 5.56 5.57 5.58 5.59 5.60 5.61 5.62 5.63 5.64 5.65
5.66 5.67 5.68 5.69 5.70 5.71 5.72 5.73 5.74 5.75 5.76 5.77 5.78 5.79 5.80
5.81 5.82 5.83 5.84 5.85 5.86 5.87 5.88 5.89 5.90 5.91 5.92 5.93 5.94 5.95
5.96 5.97 5.98 5.99 6.00 6.01 6.02 6.03 6.04 6.05 6.06 6.07 6.08 6.09 6.10
6.11 6.12 6.13 6.14 6.15 6.16 6.17 6.18 6.19 6.20 6.21 6.22 6.23 6.24 6.25
6.26 6.27 6.28 6.29 6.30 6.31 6.32 6.33 6.34 6.35 6.36 6.37 6.38 6.39 6.40
6.41 6.42 6.43 6.44 6.45
F38:p 15
E38 0 0.01 0.02 0.03 0.04 0.05 0.06 0.07 0.08 0.09 0.10 0.11 0.12 0.13
0.14 0.15 0.16 0.17 0.18 0.19 0.20 0.21 0.22 0.23 0.24 0.25 0.26 0.27 0.28
0.29 0.30 0.31 0.32 0.33 0.34 0.35 0.36 0.37 0.38 0.39 0.4 0.41 0.42 0.43
0.44 0.45 0.46 0.47 0.48 0.49 0.50 0.51 0.52 0.53 0.54 0.55 0.56 0.57
0.58 0.59 0.60 0.61 0.62 0.63 0.64 0.65 0.66 0.67 0.68 0.69 0.70 0.71
0.72 0.73 0.74 0.75 0.76 0.77 0.78 0.79 0.80 0.81 0.82 0.83 0.84 0.85
0.86 0.87 0.88 0.89 0.90 0.91 0.92 0.93 0.94 0.95 0.96 0.97 0.98 0.99 1.00
1.01 1.02 1.03 1.04 1.05 1.06 1.07 1.08 1.09 1.10 1.11 1.12 1.13 1.14 1.15
1.16 1.17 1.18 1.19 1.20 1.21 1.22 1.23 1.24 1.25 1.26 1.27 1.28 1.29 1.30
1.31 1.32 1.33 1.34 1.35 1.36 1.37 1.38 1.39 1.40 1.41 1.42 1.43 1.44 1.45
1.46 1.47 1.48 1.49 1.50 1.51 1.52 1.53 1.54 1.55 1.56 1.57 1.58 1.59 1.60
1.61 1.62 1.63 1.64 1.65 1.66 1.67 1.68 1.69 1.70 1.71 1.72 1.73 1.74 1.75
1.76 1.77 1.78 1.79 1.80 1.81 1.82 1.83 1.84 1.85 1.86 1.87 1.88 1.89 1.90
1.91 1.92 1.93 1.94 1.95 1.96 1.97 1.98 1.99 2.00 2.01 2.02 2.03 2.04 2.05
2.06 2.07 2.08 2.09 2.10 2.11 2.12 2.13 2.14 2.15 2.16 2.17 2.18 2.19 2.20

2.21 2.22 2.23 2.24 2.25 2.26 2.27 2.28 2.29 2.30 2.31 2.32 2.33 2.34 2.35
2.36 2.37 2.38 2.39 2.40 2.41 2.42 2.43 2.44 2.45 2.46 2.47 2.48 2.49 2.50
2.51 2.52 2.53 2.54 2.55 2.56 2.57 2.58 2.59 2.60 2.61 2.62 2.63 2.64 2.65
2.66 2.67 2.68 2.69 2.70 2.71 2.72 2.73 2.74 2.75 2.76 2.77 2.78 2.79 2.80
2.81 2.82 2.83 2.84 2.85 2.86 2.87 2.88 2.89 2.90 2.91 2.92 2.93 2.94 2.95
2.96 2.97 2.98 2.99 3.00 3.01 3.02 3.03 3.04 3.05 3.06 3.07 3.08 3.09 3.10
3.11 3.12 3.13 3.14 3.15 3.16 3.17 3.18 3.19 3.20 3.21 3.22 3.23 3.24 3.25
3.26 3.27 3.28 3.29 3.30 3.31 3.32 3.33 3.34 3.35 3.36 3.37 3.38 3.39 3.40
3.41 3.42 3.43 3.44 3.45 3.46 3.47 3.48 3.49 3.50 3.51 3.52 3.53 3.54 3.55
3.56 3.57 3.58 3.59 3.60 3.61 3.62 3.63 3.64 3.65 3.66 3.67 3.68 3.69 3.70
3.71 3.72 3.73 3.74 3.75 3.76 3.77 3.78 3.79 3.80 3.81 3.82 3.83 3.84 3.85
3.86 3.87 3.88 3.89 3.90 3.91 3.92 3.93 3.94 3.95 3.96 3.97 3.98 3.99 4.00
4.01 4.02 4.03 4.04 4.05 4.06 4.07 4.08 4.09 4.10 4.11 4.12 4.13 4.14 4.15
4.16 4.17 4.18 4.19 4.20 4.21 4.22 4.23 4.24 4.25 4.26 4.27 4.28 4.29 4.30
4.31 4.32 4.33 4.34 4.35 4.36 4.37 4.38 4.39 4.40 4.41 4.42 4.43 4.44 4.45
4.46 4.47 4.48 4.49 4.50 4.51 4.52 4.53 4.54 4.55 4.56 4.57 4.58 4.59 4.60
4.61 4.62 4.63 4.64 4.65 4.66 4.67 4.68 4.69 4.70 4.71 4.72 4.73 4.74 4.75
4.76 4.77 4.78 4.79 4.80 4.81 4.82 4.83 4.84 4.85 4.86 4.87 4.88 4.89 4.90
4.91 4.92 4.93 4.94 4.95 4.96 4.97 4.98 4.99 5.00 5.01 5.02 5.03 5.04 5.05
5.06 5.07 5.08 5.09 5.10 5.11 5.12 5.13 5.14 5.15 5.16 5.17 5.18 5.19 5.20
5.21 5.22 5.23 5.24 5.25 5.26 5.27 5.28 5.29 5.30 5.31 5.32 5.33 5.34 5.35
5.36 5.37 5.38 5.39 5.40 5.41 5.42 5.43 5.44 5.45 5.46 5.47 5.48 5.49 5.50
5.51 5.52 5.53 5.54 5.55 5.56 5.57 5.58 5.59 5.60 5.61 5.62 5.63 5.64 5.65
5.66 5.67 5.68 5.69 5.70 5.71 5.72 5.73 5.74 5.75 5.76 5.77 5.78 5.79 5.80
5.81 5.82 5.83 5.84 5.85 5.86 5.87 5.88 5.89 5.90 5.91 5.92 5.93 5.94 5.95
5.96 5.97 5.98 5.99 6.00 6.01 6.02 6.03 6.04 6.05 6.06 6.07 6.08 6.09 6.10
6.11 6.12 6.13 6.14 6.15 6.16 6.17 6.18 6.19 6.20 6.21 6.22 6.23 6.24 6.25
6.26 6.27 6.28 6.29 6.30 6.31 6.32 6.33 6.34 6.35 6.36 6.37 6.38 6.39 6.40
6.41 6.42 6.43 6.44 6.45
F48:p 19
E48 0 0.01 0.02 0.03 0.04 0.05 0.06 0.07 0.08 0.09 0.10 0.11 0.12 0.13
0.14 0.15 0.16 0.17 0.18 0.19 0.20 0.21 0.22 0.23 0.24 0.25 0.26 0.27 0.28
0.29 0.30 0.31 0.32 0.33 0.34 0.35 0.36 0.37 0.38 0.39 0.4 0.41 0.42 0.43
0.44 0.45 0.46 0.47 0.48 0.49 0.50 0.51 0.52 0.53 0.54 0.55 0.56 0.57
0.58 0.59 0.60 0.61 0.62 0.63 0.64 0.65 0.66 0.67 0.68 0.69 0.70 0.71
0.72 0.73 0.74 0.75 0.76 0.77 0.78 0.79 0.80 0.81 0.82 0.83 0.84 0.85
0.86 0.87 0.88 0.89 0.90 0.91 0.92 0.93 0.94 0.95 0.96 0.97 0.98 0.99 1.00
1.01 1.02 1.03 1.04 1.05 1.06 1.07 1.08 1.09 1.10 1.11 1.12 1.13 1.14 1.15
1.16 1.17 1.18 1.19 1.20 1.21 1.22 1.23 1.24 1.25 1.26 1.27 1.28 1.29 1.30
1.31 1.32 1.33 1.34 1.35 1.36 1.37 1.38 1.39 1.40 1.41 1.42 1.43 1.44 1.45
1.46 1.47 1.48 1.49 1.50 1.51 1.52 1.53 1.54 1.55 1.56 1.57 1.58 1.59 1.60
1.61 1.62 1.63 1.64 1.65 1.66 1.67 1.68 1.69 1.70 1.71 1.72 1.73 1.74 1.75
1.76 1.77 1.78 1.79 1.80 1.81 1.82 1.83 1.84 1.85 1.86 1.87 1.88 1.89 1.90
1.91 1.92 1.93 1.94 1.95 1.96 1.97 1.98 1.99 2.00 2.01 2.02 2.03 2.04 2.05
2.06 2.07 2.08 2.09 2.10 2.11 2.12 2.13 2.14 2.15 2.16 2.17 2.18 2.19 2.20
2.21 2.22 2.23 2.24 2.25 2.26 2.27 2.28 2.29 2.30 2.31 2.32 2.33 2.34 2.35
2.36 2.37 2.38 2.39 2.40 2.41 2.42 2.43 2.44 2.45 2.46 2.47 2.48 2.49 2.50
2.51 2.52 2.53 2.54 2.55 2.56 2.57 2.58 2.59 2.60 2.61 2.62 2.63 2.64 2.65

2.66 2.67 2.68 2.69 2.70 2.71 2.72 2.73 2.74 2.75 2.76 2.77 2.78 2.79 2.80
2.81 2.82 2.83 2.84 2.85 2.86 2.87 2.88 2.89 2.90 2.91 2.92 2.93 2.94 2.95
2.96 2.97 2.98 2.99 3.00 3.01 3.02 3.03 3.04 3.05 3.06 3.07 3.08 3.09 3.10
3.11 3.12 3.13 3.14 3.15 3.16 3.17 3.18 3.19 3.20 3.21 3.22 3.23 3.24 3.25
3.26 3.27 3.28 3.29 3.30 3.31 3.32 3.33 3.34 3.35 3.36 3.37 3.38 3.39 3.40
3.41 3.42 3.43 3.44 3.45 3.46 3.47 3.48 3.49 3.50 3.51 3.52 3.53 3.54 3.55
3.56 3.57 3.58 3.59 3.60 3.61 3.62 3.63 3.64 3.65 3.66 3.67 3.68 3.69 3.70
3.71 3.72 3.73 3.74 3.75 3.76 3.77 3.78 3.79 3.80 3.81 3.82 3.83 3.84 3.85
3.86 3.87 3.88 3.89 3.90 3.91 3.92 3.93 3.94 3.95 3.96 3.97 3.98 3.99 4.00
4.01 4.02 4.03 4.04 4.05 4.06 4.07 4.08 4.09 4.10 4.11 4.12 4.13 4.14 4.15
4.16 4.17 4.18 4.19 4.20 4.21 4.22 4.23 4.24 4.25 4.26 4.27 4.28 4.29 4.30
4.31 4.32 4.33 4.34 4.35 4.36 4.37 4.38 4.39 4.40 4.41 4.42 4.43 4.44 4.45
4.46 4.47 4.48 4.49 4.50 4.51 4.52 4.53 4.54 4.55 4.56 4.57 4.58 4.59 4.60
4.61 4.62 4.63 4.64 4.65 4.66 4.67 4.68 4.69 4.70 4.71 4.72 4.73 4.74 4.75
4.76 4.77 4.78 4.79 4.80 4.81 4.82 4.83 4.84 4.85 4.86 4.87 4.88 4.89 4.90
4.91 4.92 4.93 4.94 4.95 4.96 4.97 4.98 4.99 5.00 5.01 5.02 5.03 5.04 5.05
5.06 5.07 5.08 5.09 5.10 5.11 5.12 5.13 5.14 5.15 5.16 5.17 5.18 5.19 5.20
5.21 5.22 5.23 5.24 5.25 5.26 5.27 5.28 5.29 5.30 5.31 5.32 5.33 5.34 5.35
5.36 5.37 5.38 5.39 5.40 5.41 5.42 5.43 5.44 5.45 5.46 5.47 5.48 5.49 5.50
5.51 5.52 5.53 5.54 5.55 5.56 5.57 5.58 5.59 5.60 5.61 5.62 5.63 5.64 5.65
5.66 5.67 5.68 5.69 5.70 5.71 5.72 5.73 5.74 5.75 5.76 5.77 5.78 5.79 5.80
5.81 5.82 5.83 5.84 5.85 5.86 5.87 5.88 5.89 5.90 5.91 5.92 5.93 5.94 5.95
5.96 5.97 5.98 5.99 6.00 6.01 6.02 6.03 6.04 6.05 6.06 6.07 6.08 6.09 6.10
6.11 6.12 6.13 6.14 6.15 6.16 6.17 6.18 6.19 6.20 6.21 6.22 6.23 6.24 6.25
6.26 6.27 6.28 6.29 6.30 6.31 6.32 6.33 6.34 6.35 6.36 6.37 6.38 6.39 6.40
6.41 6.42 6.43 6.44 6.45
F58:p 23
E58 0 0.01 0.02 0.03 0.04 0.05 0.06 0.07 0.08 0.09 0.10 0.11 0.12 0.13
0.14 0.15 0.16 0.17 0.18 0.19 0.20 0.21 0.22 0.23 0.24 0.25 0.26 0.27 0.28
0.29 0.30 0.31 0.32 0.33 0.34 0.35 0.36 0.37 0.38 0.39 0.4 0.41 0.42 0.43
0.44 0.45 0.46 0.47 0.48 0.49 0.50 0.51 0.52 0.53 0.54 0.55 0.56 0.57
0.58 0.59 0.60 0.61 0.62 0.63 0.64 0.65 0.66 0.67 0.68 0.69 0.70 0.71
0.72 0.73 0.74 0.75 0.76 0.77 0.78 0.79 0.80 0.81 0.82 0.83 0.84 0.85
0.86 0.87 0.88 0.89 0.90 0.91 0.92 0.93 0.94 0.95 0.96 0.97 0.98 0.99 1.00
1.01 1.02 1.03 1.04 1.05 1.06 1.07 1.08 1.09 1.10 1.11 1.12 1.13 1.14 1.15
1.16 1.17 1.18 1.19 1.20 1.21 1.22 1.23 1.24 1.25 1.26 1.27 1.28 1.29 1.30
1.31 1.32 1.33 1.34 1.35 1.36 1.37 1.38 1.39 1.40 1.41 1.42 1.43 1.44 1.45
1.46 1.47 1.48 1.49 1.50 1.51 1.52 1.53 1.54 1.55 1.56 1.57 1.58 1.59 1.60
1.61 1.62 1.63 1.64 1.65 1.66 1.67 1.68 1.69 1.70 1.71 1.72 1.73 1.74 1.75
1.76 1.77 1.78 1.79 1.80 1.81 1.82 1.83 1.84 1.85 1.86 1.87 1.88 1.89 1.90
1.91 1.92 1.93 1.94 1.95 1.96 1.97 1.98 1.99 2.00 2.01 2.02 2.03 2.04 2.05
2.06 2.07 2.08 2.09 2.10 2.11 2.12 2.13 2.14 2.15 2.16 2.17 2.18 2.19 2.20
2.21 2.22 2.23 2.24 2.25 2.26 2.27 2.28 2.29 2.30 2.31 2.32 2.33 2.34 2.35
2.36 2.37 2.38 2.39 2.40 2.41 2.42 2.43 2.44 2.45 2.46 2.47 2.48 2.49 2.50
2.51 2.52 2.53 2.54 2.55 2.56 2.57 2.58 2.59 2.60 2.61 2.62 2.63 2.64 2.65
2.66 2.67 2.68 2.69 2.70 2.71 2.72 2.73 2.74 2.75 2.76 2.77 2.78 2.79 2.80
2.81 2.82 2.83 2.84 2.85 2.86 2.87 2.88 2.89 2.90 2.91 2.92 2.93 2.94 2.95
2.96 2.97 2.98 2.99 3.00 3.01 3.02 3.03 3.04 3.05 3.06 3.07 3.08 3.09 3.10

3.11 3.12 3.13 3.14 3.15 3.16 3.17 3.18 3.19 3.20 3.21 3.22 3.23 3.24 3.25
3.26 3.27 3.28 3.29 3.30 3.31 3.32 3.33 3.34 3.35 3.36 3.37 3.38 3.39 3.40
3.41 3.42 3.43 3.44 3.45 3.46 3.47 3.48 3.49 3.50 3.51 3.52 3.53 3.54 3.55
3.56 3.57 3.58 3.59 3.60 3.61 3.62 3.63 3.64 3.65 3.66 3.67 3.68 3.69 3.70
3.71 3.72 3.73 3.74 3.75 3.76 3.77 3.78 3.79 3.80 3.81 3.82 3.83 3.84 3.85
3.86 3.87 3.88 3.89 3.90 3.91 3.92 3.93 3.94 3.95 3.96 3.97 3.98 3.99 4.00
4.01 4.02 4.03 4.04 4.05 4.06 4.07 4.08 4.09 4.10 4.11 4.12 4.13 4.14 4.15
4.16 4.17 4.18 4.19 4.20 4.21 4.22 4.23 4.24 4.25 4.26 4.27 4.28 4.29 4.30
4.31 4.32 4.33 4.34 4.35 4.36 4.37 4.38 4.39 4.40 4.41 4.42 4.43 4.44 4.45
4.46 4.47 4.48 4.49 4.50 4.51 4.52 4.53 4.54 4.55 4.56 4.57 4.58 4.59 4.60
4.61 4.62 4.63 4.64 4.65 4.66 4.67 4.68 4.69 4.70 4.71 4.72 4.73 4.74 4.75
4.76 4.77 4.78 4.79 4.80 4.81 4.82 4.83 4.84 4.85 4.86 4.87 4.88 4.89 4.90
4.91 4.92 4.93 4.94 4.95 4.96 4.97 4.98 4.99 5.00 5.01 5.02 5.03 5.04 5.05
5.06 5.07 5.08 5.09 5.10 5.11 5.12 5.13 5.14 5.15 5.16 5.17 5.18 5.19 5.20
5.21 5.22 5.23 5.24 5.25 5.26 5.27 5.28 5.29 5.30 5.31 5.32 5.33 5.34 5.35
5.36 5.37 5.38 5.39 5.40 5.41 5.42 5.43 5.44 5.45 5.46 5.47 5.48 5.49 5.50
5.51 5.52 5.53 5.54 5.55 5.56 5.57 5.58 5.59 5.60 5.61 5.62 5.63 5.64 5.65
5.66 5.67 5.68 5.69 5.70 5.71 5.72 5.73 5.74 5.75 5.76 5.77 5.78 5.79 5.80
5.81 5.82 5.83 5.84 5.85 5.86 5.87 5.88 5.89 5.90 5.91 5.92 5.93 5.94 5.95
5.96 5.97 5.98 5.99 6.00 6.01 6.02 6.03 6.04 6.05 6.06 6.07 6.08 6.09 6.10
6.11 6.12 6.13 6.14 6.15 6.16 6.17 6.18 6.19 6.20 6.21 6.22 6.23 6.24 6.25
6.26 6.27 6.28 6.29 6.30 6.31 6.32 6.33 6.34 6.35 6.36 6.37 6.38 6.39 6.40
6.41 6.42 6.43 6.44 6.45

F68:p 27

E68 0 0.01 0.02 0.03 0.04 0.05 0.06 0.07 0.08 0.09 0.10 0.11 0.12 0.13
0.14 0.15 0.16 0.17 0.18 0.19 0.20 0.21 0.22 0.23 0.24 0.25 0.26 0.27 0.28
0.29 0.30 0.31 0.32 0.33 0.34 0.35 0.36 0.37 0.38 0.39 0.4 0.41 0.42 0.43
0.44 0.45 0.46 0.47 0.48 0.49 0.50 0.51 0.52 0.53 0.54 0.55 0.56 0.57
0.58 0.59 0.60 0.61 0.62 0.63 0.64 0.65 0.66 0.67 0.68 0.69 0.70 0.71
0.72 0.73 0.74 0.75 0.76 0.77 0.78 0.79 0.80 0.81 0.82 0.83 0.84 0.85
0.86 0.87 0.88 0.89 0.90 0.91 0.92 0.93 0.94 0.95 0.96 0.97 0.98 0.99 1.00
1.01 1.02 1.03 1.04 1.05 1.06 1.07 1.08 1.09 1.10 1.11 1.12 1.13 1.14 1.15
1.16 1.17 1.18 1.19 1.20 1.21 1.22 1.23 1.24 1.25 1.26 1.27 1.28 1.29 1.30
1.31 1.32 1.33 1.34 1.35 1.36 1.37 1.38 1.39 1.40 1.41 1.42 1.43 1.44 1.45
1.46 1.47 1.48 1.49 1.50 1.51 1.52 1.53 1.54 1.55 1.56 1.57 1.58 1.59 1.60
1.61 1.62 1.63 1.64 1.65 1.66 1.67 1.68 1.69 1.70 1.71 1.72 1.73 1.74 1.75
1.76 1.77 1.78 1.79 1.80 1.81 1.82 1.83 1.84 1.85 1.86 1.87 1.88 1.89 1.90
1.91 1.92 1.93 1.94 1.95 1.96 1.97 1.98 1.99 2.00 2.01 2.02 2.03 2.04 2.05
2.06 2.07 2.08 2.09 2.10 2.11 2.12 2.13 2.14 2.15 2.16 2.17 2.18 2.19 2.20
2.21 2.22 2.23 2.24 2.25 2.26 2.27 2.28 2.29 2.30 2.31 2.32 2.33 2.34 2.35
2.36 2.37 2.38 2.39 2.40 2.41 2.42 2.43 2.44 2.45 2.46 2.47 2.48 2.49 2.50
2.51 2.52 2.53 2.54 2.55 2.56 2.57 2.58 2.59 2.60 2.61 2.62 2.63 2.64 2.65
2.66 2.67 2.68 2.69 2.70 2.71 2.72 2.73 2.74 2.75 2.76 2.77 2.78 2.79 2.80
2.81 2.82 2.83 2.84 2.85 2.86 2.87 2.88 2.89 2.90 2.91 2.92 2.93 2.94 2.95
2.96 2.97 2.98 2.99 3.00 3.01 3.02 3.03 3.04 3.05 3.06 3.07 3.08 3.09 3.10
3.11 3.12 3.13 3.14 3.15 3.16 3.17 3.18 3.19 3.20 3.21 3.22 3.23 3.24 3.25
3.26 3.27 3.28 3.29 3.30 3.31 3.32 3.33 3.34 3.35 3.36 3.37 3.38 3.39 3.40
3.41 3.42 3.43 3.44 3.45 3.46 3.47 3.48 3.49 3.50 3.51 3.52 3.53 3.54 3.55

3.56 3.57 3.58 3.59 3.60 3.61 3.62 3.63 3.64 3.65 3.66 3.67 3.68 3.69 3.70
3.71 3.72 3.73 3.74 3.75 3.76 3.77 3.78 3.79 3.80 3.81 3.82 3.83 3.84 3.85
3.86 3.87 3.88 3.89 3.90 3.91 3.92 3.93 3.94 3.95 3.96 3.97 3.98 3.99 4.00
4.01 4.02 4.03 4.04 4.05 4.06 4.07 4.08 4.09 4.10 4.11 4.12 4.13 4.14 4.15
4.16 4.17 4.18 4.19 4.20 4.21 4.22 4.23 4.24 4.25 4.26 4.27 4.28 4.29 4.30
4.31 4.32 4.33 4.34 4.35 4.36 4.37 4.38 4.39 4.40 4.41 4.42 4.43 4.44 4.45
4.46 4.47 4.48 4.49 4.50 4.51 4.52 4.53 4.54 4.55 4.56 4.57 4.58 4.59 4.60
4.61 4.62 4.63 4.64 4.65 4.66 4.67 4.68 4.69 4.70 4.71 4.72 4.73 4.74 4.75
4.76 4.77 4.78 4.79 4.80 4.81 4.82 4.83 4.84 4.85 4.86 4.87 4.88 4.89 4.90
4.91 4.92 4.93 4.94 4.95 4.96 4.97 4.98 4.99 5.00 5.01 5.02 5.03 5.04 5.05
5.06 5.07 5.08 5.09 5.10 5.11 5.12 5.13 5.14 5.15 5.16 5.17 5.18 5.19 5.20
5.21 5.22 5.23 5.24 5.25 5.26 5.27 5.28 5.29 5.30 5.31 5.32 5.33 5.34 5.35
5.36 5.37 5.38 5.39 5.40 5.41 5.42 5.43 5.44 5.45 5.46 5.47 5.48 5.49 5.50
5.51 5.52 5.53 5.54 5.55 5.56 5.57 5.58 5.59 5.60 5.61 5.62 5.63 5.64 5.65
5.66 5.67 5.68 5.69 5.70 5.71 5.72 5.73 5.74 5.75 5.76 5.77 5.78 5.79 5.80
5.81 5.82 5.83 5.84 5.85 5.86 5.87 5.88 5.89 5.90 5.91 5.92 5.93 5.94 5.95
5.96 5.97 5.98 5.99 6.00 6.01 6.02 6.03 6.04 6.05 6.06 6.07 6.08 6.09 6.10
6.11 6.12 6.13 6.14 6.15 6.16 6.17 6.18 6.19 6.20 6.21 6.22 6.23 6.24 6.25
6.26 6.27 6.28 6.29 6.30 6.31 6.32 6.33 6.34 6.35 6.36 6.37 6.38 6.39 6.40
6.41 6.42 6.43 6.44 6.45

F78:p 31

E78 0 0.01 0.02 0.03 0.04 0.05 0.06 0.07 0.08 0.09 0.10 0.11 0.12 0.13
0.14 0.15 0.16 0.17 0.18 0.19 0.20 0.21 0.22 0.23 0.24 0.25 0.26 0.27 0.28
0.29 0.30 0.31 0.32 0.33 0.34 0.35 0.36 0.37 0.38 0.39 0.4 0.41 0.42 0.43
0.44 0.45 0.46 0.47 0.48 0.49 0.50 0.51 0.52 0.53 0.54 0.55 0.56 0.57
0.58 0.59 0.60 0.61 0.62 0.63 0.64 0.65 0.66 0.67 0.68 0.69 0.70 0.71
0.72 0.73 0.74 0.75 0.76 0.77 0.78 0.79 0.80 0.81 0.82 0.83 0.84 0.85
0.86 0.87 0.88 0.89 0.90 0.91 0.92 0.93 0.94 0.95 0.96 0.97 0.98 0.99 1.00
1.01 1.02 1.03 1.04 1.05 1.06 1.07 1.08 1.09 1.10 1.11 1.12 1.13 1.14 1.15
1.16 1.17 1.18 1.19 1.20 1.21 1.22 1.23 1.24 1.25 1.26 1.27 1.28 1.29 1.30
1.31 1.32 1.33 1.34 1.35 1.36 1.37 1.38 1.39 1.40 1.41 1.42 1.43 1.44 1.45
1.46 1.47 1.48 1.49 1.50 1.51 1.52 1.53 1.54 1.55 1.56 1.57 1.58 1.59 1.60
1.61 1.62 1.63 1.64 1.65 1.66 1.67 1.68 1.69 1.70 1.71 1.72 1.73 1.74 1.75
1.76 1.77 1.78 1.79 1.80 1.81 1.82 1.83 1.84 1.85 1.86 1.87 1.88 1.89 1.90
1.91 1.92 1.93 1.94 1.95 1.96 1.97 1.98 1.99 2.00 2.01 2.02 2.03 2.04 2.05
2.06 2.07 2.08 2.09 2.10 2.11 2.12 2.13 2.14 2.15 2.16 2.17 2.18 2.19 2.20
2.21 2.22 2.23 2.24 2.25 2.26 2.27 2.28 2.29 2.30 2.31 2.32 2.33 2.34 2.35
2.36 2.37 2.38 2.39 2.40 2.41 2.42 2.43 2.44 2.45 2.46 2.47 2.48 2.49 2.50
2.51 2.52 2.53 2.54 2.55 2.56 2.57 2.58 2.59 2.60 2.61 2.62 2.63 2.64 2.65
2.66 2.67 2.68 2.69 2.70 2.71 2.72 2.73 2.74 2.75 2.76 2.77 2.78 2.79 2.80
2.81 2.82 2.83 2.84 2.85 2.86 2.87 2.88 2.89 2.90 2.91 2.92 2.93 2.94 2.95
2.96 2.97 2.98 2.99 3.00 3.01 3.02 3.03 3.04 3.05 3.06 3.07 3.08 3.09 3.10
3.11 3.12 3.13 3.14 3.15 3.16 3.17 3.18 3.19 3.20 3.21 3.22 3.23 3.24 3.25
3.26 3.27 3.28 3.29 3.30 3.31 3.32 3.33 3.34 3.35 3.36 3.37 3.38 3.39 3.40
3.41 3.42 3.43 3.44 3.45 3.46 3.47 3.48 3.49 3.50 3.51 3.52 3.53 3.54 3.55
3.56 3.57 3.58 3.59 3.60 3.61 3.62 3.63 3.64 3.65 3.66 3.67 3.68 3.69 3.70
3.71 3.72 3.73 3.74 3.75 3.76 3.77 3.78 3.79 3.80 3.81 3.82 3.83 3.84 3.85
3.86 3.87 3.88 3.89 3.90 3.91 3.92 3.93 3.94 3.95 3.96 3.97 3.98 3.99 4.00

4.01 4.02 4.03 4.04 4.05 4.06 4.07 4.08 4.09 4.10 4.11 4.12 4.13 4.14 4.15
4.16 4.17 4.18 4.19 4.20 4.21 4.22 4.23 4.24 4.25 4.26 4.27 4.28 4.29 4.30
4.31 4.32 4.33 4.34 4.35 4.36 4.37 4.38 4.39 4.40 4.41 4.42 4.43 4.44 4.45
4.46 4.47 4.48 4.49 4.50 4.51 4.52 4.53 4.54 4.55 4.56 4.57 4.58 4.59 4.60
4.61 4.62 4.63 4.64 4.65 4.66 4.67 4.68 4.69 4.70 4.71 4.72 4.73 4.74 4.75
4.76 4.77 4.78 4.79 4.80 4.81 4.82 4.83 4.84 4.85 4.86 4.87 4.88 4.89 4.90
4.91 4.92 4.93 4.94 4.95 4.96 4.97 4.98 4.99 5.00 5.01 5.02 5.03 5.04 5.05
5.06 5.07 5.08 5.09 5.10 5.11 5.12 5.13 5.14 5.15 5.16 5.17 5.18 5.19 5.20
5.21 5.22 5.23 5.24 5.25 5.26 5.27 5.28 5.29 5.30 5.31 5.32 5.33 5.34 5.35
5.36 5.37 5.38 5.39 5.40 5.41 5.42 5.43 5.44 5.45 5.46 5.47 5.48 5.49 5.50
5.51 5.52 5.53 5.54 5.55 5.56 5.57 5.58 5.59 5.60 5.61 5.62 5.63 5.64 5.65
5.66 5.67 5.68 5.69 5.70 5.71 5.72 5.73 5.74 5.75 5.76 5.77 5.78 5.79 5.80
5.81 5.82 5.83 5.84 5.85 5.86 5.87 5.88 5.89 5.90 5.91 5.92 5.93 5.94 5.95
5.96 5.97 5.98 5.99 6.00 6.01 6.02 6.03 6.04 6.05 6.06 6.07 6.08 6.09 6.10
6.11 6.12 6.13 6.14 6.15 6.16 6.17 6.18 6.19 6.20 6.21 6.22 6.23 6.24 6.25
6.26 6.27 6.28 6.29 6.30 6.31 6.32 6.33 6.34 6.35 6.36 6.37 6.38 6.39 6.40
6.41 6.42 6.43 6.44 6.45
F88:p 35
E88 0 0.01 0.02 0.03 0.04 0.05 0.06 0.07 0.08 0.09 0.10 0.11 0.12 0.13
0.14 0.15 0.16 0.17 0.18 0.19 0.20 0.21 0.22 0.23 0.24 0.25 0.26 0.27 0.28
0.29 0.30 0.31 0.32 0.33 0.34 0.35 0.36 0.37 0.38 0.39 0.4 0.41 0.42 0.43
0.44 0.45 0.46 0.47 0.48 0.49 0.50 0.51 0.52 0.53 0.54 0.55 0.56 0.57
0.58 0.59 0.60 0.61 0.62 0.63 0.64 0.65 0.66 0.67 0.68 0.69 0.70 0.71
0.72 0.73 0.74 0.75 0.76 0.77 0.78 0.79 0.80 0.81 0.82 0.83 0.84 0.85
0.86 0.87 0.88 0.89 0.90 0.91 0.92 0.93 0.94 0.95 0.96 0.97 0.98 0.99 1.00
1.01 1.02 1.03 1.04 1.05 1.06 1.07 1.08 1.09 1.10 1.11 1.12 1.13 1.14 1.15
1.16 1.17 1.18 1.19 1.20 1.21 1.22 1.23 1.24 1.25 1.26 1.27 1.28 1.29 1.30
1.31 1.32 1.33 1.34 1.35 1.36 1.37 1.38 1.39 1.40 1.41 1.42 1.43 1.44 1.45
1.46 1.47 1.48 1.49 1.50 1.51 1.52 1.53 1.54 1.55 1.56 1.57 1.58 1.59 1.60
1.61 1.62 1.63 1.64 1.65 1.66 1.67 1.68 1.69 1.70 1.71 1.72 1.73 1.74 1.75
1.76 1.77 1.78 1.79 1.80 1.81 1.82 1.83 1.84 1.85 1.86 1.87 1.88 1.89 1.90
1.91 1.92 1.93 1.94 1.95 1.96 1.97 1.98 1.99 2.00 2.01 2.02 2.03 2.04 2.05
2.06 2.07 2.08 2.09 2.10 2.11 2.12 2.13 2.14 2.15 2.16 2.17 2.18 2.19 2.20
2.21 2.22 2.23 2.24 2.25 2.26 2.27 2.28 2.29 2.30 2.31 2.32 2.33 2.34 2.35
2.36 2.37 2.38 2.39 2.40 2.41 2.42 2.43 2.44 2.45 2.46 2.47 2.48 2.49 2.50
2.51 2.52 2.53 2.54 2.55 2.56 2.57 2.58 2.59 2.60 2.61 2.62 2.63 2.64 2.65
2.66 2.67 2.68 2.69 2.70 2.71 2.72 2.73 2.74 2.75 2.76 2.77 2.78 2.79 2.80
2.81 2.82 2.83 2.84 2.85 2.86 2.87 2.88 2.89 2.90 2.91 2.92 2.93 2.94 2.95
2.96 2.97 2.98 2.99 3.00 3.01 3.02 3.03 3.04 3.05 3.06 3.07 3.08 3.09 3.10
3.11 3.12 3.13 3.14 3.15 3.16 3.17 3.18 3.19 3.20 3.21 3.22 3.23 3.24 3.25
3.26 3.27 3.28 3.29 3.30 3.31 3.32 3.33 3.34 3.35 3.36 3.37 3.38 3.39 3.40
3.41 3.42 3.43 3.44 3.45 3.46 3.47 3.48 3.49 3.50 3.51 3.52 3.53 3.54 3.55
3.56 3.57 3.58 3.59 3.60 3.61 3.62 3.63 3.64 3.65 3.66 3.67 3.68 3.69 3.70
3.71 3.72 3.73 3.74 3.75 3.76 3.77 3.78 3.79 3.80 3.81 3.82 3.83 3.84 3.85
3.86 3.87 3.88 3.89 3.90 3.91 3.92 3.93 3.94 3.95 3.96 3.97 3.98 3.99 4.00
4.01 4.02 4.03 4.04 4.05 4.06 4.07 4.08 4.09 4.10 4.11 4.12 4.13 4.14 4.15
4.16 4.17 4.18 4.19 4.20 4.21 4.22 4.23 4.24 4.25 4.26 4.27 4.28 4.29 4.30
4.31 4.32 4.33 4.34 4.35 4.36 4.37 4.38 4.39 4.40 4.41 4.42 4.43 4.44 4.45

```
     4.46 4.47 4.48 4.49 4.50 4.51 4.52 4.53 4.54 4.55 4.56 4.57 4.58 4.59 4.60
     4.61 4.62 4.63 4.64 4.65 4.66 4.67 4.68 4.69 4.70 4.71 4.72 4.73 4.74 4.75
     4.76 4.77 4.78 4.79 4.80 4.81 4.82 4.83 4.84 4.85 4.86 4.87 4.88 4.89 4.90
     4.91 4.92 4.93 4.94 4.95 4.96 4.97 4.98 4.99 5.00 5.01 5.02 5.03 5.04 5.05
     5.06 5.07 5.08 5.09 5.10 5.11 5.12 5.13 5.14 5.15 5.16 5.17 5.18 5.19 5.20
     5.21 5.22 5.23 5.24 5.25 5.26 5.27 5.28 5.29 5.30 5.31 5.32 5.33 5.34 5.35
     5.36 5.37 5.38 5.39 5.40 5.41 5.42 5.43 5.44 5.45 5.46 5.47 5.48 5.49 5.50
     5.51 5.52 5.53 5.54 5.55 5.56 5.57 5.58 5.59 5.60 5.61 5.62 5.63 5.64 5.65
     5.66 5.67 5.68 5.69 5.70 5.71 5.72 5.73 5.74 5.75 5.76 5.77 5.78 5.79 5.80
     5.81 5.82 5.83 5.84 5.85 5.86 5.87 5.88 5.89 5.90 5.91 5.92 5.93 5.94 5.95
     5.96 5.97 5.98 5.99 6.00 6.01 6.02 6.03 6.04 6.05 6.06 6.07 6.08 6.09 6.10
     6.11 6.12 6.13 6.14 6.15 6.16 6.17 6.18 6.19 6.20 6.21 6.22 6.23 6.24 6.25
     6.26 6.27 6.28 6.29 6.30 6.31 6.32 6.33 6.34 6.35 6.36 6.37 6.38 6.39 6.40
     6.41 6.42 6.43 6.44 6.45
sdef   par=2 rad=d1 pos=-9.839 10.302 0 axs=0 0 1 erg=1.3320 ext=d2
si1    h 0 0.25
sp1    -21 1
si2    0 0.5
sp2    -21 0
m1     11000 1 53000 1 $ NaI (ignore Thallium doping)
m2     26000 1 $ steel
m3     8000 2 14000 1 $ Quartz
nps    1000000
```

A2 MCNP Input file for 60 ml cylindrical volume source with energy of 1332 keV

[MCNP User Manual, Version 5, 2003]

```
4pi: Detector Response Function of 4Pi NaI(Tl) for Mono-Energetic Volume Source
c      Eight 10.2 x 10.2 x 40.6 cm Long crystals w/1mm thick steel can
c      Ninth 10.2 x 10.2 x 10.2 cm crystal w/1mm thick steel can
c      Nine Thin Quartz Optical Windows 2.69 x 10 x 10 cm
1      1 -3.67 -1 $imp:p=1 $ NaI crystal
2      2 -8.0 -2 1 3 4 $imp:p=1 $ Steel can
3      3 -2.65 -3 $imp:p=1 $ Quartz Window
4      0 -4 $ $imp:p=1 PMT Vaccuum
5      0 2 7 11 15 19 23 27 31 35 38 -5 $imp:p=1 $ Sphere of Exclusion
6      0 5 $ $imp:p=0 $ Universe
7      1 -3.67 -6 $ NaI Crystal
8      2 -8.0 -7 6 8 9 $ Steel can
9      3 -2.65 -8 $ Quartz Window
10     0 -9 $ PMT Vaccuum
11     1 -3.67 -10 $ NaI Crystal
12     2 -8.0 -11 10 12 13 $ Steel can
13     3 -2.65 -12 $ Quartz Window
14     0 -13 $ PMT Vaccuum
15     1 -3.67 -14 $ NaI Crystal
16     2 -8.0 -15 14 16 17 $ Steel can
17     3 -2.65 -16 $ Quartz Window
```

```
18    0 -17 $ PMT Vaccuum
19    1 -3.67 -18 $ NaI Crystal
20    2 -8.0 -19 18 20 21 $ Steel can
21    3 -2.65 -20 $ Quartz Window
22    0 -21 $ PMT Vaccuum
23    1 -3.67 -22 $ NaI Crystal
24    2 -8.0 -23 22 24 25 $ Steel can
25    3 -2.65 -24 $ Quartz Window
26    0 -25 $ PMT Vaccuum
27    1 -3.67 -26 $ NaI Crystal
28    2 -8.0 -27 26 28 29 $ Steel can
29    3 -2.65 -28 $ Quartz Window
30    0 -29 $ PMT Vaccuum
31    1 -3.67 -30 $ NaI Crystal
32    2 -8.0 -31 30 32 33 $ Steel can
33    3 -2.65 -32 $ Quartz Window
34    0 -33 $ PMT Vaccuum
35    1 -3.67 -34 $ NaI Crystal
36    2 -8.0 -35 34 36 37 $ Steel can
37    3 -2.65 -36 $ Quartz Window
38    0 -37 $ PMT Vaccuum
39    4 -1.00 -38 $ Volume Source Filled with Water

1     RPP -20.3 20.3 -5.1 5.1 -10.251 -0.051 $ NaI Crystal
2     RPP -28.779 20.351 -5.151 5.151 -10.302 0 $ Steel can
3     RPP -23.069 -20.3 -5.1 5.1 -10.251 -0.051 $ Quartz Window
4     RPP -28.779 -23.069 -5.1 5.1 -10.251 -0.051 $ PMT Vaccuum
5     SO 100
6     RPP -20.3 20.3 5.202 15.402 -10.251 -0.051 $ NaI Crystal
7     RPP -28.779 20.351 5.151 15.453 -10.302 0 $ Steel can
8     RPP -23.069 -20.3 5.202 15.402 -10.251 -0.051 $ Quartz Window
9     RPP -28.779 -23.069 5.202 15.402 -10.251 -0.051 $ PMT Vaccuum
10    RPP -20.3 20.3 15.504 25.704 -10.251 -0.051 $ NaI Crystal
11    RPP -28.779 20.351 15.453 25.755 -10.302 0 $ Steel can
12    RPP -23.069 -20.3 15.504 25.704 -10.251 -0.051 $ Quartz Window
13    RPP -28.779 -23.069 15.504 25.704 -10.251 -0.051 $ PMT Vaccuum
14    RPP -20.3 20.3 -5.1 5.1 0.051 10.251 $ NaI Crystal
15    RPP -28.779 20.351 -5.151 5.151 0 10.302 $ Steel can
16    RPP -23.069 -20.3 -5.1 5.1 0.051 10.251 $ Quartz Window
17    RPP -28.779 -23.069 -5.1 5.1 0.051 10.251 $ PMT Vaccuum
18    RPP -20.3 20.3 -5.1 5.1 10.353 20.553 $ NaI Crystal
19    RPP -28.779 20.351 -5.151 5.151 10.302 20.604 $ Steel can
20    RPP -23.069 -20.3 -5.1 5.1 10.353 20.553 $ Quartz Window
21    RPP -28.779 -23.069 -5.1 5.1 10.353 20.553 $ PMT Vaccuum
22    RPP -20.3 20.3 5.202 15.402 10.353 20.553 $ NaI Crystal
23    RPP -28.779 20.351 5.151 15.453 10.302 20.604 $ Steel can
24    RPP -23.069 -20.3 5.202 15.402 10.353 20.553 $ Quartz Window
25    RPP -28.779 -23.069 5.202 15.402 10.353 20.553 $ PMT Vaccuum
```

```
26    RPP -20.3 20.3 15.504 25.704 10.353 20.553 $ NaI Crystal
27    RPP -28.779 20.351 15.453 25.755 10.302 20.604 $ Steel can
28    RPP -23.069 -20.3 15.504 25.704 10.353 20.553 $ Quartz Window
29    RPP -28.779 -23.069 15.504 25.704 10.353 20.553 $ PMT Vaccuum
30    RPP -20.3 20.3 15.504 25.704 0.051 10.251 $ NaI Crystal
31    RPP -28.779 20.351 15.453 25.755 0 10.302 $ Steel can
32    RPP -23.069 -20.3 15.504 25.704 0.051 10.251 $ Quartz Window
33    RPP -28.779 -23.069 15.504 25.704 0.051 10.251 $ PMT Vaccuum
34    RPP -20.3 -10.14 5.202 15.402 0.051 10.251 $ NaI Crystal
35    RPP -28.779 -10.089 5.151 15.453 0 10.302 $ Steel can
36    RPP -23.069 -20.3 5.202 15.402 0.051 10.251 $ Quartz Window
37    RPP -28.779 -23.069 5.202 15.402 0.051 10.251 $ PMT Vaccuum
38    RCC -8.000 10.302 0 0 0 6 1.945 $ Volume Source Container

mode    p
imp:p 1 1 1 1 1 0 1 1 1 1 1 1 1 1 1 1 1 1 1 1 1 1 1 1 1 1 1 1 1 1 1 1 1 1 1 1 1
    1 1
F8:p 1
E8 0 1e-10 0.01 0.02 0.03 0.04 0.05 0.06 0.07 0.08 0.09 0.10 0.11 0.12 0.13
    0.14 0.15 0.16 0.17 0.18 0.19 0.20 0.21 0.22 0.23 0.24 0.25 0.26 0.27 0.28
    0.29 0.30 0.31 0.32 0.33 0.34 0.35 0.36 0.37 0.38 0.39 0.4 0.41 0.42 0.43
    0.44 0.45 0.46 0.47 0.48 0.49 0.50 0.51 0.52 0.53 0.54 0.55 0.56 0.57
    0.58 0.59 0.60 0.61 0.62 0.63 0.64 0.65 0.66 0.67 0.68 0.69 0.70 0.71
    0.72 0.73 0.74 0.75 0.76 0.77 0.78 0.79 0.80 0.81 0.82 0.83 0.84 0.85
    0.86 0.87 0.88 0.89 0.90 0.91 0.92 0.93 0.94 0.95 0.96 0.97 0.98 0.99 1.00
    1.01 1.02 1.03 1.04 1.05 1.06 1.07 1.08 1.09 1.10 1.11 1.12 1.13 1.14 1.15
    1.16 1.17 1.18 1.19 1.20 1.21 1.22 1.23 1.24 1.25 1.26 1.27 1.28 1.29 1.30
    1.31 1.32 1.33 1.34 1.35 1.36 1.37 1.38 1.39 1.40 1.41 1.42 1.43 1.44 1.45
    1.46 1.47 1.48 1.49 1.50 1.51 1.52 1.53 1.54 1.55 1.56 1.57 1.58 1.59 1.60
    1.61 1.62 1.63 1.64 1.65 1.66 1.67 1.68 1.69 1.70 1.71 1.72 1.73 1.74 1.75
    1.76 1.77 1.78 1.79 1.80 1.81 1.82 1.83 1.84 1.85 1.86 1.87 1.88 1.89 1.90
    1.91 1.92 1.93 1.94 1.95 1.96 1.97 1.98 1.99 2.00 2.01 2.02 2.03 2.04 2.05
    2.06 2.07 2.08 2.09 2.10 2.11 2.12 2.13 2.14 2.15 2.16 2.17 2.18 2.19 2.20
    2.21 2.22 2.23 2.24 2.25 2.26 2.27 2.28 2.29 2.30 2.31 2.32 2.33 2.34 2.35
    2.36 2.37 2.38 2.39 2.40 2.41 2.42 2.43 2.44 2.45 2.46 2.47 2.48 2.49 2.50
    2.51 2.52 2.53 2.54 2.55 2.56 2.57 2.58 2.59 2.60 2.61 2.62 2.63 2.64 2.65
    2.66 2.67 2.68 2.69 2.70 2.71 2.72 2.73 2.74 2.75 2.76 2.77 2.78 2.79 2.80
    2.81 2.82 2.83 2.84 2.85 2.86 2.87 2.88 2.89 2.90 2.91 2.92 2.93 2.94 2.95
    2.96 2.97 2.98 2.99 3.00 3.01 3.02 3.03 3.04 3.05 3.06 3.07 3.08 3.09 3.10
    3.11 3.12 3.13 3.14 3.15 3.16 3.17 3.18 3.19 3.20 3.21 3.22 3.23 3.24 3.25
    3.26 3.27 3.28 3.29 3.30 3.31 3.32 3.33 3.34 3.35 3.36 3.37 3.38 3.39 3.40
    3.41 3.42 3.43 3.44 3.45 3.46 3.47 3.48 3.49 3.50 3.51 3.52 3.53 3.54 3.55
    3.56 3.57 3.58 3.59 3.60 3.61 3.62 3.63 3.64 3.65 3.66 3.67 3.68 3.69 3.70
    3.71 3.72 3.73 3.74 3.75 3.76 3.77 3.78 3.79 3.80 3.81 3.82 3.83 3.84 3.85
    3.86 3.87 3.88 3.89 3.90 3.91 3.92 3.93 3.94 3.95 3.96 3.97 3.98 3.99 4.00
    4.01 4.02 4.03 4.04 4.05 4.06 4.07 4.08 4.09 4.10 4.11 4.12 4.13 4.14 4.15
    4.16 4.17 4.18 4.19 4.20 4.21 4.22 4.23 4.24 4.25 4.26 4.27 4.28 4.29 4.30
    4.31 4.32 4.33 4.34 4.35 4.36 4.37 4.38 4.39 4.40 4.41 4.42 4.43 4.44 4.45
```

4.46 4.47 4.48 4.49 4.50 4.51 4.52 4.53 4.54 4.55 4.56 4.57 4.58 4.59 4.60
4.61 4.62 4.63 4.64 4.65 4.66 4.67 4.68 4.69 4.70 4.71 4.72 4.73 4.74 4.75
4.76 4.77 4.78 4.79 4.80 4.81 4.82 4.83 4.84 4.85 4.86 4.87 4.88 4.89 4.90
4.91 4.92 4.93 4.94 4.95 4.96 4.97 4.98 4.99 5.00 5.01 5.02 5.03 5.04 5.05
5.06 5.07 5.08 5.09 5.10 5.11 5.12 5.13 5.14 5.15 5.16 5.17 5.18 5.19 5.20
5.21 5.22 5.23 5.24 5.25 5.26 5.27 5.28 5.29 5.30 5.31 5.32 5.33 5.34 5.35
5.36 5.37 5.38 5.39 5.40 5.41 5.42 5.43 5.44 5.45 5.46 5.47 5.48 5.49 5.50
5.51 5.52 5.53 5.54 5.55 5.56 5.57 5.58 5.59 5.60 5.61 5.62 5.63 5.64 5.65
5.66 5.67 5.68 5.69 5.70 5.71 5.72 5.73 5.74 5.75 5.76 5.77 5.78 5.79 5.80
5.81 5.82 5.83 5.84 5.85 5.86 5.87 5.88 5.89 5.90 5.91 5.92 5.93 5.94 5.95
5.96 5.97 5.98 5.99 6.00 6.01 6.02 6.03 6.04 6.05 6.06 6.07 6.08 6.09 6.10
6.11 6.12 6.13 6.14 6.15 6.16 6.17 6.18 6.19 6.20 6.21 6.22 6.23 6.24 6.25
6.26 6.27 6.28 6.29 6.30 6.31 6.32 6.33 6.34 6.35 6.36 6.37 6.38 6.39 6.40
6.41 6.42 6.43 6.44 6.45
F18:p 7
E18 0 1e-10 0.01 0.02 0.03 0.04 0.05 0.06 0.07 0.08 0.09 0.10 0.11 0.12 0.13
0.14 0.15 0.16 0.17 0.18 0.19 0.20 0.21 0.22 0.23 0.24 0.25 0.26 0.27 0.28
0.29 0.30 0.31 0.32 0.33 0.34 0.35 0.36 0.37 0.38 0.39 0.4 0.41 0.42 0.43
0.44 0.45 0.46 0.47 0.48 0.49 0.50 0.51 0.52 0.53 0.54 0.55 0.56 0.57
0.58 0.59 0.60 0.61 0.62 0.63 0.64 0.65 0.66 0.67 0.68 0.69 0.70 0.71
0.72 0.73 0.74 0.75 0.76 0.77 0.78 0.79 0.80 0.81 0.82 0.83 0.84 0.85
0.86 0.87 0.88 0.89 0.90 0.91 0.92 0.93 0.94 0.95 0.96 0.97 0.98 0.99 1.00
1.01 1.02 1.03 1.04 1.05 1.06 1.07 1.08 1.09 1.10 1.11 1.12 1.13 1.14 1.15
1.16 1.17 1.18 1.19 1.20 1.21 1.22 1.23 1.24 1.25 1.26 1.27 1.28 1.29 1.30
1.31 1.32 1.33 1.34 1.35 1.36 1.37 1.38 1.39 1.40 1.41 1.42 1.43 1.44 1.45
1.46 1.47 1.48 1.49 1.50 1.51 1.52 1.53 1.54 1.55 1.56 1.57 1.58 1.59 1.60
1.61 1.62 1.63 1.64 1.65 1.66 1.67 1.68 1.69 1.70 1.71 1.72 1.73 1.74 1.75
1.76 1.77 1.78 1.79 1.80 1.81 1.82 1.83 1.84 1.85 1.86 1.87 1.88 1.89 1.90
1.91 1.92 1.93 1.94 1.95 1.96 1.97 1.98 1.99 2.00 2.01 2.02 2.03 2.04 2.05
2.06 2.07 2.08 2.09 2.10 2.11 2.12 2.13 2.14 2.15 2.16 2.17 2.18 2.19 2.20
2.21 2.22 2.23 2.24 2.25 2.26 2.27 2.28 2.29 2.30 2.31 2.32 2.33 2.34 2.35
2.36 2.37 2.38 2.39 2.40 2.41 2.42 2.43 2.44 2.45 2.46 2.47 2.48 2.49 2.50
2.51 2.52 2.53 2.54 2.55 2.56 2.57 2.58 2.59 2.60 2.61 2.62 2.63 2.64 2.65
2.66 2.67 2.68 2.69 2.70 2.71 2.72 2.73 2.74 2.75 2.76 2.77 2.78 2.79 2.80
2.81 2.82 2.83 2.84 2.85 2.86 2.87 2.88 2.89 2.90 2.91 2.92 2.93 2.94 2.95
2.96 2.97 2.98 2.99 3.00 3.01 3.02 3.03 3.04 3.05 3.06 3.07 3.08 3.09 3.10
3.11 3.12 3.13 3.14 3.15 3.16 3.17 3.18 3.19 3.20 3.21 3.22 3.23 3.24 3.25
3.26 3.27 3.28 3.29 3.30 3.31 3.32 3.33 3.34 3.35 3.36 3.37 3.38 3.39 3.40
3.41 3.42 3.43 3.44 3.45 3.46 3.47 3.48 3.49 3.50 3.51 3.52 3.53 3.54 3.55
3.56 3.57 3.58 3.59 3.60 3.61 3.62 3.63 3.64 3.65 3.66 3.67 3.68 3.69 3.70
3.71 3.72 3.73 3.74 3.75 3.76 3.77 3.78 3.79 3.80 3.81 3.82 3.83 3.84 3.85
3.86 3.87 3.88 3.89 3.90 3.91 3.92 3.93 3.94 3.95 3.96 3.97 3.98 3.99 4.00
4.01 4.02 4.03 4.04 4.05 4.06 4.07 4.08 4.09 4.10 4.11 4.12 4.13 4.14 4.15
4.16 4.17 4.18 4.19 4.20 4.21 4.22 4.23 4.24 4.25 4.26 4.27 4.28 4.29 4.30
4.31 4.32 4.33 4.34 4.35 4.36 4.37 4.38 4.39 4.40 4.41 4.42 4.43 4.44 4.45
4.46 4.47 4.48 4.49 4.50 4.51 4.52 4.53 4.54 4.55 4.56 4.57 4.58 4.59 4.60
4.61 4.62 4.63 4.64 4.65 4.66 4.67 4.68 4.69 4.70 4.71 4.72 4.73 4.74 4.75
4.76 4.77 4.78 4.79 4.80 4.81 4.82 4.83 4.84 4.85 4.86 4.87 4.88 4.89 4.90

4.91 4.92 4.93 4.94 4.95 4.96 4.97 4.98 4.99 5.00 5.01 5.02 5.03 5.04 5.05
5.06 5.07 5.08 5.09 5.10 5.11 5.12 5.13 5.14 5.15 5.16 5.17 5.18 5.19 5.20
5.21 5.22 5.23 5.24 5.25 5.26 5.27 5.28 5.29 5.30 5.31 5.32 5.33 5.34 5.35
5.36 5.37 5.38 5.39 5.40 5.41 5.42 5.43 5.44 5.45 5.46 5.47 5.48 5.49 5.50
5.51 5.52 5.53 5.54 5.55 5.56 5.57 5.58 5.59 5.60 5.61 5.62 5.63 5.64 5.65
5.66 5.67 5.68 5.69 5.70 5.71 5.72 5.73 5.74 5.75 5.76 5.77 5.78 5.79 5.80
5.81 5.82 5.83 5.84 5.85 5.86 5.87 5.88 5.89 5.90 5.91 5.92 5.93 5.94 5.95
5.96 5.97 5.98 5.99 6.00 6.01 6.02 6.03 6.04 6.05 6.06 6.07 6.08 6.09 6.10
6.11 6.12 6.13 6.14 6.15 6.16 6.17 6.18 6.19 6.20 6.21 6.22 6.23 6.24 6.25
6.26 6.27 6.28 6.29 6.30 6.31 6.32 6.33 6.34 6.35 6.36 6.37 6.38 6.39 6.40
6.41 6.42 6.43 6.44 6.45
F28:p 11
E28 0 1e-10 0.01 0.02 0.03 0.04 0.05 0.06 0.07 0.08 0.09 0.10 0.11 0.12 0.13
0.14 0.15 0.16 0.17 0.18 0.19 0.20 0.21 0.22 0.23 0.24 0.25 0.26 0.27 0.28
0.29 0.30 0.31 0.32 0.33 0.34 0.35 0.36 0.37 0.38 0.39 0.4 0.41 0.42 0.43
0.44 0.45 0.46 0.47 0.48 0.49 0.50 0.51 0.52 0.53 0.54 0.55 0.56 0.57
0.58 0.59 0.60 0.61 0.62 0.63 0.64 0.65 0.66 0.67 0.68 0.69 0.70 0.71
0.72 0.73 0.74 0.75 0.76 0.77 0.78 0.79 0.80 0.81 0.82 0.83 0.84 0.85
0.86 0.87 0.88 0.89 0.90 0.91 0.92 0.93 0.94 0.95 0.96 0.97 0.98 0.99 1.00
1.01 1.02 1.03 1.04 1.05 1.06 1.07 1.08 1.09 1.10 1.11 1.12 1.13 1.14 1.15
1.16 1.17 1.18 1.19 1.20 1.21 1.22 1.23 1.24 1.25 1.26 1.27 1.28 1.29 1.30
1.31 1.32 1.33 1.34 1.35 1.36 1.37 1.38 1.39 1.40 1.41 1.42 1.43 1.44 1.45
1.46 1.47 1.48 1.49 1.50 1.51 1.52 1.53 1.54 1.55 1.56 1.57 1.58 1.59 1.60
1.61 1.62 1.63 1.64 1.65 1.66 1.67 1.68 1.69 1.70 1.71 1.72 1.73 1.74 1.75
1.76 1.77 1.78 1.79 1.80 1.81 1.82 1.83 1.84 1.85 1.86 1.87 1.88 1.89 1.90
1.91 1.92 1.93 1.94 1.95 1.96 1.97 1.98 1.99 2.00 2.01 2.02 2.03 2.04 2.05
2.06 2.07 2.08 2.09 2.10 2.11 2.12 2.13 2.14 2.15 2.16 2.17 2.18 2.19 2.20
2.21 2.22 2.23 2.24 2.25 2.26 2.27 2.28 2.29 2.30 2.31 2.32 2.33 2.34 2.35
2.36 2.37 2.38 2.39 2.40 2.41 2.42 2.43 2.44 2.45 2.46 2.47 2.48 2.49 2.50
2.51 2.52 2.53 2.54 2.55 2.56 2.57 2.58 2.59 2.60 2.61 2.62 2.63 2.64 2.65
2.66 2.67 2.68 2.69 2.70 2.71 2.72 2.73 2.74 2.75 2.76 2.77 2.78 2.79 2.80
2.81 2.82 2.83 2.84 2.85 2.86 2.87 2.88 2.89 2.90 2.91 2.92 2.93 2.94 2.95
2.96 2.97 2.98 2.99 3.00 3.01 3.02 3.03 3.04 3.05 3.06 3.07 3.08 3.09 3.10
3.11 3.12 3.13 3.14 3.15 3.16 3.17 3.18 3.19 3.20 3.21 3.22 3.23 3.24 3.25
3.26 3.27 3.28 3.29 3.30 3.31 3.32 3.33 3.34 3.35 3.36 3.37 3.38 3.39 3.40
3.41 3.42 3.43 3.44 3.45 3.46 3.47 3.48 3.49 3.50 3.51 3.52 3.53 3.54 3.55
3.56 3.57 3.58 3.59 3.60 3.61 3.62 3.63 3.64 3.65 3.66 3.67 3.68 3.69 3.70
3.71 3.72 3.73 3.74 3.75 3.76 3.77 3.78 3.79 3.80 3.81 3.82 3.83 3.84 3.85
3.86 3.87 3.88 3.89 3.90 3.91 3.92 3.93 3.94 3.95 3.96 3.97 3.98 3.99 4.00
4.01 4.02 4.03 4.04 4.05 4.06 4.07 4.08 4.09 4.10 4.11 4.12 4.13 4.14 4.15
4.16 4.17 4.18 4.19 4.20 4.21 4.22 4.23 4.24 4.25 4.26 4.27 4.28 4.29 4.30
4.31 4.32 4.33 4.34 4.35 4.36 4.37 4.38 4.39 4.40 4.41 4.42 4.43 4.44 4.45
4.46 4.47 4.48 4.49 4.50 4.51 4.52 4.53 4.54 4.55 4.56 4.57 4.58 4.59 4.60
4.61 4.62 4.63 4.64 4.65 4.66 4.67 4.68 4.69 4.70 4.71 4.72 4.73 4.74 4.75
4.76 4.77 4.78 4.79 4.80 4.81 4.82 4.83 4.84 4.85 4.86 4.87 4.88 4.89 4.90
4.91 4.92 4.93 4.94 4.95 4.96 4.97 4.98 4.99 5.00 5.01 5.02 5.03 5.04 5.05
5.06 5.07 5.08 5.09 5.10 5.11 5.12 5.13 5.14 5.15 5.16 5.17 5.18 5.19 5.20
5.21 5.22 5.23 5.24 5.25 5.26 5.27 5.28 5.29 5.30 5.31 5.32 5.33 5.34 5.35

5.36 5.37 5.38 5.39 5.40 5.41 5.42 5.43 5.44 5.45 5.46 5.47 5.48 5.49 5.50
5.51 5.52 5.53 5.54 5.55 5.56 5.57 5.58 5.59 5.60 5.61 5.62 5.63 5.64 5.65
5.66 5.67 5.68 5.69 5.70 5.71 5.72 5.73 5.74 5.75 5.76 5.77 5.78 5.79 5.80
5.81 5.82 5.83 5.84 5.85 5.86 5.87 5.88 5.89 5.90 5.91 5.92 5.93 5.94 5.95
5.96 5.97 5.98 5.99 6.00 6.01 6.02 6.03 6.04 6.05 6.06 6.07 6.08 6.09 6.10
6.11 6.12 6.13 6.14 6.15 6.16 6.17 6.18 6.19 6.20 6.21 6.22 6.23 6.24 6.25
6.26 6.27 6.28 6.29 6.30 6.31 6.32 6.33 6.34 6.35 6.36 6.37 6.38 6.39 6.40
6.41 6.42 6.43 6.44 6.45
F38:p 15
E38 0 1e-10 0.01 0.02 0.03 0.04 0.05 0.06 0.07 0.08 0.09 0.10 0.11 0.12 0.13
0.14 0.15 0.16 0.17 0.18 0.19 0.20 0.21 0.22 0.23 0.24 0.25 0.26 0.27 0.28
0.29 0.30 0.31 0.32 0.33 0.34 0.35 0.36 0.37 0.38 0.39 0.4 0.41 0.42 0.43
0.44 0.45 0.46 0.47 0.48 0.49 0.50 0.51 0.52 0.53 0.54 0.55 0.56 0.57
0.58 0.59 0.60 0.61 0.62 0.63 0.64 0.65 0.66 0.67 0.68 0.69 0.70 0.71
0.72 0.73 0.74 0.75 0.76 0.77 0.78 0.79 0.80 0.81 0.82 0.83 0.84 0.85
0.86 0.87 0.88 0.89 0.90 0.91 0.92 0.93 0.94 0.95 0.96 0.97 0.98 0.99 1.00
1.01 1.02 1.03 1.04 1.05 1.06 1.07 1.08 1.09 1.10 1.11 1.12 1.13 1.14 1.15
1.16 1.17 1.18 1.19 1.20 1.21 1.22 1.23 1.24 1.25 1.26 1.27 1.28 1.29 1.30
1.31 1.32 1.33 1.34 1.35 1.36 1.37 1.38 1.39 1.40 1.41 1.42 1.43 1.44 1.45
1.46 1.47 1.48 1.49 1.50 1.51 1.52 1.53 1.54 1.55 1.56 1.57 1.58 1.59 1.60
1.61 1.62 1.63 1.64 1.65 1.66 1.67 1.68 1.69 1.70 1.71 1.72 1.73 1.74 1.75
1.76 1.77 1.78 1.79 1.80 1.81 1.82 1.83 1.84 1.85 1.86 1.87 1.88 1.89 1.90
1.91 1.92 1.93 1.94 1.95 1.96 1.97 1.98 1.99 2.00 2.01 2.02 2.03 2.04 2.05
2.06 2.07 2.08 2.09 2.10 2.11 2.12 2.13 2.14 2.15 2.16 2.17 2.18 2.19 2.20
2.21 2.22 2.23 2.24 2.25 2.26 2.27 2.28 2.29 2.30 2.31 2.32 2.33 2.34 2.35
2.36 2.37 2.38 2.39 2.40 2.41 2.42 2.43 2.44 2.45 2.46 2.47 2.48 2.49 2.50
2.51 2.52 2.53 2.54 2.55 2.56 2.57 2.58 2.59 2.60 2.61 2.62 2.63 2.64 2.65
2.66 2.67 2.68 2.69 2.70 2.71 2.72 2.73 2.74 2.75 2.76 2.77 2.78 2.79 2.80
2.81 2.82 2.83 2.84 2.85 2.86 2.87 2.88 2.89 2.90 2.91 2.92 2.93 2.94 2.95
2.96 2.97 2.98 2.99 3.00 3.01 3.02 3.03 3.04 3.05 3.06 3.07 3.08 3.09 3.10
3.11 3.12 3.13 3.14 3.15 3.16 3.17 3.18 3.19 3.20 3.21 3.22 3.23 3.24 3.25
3.26 3.27 3.28 3.29 3.30 3.31 3.32 3.33 3.34 3.35 3.36 3.37 3.38 3.39 3.40
3.41 3.42 3.43 3.44 3.45 3.46 3.47 3.48 3.49 3.50 3.51 3.52 3.53 3.54 3.55
3.56 3.57 3.58 3.59 3.60 3.61 3.62 3.63 3.64 3.65 3.66 3.67 3.68 3.69 3.70
3.71 3.72 3.73 3.74 3.75 3.76 3.77 3.78 3.79 3.80 3.81 3.82 3.83 3.84 3.85
3.86 3.87 3.88 3.89 3.90 3.91 3.92 3.93 3.94 3.95 3.96 3.97 3.98 3.99 4.00
4.01 4.02 4.03 4.04 4.05 4.06 4.07 4.08 4.09 4.10 4.11 4.12 4.13 4.14 4.15
4.16 4.17 4.18 4.19 4.20 4.21 4.22 4.23 4.24 4.25 4.26 4.27 4.28 4.29 4.30
4.31 4.32 4.33 4.34 4.35 4.36 4.37 4.38 4.39 4.40 4.41 4.42 4.43 4.44 4.45
4.46 4.47 4.48 4.49 4.50 4.51 4.52 4.53 4.54 4.55 4.56 4.57 4.58 4.59 4.60
4.61 4.62 4.63 4.64 4.65 4.66 4.67 4.68 4.69 4.70 4.71 4.72 4.73 4.74 4.75
4.76 4.77 4.78 4.79 4.80 4.81 4.82 4.83 4.84 4.85 4.86 4.87 4.88 4.89 4.90
4.91 4.92 4.93 4.94 4.95 4.96 4.97 4.98 4.99 5.00 5.01 5.02 5.03 5.04 5.05
5.06 5.07 5.08 5.09 5.10 5.11 5.12 5.13 5.14 5.15 5.16 5.17 5.18 5.19 5.20
5.21 5.22 5.23 5.24 5.25 5.26 5.27 5.28 5.29 5.30 5.31 5.32 5.33 5.34 5.35
5.36 5.37 5.38 5.39 5.40 5.41 5.42 5.43 5.44 5.45 5.46 5.47 5.48 5.49 5.50
5.51 5.52 5.53 5.54 5.55 5.56 5.57 5.58 5.59 5.60 5.61 5.62 5.63 5.64 5.65
5.66 5.67 5.68 5.69 5.70 5.71 5.72 5.73 5.74 5.75 5.76 5.77 5.78 5.79 5.80

5.81 5.82 5.83 5.84 5.85 5.86 5.87 5.88 5.89 5.90 5.91 5.92 5.93 5.94 5.95
5.96 5.97 5.98 5.99 6.00 6.01 6.02 6.03 6.04 6.05 6.06 6.07 6.08 6.09 6.10
6.11 6.12 6.13 6.14 6.15 6.16 6.17 6.18 6.19 6.20 6.21 6.22 6.23 6.24 6.25
6.26 6.27 6.28 6.29 6.30 6.31 6.32 6.33 6.34 6.35 6.36 6.37 6.38 6.39 6.40
6.41 6.42 6.43 6.44 6.45
F48:p 19
E48 0 1e-10 0.01 0.02 0.03 0.04 0.05 0.06 0.07 0.08 0.09 0.10 0.11 0.12 0.13
0.14 0.15 0.16 0.17 0.18 0.19 0.20 0.21 0.22 0.23 0.24 0.25 0.26 0.27 0.28
0.29 0.30 0.31 0.32 0.33 0.34 0.35 0.36 0.37 0.38 0.39 0.4 0.41 0.42 0.43
0.44 0.45 0.46 0.47 0.48 0.49 0.50 0.51 0.52 0.53 0.54 0.55 0.56 0.57
0.58 0.59 0.60 0.61 0.62 0.63 0.64 0.65 0.66 0.67 0.68 0.69 0.70 0.71
0.72 0.73 0.74 0.75 0.76 0.77 0.78 0.79 0.80 0.81 0.82 0.83 0.84 0.85
0.86 0.87 0.88 0.89 0.90 0.91 0.92 0.93 0.94 0.95 0.96 0.97 0.98 0.99 1.00
1.01 1.02 1.03 1.04 1.05 1.06 1.07 1.08 1.09 1.10 1.11 1.12 1.13 1.14 1.15
1.16 1.17 1.18 1.19 1.20 1.21 1.22 1.23 1.24 1.25 1.26 1.27 1.28 1.29 1.30
1.31 1.32 1.33 1.34 1.35 1.36 1.37 1.38 1.39 1.40 1.41 1.42 1.43 1.44 1.45
1.46 1.47 1.48 1.49 1.50 1.51 1.52 1.53 1.54 1.55 1.56 1.57 1.58 1.59 1.60
1.61 1.62 1.63 1.64 1.65 1.66 1.67 1.68 1.69 1.70 1.71 1.72 1.73 1.74 1.75
1.76 1.77 1.78 1.79 1.80 1.81 1.82 1.83 1.84 1.85 1.86 1.87 1.88 1.89 1.90
1.91 1.92 1.93 1.94 1.95 1.96 1.97 1.98 1.99 2.00 2.01 2.02 2.03 2.04 2.05
2.06 2.07 2.08 2.09 2.10 2.11 2.12 2.13 2.14 2.15 2.16 2.17 2.18 2.19 2.20
2.21 2.22 2.23 2.24 2.25 2.26 2.27 2.28 2.29 2.30 2.31 2.32 2.33 2.34 2.35
2.36 2.37 2.38 2.39 2.40 2.41 2.42 2.43 2.44 2.45 2.46 2.47 2.48 2.49 2.50
2.51 2.52 2.53 2.54 2.55 2.56 2.57 2.58 2.59 2.60 2.61 2.62 2.63 2.64 2.65
2.66 2.67 2.68 2.69 2.70 2.71 2.72 2.73 2.74 2.75 2.76 2.77 2.78 2.79 2.80
2.81 2.82 2.83 2.84 2.85 2.86 2.87 2.88 2.89 2.90 2.91 2.92 2.93 2.94 2.95
2.96 2.97 2.98 2.99 3.00 3.01 3.02 3.03 3.04 3.05 3.06 3.07 3.08 3.09 3.10
3.11 3.12 3.13 3.14 3.15 3.16 3.17 3.18 3.19 3.20 3.21 3.22 3.23 3.24 3.25
3.26 3.27 3.28 3.29 3.30 3.31 3.32 3.33 3.34 3.35 3.36 3.37 3.38 3.39 3.40
3.41 3.42 3.43 3.44 3.45 3.46 3.47 3.48 3.49 3.50 3.51 3.52 3.53 3.54 3.55
3.56 3.57 3.58 3.59 3.60 3.61 3.62 3.63 3.64 3.65 3.66 3.67 3.68 3.69 3.70
3.71 3.72 3.73 3.74 3.75 3.76 3.77 3.78 3.79 3.80 3.81 3.82 3.83 3.84 3.85
3.86 3.87 3.88 3.89 3.90 3.91 3.92 3.93 3.94 3.95 3.96 3.97 3.98 3.99 4.00
4.01 4.02 4.03 4.04 4.05 4.06 4.07 4.08 4.09 4.10 4.11 4.12 4.13 4.14 4.15
4.16 4.17 4.18 4.19 4.20 4.21 4.22 4.23 4.24 4.25 4.26 4.27 4.28 4.29 4.30
4.31 4.32 4.33 4.34 4.35 4.36 4.37 4.38 4.39 4.40 4.41 4.42 4.43 4.44 4.45
4.46 4.47 4.48 4.49 4.50 4.51 4.52 4.53 4.54 4.55 4.56 4.57 4.58 4.59 4.60
4.61 4.62 4.63 4.64 4.65 4.66 4.67 4.68 4.69 4.70 4.71 4.72 4.73 4.74 4.75
4.76 4.77 4.78 4.79 4.80 4.81 4.82 4.83 4.84 4.85 4.86 4.87 4.88 4.89 4.90
4.91 4.92 4.93 4.94 4.95 4.96 4.97 4.98 4.99 5.00 5.01 5.02 5.03 5.04 5.05
5.06 5.07 5.08 5.09 5.10 5.11 5.12 5.13 5.14 5.15 5.16 5.17 5.18 5.19 5.20
5.21 5.22 5.23 5.24 5.25 5.26 5.27 5.28 5.29 5.30 5.31 5.32 5.33 5.34 5.35
5.36 5.37 5.38 5.39 5.40 5.41 5.42 5.43 5.44 5.45 5.46 5.47 5.48 5.49 5.50
5.51 5.52 5.53 5.54 5.55 5.56 5.57 5.58 5.59 5.60 5.61 5.62 5.63 5.64 5.65
5.66 5.67 5.68 5.69 5.70 5.71 5.72 5.73 5.74 5.75 5.76 5.77 5.78 5.79 5.80
5.81 5.82 5.83 5.84 5.85 5.86 5.87 5.88 5.89 5.90 5.91 5.92 5.93 5.94 5.95
5.96 5.97 5.98 5.99 6.00 6.01 6.02 6.03 6.04 6.05 6.06 6.07 6.08 6.09 6.10
6.11 6.12 6.13 6.14 6.15 6.16 6.17 6.18 6.19 6.20 6.21 6.22 6.23 6.24 6.25

6.26 6.27 6.28 6.29 6.30 6.31 6.32 6.33 6.34 6.35 6.36 6.37 6.38 6.39 6.40
6.41 6.42 6.43 6.44 6.45
F58:p 23
E58 0 1e-10 0.01 0.02 0.03 0.04 0.05 0.06 0.07 0.08 0.09 0.10 0.11 0.12 0.13
0.14 0.15 0.16 0.17 0.18 0.19 0.20 0.21 0.22 0.23 0.24 0.25 0.26 0.27 0.28
0.29 0.30 0.31 0.32 0.33 0.34 0.35 0.36 0.37 0.38 0.39 0.4 0.41 0.42 0.43
0.44 0.45 0.46 0.47 0.48 0.49 0.50 0.51 0.52 0.53 0.54 0.55 0.56 0.57
0.58 0.59 0.60 0.61 0.62 0.63 0.64 0.65 0.66 0.67 0.68 0.69 0.70 0.71
0.72 0.73 0.74 0.75 0.76 0.77 0.78 0.79 0.80 0.81 0.82 0.83 0.84 0.85
0.86 0.87 0.88 0.89 0.90 0.91 0.92 0.93 0.94 0.95 0.96 0.97 0.98 0.99 1.00
1.01 1.02 1.03 1.04 1.05 1.06 1.07 1.08 1.09 1.10 1.11 1.12 1.13 1.14 1.15
1.16 1.17 1.18 1.19 1.20 1.21 1.22 1.23 1.24 1.25 1.26 1.27 1.28 1.29 1.30
1.31 1.32 1.33 1.34 1.35 1.36 1.37 1.38 1.39 1.40 1.41 1.42 1.43 1.44 1.45
1.46 1.47 1.48 1.49 1.50 1.51 1.52 1.53 1.54 1.55 1.56 1.57 1.58 1.59 1.60
1.61 1.62 1.63 1.64 1.65 1.66 1.67 1.68 1.69 1.70 1.71 1.72 1.73 1.74 1.75
1.76 1.77 1.78 1.79 1.80 1.81 1.82 1.83 1.84 1.85 1.86 1.87 1.88 1.89 1.90
1.91 1.92 1.93 1.94 1.95 1.96 1.97 1.98 1.99 2.00 2.01 2.02 2.03 2.04 2.05
2.06 2.07 2.08 2.09 2.10 2.11 2.12 2.13 2.14 2.15 2.16 2.17 2.18 2.19 2.20
2.21 2.22 2.23 2.24 2.25 2.26 2.27 2.28 2.29 2.30 2.31 2.32 2.33 2.34 2.35
2.36 2.37 2.38 2.39 2.40 2.41 2.42 2.43 2.44 2.45 2.46 2.47 2.48 2.49 2.50
2.51 2.52 2.53 2.54 2.55 2.56 2.57 2.58 2.59 2.60 2.61 2.62 2.63 2.64 2.65
2.66 2.67 2.68 2.69 2.70 2.71 2.72 2.73 2.74 2.75 2.76 2.77 2.78 2.79 2.80
2.81 2.82 2.83 2.84 2.85 2.86 2.87 2.88 2.89 2.90 2.91 2.92 2.93 2.94 2.95
2.96 2.97 2.98 2.99 3.00 3.01 3.02 3.03 3.04 3.05 3.06 3.07 3.08 3.09 3.10
3.11 3.12 3.13 3.14 3.15 3.16 3.17 3.18 3.19 3.20 3.21 3.22 3.23 3.24 3.25
3.26 3.27 3.28 3.29 3.30 3.31 3.32 3.33 3.34 3.35 3.36 3.37 3.38 3.39 3.40
3.41 3.42 3.43 3.44 3.45 3.46 3.47 3.48 3.49 3.50 3.51 3.52 3.53 3.54 3.55
3.56 3.57 3.58 3.59 3.60 3.61 3.62 3.63 3.64 3.65 3.66 3.67 3.68 3.69 3.70
3.71 3.72 3.73 3.74 3.75 3.76 3.77 3.78 3.79 3.80 3.81 3.82 3.83 3.84 3.85
3.86 3.87 3.88 3.89 3.90 3.91 3.92 3.93 3.94 3.95 3.96 3.97 3.98 3.99 4.00
4.01 4.02 4.03 4.04 4.05 4.06 4.07 4.08 4.09 4.10 4.11 4.12 4.13 4.14 4.15
4.16 4.17 4.18 4.19 4.20 4.21 4.22 4.23 4.24 4.25 4.26 4.27 4.28 4.29 4.30
4.31 4.32 4.33 4.34 4.35 4.36 4.37 4.38 4.39 4.40 4.41 4.42 4.43 4.44 4.45
4.46 4.47 4.48 4.49 4.50 4.51 4.52 4.53 4.54 4.55 4.56 4.57 4.58 4.59 4.60
4.61 4.62 4.63 4.64 4.65 4.66 4.67 4.68 4.69 4.70 4.71 4.72 4.73 4.74 4.75
4.76 4.77 4.78 4.79 4.80 4.81 4.82 4.83 4.84 4.85 4.86 4.87 4.88 4.89 4.90
4.91 4.92 4.93 4.94 4.95 4.96 4.97 4.98 4.99 5.00 5.01 5.02 5.03 5.04 5.05
5.06 5.07 5.08 5.09 5.10 5.11 5.12 5.13 5.14 5.15 5.16 5.17 5.18 5.19 5.20
5.21 5.22 5.23 5.24 5.25 5.26 5.27 5.28 5.29 5.30 5.31 5.32 5.33 5.34 5.35
5.36 5.37 5.38 5.39 5.40 5.41 5.42 5.43 5.44 5.45 5.46 5.47 5.48 5.49 5.50
5.51 5.52 5.53 5.54 5.55 5.56 5.57 5.58 5.59 5.60 5.61 5.62 5.63 5.64 5.65
5.66 5.67 5.68 5.69 5.70 5.71 5.72 5.73 5.74 5.75 5.76 5.77 5.78 5.79 5.80
5.81 5.82 5.83 5.84 5.85 5.86 5.87 5.88 5.89 5.90 5.91 5.92 5.93 5.94 5.95
5.96 5.97 5.98 5.99 6.00 6.01 6.02 6.03 6.04 6.05 6.06 6.07 6.08 6.09 6.10
6.11 6.12 6.13 6.14 6.15 6.16 6.17 6.18 6.19 6.20 6.21 6.22 6.23 6.24 6.25
6.26 6.27 6.28 6.29 6.30 6.31 6.32 6.33 6.34 6.35 6.36 6.37 6.38 6.39 6.40
6.41 6.42 6.43 6.44 6.45
F68:p 27

E68 0 1e-10 0.01 0.02 0.03 0.04 0.05 0.06 0.07 0.08 0.09 0.10 0.11 0.12 0.13
0.14 0.15 0.16 0.17 0.18 0.19 0.20 0.21 0.22 0.23 0.24 0.25 0.26 0.27 0.28
0.29 0.30 0.31 0.32 0.33 0.34 0.35 0.36 0.37 0.38 0.39 0.4 0.41 0.42 0.43
0.44 0.45 0.46 0.47 0.48 0.49 0.50 0.51 0.52 0.53 0.54 0.55 0.56 0.57
0.58 0.59 0.60 0.61 0.62 0.63 0.64 0.65 0.66 0.67 0.68 0.69 0.70 0.71
0.72 0.73 0.74 0.75 0.76 0.77 0.78 0.79 0.80 0.81 0.82 0.83 0.84 0.85
0.86 0.87 0.88 0.89 0.90 0.91 0.92 0.93 0.94 0.95 0.96 0.97 0.98 0.99 1.00
1.01 1.02 1.03 1.04 1.05 1.06 1.07 1.08 1.09 1.10 1.11 1.12 1.13 1.14 1.15
1.16 1.17 1.18 1.19 1.20 1.21 1.22 1.23 1.24 1.25 1.26 1.27 1.28 1.29 1.30
1.31 1.32 1.33 1.34 1.35 1.36 1.37 1.38 1.39 1.40 1.41 1.42 1.43 1.44 1.45
1.46 1.47 1.48 1.49 1.50 1.51 1.52 1.53 1.54 1.55 1.56 1.57 1.58 1.59 1.60
1.61 1.62 1.63 1.64 1.65 1.66 1.67 1.68 1.69 1.70 1.71 1.72 1.73 1.74 1.75
1.76 1.77 1.78 1.79 1.80 1.81 1.82 1.83 1.84 1.85 1.86 1.87 1.88 1.89 1.90
1.91 1.92 1.93 1.94 1.95 1.96 1.97 1.98 1.99 2.00 2.01 2.02 2.03 2.04 2.05
2.06 2.07 2.08 2.09 2.10 2.11 2.12 2.13 2.14 2.15 2.16 2.17 2.18 2.19 2.20
2.21 2.22 2.23 2.24 2.25 2.26 2.27 2.28 2.29 2.30 2.31 2.32 2.33 2.34 2.35
2.36 2.37 2.38 2.39 2.40 2.41 2.42 2.43 2.44 2.45 2.46 2.47 2.48 2.49 2.50
2.51 2.52 2.53 2.54 2.55 2.56 2.57 2.58 2.59 2.60 2.61 2.62 2.63 2.64 2.65
2.66 2.67 2.68 2.69 2.70 2.71 2.72 2.73 2.74 2.75 2.76 2.77 2.78 2.79 2.80
2.81 2.82 2.83 2.84 2.85 2.86 2.87 2.88 2.89 2.90 2.91 2.92 2.93 2.94 2.95
2.96 2.97 2.98 2.99 3.00 3.01 3.02 3.03 3.04 3.05 3.06 3.07 3.08 3.09 3.10
3.11 3.12 3.13 3.14 3.15 3.16 3.17 3.18 3.19 3.20 3.21 3.22 3.23 3.24 3.25
3.26 3.27 3.28 3.29 3.30 3.31 3.32 3.33 3.34 3.35 3.36 3.37 3.38 3.39 3.40
3.41 3.42 3.43 3.44 3.45 3.46 3.47 3.48 3.49 3.50 3.51 3.52 3.53 3.54 3.55
3.56 3.57 3.58 3.59 3.60 3.61 3.62 3.63 3.64 3.65 3.66 3.67 3.68 3.69 3.70
3.71 3.72 3.73 3.74 3.75 3.76 3.77 3.78 3.79 3.80 3.81 3.82 3.83 3.84 3.85
3.86 3.87 3.88 3.89 3.90 3.91 3.92 3.93 3.94 3.95 3.96 3.97 3.98 3.99 4.00
4.01 4.02 4.03 4.04 4.05 4.06 4.07 4.08 4.09 4.10 4.11 4.12 4.13 4.14 4.15
4.16 4.17 4.18 4.19 4.20 4.21 4.22 4.23 4.24 4.25 4.26 4.27 4.28 4.29 4.30
4.31 4.32 4.33 4.34 4.35 4.36 4.37 4.38 4.39 4.40 4.41 4.42 4.43 4.44 4.45
4.46 4.47 4.48 4.49 4.50 4.51 4.52 4.53 4.54 4.55 4.56 4.57 4.58 4.59 4.60
4.61 4.62 4.63 4.64 4.65 4.66 4.67 4.68 4.69 4.70 4.71 4.72 4.73 4.74 4.75
4.76 4.77 4.78 4.79 4.80 4.81 4.82 4.83 4.84 4.85 4.86 4.87 4.88 4.89 4.90
4.91 4.92 4.93 4.94 4.95 4.96 4.97 4.98 4.99 5.00 5.01 5.02 5.03 5.04 5.05
5.06 5.07 5.08 5.09 5.10 5.11 5.12 5.13 5.14 5.15 5.16 5.17 5.18 5.19 5.20
5.21 5.22 5.23 5.24 5.25 5.26 5.27 5.28 5.29 5.30 5.31 5.32 5.33 5.34 5.35
5.36 5.37 5.38 5.39 5.40 5.41 5.42 5.43 5.44 5.45 5.46 5.47 5.48 5.49 5.50
5.51 5.52 5.53 5.54 5.55 5.56 5.57 5.58 5.59 5.60 5.61 5.62 5.63 5.64 5.65
5.66 5.67 5.68 5.69 5.70 5.71 5.72 5.73 5.74 5.75 5.76 5.77 5.78 5.79 5.80
5.81 5.82 5.83 5.84 5.85 5.86 5.87 5.88 5.89 5.90 5.91 5.92 5.93 5.94 5.95
5.96 5.97 5.98 5.99 6.00 6.01 6.02 6.03 6.04 6.05 6.06 6.07 6.08 6.09 6.10
6.11 6.12 6.13 6.14 6.15 6.16 6.17 6.18 6.19 6.20 6.21 6.22 6.23 6.24 6.25
6.26 6.27 6.28 6.29 6.30 6.31 6.32 6.33 6.34 6.35 6.36 6.37 6.38 6.39 6.40
6.41 6.42 6.43 6.44 6.45
F78:p 31
E78 0 1e-10 0.01 0.02 0.03 0.04 0.05 0.06 0.07 0.08 0.09 0.10 0.11 0.12 0.13
0.14 0.15 0.16 0.17 0.18 0.19 0.20 0.21 0.22 0.23 0.24 0.25 0.26 0.27 0.28
0.29 0.30 0.31 0.32 0.33 0.34 0.35 0.36 0.37 0.38 0.39 0.4 0.41 0.42 0.43

0.44 0.45 0.46 0.47 0.48 0.49 0.50 0.51 0.52 0.53 0.54 0.55 0.56 0.57
0.58 0.59 0.60 0.61 0.62 0.63 0.64 0.65 0.66 0.67 0.68 0.69 0.70 0.71
0.72 0.73 0.74 0.75 0.76 0.77 0.78 0.79 0.80 0.81 0.82 0.83 0.84 0.85
0.86 0.87 0.88 0.89 0.90 0.91 0.92 0.93 0.94 0.95 0.96 0.97 0.98 0.99 1.00
1.01 1.02 1.03 1.04 1.05 1.06 1.07 1.08 1.09 1.10 1.11 1.12 1.13 1.14 1.15
1.16 1.17 1.18 1.19 1.20 1.21 1.22 1.23 1.24 1.25 1.26 1.27 1.28 1.29 1.30
1.31 1.32 1.33 1.34 1.35 1.36 1.37 1.38 1.39 1.40 1.41 1.42 1.43 1.44 1.45
1.46 1.47 1.48 1.49 1.50 1.51 1.52 1.53 1.54 1.55 1.56 1.57 1.58 1.59 1.60
1.61 1.62 1.63 1.64 1.65 1.66 1.67 1.68 1.69 1.70 1.71 1.72 1.73 1.74 1.75
1.76 1.77 1.78 1.79 1.80 1.81 1.82 1.83 1.84 1.85 1.86 1.87 1.88 1.89 1.90
1.91 1.92 1.93 1.94 1.95 1.96 1.97 1.98 1.99 2.00 2.01 2.02 2.03 2.04 2.05
2.06 2.07 2.08 2.09 2.10 2.11 2.12 2.13 2.14 2.15 2.16 2.17 2.18 2.19 2.20
2.21 2.22 2.23 2.24 2.25 2.26 2.27 2.28 2.29 2.30 2.31 2.32 2.33 2.34 2.35
2.36 2.37 2.38 2.39 2.40 2.41 2.42 2.43 2.44 2.45 2.46 2.47 2.48 2.49 2.50
2.51 2.52 2.53 2.54 2.55 2.56 2.57 2.58 2.59 2.60 2.61 2.62 2.63 2.64 2.65
2.66 2.67 2.68 2.69 2.70 2.71 2.72 2.73 2.74 2.75 2.76 2.77 2.78 2.79 2.80
2.81 2.82 2.83 2.84 2.85 2.86 2.87 2.88 2.89 2.90 2.91 2.92 2.93 2.94 2.95
2.96 2.97 2.98 2.99 3.00 3.01 3.02 3.03 3.04 3.05 3.06 3.07 3.08 3.09 3.10
3.11 3.12 3.13 3.14 3.15 3.16 3.17 3.18 3.19 3.20 3.21 3.22 3.23 3.24 3.25
3.26 3.27 3.28 3.29 3.30 3.31 3.32 3.33 3.34 3.35 3.36 3.37 3.38 3.39 3.40
3.41 3.42 3.43 3.44 3.45 3.46 3.47 3.48 3.49 3.50 3.51 3.52 3.53 3.54 3.55
3.56 3.57 3.58 3.59 3.60 3.61 3.62 3.63 3.64 3.65 3.66 3.67 3.68 3.69 3.70
3.71 3.72 3.73 3.74 3.75 3.76 3.77 3.78 3.79 3.80 3.81 3.82 3.83 3.84 3.85
3.86 3.87 3.88 3.89 3.90 3.91 3.92 3.93 3.94 3.95 3.96 3.97 3.98 3.99 4.00
4.01 4.02 4.03 4.04 4.05 4.06 4.07 4.08 4.09 4.10 4.11 4.12 4.13 4.14 4.15
4.16 4.17 4.18 4.19 4.20 4.21 4.22 4.23 4.24 4.25 4.26 4.27 4.28 4.29 4.30
4.31 4.32 4.33 4.34 4.35 4.36 4.37 4.38 4.39 4.40 4.41 4.42 4.43 4.44 4.45
4.46 4.47 4.48 4.49 4.50 4.51 4.52 4.53 4.54 4.55 4.56 4.57 4.58 4.59 4.60
4.61 4.62 4.63 4.64 4.65 4.66 4.67 4.68 4.69 4.70 4.71 4.72 4.73 4.74 4.75
4.76 4.77 4.78 4.79 4.80 4.81 4.82 4.83 4.84 4.85 4.86 4.87 4.88 4.89 4.90
4.91 4.92 4.93 4.94 4.95 4.96 4.97 4.98 4.99 5.00 5.01 5.02 5.03 5.04 5.05
5.06 5.07 5.08 5.09 5.10 5.11 5.12 5.13 5.14 5.15 5.16 5.17 5.18 5.19 5.20
5.21 5.22 5.23 5.24 5.25 5.26 5.27 5.28 5.29 5.30 5.31 5.32 5.33 5.34 5.35
5.36 5.37 5.38 5.39 5.40 5.41 5.42 5.43 5.44 5.45 5.46 5.47 5.48 5.49 5.50
5.51 5.52 5.53 5.54 5.55 5.56 5.57 5.58 5.59 5.60 5.61 5.62 5.63 5.64 5.65
5.66 5.67 5.68 5.69 5.70 5.71 5.72 5.73 5.74 5.75 5.76 5.77 5.78 5.79 5.80
5.81 5.82 5.83 5.84 5.85 5.86 5.87 5.88 5.89 5.90 5.91 5.92 5.93 5.94 5.95
5.96 5.97 5.98 5.99 6.00 6.01 6.02 6.03 6.04 6.05 6.06 6.07 6.08 6.09 6.10
6.11 6.12 6.13 6.14 6.15 6.16 6.17 6.18 6.19 6.20 6.21 6.22 6.23 6.24 6.25
6.26 6.27 6.28 6.29 6.30 6.31 6.32 6.33 6.34 6.35 6.36 6.37 6.38 6.39 6.40
6.41 6.42 6.43 6.44 6.45
F88:p 35
E88 0 1e-10 0.01 0.02 0.03 0.04 0.05 0.06 0.07 0.08 0.09 0.10 0.11 0.12 0.13
0.14 0.15 0.16 0.17 0.18 0.19 0.20 0.21 0.22 0.23 0.24 0.25 0.26 0.27 0.28
0.29 0.30 0.31 0.32 0.33 0.34 0.35 0.36 0.37 0.38 0.39 0.4 0.41 0.42 0.43
0.44 0.45 0.46 0.47 0.48 0.49 0.50 0.51 0.52 0.53 0.54 0.55 0.56 0.57
0.58 0.59 0.60 0.61 0.62 0.63 0.64 0.65 0.66 0.67 0.68 0.69 0.70 0.71
0.72 0.73 0.74 0.75 0.76 0.77 0.78 0.79 0.80 0.81 0.82 0.83 0.84 0.85

```
    0.86 0.87 0.88 0.89 0.90 0.91 0.92 0.93 0.94 0.95 0.96 0.97 0.98 0.99 1.00
    1.01 1.02 1.03 1.04 1.05 1.06 1.07 1.08 1.09 1.10 1.11 1.12 1.13 1.14 1.15
    1.16 1.17 1.18 1.19 1.20 1.21 1.22 1.23 1.24 1.25 1.26 1.27 1.28 1.29 1.30
    1.31 1.32 1.33 1.34 1.35 1.36 1.37 1.38 1.39 1.40 1.41 1.42 1.43 1.44 1.45
    1.46 1.47 1.48 1.49 1.50 1.51 1.52 1.53 1.54 1.55 1.56 1.57 1.58 1.59 1.60
    1.61 1.62 1.63 1.64 1.65 1.66 1.67 1.68 1.69 1.70 1.71 1.72 1.73 1.74 1.75
    1.76 1.77 1.78 1.79 1.80 1.81 1.82 1.83 1.84 1.85 1.86 1.87 1.88 1.89 1.90
    1.91 1.92 1.93 1.94 1.95 1.96 1.97 1.98 1.99 2.00 2.01 2.02 2.03 2.04 2.05
    2.06 2.07 2.08 2.09 2.10 2.11 2.12 2.13 2.14 2.15 2.16 2.17 2.18 2.19 2.20
    2.21 2.22 2.23 2.24 2.25 2.26 2.27 2.28 2.29 2.30 2.31 2.32 2.33 2.34 2.35
    2.36 2.37 2.38 2.39 2.40 2.41 2.42 2.43 2.44 2.45 2.46 2.47 2.48 2.49 2.50
    2.51 2.52 2.53 2.54 2.55 2.56 2.57 2.58 2.59 2.60 2.61 2.62 2.63 2.64 2.65
    2.66 2.67 2.68 2.69 2.70 2.71 2.72 2.73 2.74 2.75 2.76 2.77 2.78 2.79 2.80
    2.81 2.82 2.83 2.84 2.85 2.86 2.87 2.88 2.89 2.90 2.91 2.92 2.93 2.94 2.95
    2.96 2.97 2.98 2.99 3.00 3.01 3.02 3.03 3.04 3.05 3.06 3.07 3.08 3.09 3.10
    3.11 3.12 3.13 3.14 3.15 3.16 3.17 3.18 3.19 3.20 3.21 3.22 3.23 3.24 3.25
    3.26 3.27 3.28 3.29 3.30 3.31 3.32 3.33 3.34 3.35 3.36 3.37 3.38 3.39 3.40
    3.41 3.42 3.43 3.44 3.45 3.46 3.47 3.48 3.49 3.50 3.51 3.52 3.53 3.54 3.55
    3.56 3.57 3.58 3.59 3.60 3.61 3.62 3.63 3.64 3.65 3.66 3.67 3.68 3.69 3.70
    3.71 3.72 3.73 3.74 3.75 3.76 3.77 3.78 3.79 3.80 3.81 3.82 3.83 3.84 3.85
    3.86 3.87 3.88 3.89 3.90 3.91 3.92 3.93 3.94 3.95 3.96 3.97 3.98 3.99 4.00
    4.01 4.02 4.03 4.04 4.05 4.06 4.07 4.08 4.09 4.10 4.11 4.12 4.13 4.14 4.15
    4.16 4.17 4.18 4.19 4.20 4.21 4.22 4.23 4.24 4.25 4.26 4.27 4.28 4.29 4.30
    4.31 4.32 4.33 4.34 4.35 4.36 4.37 4.38 4.39 4.40 4.41 4.42 4.43 4.44 4.45
    4.46 4.47 4.48 4.49 4.50 4.51 4.52 4.53 4.54 4.55 4.56 4.57 4.58 4.59 4.60
    4.61 4.62 4.63 4.64 4.65 4.66 4.67 4.68 4.69 4.70 4.71 4.72 4.73 4.74 4.75
    4.76 4.77 4.78 4.79 4.80 4.81 4.82 4.83 4.84 4.85 4.86 4.87 4.88 4.89 4.90
    4.91 4.92 4.93 4.94 4.95 4.96 4.97 4.98 4.99 5.00 5.01 5.02 5.03 5.04 5.05
    5.06 5.07 5.08 5.09 5.10 5.11 5.12 5.13 5.14 5.15 5.16 5.17 5.18 5.19 5.20
    5.21 5.22 5.23 5.24 5.25 5.26 5.27 5.28 5.29 5.30 5.31 5.32 5.33 5.34 5.35
    5.36 5.37 5.38 5.39 5.40 5.41 5.42 5.43 5.44 5.45 5.46 5.47 5.48 5.49 5.50
    5.51 5.52 5.53 5.54 5.55 5.56 5.57 5.58 5.59 5.60 5.61 5.62 5.63 5.64 5.65
    5.66 5.67 5.68 5.69 5.70 5.71 5.72 5.73 5.74 5.75 5.76 5.77 5.78 5.79 5.80
    5.81 5.82 5.83 5.84 5.85 5.86 5.87 5.88 5.89 5.90 5.91 5.92 5.93 5.94 5.95
    5.96 5.97 5.98 5.99 6.00 6.01 6.02 6.03 6.04 6.05 6.06 6.07 6.08 6.09 6.10
    6.11 6.12 6.13 6.14 6.15 6.16 6.17 6.18 6.19 6.20 6.21 6.22 6.23 6.24 6.25
    6.26 6.27 6.28 6.29 6.30 6.31 6.32 6.33 6.34 6.35 6.36 6.37 6.38 6.39 6.40
    6.41 6.42 6.43 6.44 6.45
sdef   par=2 rad=d1 pos=-8.000 10.302 0 axs=0 0 1 erg=1.3320 ext=d2 cel=39
si1    h 0 1.945
sp1    -21 1
si2    0 6
sp2    -21 0
 m1     11000 1 53000 1 $ NaI (ignore Thallium doping)
m2     26000 1 $ steel
m3     8000 2 14000 1 $ Quartz
m4     1000 2 8000 1  $ Water
nps    1000000
```

APPENDIX B:

B1 Error Propagation for Absolute Efficiency Calculations

[Bevington & Robinson, 1992]

Chapter 3, section 3.1.2 deals with the calculation of the absolute efficiency of the HPGe detector used for the $^{152/154}$Eu and ^{226}Ra Point Source Measurements. The calculations for simple error propagation this section of chapter 3 are given below. The error in absolute efficiency, ε_{abs}, is given by:

$$\delta\varepsilon_{abs} = \left(\sqrt{\left(\frac{\delta count \quad rate}{count \quad rate} \right)^2 + \left(\frac{\delta emission \quad rate}{emission \quad rate} \right)^2} \right) * \quad \varepsilon_{abs} \qquad \text{Eq B1.1}$$

Where

$\delta count\ rate = \left(\frac{\delta counts}{counts} \right) * count\ rate$, and

$\delta emission\ rate = \left(\frac{\delta activity}{activity} \right) * Activity$, and

$\delta Activity = Uncertainty\ in\ Calibratin\ Source * Activity$

REFERENCES:

Agarwal, C. (2011). *Nondestructive Assay of Nuclear Materials by Gamma Ray Spectrometry,*

Alrefae, T., Nageswaran, T. N., & Al-Shemali, T. (2014). Radioactivity of long lived gamma emitters in canned seafood consumed in Kuwait. *Journal of the Association of Arab Universities for Basic and Applied Sciences, 15*, 6-9.

Bevington, P. R., & Robinson, D. K. (1969). *Data reduction and error analysis for the physical sciences* McGraw-Hill New York.

Briesmeister, J. F. (2000). MCNPTM-A general Monte Carlo N-particle transport code. *Version 4C, LA-13709-M, Los Alamos National Laboratory,*

Byun, S. H. (2007). *McMaster University Med Phys 4R06/6R03 lecture notes chapter 2: General properties of radiation detectors.* Retrieved 06/10, 2014, from http://www.science.mcmaster.ca/medphys/images/files/courses/4R06/4R6Notes2_General_Property.pdf

Byun, S. H., Prestwich, W. V., Chin, K., McNeill, F. E., & Chettle, D. R. (2004). Efficiency calibration and coincidence summing correction for a 4π NaI(tl) detector array. *Nuclear Instruments and Methods in Physics Research Section A: Accelerators, Spectrometers, Detectors and Associated Equipment, 535*(3), 674-685. doi:http://dx.doi.org/10.1016/j.nima.2004.06.174

Byun, S. H., Prestwich, W. V., Chin, K., McNeill, F. E., & Chettle, D. R. (2006). NaI(tl) detector array for in vivo neutron activation analysis. *Nuclear Science, IEEE Transactions on, 53*(5), 2944-2947. doi:10.1109/TNS.2006.880115

Chinnaesakki, S., Bara, S., Sartandel, S., Tripathi, R., & Puranik, V. (2012). Performance of HPGe gamma spectrometry system for the measurement of low level radioactivity. *Journal of Radioanalytical and Nuclear Chemistry*, *294*(1), 143-147.

Damon, R. W. (2005). *Determination of the Photopeak Detection Efficiency of a HPGe Detector, for Volume Sources, Via Monte Carlo Simulations,*

DARABAN, L., IANCU, D., NITA, D., & DARABAN, L. (2012). Efficiency calibration in gamma spectrometry by using 232th series radionuclides. Paper presented at the *Paper Presented at the First East European Radon Symposium–FERAS,*

Diab, H. M., & Abdellah, W. M. (2013). Validation of ^{226}Ra and ^{228}Ra measurements in water samples using gamma spectrometric analysis. *Journal of Water Resource and Protection, 5*, 53.

Faanu, A., Emi-Reynolds, G., Darko, E., Awudu, R., Glover, E., Adukpo, O., et al. (2011). Calibration and performance testing of sodium iodide, NaI(Tl), detector at the food and

environmental laboratory of the radiation protection institute of the Ghana atomic energy commission. *West African Journal of Applied Ecology, 19*(1)

Gilmore, G. (2011). *Practical gamma-ray spectroscopy* John Wiley & Sons.

Goldstein, S. J., & Stirling, C. H. (2003). Techniques for measuring uranium-series nuclides: 1992–2002. *Reviews in Mineralogy and Geochemistry, 52*(1), 23-57.

Hameed, P. S., Shaheed, K., Somasundaram, S., & Riyengar, M. (1997). Radium-226 levels in the Cauvery river ecosystem, India. *Journal of Biosciences, 22*(2), 225-231.

Harb, S., El-Kamel, A. H., Zahran, A. M., & Abbady, A. (2014). Assessment of natural radioactivity in soil and water samples from Aden governorate south of Yemen region. *International Journal of Recent Research in Physics and Chemical Sciences (IJRRPCS), 1*(1), April 2014 - June 2014.

Heath RL (1997) Scintillation spectrometry gamma-ray spectrum catalogue, *USAEC Report IDO-16880-1*, United States Atomic Energy Commission

Hou, X., & Roos, P. (2008). Critical comparison of radiometric and mass spectrometric methods for the determination of radionuclides in environmental, biological and nuclear waste samples. *Analytica Chimica Acta, 608*(2), 105-139.

Hubbell, J. H., & Seltzer, S. M. (1996). Tables of x-ray mass attenuation coefficients and mass energy-absorption coefficients. *National Institute of Standards and Technology,*

Hussein, E. M. (1997). *Monte Carlo particle transport with the MCNP code chapter 6: MCNP source parameters.* Unpublished manuscript.

Jabbar, A. (2011). *Measurement of environmental radioactivity and assessment of doses to the general public in Rechna Doab, Pakistan* Unpublished PhD, Comsats Institute of Information Technology, Islamabad, Pakistan.

Keyser, R. (2011). Performance and characteristics of a low-background germanium well detector for low-energy gamma-ray nuclides. doi:10.1039/9781849732949-00122

Keyser, R. M., & Hensley, W. K. (2002). Efficiency and resolution of germanium detectors as a function of energy and incident geometry. Paper presented at the *Nuclear Science Symposium Conference Record, 2002 IEEE, 1.* pp. 375-381.

Khandaker, M. U., Jojo, P. J., & Kassim, H. A. (2012). Determination of primordial radionuclides in natural samples using HPGe gamma-ray spectrometry. *APCBEE Procedia, 1*, 187-192.

Kinsara, A., Shabana, E., & Qutub, M. (204). Natural radioactivity in some building materials originating from a high background radiation area. *International Journal for Innovation*

Education and Research (IJIER), 2(6), 70-78. Retrieved from http://www.ijier.net/june2014.html

Laborie, J., Petit, G. L., Abt, D., & Girard, M. (2002). Monte Carlo calculation of the efficiency response of a low-background well-type HPGe detector. *Nuclear Instruments and Methods in Physics Research Section A: Accelerators, Spectrometers, Detectors and Associated Equipment, 479*(2), 618-630.

L'Annunziata, M. F. (2012). *Handbook of radioactivity analysis* Academic Press.

Luca, A., Neacsu, B., Antohe, A., & Sahagia, M. (2012). Calibration of the high and low resolution gamma-ray spectrometers. *Romanian Reports in Physics, 64*(4), 968-976.

Mann, W. B., Rytz, A., & Spernol, A. (2012). *Radioactivity measurements: Principles and practice* Elsevier.

MCNP User Manual, Version 5. (2003). *Radiation Safety Information Computational Centre (RSICC). Los Alamos National Laboratory*, University of California, USA. Available at http://mcnp-green.lanl.gov.s

Mothersill, C., Larivière, D., Smith, R. W., Thompson, M. P., Byun, S. H., Prestwich, W., et al. (2014). Dosimetric analysis of fathead minnow (pimephales promelas, rafinesque, 1820) exposed via ingestion to environmentally relevant activities of Ra-226 for two years. *International Journal of Radiation Biology, 90*(2), 169-178.

Najafi, S., & Fedoroff, M. (1985). Accurate gamma ray spectrum analysis. *Journal of Radioanalytical and Nuclear Chemistry, 89*(1), 143-152.

National Air and Radiation Environmental Laboratory (U.S.). (2006). *Inventory of radiological methodologies for sites contaminated with radioactive materials*. Montgomery, AL: U.S. Environmental Protection Agency, Office of Air and Radiation, Office of Radiation and Indoor Air, National Air and Radiation Environmental Laboratory

New Mexico State University: Department of agricultural, consumer and environmental sciences. (2013). Retrieved 09/08, 2014, from http://aces.nmsu.edu/thecenter/cail/inductively-coupled-plas.html

ORTEC. (2011). *GMX Series Coaxial HPGe Detector Product Configuration Guide*. Retrieved Sep 7, 2014, from http://www.ortec-online.com/download/GAMMA-X.pdf

Peralta, L. (2004). Measuring the activity of a radioactive source in the classroom. *European Journal of Physics, 25*(2), 211.

Radu, D., Stanga, D., & Sima, O. (2010). Transfer of detector efficiency calibration from a point source to other geometries using ETNA software. *Romanian Reports in Physics, 62*(1), 57-64.

Redd, R. A. (2003). *Radiation Dosimetry and Medical Physics Calculations using MCNP 5,*

Saint-Gobain Industrial Ceramics, inc. Bicron: Squareline square scintillation detector with demountable PMT. (1997). Retrieved 06/15, 2013, from http://pe2bz.philpem.me.uk/Comm01/-%20-%20Ion-Photon-RF/-%20-%20Scintillation/Site-001/Crystals/Geophysical/Lab/squareline.pdf

Saleh, I. H. (2012). Radioactivity of ^{238}U, ^{232}th, ^{40}K, and ^{137}cs and assessment of depleted uranium in soil of the Musandam peninsula, sultanate of Oman. *Turkish Journal of Engineering and Environmental Sciences, 36*(3), 236-248.

Samah, D. (2013). Computation of the efficiency of NaI(Tl) detectors using radioactive inverted well beaker sources based on efficiency transfer technique. *Journal of Advanced Research in Physics, 4*(1)

ŞİMŞEK, F. B., & CATAGAY, M. N. (2013). Geochronology of lake sediments using ^{210}Pb with double energetic window method by LSC. *LSC 2013 - Advances in Liquid Scintillation Spectrometry,* Barcelona.

Thompson, M. A. (2012). Determination of ^{226}ra in fish using liquid scintillation analysis.

Valkovic, V. (2000). *Radioactivity in the environment: Physicochemical aspects and applications* Elsevier.

Vandenhove, H., Verrezen, F., & Landa, E. R. (2010). Radium: Radionuclides. *Encyclopedia of Inorganic Chemistry,*

Varga, Z. (2008). Ultratrace-level radium-226 determination in seawater samples by isotope dilution inductively coupled plasma mass spectrometry. *Analytical and Bioanalytical Chemistry, 390*(2), 511-519.

Verplancke, J. (1992). Low level gamma spectroscopy: Low, lower, lowest. *Nuclear Instruments and Methods in Physics Research Section A: Accelerators, Spectrometers, Detectors and Associated Equipment, 312*(1), 174-182.

Vo, D. T. (1999). Comparisons of the DSPEC and DSPEC Plus Spectrometer Systems, *Los Alamos National Laboratory report LA-13671-MS.*

Vogt, J. (2009). *University of Leipzig faculty of physics and geosciences: Advanced physics lab - alpha-particle spectroscopy with a semiconductor detector.* Retrieved 09/08, 2014, from http://www.unileipzig.de/~physfp/versuche/alp_e.html

Ward, A. K. (2002). *University of Alabama department of aquatic biology - aquatic chemistry lab.* Retrieved 09/08, 2014, from http://biolaqua.as.ua.edu/waterchem.html

Weiner, E. R. (2012). *Applications of environmental aquatic chemistry: A practical guide* CRC Press.